# The Effect of Surface Topography on Crystallisation

Thomas Henry Dunn

Submitted in accordance with the requirements for the degree of
Doctor of Philosophy

The University of Leeds
School of Chemistry

August 2023

The candidate confirms that the work submitted is his/her own and that appropriate credit has been given where reference has been made to the work of others.

## Acknowledgements

There are lots of names of people who have gone above and beyond to help me to produce this work, but only one is printed on the cover.

I would firstly like to thank Fiona for investing so much time into developing me as a scientist, and pushing me to achieve things that I feel proud of.

I am also very grateful to Yi-Yeoun Kim, whose wisdom, creativity and words of encouragement helped me to keep going at the most challenging times.

I would like to thank past members of the Meldrum group who helped to create a supportive environment, which I felt proud to be a part of. Mark Levenstein and Shuheng Zhang supervised the short summer project I undertook in 2018, introducing me to Materials Science whilst inspiring and nurturing my curiosity. Once I started my PhD a year later, Tom Whale, James Campbell and Mark Holden worked patiently with me, talking through theory and showing me practical techniques. The work of Phillip Lee laid an immense foundation for the work in this thesis, and whilst we never personally met, he offered detailed guidance and support over email.

Xuefeng He, Cedrick O'Shaughnessy, Jo Galloway, Liam Hunter, David Green, and Tom Turner – thank you for not only offering me help and reassurance when I needed it, but teaching me to have fun with my research.

Huge thanks are also due to Alex Kulak and Stuart Micklethwaite, for taking all of my SEM images and adding artistic flair. Thank you to Matt Broadbent and Phil Thornton, a skilful machinist and electronics expert respectively, whose enthusiasm for building stuff and eye-wateringly quick turnarounds were a godsend.

I was surrounded by an amazing bunch of PhD students and postdocs throughout my studies. Ollie Ayre, whose boundless energy and optimism brought colour and laughter, and made me look forward to coming in to work every day. Ilaria Sandei and Steph Foster, who proved that a problem shared is a problem halved. For every brain cell I gained by studying, I lost approximately five courtesy of lunchtime and pub conversations with Zhao Jiang, Joe Barker, Raph Stone, Maxime Durelle, Xiaoyue Wu and Bidisha Tah Roy. Additional thanks are due to

Zhao for never rolling her eyes at me when I kept asking for more of her hair to grow crystals on, and Maxime for tirelessly explaining Kashchiev's work to me.

I am very grateful to have been involved with the EPSRC funded '*Crystallisation in the Real World*' research programme. Through a series of meetings, I have had the pleasure of watching the development of experimental and computational research from Helen Freeman, Martha Ilett, Adriana Matamoros Veloza, Maryam Azfali Haji Dela, Blane Keating, Vittoria Fantauzzo, Emma Armstrong, Alex Broad, Peter Morris, James Coe, Veselina Marinova, Aaron Finney, Dipanjan Mandal and Stephen Yeandel.

I would also like to thank my collaborators Sebastian Amland Skaanvik and Ian McPherson for their contribution to the body of work that makes up Chapter 5. They have been good friends, and are impressive researchers whose work I look forward to following throughout their careers in science.

Next I would like to thank senior academics, firstly those at Leeds – Malcolm Halcrow, Terry Kee, Rob Menzel, Chris Pask and Stuart Warriner, for investing time into my academic and personal development. From various other institutions, thanks are due to Pat Unwin, Colin Freeman, Ian Ford, David Quigley, Rik Drummond-Brydson, Jim De Yoreo, Susan Stipp, Daan Frenkel, John Harding, Matteo Salvalaglio, Hugo Christenson and Kevin Critchley for listening to me and offering advice. I deeply respect the geniality and approachability of each of you.

Additional thanks are due to Jim de Yoreo and Michaele Hardie for agreeing to examine this work, taking time to read and understand it, and hosting a challenging but fair viva. I enjoyed every moment of it.

On a personal note, there are four people to whom I owe endless gratitude. Thank you to my mum, dad, and brother, for checking up on me and offering me love when I needed it. I love you all. Lastly, my girlfriend Aimee. When cycling through dark and rainy Leeds in the middle of winter after a month of failing experiments, I always felt blessed to be able to come home to your warmth, and curl up in front of the telly with a cup of tea. You've seen me through my PhD from beginning to end, you're the world's best cheerleader and my best friend.

*“God made the bulk; surfaces were invented by the devil”*

**~ Wolfgang Pauli**

## Abstract

Nucleation is the most important event concerning formation of a crystal, since it decides where, how quickly and in what form the crystal grows – features which underpin key processes of multi-trillion-dollar industrial and consumer goods companies worldwide. Real surfaces are never perfectly flat, therefore, to demystify and control nucleation in real systems, we need to understand the profound and surprising effect of topographical features. Alongside surface chemistry, topography is one of the two determinants of a surface's ability to act as a heterogeneous nucleant, and over recent years evidence has shown topography to be a versatile tool. Surface topography is a hugely important but rarely considered factor in a wide range of natural crystallisation phenomena, from ice nucleation in the atmosphere to geological crystallisation and biomineralization. Controlling surface topography also offers a valuable practical tool to various industrial operations in controlling the position, polymorph and orientation of crystal nuclei, which is of importance for enhancement of crystalline materials processing, reduction in crystalline fouling, and the bottom-up design of novel functional nanomaterials. In this work, the impact of various surface topographies on crystallisation processes are investigated experimentally. Firstly, crystallisation on fractured glassy surfaces is explored, and this is discussed with respect to the effect of surface roughness on nucleation. Then, the theory of angle-directed nucleation is tested by fabricating two types of surfaces with features expressing defined angles, and investigating whether these can promote formation of crystals which match these angles. In chapters 3 and 4, a functionalised cracked iridium film is found to abundantly crystallise calcite selectively at the cracks. The mechanism underpinning this phenomenon is explored, and the apparent stochasticity of crack formation is controlled to pattern where crystallisation occurs at the surface. In the final chapter, the excellent nucleating properties of hair are quantified, and rationalised in terms of topography, charge and chemistry of the hair surface. Overall, this thesis aims to draw attention to the surprising and potent effect of using surface topography to control crystallisation.

# Table of Contents

# List of Figures

# List of Tables

# Abbreviations

| | |
|---|---|
| 16MHDA | 16-mercaptohexadecanoic acid |
| ACC | Amorphous calcium carbonate |
| ADM | Ammonia diffusion method |
| AFM | Atomic force microscopy |
| ALD | Atomic layer deposition |
| AP | Activity product |
| CBS | Circular backscatter detector |
| CDFT | Constrained density functional theory |
| CNT | Classical nucleation theory |
| CPG | Controlled pore glass |
| CVD | Chemical vapour deposition |
| EC solvent | Ethylene carbonate |
| EDX | Energy dispersive x-ray spectroscopy |
| EELS | Electron energy loss spectroscopy |
| ETD | Everhart-Thornley detector |
| FCC | Face-centred cubic |
| FC-Ir-PDMS | Functionalised cracked iridium-coated PDMS |
| FFT | Fast Fourier transform |
| FIB | Focused ion beam |
| GIS | Gas injection system |
| GRACE | Geometric real-space analysis of crystal epitaxy (software) |
| HAADF | High-angle annular darkfield imaging |
| hBN | Hexagonal boron nitride |
| HCP | Hexagonal close packed |
| HRTEM | High-resolution transmission electron microscopy |

| | |
|---|---|
| IPA | Isopropyl alcohol |
| ITO | Indium tin oxide |
| MOF | Metal-organic framework |
| NAP-XPS | Near-ambient pressure XPS |
| OM | Optical microscopy |
| PDMS | Polydimethylsiloxane |
| SAM | Self-assembled monolayer |
| SEM | Scanning electron microscopy |
| SFA | Surface force apparatus |
| SP | Solubility product |
| TEM | Transmission electron microscopy |
| TLD | Through lens detector |
| SAED | Selected area electron diffraction |
| SICM | Scanning ion-conductance microscopy |
| XPS | X-ray photoelectron spectroscopy |
| ZIF | Zeolitic imidazolate framework |

# Chapter 1 – Introduction

## 1.1 The Importance of Nucleation and Crystallisation

Nucleation is a fundamental process, whereby one state of matter is born from within another. The nucleation of gases from liquids behaves predictably, and as a result this is a process which is well-understood and can be tightly controlled. Artificially roughening the bottom of glassware (called 'cutting') allows for the steady release of bubbles from carbonated liquids, producing a long-lasting fluffy head on a cool crisp pint of beer. Nucleation of $CO_2$ bubbles is also responsible for the holes in Swiss cheese, which is achieved by suspending small amounts of hay powder in the fermenting curds as they cool. Whilst gas bubble nucleation is relatively easy to understand, scientists are routinely left baffled by the nucleation of crystals, which is a far more complex and unpredictable phenomenon.

Human existence is undeniably linked to crystals. Within our body are bones and teeth (hydroxyapatite), gravity-sensing otoliths in our ears (calcite), and in some unfortunate individuals, kidney stones (calcium oxalate). We live in houses made of concrete (various silicates and aluminosilicates), travel to work in crystalline steel vehicles and medicate our ailments with crystalline pharmaceuticals. Perhaps we decide to enjoy our dinner with a sprinkling of some salt or place a few ice cubes in our drink.

And if our lives weren't already full of crystals, we also hoard crystals for no apparent purpose other than to enjoy their curious and alluring beauty. Mankind's obsession with crystals dates back at least 105,000 years, with the uncovering of 'non-utilitarian' calcite crystals amongst other stone-age artefacts in the southern Kalahari Basin[1]. Similarly, a large smoky quartz specimen was uncovered at Alberite in Spain, a prehistoric burial site dated to around 5000 BC[2] (Figure 1). Geological evidence suggests that humans must have carried this crystal hundreds of kilometres from where it most likely originated. The writings of Pliny the Elder include the first written record of usage of crystal balls for 'soothsaying', or fortune-telling in 77 AD[3]. This unique relationship between humanity and crystals has been an important cultural practice throughout history and even exists into the present day.


**Figure 1: Smoky quartz specimen uncovered at Alberite, Spain[2]. *Copyright © Sociedad Española de Mineralogía.***

Crystallinity is also often cited as the inspiration for artistic expression, where one striking example is the Futuroscope Kinemax in Chasseneuil-du-Poitou, France (Figure 2A), which resembles a cluster of quartz crystals (Figure 2B). Other more renowned architectural designs such as the Louvre Pyramid, the Shard, and the Empire State Building may be described as examples of crystalline architecture, with unnatural perfect geometries and sharp edges which contrast with the rounded edges and fractal structures much more commonly found in nature (e.g. rocks, trees, rivers).

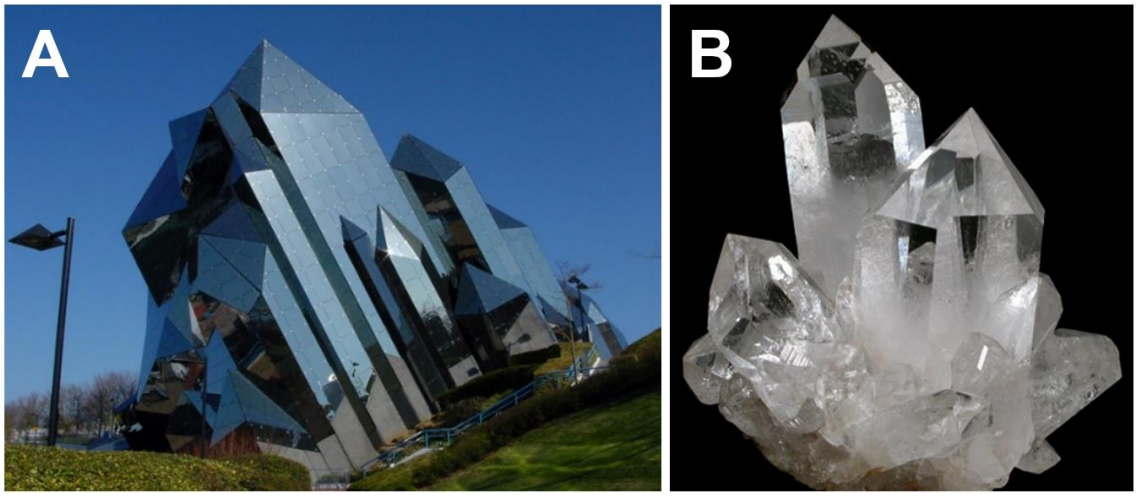


**Figure 2: (A) Futuroscope Kinemax in Chasseneuil-du-Poitou[4] *Copyright © Parc du Futuroscope 2023*. (B) Cluster of quartz crystals[5]. *Copyright © John H. Betts, All Rights Reserved.***

### 1.1.1 Scientific History of Crystals

It is thought that the first step in understanding crystal growth was the work of Nicholas Steno in the mid-17$^{th}$ century[6]. He observed that quartz crystals, although varied in shape and size, always contained exactly the same angles between adjacent faces, and speculated that these must have grown layer-by-layer on the faces of a nucleus. A few years later Robert Boyle published '*The Origin of Formes and Qualities*'[7], in which he described his observation that the addition of different salts to a crystallising solution could change the crystal 'habit'. The habit of a crystal is a general description of its shape, including defects such as twinning. The work of these early scientists demonstrated an important point about the nature of crystallisation – a chemical system contains intrinsic rules which predetermine the structure of a crystal grown from it.

In 1832, Wohler and von Liebeg are credited with discovering crystal polymorphism when investigating the crystallisation of benzamide, observing that the silky needle crystals gradually converted to a blocky form[8]. Nearly a century later, Volmer and Weber published '*Keimbildung in übersättigten Gebilden*'[9], which translates to 'Nucleus Formation in Supersaturated Solutions'. Here, they described what is now referred to as Classical Nucleation Theory (CNT), a fundamental model which is introduced in Section 1.3. This theory explains the thermodynamics involved in formation of a crystalline phase from melt, vapour or solution.

## 1.2 Crystal Structure and Polymorphism

A crystal is a material which comprises a series of structural units arranged in an ordered lattice that extends in three dimensions. The simplest repeating unit of a crystal is known as a unit cell, which can be expressed by three edge lengths (*a,b,c*) and three angles between these edges (*α,β,γ*). There are 14 distinct unit cell arrangements, known as Bravais lattices, grouped into seven lattice systems (Table 1). Beyond this classification system, every possible unit cell can also be described using symmetry operators, which allows them to be categorised by 'space group', of which there are 230 distinct types[10].

| Lattice System | Edge Lengths | Axial Angles | **Lattice Types** (P = Primitive C = Base Centred I = Body Centred F = Face Centred) |
|---|---|---|---|
| **Cubic** | $a = b = c$ | $\alpha = \beta = \gamma = 90^o$ | P I F |
| **Orthorhombic** | $a \neq b \neq c$ | $\alpha = \beta = \gamma = 90^o$ | P C I F |
| **Hexagonal** | $a = b \neq c$ | $\alpha = 120^o$<br>$\beta = \gamma = 90^o$ | P |
| **Rhombohedral** | $a = b = c$ | $\alpha = \beta = \gamma > 120^o$ | P |
| **Tetragonal** | $a = b \neq c$ | $\alpha = \beta = \gamma = 90^o$ | P I |
| **Monoclinic** | $a \neq b \neq c$ | $\alpha \neq 90^o$<br>$\beta = \gamma = 90^o$ | P C |
| **Triclinic** | $a \neq b \neq c$ | $\alpha \neq \beta \neq \gamma$ | P |

**Table 1: Unit cell dimensions for the 14 Bravais lattices.**

The crystal structure adopted by a compound in a particular environment is usually its lowest-energy configuration. This results from maximising intermolecular or interatomic bonding interactions, both internally and with its surrounding environment. There are sometimes multiple crystal structures of the same compound which are close in energy however, and these are known as polymorphs. It is often stated that the number of (discovered) polymorphs for a given compound is proportional to the time and money spent in research on that compound[11]. Organic crystals are generally regarded as more polymorphic than ionic, covalent or metallic crystals, since they can organise into a wider variety of bonding arrangements.

Polymorphism is extremely important to a range of industrial and natural processes, as the structure of a crystal defines its morphology, hardness, electronic/magnetic properties, melting point and dissolution rate. In turn these properties can impact the application of a range of materials such as the tabletability/bioavailability of drug formulations and the strength/resistance of building materials.

## 1.3 Classical Nucleation Theory

### 1.3.1 Thermodynamics of Homogeneous Nucleation

As with any phase transition, there are enthalpic/ entropic costs and gains associated with nucleation. The Gibbs free-energy of crystal nucleation is detailed in Equation 1, where $\Delta G_c$ is the Gibbs free-energy change, $\Delta H_c$ and $\Delta S_c$ are the enthalpy and entropy changes (respectively) associated with formation of a crystalline body from its parent phase, and $T$ is the temperature (in Kelvin).

$$\Delta G_c = \Delta H_c - T\Delta S_c \qquad \textbf{Equation 1}$$

The thermodynamics of nucleation can be related to familiar concepts such as concentration using the notion of the activity product ($K_{AP}$) and solubility product ($K_{SP}$). Equation 2 gives a generic chemical equation for dissolution of a solid $A_aB_b$ into its soluble constituents A and B.

$$A_aB_{b(s)} \rightleftharpoons aA_{(aq)} + bB_{(aq)} \qquad \textbf{Equation 2}$$

The equilibrium constant $K_{eq}$ for such a process is shown in Equation 3, where the square brackets refer to the concentrations of each species. In the equation, these are raised to the exponent of their respective stoichiometries.

$$K_{eq} = \frac{[A]^a[B]^b}{[A_aB_{b(s)}]} \qquad \textbf{Equation 3}$$

Solids have an activity of 1, and since we define the system at dynamic equilibrium, the equilibrium constant is expressed simply as the product of solute concentrations. If enough of the solid $A_aB_b$ is added, the solution will become saturated with respect to the solid $A_aB_b$, at which point the equilibrium constant is replaced by a new term called the solubility product $K_{SP}$ (Equation 4).

$$K_{SP} = [A]^a[B]^b \qquad \textbf{Equation 4}$$

Solubility products have been measured for a wide range of pure solids in various solvents and are constant at a specified temperature. It is however possible for more of a substance to be dissolved in a system than its solubility product. This is known as a supersaturated (non-equilibrium) state. Supersaturation $S$ and supersaturation index $SI$ are calculated by Equation 5 and Equation 6 respectively, where $AP$, the activity product, is the product of the actual

concentrations of solute species. *AP* can be larger than $K_{SP}$ when the solution is supersaturated.

$$S = \frac{[A][B]}{[A]_{sat}[B]_{sat}} = \frac{AP}{K_{SP}}$$ **Equation 5**

$$SI = ln\frac{AP}{K_{SP}}$$ **Equation 6**

Another simple and commonly-used term is supersaturation ratio, which is expressed as the ratio of the concentration of a solute to its solubility (Equation 7).

$$S_R = \frac{[A]}{[A]_{sat}}$$ **Equation 7**

For any of these definitions of supersaturation, if they are equal to 1, the system is saturated with respect to a particular species. When below 1, the system is undersaturated, and above 1, the system is supersaturated. From a supersaturated state, nucleation of a new phase is thermodynamically favourable.

When considering nucleation of a spherical phase from within a parent phase (termed homogeneous nucleation), the free energy can be calculated by adding a surface term (the interfacial tension between the nucleus and its parent phase) and a volume term (the energy change upon forming the body of the nucleus). This is shown in Equation 8, where $\Delta\mu$ is the change in chemical potential following crystallisation, $\nu$ is the volume of a single constituent particle in the crystal, $r$ is the radius of the nucleus and $\gamma$ is the interfacial tension between the nucleus and its parent phase.

$$\Delta G = \frac{-4\pi r^3}{3\nu}\Delta\mu + 4\pi r^2\gamma$$ **Equation 8**

A graph of the function shown in Equation 8 is shown in Figure 3. Initially, nucleation is unfavourable ($\frac{\partial G}{\partial r} > 0$) as the energy cost of forming an interface between the nucleus and parent phase dominates over the energy gain associated with forming the bulk of the condensed phase. However, at a certain radius known as the critical radius $r_c$, $\frac{\partial G}{\partial r} = 0$, and at larger sizes $\frac{\partial G}{\partial r} < 0$,

meaning that beyond the critical radius, growth of a nucleus becomes spontaneous. For a specific crystal system, the size of the critical radius is dependent on supersaturation and temperature.

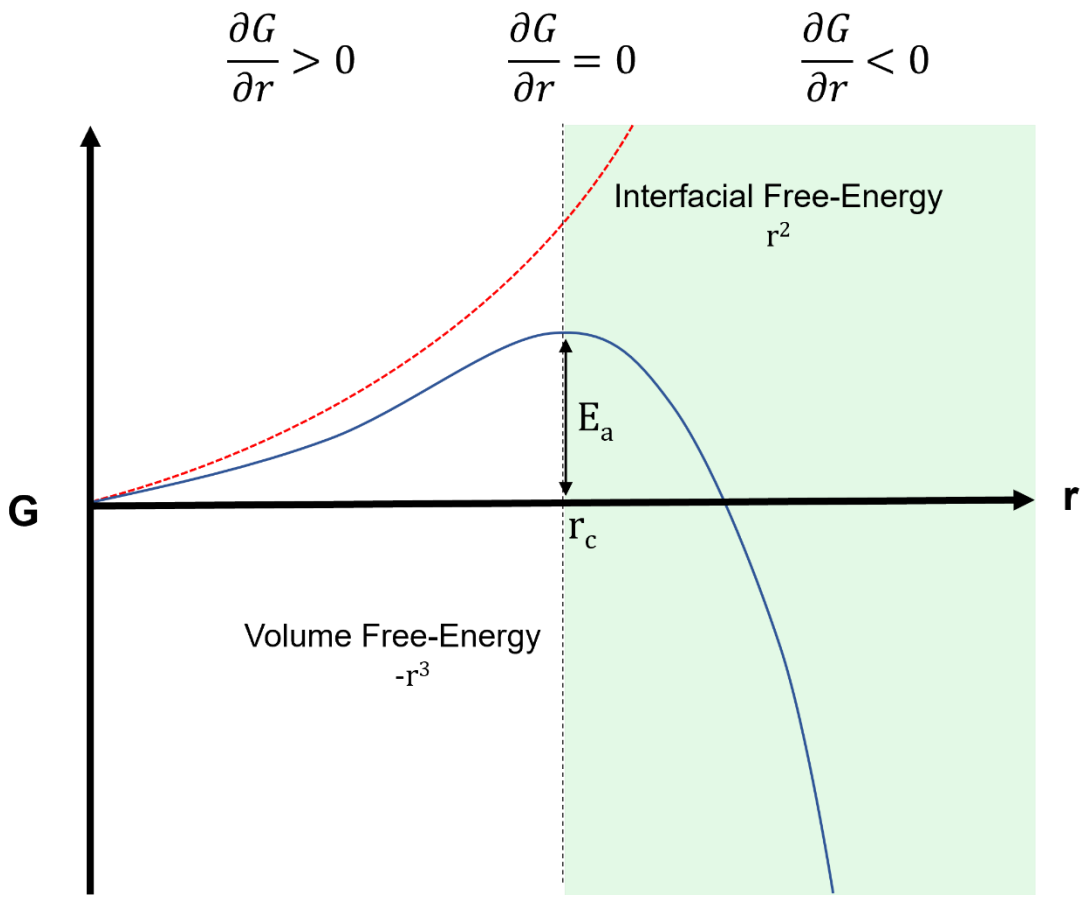


**Figure 3: Diagram detailing how free-energy of nucleus growth changes as a function of its size at constant temperature and supersaturation. The green region indicates the nuclear size at which growth becomes spontaneous.**

### 1.3.2 Nucleation Kinetics

Thermodynamics identifies which transitions between phases are energetically favourable, but when many pathways are possible, thermodynamics is inadequate for predicting which pathway happens first, or how quickly nucleation will occur. Analysing nucleation kinetics can help to rationalise why highly supersaturated systems routinely fail to crystallise, and why metastable polymorphs may preferentially nucleate from solution. Equation 9 gives the rate

of nucleation of a particular phase as a function of the energy barrier height and temperature. $k_B$ is the Boltzmann constant and $A$ is the exponential prefactor, which depends on the attachment frequency $v^*$, the Zeldovich factor $Z$ (relating to the likelihood of critical nuclei growing or dissolving) and the number of nucleation sites $n$. Equation 11 is an alternate form of Equation 9, and expresses the rate as a function of supersaturation $S$, where $B$ is the thermodynamic rate parameter given by Equation 12. Here, $\gamma$ is the interfacial tension, $v_m$ is the volume of a molecular unit and $T$ is temperature.

$$J = A \exp\left(-\frac{E_a}{k_B T}\right) \quad \textbf{Equation 9}$$

$$A = v^* Z n \quad \textbf{Equation 10}$$

$$J = AS \exp\left(-\frac{B}{ln^2 S}\right) \quad \textbf{Equation 11}$$

$$B = \left(\frac{16\pi\gamma^3 {v_m}^2}{3(k_B T)^3}\right) \quad \textbf{Equation 12}$$

The probability $P$ of nucleation occurring at a time $t$ is given by Equation 13, where $V$ is volume and $t_g$ is a time correction, accounting for any lag between the actual nucleation time and the point where it can be measured.

$$P(t) = 1 - \exp\left(-JV\left(t - t_g\right)\right) \quad \textbf{Equation 13}$$

### 1.3.3 Multi-Step Classical Nucleation

Ostwald's 'rule of stages' states that a system with the thermodynamic driving force to undergo phase transformation to a crystalline state can do so via several metastable phases[12]. By lowering its free energy in small steps, the system avoids the large free energy barrier associated with a single nucleation step; this is kinetically favourable. 1-step nucleation is always possible, however multistep phase transformations with reduced nucleation barriers are often more likely to be successful. Importantly, multistep models consider regard the phase transformation between metastable and crystalline phases as a secondary nucleation event isolated from the bulk solution.

This means that the thermodynamics and kinetics of transformation of the metastable phase into the crystalline phase are independent of the concentration of the original phase[13].

### 1.3.4 Heterogeneous Nucleation

Heterogeneous nucleation is where nucleation is facilitated by a solid surface. It is thought that the vast majority of crystals formed by a process of heterogeneous rather than homogeneous nucleation, since removal of heterogeneous contaminants is extremely challenging and these contaminants can be highly effective at promoting nucleation. The Gibbs free-energy change of nucleation can be modified to describe heterogeneous nucleation by introduction of a pre-factor φ, which describes the magnitude of the free-energy reducing effect of a heterogeneous surface (Equation 14).

$$\Delta G_{hetero} = \phi \Delta G_{homo} \qquad \textbf{Equation 14}$$

The activity of surfaces towards promoting nucleation is usually attributed to the reduction in area of the solid-liquid interface. The contact angle between the nucleus and surface can be used to quantify the magnitude of this reduction in nucleus-liquid interfacial area. Contact angle is related to the interfacial energies between the nucleus, surface and liquid by Young's relation (Equation 15 and Figure 4), and the pre-factor φ by Equation 13.

$$cos\theta = \frac{\gamma_{sl} - \gamma_{ns}}{\gamma_{nl}} \qquad \textbf{Equation 15}$$

$$\phi = \frac{(2 + cos\theta)(1 - cos\theta)^2}{4} \qquad \textbf{Equation 16}$$

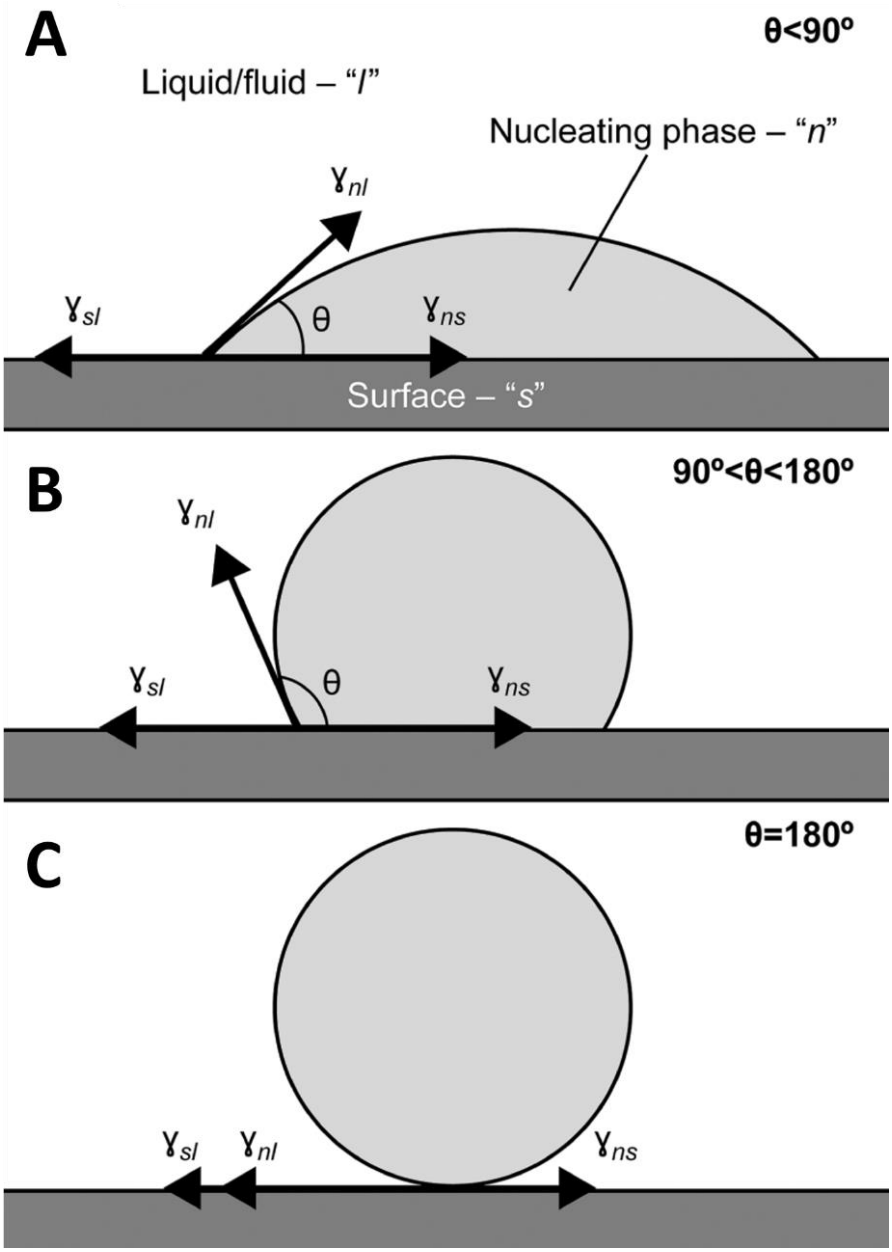


**Figure 4: Diagram showing contact angles of nuclei on surfaces with different interfacial tensions. (A) A strongly nucleating surface. (B) A poorly nucleating surface. (C) a non-nucleating surface**[14].

While contact angles of liquid nuclei can be easily measured, this is much harder for solid crystalline nuclei. Crystal nuclei possess structural order, such that their shapes are not solely dependent on interfacial tensions. In this case, calculations based on the interfacial energies of the nucleus, surface and liquid may predict a contact angle of 10°, but this will not be the actual measured contact angle. Instead, it is simpler to consider the physical implications of varying surface-nucleus contact angles. At a contact angle of 0° (perfect wetting) the free energy

barrier to nucleation would be removed completely, which would imply that the surface behaves as a seed crystal. At contact angles approaching 180°, there would be no interaction between the surface and the nucleus so the energy barrier to nucleation would approach homogeneous values.

### 1.3.5 Heterogeneous Nucleation at a 2D Step

CNT for nucleation on a flat plane can be adapted to describe nucleation within a 2D step[15]. The free-energy of formation of a critical nucleus $\Delta G_S^*$ at a step edge with angle η is given by Equation 17. F is a structural factor comprising a complex function of step angle η and contact angle θ.

$$\Delta G_S^* = \left(\frac{4\pi\gamma_{nl}^3}{3\Delta G^2}\right) F(\theta,\eta) \qquad \textbf{Equation 17}$$

Sholl and Fletcher evaluated the structure factor F in terms of θ and η (Equation 18) [16]. ψ is related to θ and η by Equation 19.

$$F(\theta,\eta) = \frac{1}{\pi}\Big[\cos\theta\sin^2\theta\sin\psi - \cos\theta\,(3-\cos^2\theta)\psi + 4\sin^{-1}(\sin\frac{\psi}{2}\sin\frac{\eta}{2})\Big] \qquad \textbf{Equation 18}$$

$$\cos\frac{\psi}{2} = \cot\theta\cot\frac{\eta}{2} \qquad \textbf{Equation 19}$$

Equation 20 expresses the ratio of nucleation frequency at a step $I_S$ to that on the flat surface $I_F$. $\Delta G_v$ is the free energy of forming one unit volume of a solid nucleus, g is the fraction of step-sites compared to flat surface sites, and [K(θ) – F(θ,η)] is the difference between the 'structural factors' of the flat surface K and step F.

$$ln\frac{I_S}{I_F} = \ln g + \exp\left(\frac{4\pi\gamma_{nv}^3}{3\Delta G_v^2 kT}[K(\theta) - F(\theta,\eta)]\right) \qquad \textbf{Equation 20}$$

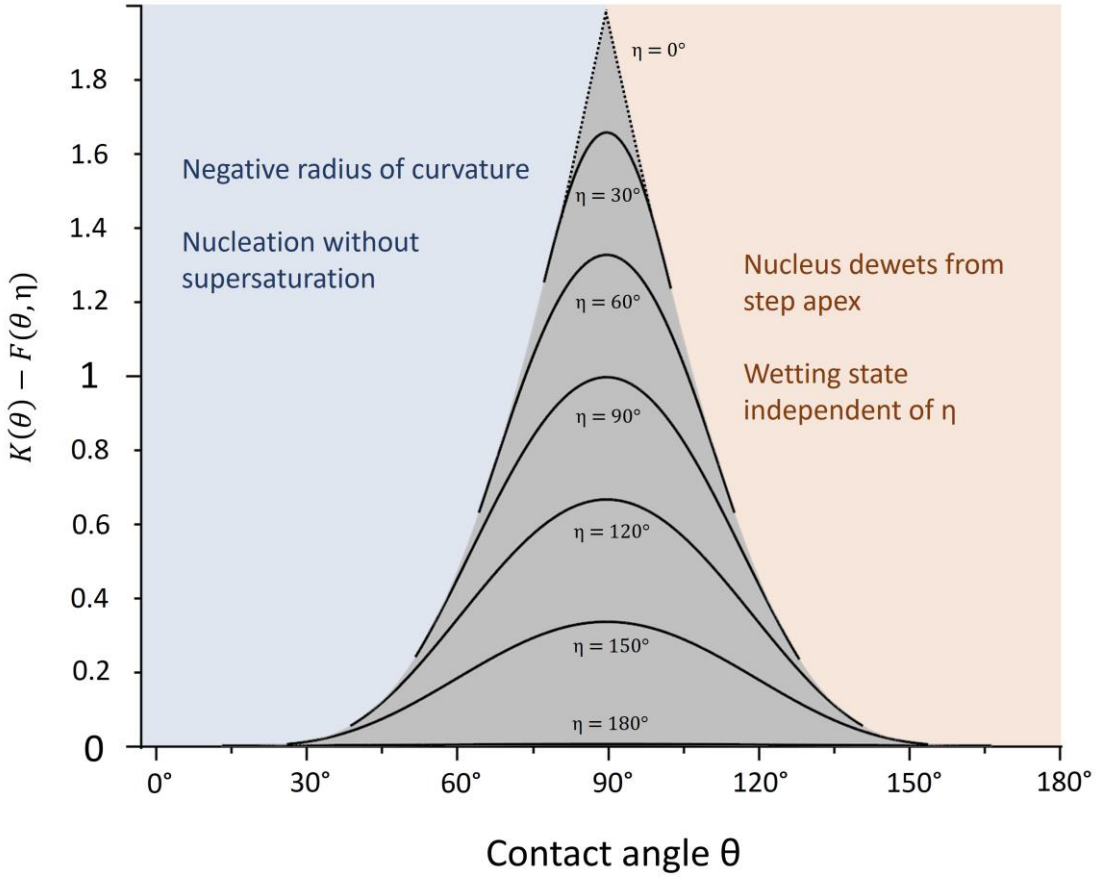


**Figure 5: Difference between K([θ]) (the geometric factor for a flat surface) and F(η,[θ]) (the geometric factor for a step with angle η as a function of contact angle [θ] at representative values of step angle η[16]. *Replotted with permission from University of Toronto Press.***

Figure 5 shows a plot of [K(θ) – F(θ,η)]. When considered with respect to Equation 20, it shows that as long as the contact angle θ is between 0 and 180, and the step angle is also between 0 and 180 (i.e. it is concave, not convex), the formation of a liquid nucleus is faster at a step than on a flat surface. For the real part of the function (i.e. not under conditions by which spontaneous nucleation would occur, or dewetted states), it can be seen that the greatest ratio of structure factors is reached at a contact angle of 90° for any step angle. This means that the key to *selectively* forming nuclei at step sites is to ensure that the substrate-nucleus interaction is of intermediate strength. This does not however suggest that a contact angle of 90° will lead to high nucleation rates, but that the *ratio* of nucleation events at the step compared to an adjacent flat plane will be highest.

To visualise the physical states at the regions of the function that are outside of the bounds $\frac{\pi-\eta}{2} < \theta < \frac{\pi+\eta}{2}$, Figure 6 shows three cases with varying values of θ and η, where nuclei are depicted as sections of an imaginary circle, bounded by the walls of the step. In this model, the ratio R of the real area of the circular droplet compared with its imaginary counterpart for a particular value of θ and η can be used to estimate the likelihood of forming a nucleus in that state. As the imaginary area grows at the expense of the real area, the propensity to nucleate in that condition increases. Simply put, nucleation is favourable if R is close to 0, and unfavourable if R is close to 1.

In the left (blue) region of the plot shown in Figure 5, nucleation can occur without supersaturation, which is always the case when the radius of curvature of a nucleus is negative. Figure 6B illustrates this condition, which has only been observed experimentally for liquids condensing from vapour[17]. As shown by the boundary between the grey and blue regions in Figure 5, nuclei with a contact angle greater than 90$^{o}$ will always face a barrier to nucleation, regardless of how acute the step is (Figure 6C).

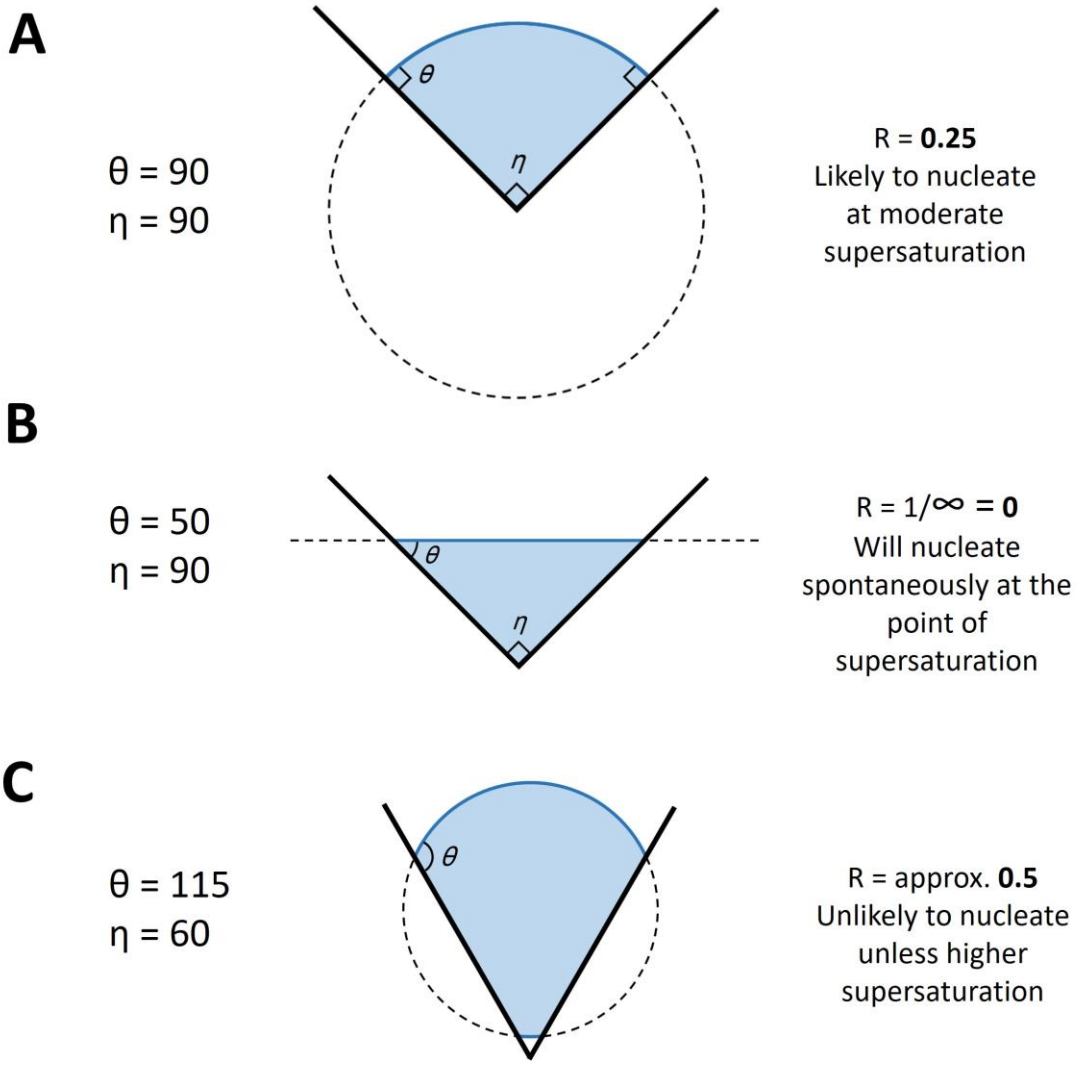


**Figure 6: Three characteristic cases for nucleus wetting are summarised in A, B and C, where R represents the fraction of an imaginary circle occupied by the droplet. Large values of R correspond to high barriers to nucleation, and reducing R towards zero represents a move towards a barrierless transition.**

## 1.4 Deviations From Classical Nucleation Theory

Classical nucleation theory is a good starting point for understanding the fundamentals of crystallisation. However, it is important to consider deviations from this[18]. Non-classical nucleation theories may be applicable for complex phenomena such as polymorphism and crystallisation in confinement[19,20]. Furthermore, due to the fact that crystallisation is so fundamentally challenging to investigate, little is known about whether classical or non-classical nucleation theories can be applied to even simple systems such as nucleation in bulk solution [21,22]. Common non-classical deviations from assumptions made by CNT are summarised by Table 2.

There are systems in which classical models can accurately predict nucleation kinetics[23,24], and others where non-classical approaches are required[25,26]. Researching which systems exhibit classical and non-classical behaviour is paramount to understanding more about the fundamentals of crystallisation and aligning computational and experimental methods of research.

| Classical Nucleation Model | Non-Classical Nucleation Model |
|---|---|
| Nuclei are spherical in shape. | Nuclei may resemble any shape (cubic, rod-shaped etc.)[27]. |
| The phase which nucleation occurs from is chemically and thermally uniform. | Clustering, surface accumulation and local fluctuations in chemical composition/thermal energy can inhibit or initiate nucleation[28,29]. |
| Nucleation follows steady-state kinetics. | The system may establish a steady distribution of pre-nucleation clusters before anything can nucleate[30]. For multistep nucleation, the rate determining step may be the formation of a dense liquid intermediate [31]. |
| Interfaces are discrete boundaries without volume. | Interfaces are regions which may be large, diffuse and possess some ordering[32]. |
| The system transforms from the old phase to crystal through discrete states with defined free energy barriers. | Any cluster of monomer larger than 1 unit is associated with a free energy cost, which is highly dependent on partial ordering of the cluster[32]. |

**Table 2: Assumptions made by CNT and respective non-classical approaches, adapted from [30].**

## 1.5 Calcium Carbonate

### 1.5.1 Polymorphism

Calcium carbonate is sparingly soluble mineral, and is one of the most abundant biominerals in nature, crystallised by corals, molluscs and phytoplankton to form intricate but highly resilient exoskeletons and shells [33]. Within these structures, calcium carbonate typically exists as the polymorphs calcite or aragonite, the unit cells of which are shown in Figure 7A & B. There also exists a third polymorph, vaterite (Figure 7C), which is metastable towards calcite and aragonite, but this is commonly only found in abiogenic calcium carbonate[34].

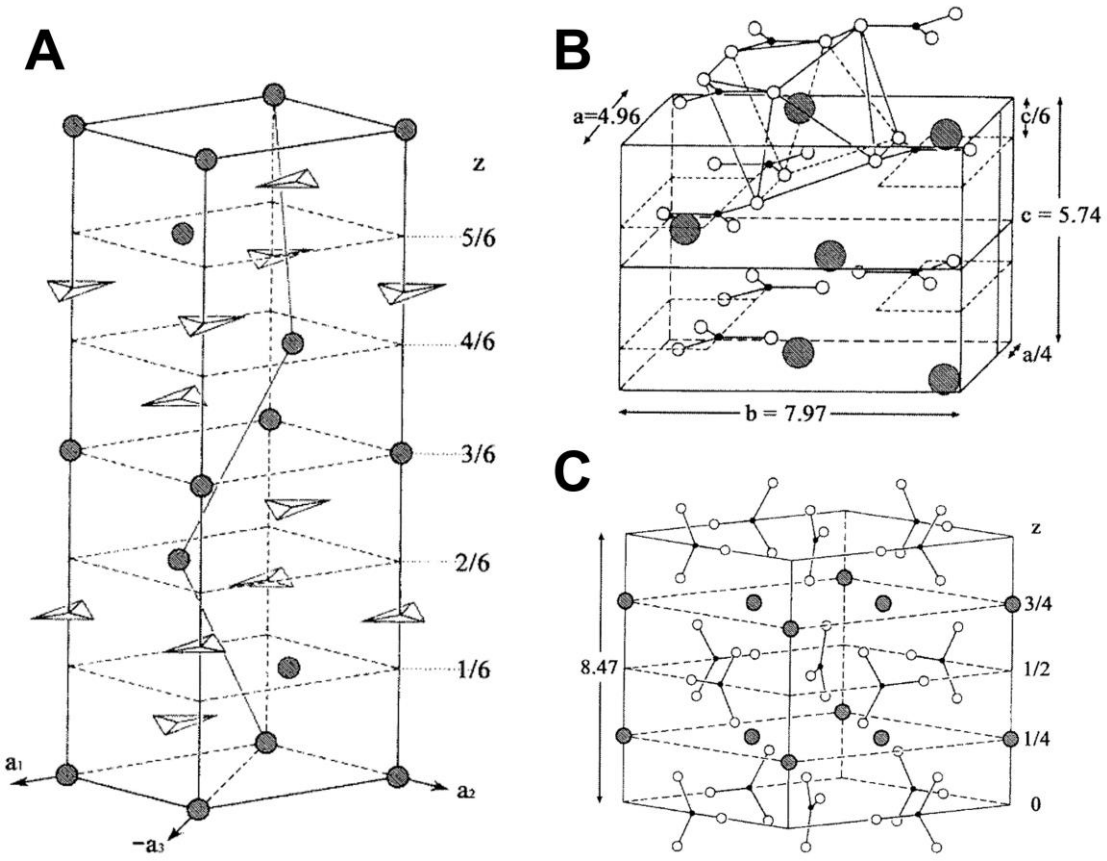


**Figure 7: Structures of (A) calcite, (B) aragonite and (C) vaterite[34]. *Reproduced with permission from Taylor and Francis.***

Calcium carbonate also exhibits an amorphous phase (ACC) which has attracted much attention for its role in the crystallisation of biogenic and abiogenic calcium carbonate. This role is still widely debated amongst the scientific community.

Where ACC has been directly observed, it typically precipitates with a large quantity of incorporated water, and has a much longer lifetime than other documented amorphous mineral phases[35] due to the energy cost of dehydration to form a crystalline phase. In biogenic systems, the lifetime of ACC is further prolonged for use as a dense storage deposit of calcium carbonate, which can be crystallised when and where required[36]. This long-lifetime of ACC is thought to be achieved by a combination of confinement (discussed further in Section 1.7.3) and incorporation of macromolecules[37] or magnesium ions[38,39].

### 1.5.2 The Effect of Magnesium Ions on Precipitation of Calcium Carbonate

The presence of over 8.5 mol% of magnesium[40], or a Mg:Ca ratio greater than 2:1[41] during the precipitation of calcium carbonate has been documented to lead to formation of aragonite rather than the room-temperature thermodynamic polymorph calcite. The cause of this phenomenon has been studied and debated for decades, which has sparked a number of general theories to emerge. Using simulation and experimental techniques, it has been found that the growth of calcite crystals is inhibited by the binding of $Mg^{2+}$, particularly at the {1010} facets[42–44], which may allow aragonite crystals time to grow to larger sizes. Magnesium may also promote formation of a proto-aragonite ACC precursor phase[45], increasing the likelihood of large stable aragonite domains forming.

## 1.6 Potassium Nitrate

$KNO_3$ is a highly water soluble mineral which occurs naturally as the mineral nitre, and exhibits three major polymorphs, known as *α* (orthorhombic), *β* (rhombohedral), and *γ* (rhombohedral). *γ*-$KNO_3$ is stable at temperatures exceeding 90$^{o}$C[46,47], however, *α* and *β* are both commonly observed under ambient conditions. At room temperature and pressure, *β* is metastable with respect to *α*, although *β* is commonly observed to crystallise first (the kinetic product) during crystallisation experiments. Laval *et al.* studied the dissolution of the *α* and *β* phase within microfluidic droplets[48], and showed that the phases are morphologically simple to distinguish (Figure 8A/B), and at room temperature,

there exists a small window of concentrations (between 3.2 and 4 M) where only the α phase is stable (Figure 8C).

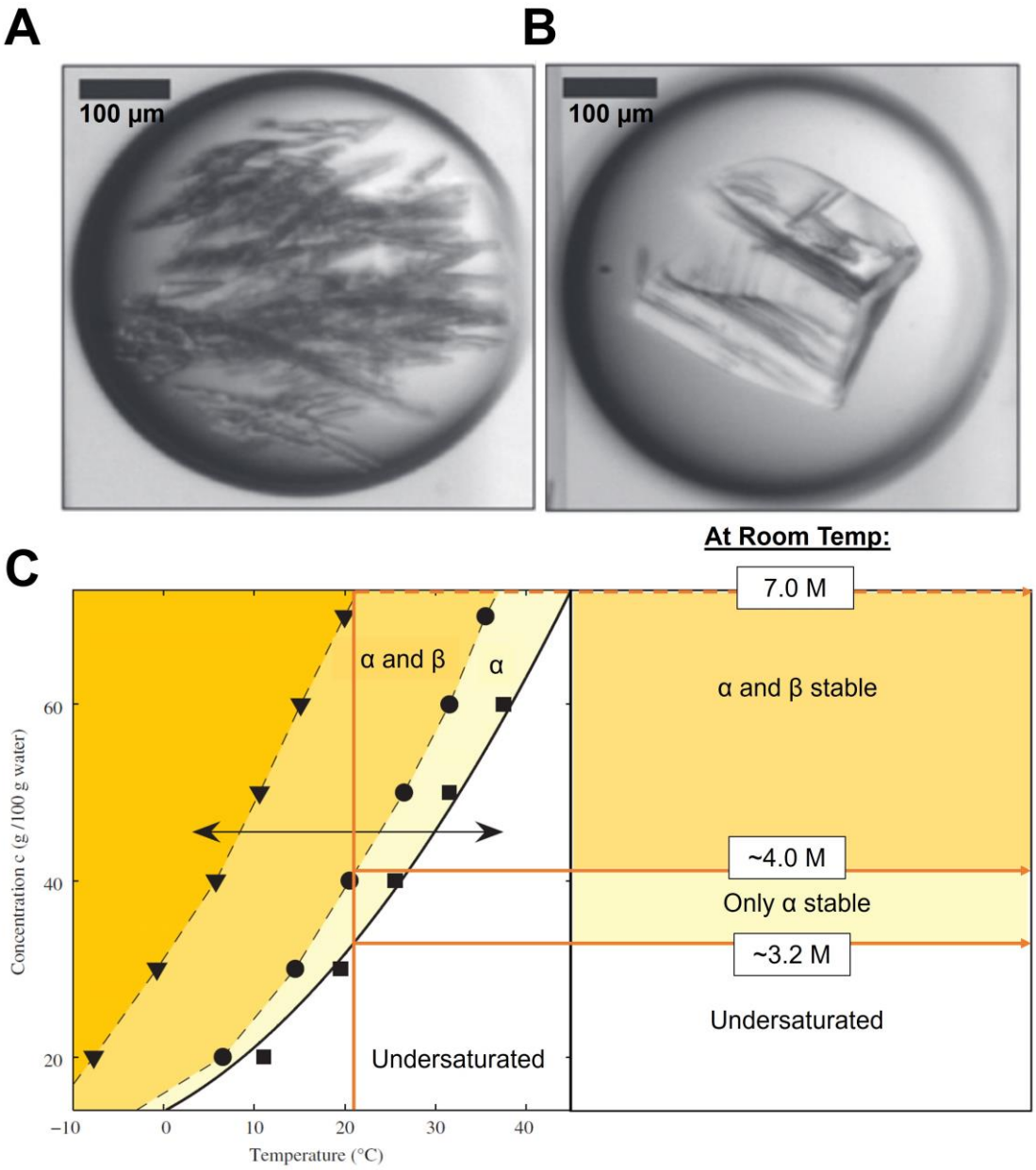


**Figure 8: Composite figure showing the work of Laval et al.[48]. (A) and (B) show OM images of *α*-$KNO_3$ and *β*-$KNO_3$ respectively, grown in microdroplets. (C) A solubility curve for *α*-$KNO_3$ and *β*-$KNO_3$ at varying temperature, with highlighted conditions for room temperature. *Figure reproduced with permission from Elsevier BV.***

## 1.7 Crystallisation at Real Surfaces

### 1.7.1 Epitaxy

Epitaxy is the mechanism by which crystallisation of one compound is promoted on the surface of another due to structural similarities between the two. Epitaxy is usually described as a growth process, although it involves a distinct nucleation step so is not a barrierless transition as is growth from a seed crystal. Layering of semiconductor materials for electronic devices is usually achieved via epitaxial growth of one layer upon another, which means there is great interest in understanding how these crystalline materials assemble upon one other[49]. Additionally the ease of searching for epitaxial matches using large databases and software such as GRACE[50] means that epitaxial nucleants are very widely explored where effective nucleants are required, for example in protein crystallisation[51–54].

Studies of ice nucleation are of enduring importance in the field of climate science, with cloud seeding offering ways to regionally augment water supply and prevent hail[55]. One of the most widely used ice nucleants in cloud seeding is silver iodide, which is thought to show enhanced ice nucleation activity due to a close lattice match. Both ice and silver iodide have a hexagonal lattice with lattice constants of 4.54 and 7.41 Å (ice) and 4.59 and 7.49 Å (silver iodide)[56]. Whilst epitaxial matches can be used to direct further investigation into crystal nucleants, their presence does not guarantee that a nucleant will be successful however. $BaF_2$ has a good epitaxial match with ice but is a poor nucleant[57], and similarly there are many effective ice nucleators including cholesterol with no obvious structural relationship[58,59].

### 1.7.2 The Impact of Surface-Induced Liquid Ordering on Crystallisation

The characteristics of a solid-liquid interface within which nucleation takes place are crucial to the kinetics of the process. The interface is an unusual region far from the classical depiction of bulk liquid in contact with a hard surface. Because the atoms constituting a surface are generally immobile, the most stable configuration of the interface must be achieved by rearrangement of the liquid in

contact with it. The degree of ordering increases as the liquid and solid interact more strongly. The extent to which ordering takes place has been explored for a variety of contrasting systems, from molecular melts[60], to electrolyte solutions[61].

Considering electrolytes first, ions in proximity to charged surfaces in solution have been shown to rearrange into alternating layers of anions and cations at the surface. Early work using surface-force-apparatus (SFA) measurements of parallel mica plates separated by electrolyte solution identified oscillating repulsive hydration forces within 2 nm of the mica surface[62]. These oscillating forces correspond to layered ions in an interfacial structure known as the electric double-layer (Figure 9)[63], which assembles because the electric field imposed on the system by a charged surface stores chemical potential energy in the solution via charge segregation.

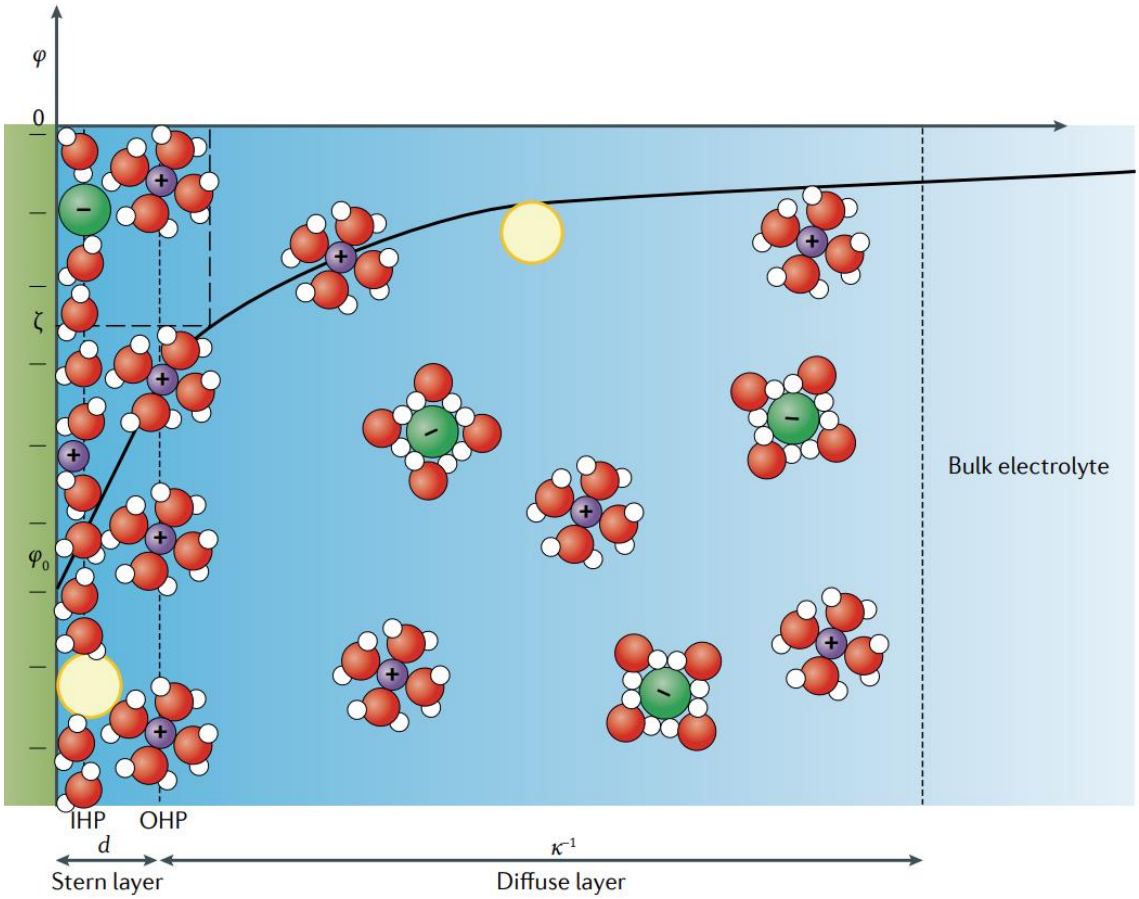


**Figure 9: - Gouy-Chapman-Stern model of the electric double layer [63]. *Reproduced with permission from Nature Research.***

The Guoy-Chapman-Stern model assumes a mean electric field at the surface, which means it does not consider any *lateral* structural factors imposed by the surface on the solution. Crystals are 3D structures, which means that energy barriers to lateral diffusion of ions may alter crystallisation pathways just as much as a barrier to diffusion perpendicular to the surface would.

3D-AFM was recently developed to probe liquid ordering at interfaces[61] and work by Martin-Jimenez *et al.* shows that aqueous KCl solutions exhibit both vertical and lateral structural order close to mica surfaces[64] (Figure 10). Complementary computational fluid density functional (CDFT) calculations from this work showed that the interfacial liquid was crystal-like in structure but retained ion and water mobilities that were bulk-liquid-like.

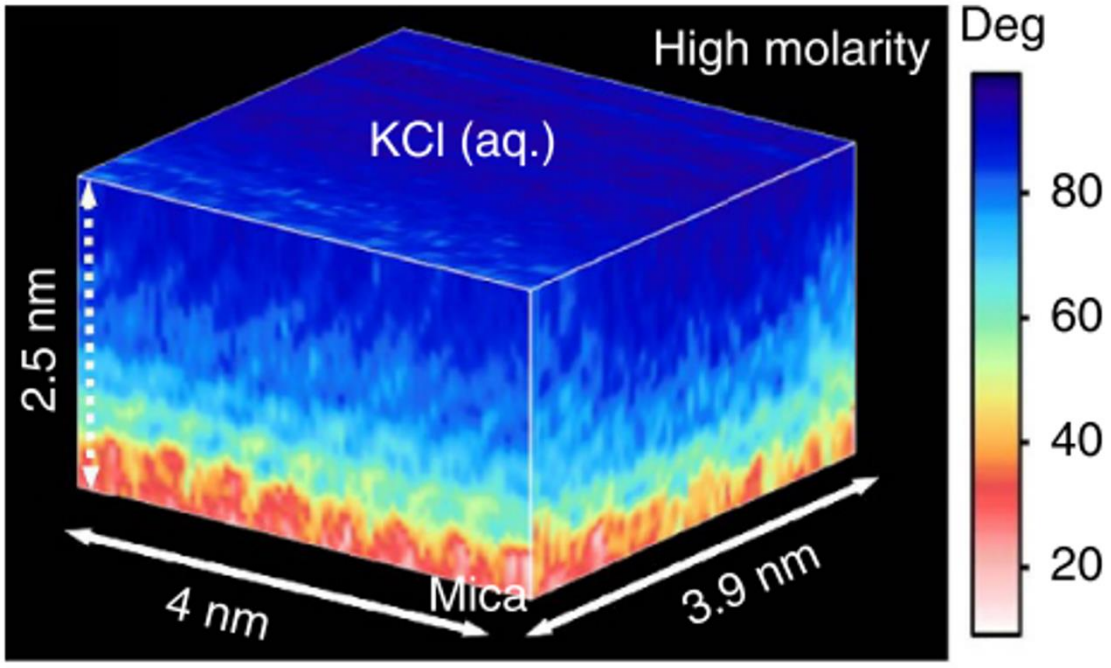


**Figure 10 – 3D-AFM map of a mica surface immersed in KCl solution, showing structuring of the solution at the mica interface** [64]**.** ***Reproduced with permission from Springer Nature.***

Melt phases may experience greater restrictions to mobility at interfaces however. Simulations of crystallisation of molten silicon upon a seed crystal showed that liquid ordering at the surface produced a highly viscous layer where diffusion of silicon atoms to the seed surface was strongly restricted[65]. In some regions this

was up to four times greater than the energy barrier for diffusion through bulk liquid silicon.

Water molecules interact strongly with polar surfaces due to their ability to form adaptive hydrogen-bonding networks, which may affect ice crystallisation[66]. Slightly changing the lattice parameters of an FCC crystal has been shown to completely change the interfacial structuring of water upon it, leading to substantially different nucleation rates[67]. This demonstrates another important principle governing the impact of liquid ordering at interfaces – if liquid is ordered into structures which do not resemble a stable crystalline phase, then this order must be broken before crystallisation can occur. A review by Kaplan and Kaufman discusses further the ways in which size and charge distribution of surface features can order liquids into structures that resemble crystalline phases[68].

It has recently been demonstrated that the orientational ordering of proteins on muscovite mica can be drastically altered by adding electrolyte[69,70]. At low electrolyte concentrations (100mM KCl), proteins adopted one of three distinct orientations (demonstrating threefold symmetry of the surface) whereas a single orientation was observed at high electrolyte concentrations (3M KCl). It was suggested that a dipole within the second layer of the solid was responsible for structuring water near the interface, and this structured water reflected the anisotropy found in the adsorbed protein structures.

### 1.7.3 Confinement

When a chemical system exists between two or more surfaces, such that the chemical system exhibits unusual behaviour *as a direct result* of the proximity of the two or more surfaces, the system is said to be confined[71]. Confinement effects can be categorised into three main factors that contribute to unusual crystallisation pathways. Firstly, the confined system is highly interfacial, which means that the relative quantity of the bulk phase diminishes. Secondly, transport of crystal monomer to a surface nucleation site is restricted, often only proceeding via diffusion, which results in much slower growth rates. Thirdly, nuclei and crystals may not be permitted to reach stable shapes, sizes or orientations in certain confined geometries. The last subsection 1.7.3.4 outlines how a confined

crystal grows into a bulk phase, a process which involves additional and potentially restrictive energy barriers.

#### 1.7.3.1 Confined Systems are Highly Interfacial

Many of the unusual phenomena associated with crystallisation in confinement arise from the high surface area available to growing nuclei. In the case of nucleation from vapour, this increased surface area enables an alternative mechanism for crystallisation to occur – pore condensation and freezing.

Pore condensation describes the process by which vapours form condensed phases in confined geometries. These geometries can often greatly enhance crystallisation rates compared to those expected for comparable flat surfaces, chiefly due to the increased surface area available to small growing condensates[72]. It is important to note, however, that whilst crystallisation from vapour is strongly *enhanced* by confining topographical features, the restricted volume of small condensates means that these still generally freeze at much lower temperatures than bulk liquids[73,74].

For chemical systems in which solid nuclei form from liquid phases, confinement crucially leads to a high ratio of interfacial to bulk liquid. With shorter and shorter confining lengths, this ratio increases further, such that systems confined on the single-digit nanoscale may contain vanishingly low quantities of true bulk-like liquid and an increased presence of ordered interfacial liquid. The ability of water to form hydrogen bonds is paramount to its ability to freeze, and disruption to hydrogen bonding networks is thought to be responsible for the Mpemba effect (the observation that hot water freezes faster than cold water). Interfacial ordering of liquids can disrupt the hydrogen bonding of water, which may be experimentally quantified by inspection of the system's dielectric constant. Local capacitance measurement of water confined between graphite and hexagonal boron nitride (hBN) plates showed that the dielectric constant of an interfacial water layer ~0.75 nm thick was hugely reduced in the zero-frequency/entropic region, indicating a significant suppression of hydrogen bonding[75]. As for the implications of this on crystallisation, the significant freezing-point depression of water confined in In <5 nm nanopores is well-documented [76–78], and correlates with an increased presence of interfacial water.

### 1.7.3.2 Transport Limitation in Confinement

The increased ratio of interfacial to bulk liquid in confinement can also lead to unusual transport phenomena. In addition to the diminishing of advective and convective means of fluid transport (which dominate in bulk solution), the highly interfacial nature of confined systems imposes restraints on diffusion. This has been shown to form an ion 'depletion zone' around confined crystals [79], whereby their growth is limited by the reduced ion diffusion rates [80].

This may also have a significant impact on the transformation of amorphous phases to crystals, in which solvent must diffuse out from within the amorphous phase. Dziadkowiec et al. discovered a liquid-like calcium carbonate precipitate which formed in electrolyte solution between two calcite surfaces brought into close-contact using surface-force apparatus (SFA)[19]. Here, it was suggested that transformation from this precipitate to a crystalline solid was hindered by a significant energy barrier to dehydration imposed by the confinement-induced restraints on water diffusion. Similarly, calcium carbonate precipitated within a COOH-functionalised-gold crossed-cylinder geometry has been shown to initially form as amorphous calcium carbonate (ACC). Furthermore, the lifetime of this amorphous precursor was far longer than would be expected in a typical bulk-phase crystallisation experiment[20]. Again, a reduced aperture through which ACC could contact the growth solution was thought to have kinetically suppressed the dehydration step.

### 1.7.3.3 Size Limitation of Nuclei in Confinement

Confinement can also strongly affect crystallisation pathways when the confining length approaches that of the radius of critical nuclei. The interfacial free-energy term for nucleation is generally larger for more thermodynamically stable polymorphs, which means that they may have larger critical nuclei. If the confining length restricts the growth of the thermodynamically stable polymorph, then the metastable/kinetic polymorph may reach criticality more easily.

According to a model proposed by Stolyarova et al., the ideal confining geometry for enhancement of a particular crystal system is when the confining length is greater than or equal to the critical nuclear size[81]. Ha et al. crystallised anthranilic acid as the metastable form II within controlled-pore-glasses (CPGs), suggesting

that the disparity in critical nuclear sizes allowed only certain polymorphs (including form II) to crystallise[82]. In a separate study, crystallisation of paracetamol was completely suppressed in CPGs with pore diameters of 4.6 nm[83], suggesting that the critical nucleus is larger than these pores.

#### 1.7.3.4 From Confined Nuclei to Bulk Crystals

After a crystal has nucleated, it is usually assumed that crystal growth will proceed for as long as the system remains supersaturated, resulting in a macroscopic crystal. This is not necessarily the case in confinement, however, as there may be significant energy barriers to the emergence of a crystalline seed from the mouth of a pore[84]. Turnbull postulated that a frozen condensate would not be able to emerge from a cylindrical pore onto an adjacent flat plane unless the radius of the (assumed spherical) condensate exceeded the critical radius for nucleation of that condensate on the flat plane [85]. Page and Sear provided 2D Ising model simulations to determine how nucleation might proceed in rectangular pores [86]. Concurrent with the theory presented by Turnbull and Fukuta, they found that there are two barriers: a barrier to nucleation within the pore (which is smaller for narrower pores) and a barrier to emergence at the top of the pore (which is smaller in wider pores). Together, these effects lead to an optimal pore size for a given surface and interacting nucleating phase.

Figure 11 demonstrates this from a geometric perspective. If a nucleus forms as a sphere bounded by a cylindrical pore, the critical radius $r^*_p$ of the sphere will be determined by the contact angle the nucleus makes with the pore wall, θ. Once supercritical, the nucleus will grow with a capsule geometry (Figure 11A), with a size-independent free energy $\Delta G_p$ as long as the supersaturation does not fall below an arbitrary value defined as $S_1$. The nucleus then continues to grow until it reaches the mouth of the pore (Figure 11B). The geometry of the pore reduces the critical nuclear size within the pore, but when the nucleus emerges from the pore it must then exceed the critical nuclear size for nucleation on a flat surface $r^*_f$, which is larger than $r^*_p$ and can only occur at a larger supersaturation $S_2$.

Splitting the single energy barrier normally associated with classical nucleation into two smaller energy barriers (one for nucleation within the pore and one for emergence) has the potential to increase nucleation rates considerably. A variety

of factors including the pore diameter and the nucleus-substrate contact angle determine the relative heights of the two energy barriers, and when they are similar in height, the nucleation rate reaches its maximum.

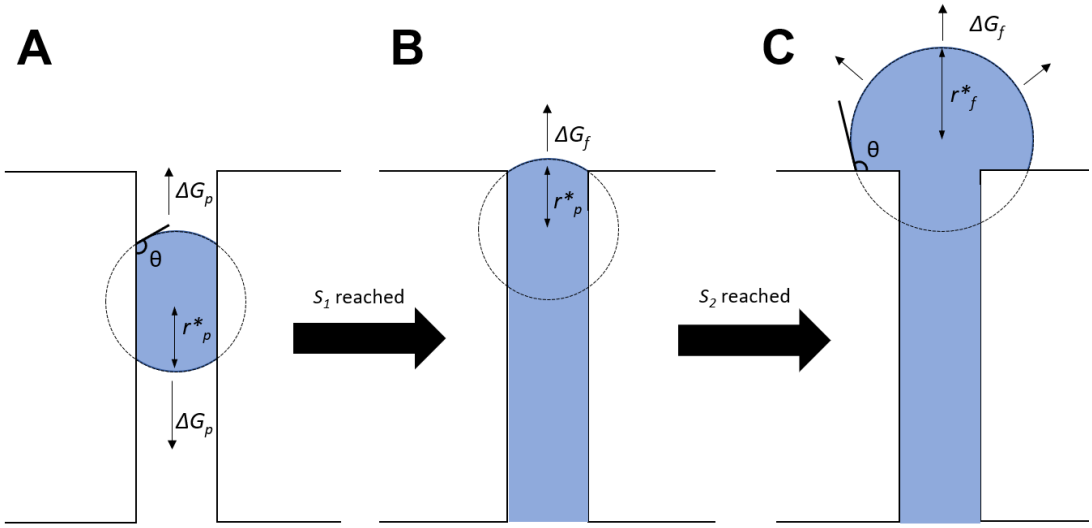


**Figure 11: Diagram showing how a nucleus formed in a pore is able to emerge from it. (A) The nucleus forms within the pore at supersaturation $S_1$. (B) It then continues to grow until it reaches the pore mouth. (C) The supersaturation must increase to $S_2$, which is the barrier to nucleation on a flat plane, before it can emerge from the pore.**

Though much of the research into emergence barriers has been theoretical or computational, Campbell et al. experimentally observed the growth from vapour of several organic compounds in mica pockets, and showed that confined solid deposits did not grow into a bulk crystal until a threshold supersaturation had been exceeded. This was attributed to an energy barrier to growing out of the mouth of their narrow geometry[87]. Campbell and Christenson performed the same experiment with ice over a range of different humidities and temperatures, and concluded that the limiting step to ice nucleation at higher temperatures was the freezing of the liquid condensate, while it was the growth of the confined ice into a bulk phase at lower temperatures[88].

## 1.8 Surface Features that Enhance Crystallisation

### 1.8.1 Rough Surfaces

An interplay of both surface chemistry and topography often enhances nucleation. Here, rough surfaces are defined as those in which a universal 'roughening' process has been applied to the surface, but there is little to no rational design of the topography. This offers a facile method of increasing the number density of crystals which form at a surface, as well as encouraging difficult species such as proteins and other macromolecules to crystallise, due to the wide range of feature geometries and sizes presented by the surface[89].

The arithmetic mean roughness $R_a$ is a widely-used measure of surface roughness, and simply represents the average deviation of the surface from the mean height. This is not always the best way to represent a surface however, as it does not take into account the asperities of surface features. Grosfils and Lutsko studied heterogeneous crystal nucleation rates using kinetic Monte Carlo simulations, and found that nucleation was affected not only by surface roughness and substrate-solute interaction energy, but also by the surface correlation length[90]. Correlation length is a statistical function which describes the distance from one point within which a reasonable estimate of the height of a second point can be made. For a surface with a fixed surface roughness, a large correlation length implies the presence of large hillocks and valleys, whereas a small correlation length is associated with shorter but more jagged features. When the interaction energy of the surface and nucleus was sufficiently increased, it was found that whilst increasing surface roughness generally led to an increase in nucleation rate, for surfaces with the same roughness, shorter correlation lengths greatly increased nucleation rates. This concurs with experimental evidence which shows that nuclei prefer to form in sharp pits and pores that exist on similar length scales to critical nuclei[91].

The nature and wetting state of the phase within which nucleation takes place also makes a large difference to how nucleation is affected by surface roughness. For example, whilst rougher surfaces are generally associated with higher nucleation rates[90,92–94], superhydrophobic rough surfaces such as those found on lotus leaves[95] exhibit slower nucleation rates than their smooth counterparts. This either results from a reduced contact area between a liquid droplet and a

surface[96], or in the case of ice nucleation from condensed water droplets, prevention of adhesion and build-up of a macroscopic crystal phase[97,98]. Whilst there is strong evidence that nucleation from vapour is enhanced on rough surfaces[99], effects can be variable for crystallisation from a melt or solution. Campbell et al. studied the crystallisation of ice on mica and glass substrates that had been roughened by abrasion with diamond powder or left unabraded[100] and found that the freezing of water droplets on mica and glass substrates (i.e. from the melt-phase) was unaffected by surface roughness[101]. This supports some theoretical predictions which show that unless an epitaxial match between the substrate and emerging crystal exists, there is little reduction in the free-energy barrier to nucleation associated with heterogeneous nucleation from the melt phase.

### 1.8.2 High-Index Surface Sites

The topographies of crystalline substrates can be manipulated by abrasion or erosion via mechanical or chemical means, to expose areas with higher surface energies and different surface chemistry. In practice, there are several commonly-employed mechanical techniques for exposing high-index facets in crystalline materials. ‘Miscutting’ involves mechanically cleaving a crystalline material at high angles on low index facets, such that large areas of high-index facets are exposed[102] (see Figure 12). This technique can produce irregularly-shaped steps, which means that high-temperature thermal annealing is often required to ‘straighten’ them[103]. Atomic layer deposition (ALD) experiments have shown that material preferentially accumulates at these high-index sites, due to an increased density of dangling bonds[104,105].

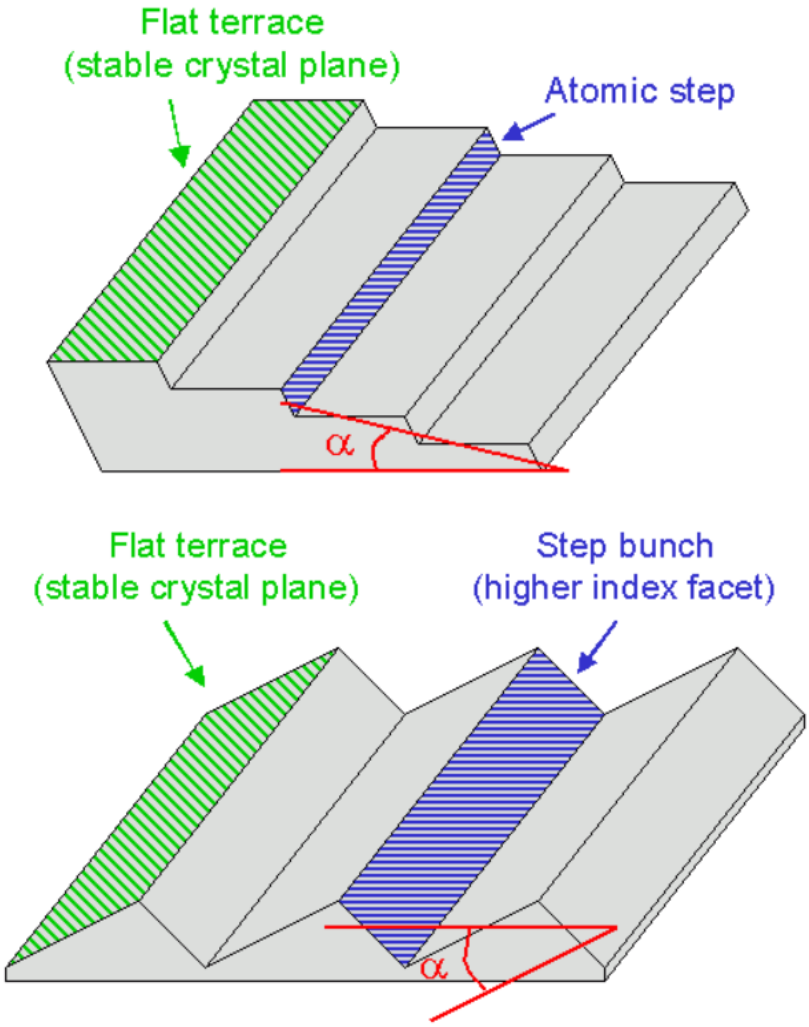


**Figure 12: The influence of miscut angle α on expression of high-index facets in a crystalline surface** [106]**.**

A much simpler means of exposing high-index facets involves abrasion of crystalline substrates with diamond powder, which has been shown to greatly increase nucleation density of diamond grown via chemical vapour deposition (CVD)[107]. Focused ion beam (FIB) milling of crystalline materials has also been shown to produce a similar effect[108]. High-index facets also show increased chemical reactivity compared to lower-index facets, allowing selective modification of the surface chemistry *prior* to the deposition of material. This can further increase the spatial selectivity for crystallisation at particular surface sites[109].

Chemical etching of substrates can also expose high-index facets in crystalline materials. Dennig and Stevenson investigated the effect of surface topography

on nucleation by depositing diamond thin films on chemically etched silicon and molybdenum surfaces[110]. Surprisingly, diamond particles nucleated from vapour at convex edges and apexes, where there were high densities of dangling bonds. Polini confirmed these results in a further study which saw diamond nuclei form exclusively at the edges of steps formed by chisel-fracturing a Si (111) crystal[111] (see Figure 13). Arnault et al. discussed the mechanisms by which diamond nuclei might form on protrusions of Si surface defects. Etching by H radicals within the CVD chamber produced active sites on the Si surface, particularly at protrusions. Electron energy-loss spectroscopy (EELS) and x-ray photoelectron spectroscopy (XPS) provided evidence of precursor thin films or 'embryos' of silicon carbide and diamond-like carbon at these activated sites[112], which then underwent a growth process to form diamond nuclei.

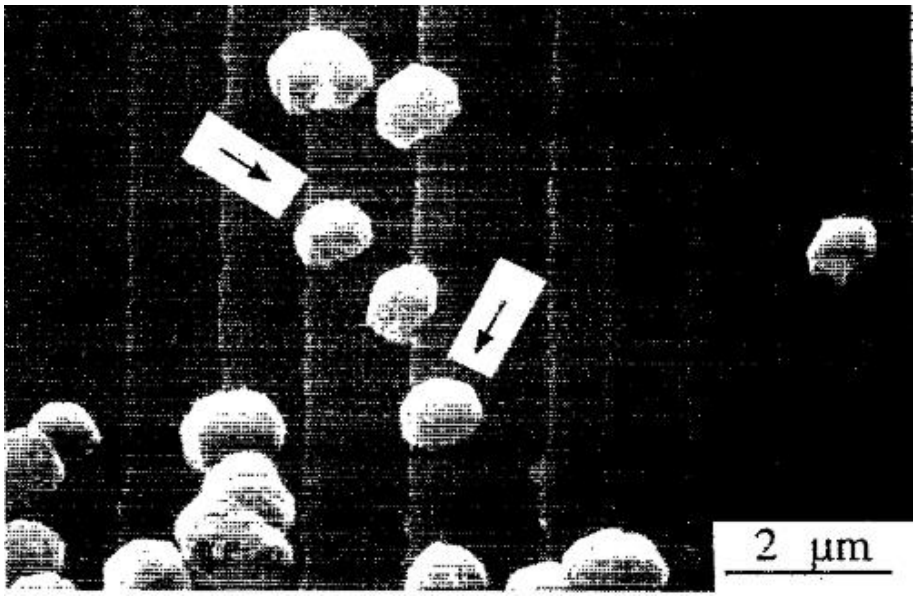


**Figure 13 – Formation of diamond nuclei via CVD on a fractured Si (111) surface which presented steps. Nucleation was observed exclusively at step edges** [111]**.**

Vescan et al. fabricated silicon mesas with intersecting {0 1 1} and {0 1 12} facets using a combination of wet etching and selective epitaxial growth. Subsequent vapour deposition of Ge demonstrated that Ge islands could be nucleated at the facet intersection with a high degree of specificity (see Figure 14). The high surface energy of this linear region was associated with a greatly reduced energy

barrier to nucleation of Ge, which accounted for the strikingly high nucleation densities.

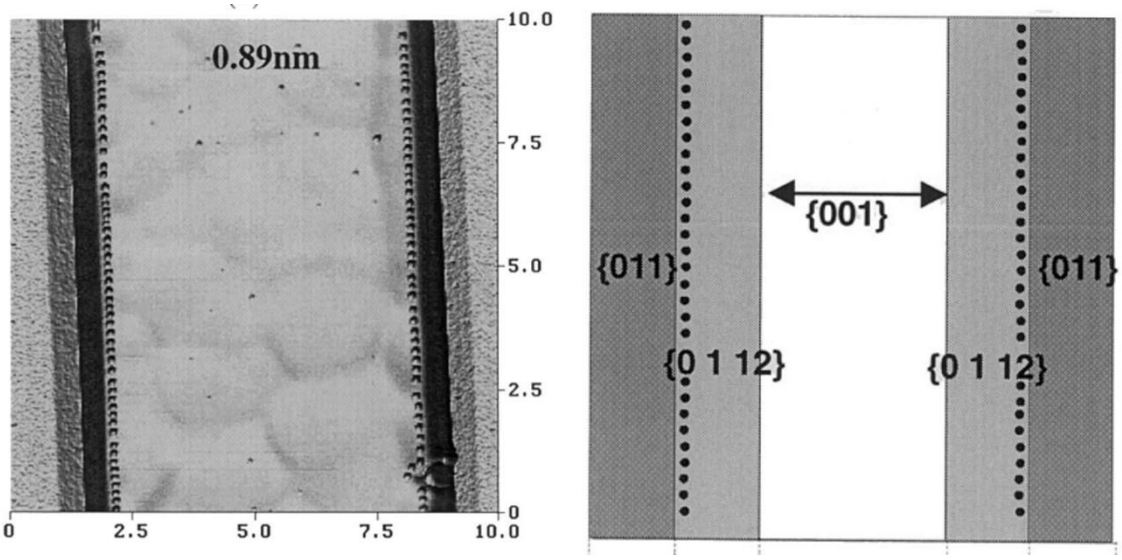


**Figure 14 – Ge islands nucleated on Si 'mesas'. Nucleation was observed with a strong preference for the intersection of {0 1 1} and {0 1 12} facets** [113]**. *Reproduced with permission from Elsevier S.A.***

### 1.8.3 Pores

It has been suggested that nanopores can prevent lateral migration of protein molecules, enabling large clusters to remain trapped at the surface until a critical size is reached[93]. This chiefly affects the Zeldovich factor, reducing the likelihood of critical nuclei re-dissolving[114,115]. Chayen et. al showed that porous silica can act as a 'universal nucleating agent' for a range of proteins[116,117], where the key to this was ensuring a wide range of pore widths existed. As it has been shown that pores can both promote and inhibit nucleation depending on their size[82,118] this ensures that an ideal pore size that promotes crystal nucleation is present. The regularity of pore shape and size has been suggested to be responsible for the ineffectiveness of zeolites as protein nucleants[86].

This effect is not specific to proteins, however. In one set of experiments, aspirin was shown to grow from solution 26 times faster at 25-400 nm pores on a polymeric substrate than on the adjacent flat surface[119].

### 1.8.4 Cracks and Scratches

Crystallisation can be highly promoted in cracks and crevices. However, the industrial interest in this process is largely focused on how to inhibit it. The detrimental processes which are of interest can be categorised as either weathering or fouling.

Weathering can drastically reduce the lifespan of buildings, roads and other infrastructure. In this process, capillary condensation or infiltration can trap water in defects in the material, which initiates leaching of minerals from within. These minerals often readily recrystallise in cracks and pores, and the pressure exerted by crystallisation (of ice[120], gypsum and sodium sulfate[121]) can either initiate or propagate cracks. This in turn enables more material to leach out and accelerate the weathering process[71]. Fouling is the general build-up of solid material on surfaces which hold or transport liquids[122]. The roughness of metal surfaces such as those used in pipelines has been shown to increase the rate of calcium carbonate scaling, and images from work by Xing *et al.* show that scratches in particular may host large numbers of crystals[123].

Whilst there is a clear demand for research in inhibiting weathering and scaling, the enhancement of crystallisation in cracks may enable better nucleants to be developed. It has been noted that nucleation densities on scratched surfaces are usually greater than on etched surfaces[110], which demonstrates how challenging it can be to mimic the results of crystallising on 'natural' surface topographies, even using high-tech lithographic techniques. In the case of brittle fracture, there is no plastic deformation of the material prior to fracture, which means that feature sharpness is often retained down to the molecular level.

Gavish and co-workers found that cracks in some materials could present confined, highly charged environments in which very strong local electric fields could exist[124]. Pairs of racemic and enantiopure amino acids were used as substrates for crystallisation of ice. One of each pair would present a polar axis, whereas the other would not. In all cases, the crystal with the polar axis consistently nucleated ice at a temperature several degrees higher than its nonpolar counterpart. This was attributed to the presence of crevices in the surface of the amino acid crystals, at which a dipole was formed between opposing faces of the crystal. Water confined in this region would therefore be

subject to the strong electric field resulting from the charge difference at such a small separation distance.

Similarly, Conrad et al. discovered that ice preferentially nucleates at microcracks and pores present in $BaF_2$ crystals, which arise from its slight dissolution in aqueous media[125]. $BaF_2$ (111) has a near perfect lattice match with the basal plane of hexagonal ice, but is a very poor nucleating agent. Dissolution of the $BaF_2$ creates pits and cracks in the surface, which are much more effective nucleation sites.

Cracks have also been found to enhance the assembly of faceted mesocrystals [126]. Mesocrystals are assemblies of nanoparticles which can arrange into a lattice similarly to conventional crystals, however they are often more challenging to produce due to the smaller attractive forces per unit surface area driving their assembly[127]. In this case the mesocrystals were assembled from antisolvent-destabilised colloidal dispersions of iron oxide nanoparticles, and their assembly was clearly enhanced along the length of a silicon surface crack (Figure 15).

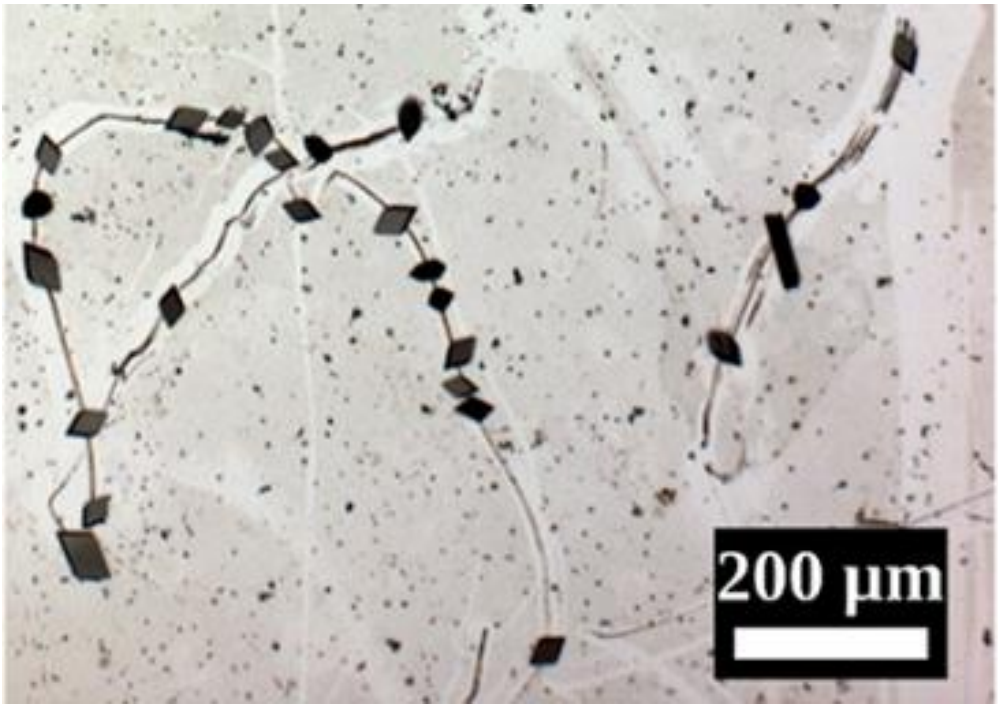


**Figure 15: Assembly of colloidal iron oxide mesocrystals was enhanced at surface cracks on silicon [126]. *Reproduced with permission from the American Chemical Society.***

Encouraging crystallisation to occur within cracks can be hugely beneficial to the formation of composite materials, where the spatial segregation of materials can

offer improved mechanical performance. Zhang et al. formed a hydroxyapatite-$TiO_2$ composite by plasma electrolytic oxidation, and found that the cracks in the $TiO_2$ were preferred nucleation sites for hydroxyapatite[128]. Similarly, Montenero and co-workers prepared $TiO_2$ films via a sol-gel process, and then exposed them to simulated body fluid (SBF) (which contains $Ca^{2+}$ and $PO_4^{3-}$ ions) at 37°C for 10 days [129]. This resulted in the formation of apatite at the cracks in the $TiO_2$ film (Figure 16), which mimics the mineralisation process that occurs in the body following bone fracture. In this way, cracks can be seen as a targeted approach for mineralisation where additional mechanical strength is required.

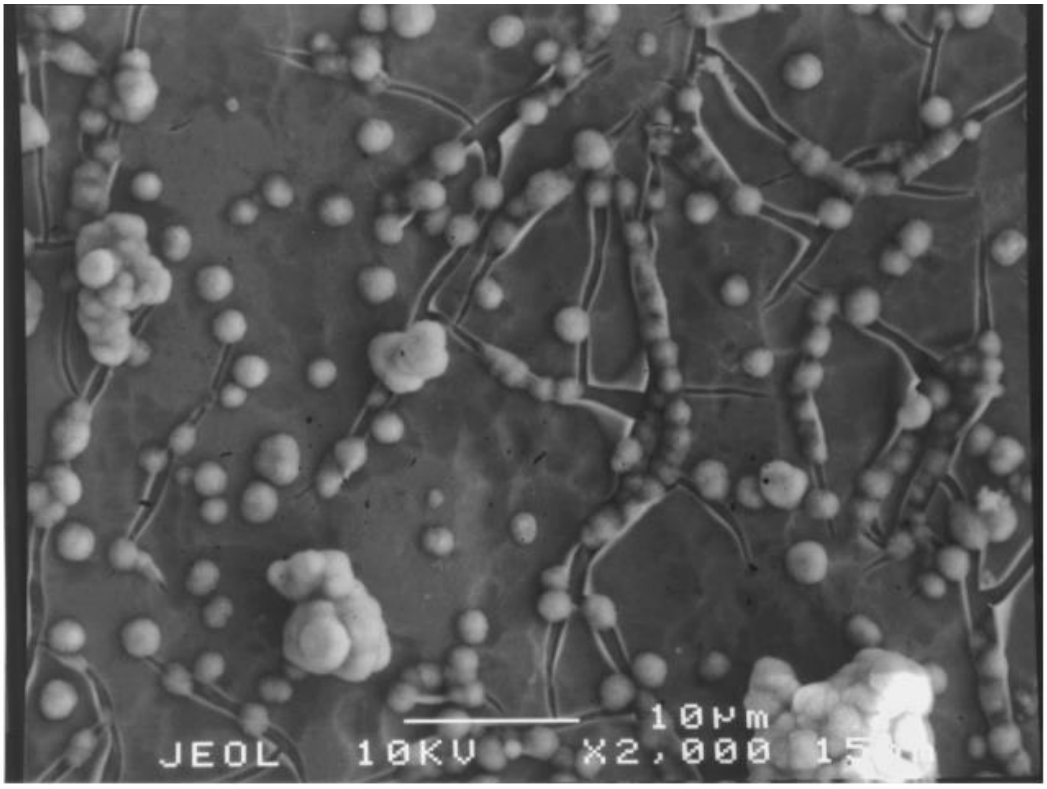


**Figure 16: Preferential crystallisation of apatite in the cracks of a $TiO_2$ film [129]. *Reproduced with permission from Springer New York LLC.***

## 1.9 Engineering Surface Topography to Control Crystallisation and Improve Crystalline Materials

Tailoring the topography of surfaces in order to influence crystallisation processes is a recent field of interest. As such, its applications are only beginning to be realised.

Controlling protein crystallisation is key to structural determination by x-ray crystallography. Self-assembled monolayers on flat surfaces (e.g. silicon or mica)

can be used to reduce the number density of nuclei formed by heterogeneous nucleation, which is useful for ensuring that large protein crystals grow[130]. Whilst some proteins such as lysozyme are readily crystallised, others are extremely challenging to nucleate. De Poel and co-workers deposited organic compounds from vapour on mica substrates with different topographies and found that macrosteps on the substrates were highly effective at nucleating insulin[131]. Similarly, 'nanowrinkled' polydimethylsiloxane (PDMS) substrates were be highly effective at crystallising ferritin and thaumatin as compared to flat PDMS[132].

Semiconductors can also benefit from greater control over their crystallinity offered by topographical patterning. Kim and co-workers found that single crystal domains of $WSe_2$ could be deposited on substrates with confining nanopores and these could then be used to create single crystal layered materials with greatly improved performance[133]. Kim *et al.* exploited the favourable conditions for crystallisation in cracks to control the structures of layered semiconductor heterostructures, which find application in solar cells, electronics and optics[134]. There, a charge-transfer complex was precipitated as micro-scale tubes, which were intentionally cracked in the middle. The crack was then 'welded' together by vapour deposition of a second charge-transfer complex, where the preferential crystallisation not only mechanically re-joined the microtubule but also created a novel heterogeneous material with spatially segregated fluorescence behaviour.

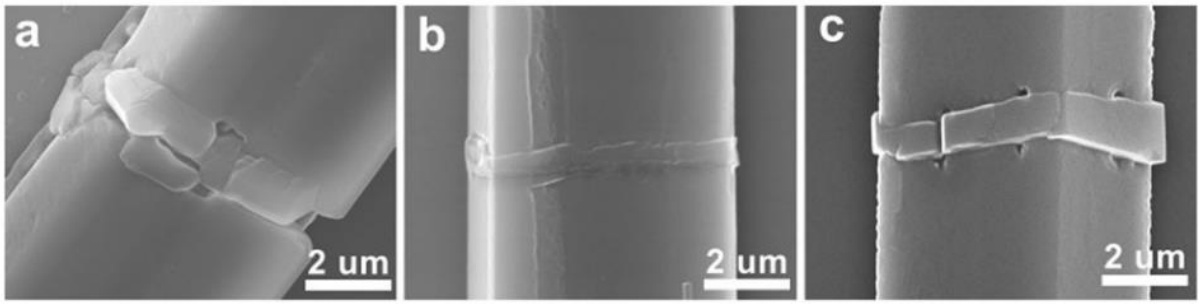


**Figure 17: (a-c) Three types of welded charge transfer microtubules produced by preferential crystallisation in the cracks** [134]**.** ***Reproduced with permission from the Royal Society of Chemistry.***

Prevention of ice adhesion is a key crystallisation problem that can be tackled by patterning surfaces with the appropriate topography. Ice adhesion causes immeasurable damage worldwide, from crop spoilage to damage to buildings and transmission lines due to excessive weight[135]. Preparation of effective coatings, which can allow surfaces to shed ice quickly and retain their effectiveness over

long periods of time, are therefore desirable. Ice formation is different to water droplet formation, in that its adhesion to a surface cannot be prevented by superhydrophobic rough surfaces alone[136]. In some cases, the rate of ice formation at a surface is increased with increasing surface area, as with many superhydrophobic rough surfaces[137]. Hou and co-workers overcame this by patterning the surface wettability, creating surfaces with hydrophilic pillars surrounded by hydrophobic 'nanograss'. When water droplets initially condensed at the surface, they were attached only to the pillar tops, and when they grew large enough to coalesce and freeze, many simply rolled off the surface[138]. Wong and Aizenberg's omniphobic 'SLIPS' used a different approach, but highly effective approach. Here a nanotextured porous surface was infiltrated with an inert, low surface energy liquid[139]. In this system, there was no direct contact between the water/ice and the solid surface as they were separated by a highly lubricating layer of liquid.

## 1.10 Materials

Unless specified, all water used was MilliQ Ultrapure water with a resistivity 18.2 MΩ·cm @ 25 °C; total organic carbon (TOC) ≤ 5 ppb.

| Material | Supplier |
|---|---|
| 16-Mercaptohexadecanoic acid (16MHDA) (99%) | Aldrich |
| 25 Compartment Square Petri Dish | Thermo Scientific |
| 2-Methylimidazole | Merck |
| Acetic Acid (99.7%) | Fisher Scientific |
| Aluminium Specimen Stubs for SEM | Agar Scientific |
| Ammonium Carbonate (99%) | Fluorochem |
| Ammonium Oxalate Monohydrate (>99%) | Sigma-Aldrich |
| Aquapel | PGW Auto Glass |
| Barium Chloride Dihydrate (99%) | Sigma-Aldrich |
| Borosilicate Glass Capillaries (GBF100-50-7.5) | WPI |
| Borosilicate Glass Microscopy Slides | Scientific Glass Laboratories Ltd |
| Borosilicate Glass Rods (GR100-4) | WPI |
| Buffer Solutions (pH 4, 7, 10) | SLS |
| Calcium Chloride Dihydrate (>99%) | Sigma-Aldrich |
| Cellulose Acetate Syringe Filter (0.22 µm) | StarLab |
| Chromium Sputter Target | Agar Scientific |
| Circular Polystyrene Petri Dish (60x15 mm) | Sarstedt |
| Circular Polystyrene Petri Dish (90x15 mm) | Thermo Scientific |
| Copper (II) Chloride Dihydrate | Fisher Chemical |
| Copper Slot Grids (1x0.2 mm) | Agar Scientific |
| Copper Tape | 3M |
| Demotec® 70 Conductive Carbon Resin | Agar Scientific |
| Diamond Powder (40-60 µm) | Alfa Aesar |
| Ethylene Carbonate (EC) Solvent | Micro Resist Technology |
| Ethanol Absolute (99.9%) | VWR Chemicals |
| Glass Vial (25 mL) | VWR |
| Glycine (>98.5%) | Sigma |
| Gold Pellets 99.999% | Kurt J. Lesker |
| Guanosine (>97%) | Sigma |
| Hydrochloric Acid (37%) | Fisher Chemical |
| Hydrogen Peroxide (30 wt%) | Fisher Scientific |
| Ibuprofen Sodium Salt (>98%) | Sigma-Aldrich |
| Iridium Sputter Target | Agar Scientific |

| | |
|---|---|
| Isopropyl Alcohol (99.9%) | Sigma-Aldrich |
| Kleenex Wipes 7432 | Kimberly-Clark |
| Magma Bond 5 Minute Epoxy Resin | Magma Acrylics |
| Natural Furs Dubbing Box | Veniard |
| Optimum Cutting Temperature Compound and Carbon Suspension (Cryogenic SEM Resin) | Agar Scientific |
| Petroleum Ether (40-60 °C) | Sigma-Aldrich |
| Porcelain Tiles (Blanc) | Winckelmans |
| Potassium Chloride (99%) | Sigma-Aldrich |
| Potassium Hydroxide (99%) | Fisher Chemicals |
| Potassium Nitrate (99%) | Fisher Scientific |
| Potassium Phosphate Dibasic (>99%) | Alfa Aesar |
| Potassium Phosphate Monobasic (>99%) | Sigma |
| P-type Silicon Wafers (100 Orientation, 2 Inch Diameter) | Agar Scientific |
| Purine Nucleotide Phosphorylase, Human, Recombinant, E Coli | Merck |
| RM1038 Nepheline Syenite | Scarva |
| Scotch® Magic™ Tape | 3M |
| Silicone Oil | Thermo Fisher |
| Sodium Benzoate (>99%) | Sigma-Aldrich |
| Sodium Carbonate Anhydrous (99.5%) | Acros Organics |
| Sodium Chloride (99%) | Fluka Analytical |
| Sodium Fluoride (>97%) | BDH Chemicals |
| Sodium Sulfate Decahydrate (99%) | Alfa Aesar |
| Strontium Chloride Hexahydrate (>99%) | Thermo Scientific |
| SU-8 2005 Photoresist | Fisher Scientific |
| Sulphuric Acid (>95%) | Fisher Scientific |
| Super Glue | Loctite® |
| Sylgard™ 184 Silicone Elastomer Kit (Base and Elastomer) | Dow Corning® |
| Syringe Needles (0.5x16 mm) | Terumo |
| Whatman B-2 Greaseproof Weighing Paper | Cytiva |
| Zinc Nitrate Hexahydrate (98%) | Thermo Scientific |

# Chapter 2

# General Studies of Surface Topography and Nucleants

## 2.1 Introduction

### 2.1.1 Overview

In this work, two prominent ideas for how surface topography can promote crystal nucleation were tested experimentally. Firstly, I explored the ability of fractured amorphous solids to express highly active nucleation sites through atomically sharp and highly acute features. Initially, features were manufactured by scratching glass with diamond powder. Calcium carbonate was crystallised on glass that had been either scratched or left pristine, and the numbers of crystals formed per unit surface area were calculated. This enabled the importance of surface area and feature topography on promoting crystallisation to be compared.

Classical nucleation theory suggests that nucleation should be enhanced at highly acute surface features, so glazes were prepared by melting nepheline syenite onto a ceramic tile and then allowing it to cool. Upon cooling, the contraction of the glaze relative to the ceramic substrate caused numerous highly acute cracks to form. Calcium carbonate was also crystallised on these substrates, and the degree of localisation of crystals to the acute features was assessed.

Secondly, I tested the practicality of theory of ‘angle-directed nucleation’. This is the idea that crystal nucleation is enhanced on substrates which express angles matching intrinsic angles of the crystal (introduced in depth in Section 2.1.2.3). Square templates with $90^{o}$ edges were fabricated using thermal gold deposition and cubic NaCl crystals. Face-centred cubic $CaF_2$ and polymorphic $KNO_3$ were crystallised on the templates, and the localised nucleation at the templates was visually assessed by microscopy. Additionally, the ability of the templates to impart polymorph control was tested, where $KNO_3$ could have crystallised as either a rhombohedral (no angles of exactly $90^{o}$) or orthorhombic polymorph (all $90^{o}$ intrinsic angles).

For further investigation into the viability of angle-directed nucleation, a separate set of substrates was also prepared. High-resolution pits were made using resin, which formed moulds of vaterite and calcite (calcium carbonate) crystals. Once the original crystals were dissolved by acid, Calcium carbonate was regrown on top and the localised crystallisation of each polymorph in each type of pit was assessed, showing how effective their specific topographies were at promoting nucleation of specific polymorphs.

## 2.1.2 Background

### 2.1.2.1 Glassy Materials and Fracture

A glass is an amorphous material that exhibits a glass transition ($T_g$) within a defined temperature range, such that the material is hard and brittle below this range but soft and malleable above it. The raw ingredients used to produce a glass can be used to control its properties. At a very basic level, a two-component inorganic glass can be made from $SiO_2$ and $Na_2O$[140]. $SiO_2$ has a high melting point but a very low linear coefficient of thermal expansion ($3.5 \times 10^{-7}$ $K^{-1}$ [141]). $Na_2O$ has a lower melting point but a higher coefficient of thermal expansion ($39 \times 10^{-7}$ $K^{-1}$ [141]). $Na_2O$ behaves as a 'fluxing agent', reducing the firing temperature of a glass. However, if the $Na_2O$ content is too high, the thermal contraction upon cooling can lead to formation of cracks, called crazes[142,143]. Applying a glass layer to a ceramic material (i.e. fired clay) is known as glazing, and is traditionally applied to produce hard, chemically resistant and aesthetically pleasing coatings on pottery. The large differences in coefficients of thermal expansion between the ceramic and glaze can exacerbate the crazing effect upon cooling, because the adhesive forces between the ceramic and the shrinking glaze applies tensile stress to the glaze layer[142].

Crazes are topographical features that are found exclusively in amorphous materials. They are produced from stress-induced brittle fracture (breaking with little to no prior plastic deformation), and are responsible for the white hazing which often appears when transparent plastics are bent. The lack of fracture planes in amorphous solids means that crazes can exhibit widths of several atoms at their tips[144] (Figure 18B). This is in stark contrast to crystals, which,

when fractured, mainly exhibit groups of atomic step edges arising from intersecting low-index faces.

When glass breaks, it also commonly exhibits conchoidal fractures (Figure 18A), which are characterised by curved fracture lines. For our prehistoric ancestors, the development of ‘knapping’ (striking natural obsidian with stones to produce conchoidal fractures) allowed them to fabricate atomically-sharp tools, where the sharp tool edge is formed at the intersection of two sets of curved conchoidal fractures[145].

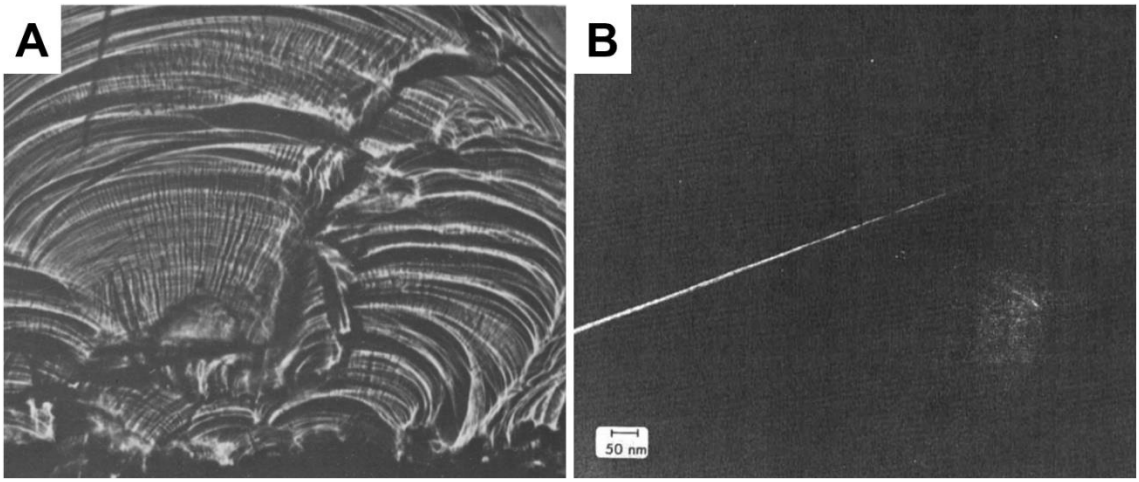


**Figure 18: (A) A ‘shell’ conchoidal fracture of a glass plate[146]. (B) TEM image showing a craze propagating through a polystyrene film[147]. *Reproduced with permission from Elsevier Sequoia and Taylor & Francis.***

Glass cracking as a result of a thermal shock is hugely problematic for most applications, and motivated the invention of borosilicate glass by Otto Schott in the late 19$^{th}$ century[148]. Borosilicate glass, commercially known as Pyrex®, has an extremely low coefficient of thermal expansion (3 x $10^{-6}$ $K^{-1}$ [149]). The added boron acts as a fluxing agent, reducing the melting temperature of the mixture and reduces the thermal expansion of the resulting glass[148]. Since its invention, borosilicate glass has found widespread use in the field of cookware, optics, lighting and electronics.

#### 2.1.2.2 Crystallisation on Glassy Materials

Glass is an ideal starting point for studying the effects of surface topography on crystallisation. The same properties that lead to widespread use of glass also make it an ideal surface on which to study crystallisation – it is cheap, durable, inert and transparent.

Many substrates that are commonly investigated as crystal nucleants such as mica or silicon are crystalline, meaning that they express a limited range of surface features, i.e. terraces, steps and kinks. Glass is by definition an amorphous solid, so cannot express such well-defined features. This means that an unlimited range of surface features can exist, compared with the limited range of surface features expressed by crystals. The lack of macroscopic crystal planes also means that when glass undergoes brittle fracture, highly 'sharp' features can be formed which exhibit high densities of dangling bonds[150]. These features can exhibit crevices with vanishingly small angles, such as is the case for crazes. These highly acute features may be effective at reducing the interfacial energy of growing nuclei, and could therefore reduce the energy barrier to the formation of critical nuclei[151].

The conchoidal fractures commonly exhibited by fractured glassy surfaces can vary significantly in size such that a single crevice may express a continuum of angles across its length. If indeed crystal nucleation can be promoted by a wedge-shaped feature with a specific angle, then crystallisation experiments on glassy surfaces may be able to deliver much-needed experimental data to compare with the plethora of theoretical work in this field[152,153].

#### 2.1.2.3 The Theory of Angle-Directed Nucleation

An important shortcoming of many theoretical models for nucleation in a 2D step[15,16] (see Section 1.3.5) is that the atomistic/molecular nature of nuclei is not considered, which in turn ignores the shape and crystallinity of that emerging nucleus. This leads to a prediction of a monotonic increase in nucleation rate with decreasing wedge-angle, as is characteristic for the formation of liquid-phase nuclei[85] which do not exhibit long-range order. However, when considering the arrangement of a few atoms or molecules to form a crystal in these spaces, the

size and structure of the emerging nucleus with respect to the surface geometry are important.

Angle-directed nucleation theorises that nucleation rates in concave step geometries vary non-monotonically with decreasing step angle[152,153]. This is similar to the concept of ledge-directed epitaxy[154], however angle-directed nucleation does not require the underlying substrate to be crystalline. This emphasises the effects of packing arrangements of a crystal nucleus within an angular surface feature rather than the effects of epitaxy. That is, a few select angles allow a crystal to form with minimal lattice strain, minimising the energy required to form a nucleus.

Simulations of the crystallisation of spherical Lennard-Jones particles within a 2D step by Page and Sear revealed a distinctly non-monotonic variation in rate with decreasing wedge angle[153]. This was largely due to geometric matching between specific wedge angles and the emerging crystal, such that when the perfect angle was reached, the emerging crystal could be perfectly accommodated by the wedge, substantially reducing its free energy. At imperfect wedge angles, stacking defects emerged in the crystal to help alleviate geometric strain. While the energetic cost of these stacking faults is relatively low, their presence increased the free-energy of a nucleus such that deviation of a few degrees from the ideal wedge angle reduced the nucleation rate (see Figure 19).

This was corroborated by simulations performed by Bi *et al*. who found that nucleation rates could be reduced, reportedly up to 90 orders of magnitude, for ice nucleating within a pyramidal pit expressing angles which matched intrinsic angles of the cubic phase of ice[152]. This yielded nearly pure cubic ice, which is typically difficult to form due to the abundance and low energetic cost of stacking defects in the cubic ice lattice[155]. It has also been shown that the induction time for ice nucleation varied non-monotonically when the width and depth of a 2D rectangular nanogrooved substrate was varied[156]. When the nanogrooves approached widths and depths which were multiples of the ice unit cell length, there was a sharp drop in the induction time for nucleation.

When studying crystallisation by computational methods, thermodynamic parameters (e.g. bulk and interfacial free energies[157]) can be extracted, as well as structural descriptors (e.g. ion coordination number or geometry[158,159]) to

explore nucleation pathways in a system. Simulations have found that angle-directed nucleation is a plausible phenomenon, but without robust experimental evidence to support this work there can be little certainty that angle-directed nucleation ever occurs outside of simulations. As yet, there is no conclusive experimental evidence to fulfil this need.

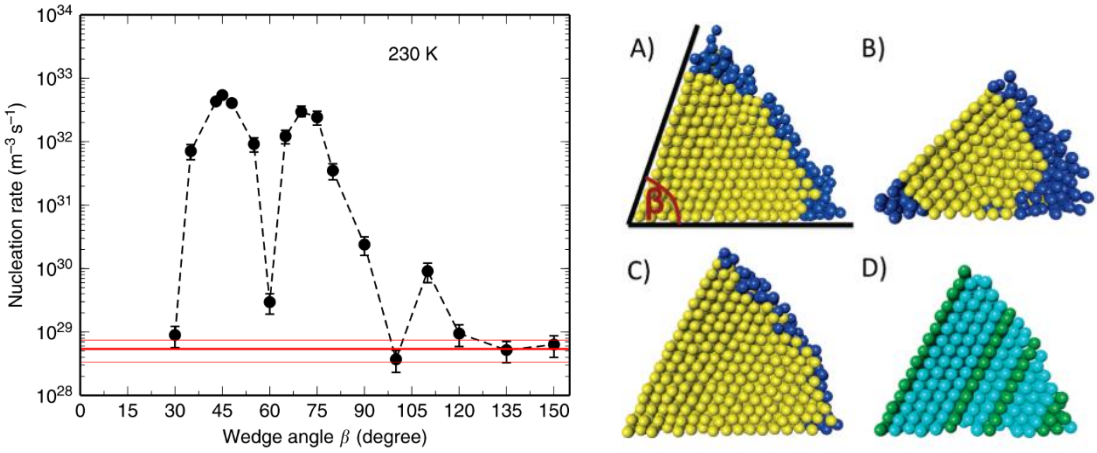


**Figure 19 – Left: Non-monotonic variation in the rate of ice nucleation with increasing wedge angle[152]. Right: Molecular dynamics simulations performed by Page and Sear[153], inside (A) a 70.5º wedge (B) a 45º wedge (C&D) a 62º wedge. Ordered FCC is represented by yellow (ABC) and green (D), while disordered atoms are blue, and HCP is cyan. The nucleation rate was highest in A), where the fewest stacking defects were present.** ***Reproduced with permission from Springer Nature and the American Chemical Society.***

### 2.1.3 Crystallisation at Physically Templated Surfaces

Modifying the micro- and nano-scale morphologies of materials can improve their key physical properties. A common strategy is reverse moulding, which involves the use of a physical template. This template remains rigid when material is grown around it, and once growth is complete, the physical template is removed, leaving a void or imprint of the original template.

Embedding soluble crystals within polymers and then dissolving the crystals has been used extensively to manufacture high-porosity polymers[160–162]. Examples include NaCl crystals which can be dissolved in water, or calcium carbonate

which readily dissolves in dilute acids. These porous matrices have many applications, including sensing[163], photocatalysis[160] and scaffolding for tissue regeneration[161]. They can also make highly effective crystallisation templates. One study showed that the intricate structure of sea urchin skeletal plates could be replicated by this method. A polymer mould of the skeletal plate was highly effective at templating mineral growth, which allowed the structure to be transferred to other minerals[164].

Whilst the impact of confining physical templates on micron-scale crystal growth is well-studied[82,164,165], little is known about how the shapes of templates influence nano-scale crystal nucleation. In particular, it is not known whether crystal nucleation can be promoted within a template with specific angles matching those of the crystal via the angle-directed nucleation mechanism.

In experimental work by Diao *et al*, it was reported that angle-directed nucleation was responsible for enhancing the crystallisation of aspirin in nanopores with a variety of shapes[166]. Crystallisation in hemispherical nanopores occurred with an average induction time of ≈425 min, in square nanopores with ≈150 min, and hexagonal nanopores with ≈25 min (Figure 20A). Additionally every crystal within a pore possessed the same orientation with respect to the shaped pore (Figure 20B), so it was therefore suggested that nucleation preferentially occurred at the square and hexagonal angular pore edges by angle-directed nucleation. However given the low resolution of these features, this seems impossible. It seems more likely that growing aspirin crystals moved into this orientation after nucleation.

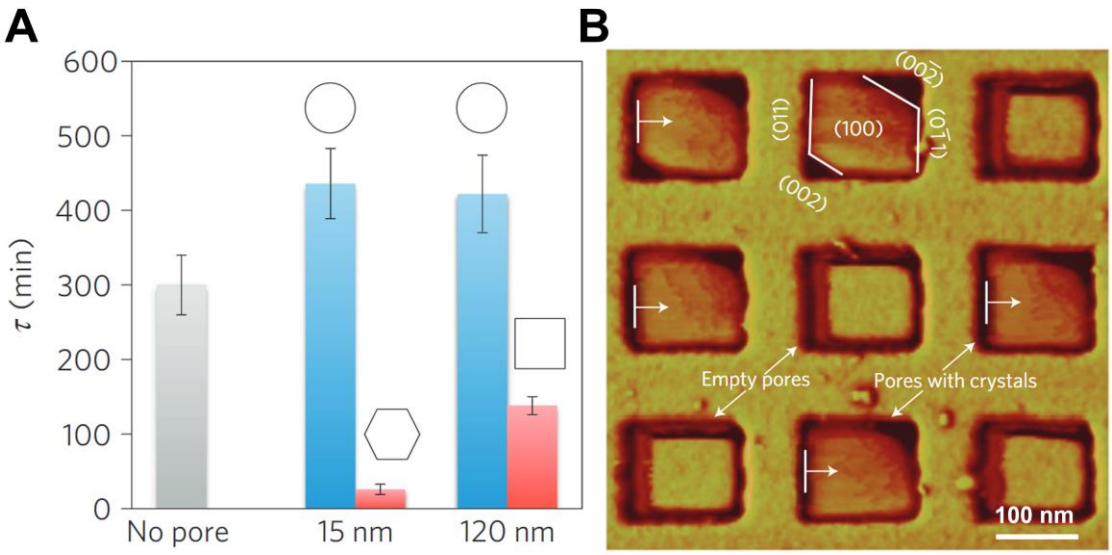


**Figure 20: (A) Influence on nanopore shape and size on nucleation induction time of aspirin[166]. (B) AFM image showing the orientation of aspirin crystals in square nanopores. *Reproduced with permission from Nature Research.***

A very similar method was used by D'Souza *et al*. to explore how surface chemistry and topography could be patterned by crystal imprinting, which was used to control calcium carbonate crystallisation. Templates were prepared by covering liquid 6-methacrylamidohexanoic acid with calcite powder, letting it cure and then etching the crystals away with acid to leave calcite-shaped templates[167]. Calcium carbonate was then crystallised on these templates, and some preferential crystallisation of calcite was observed at the pits. Additionally, calcite persisted under crystallisation conditions that normally favour aragonite formation (95 $^{o}$C), providing strong evidence that calcite crystallisation was promoted at the templates. This was attributed to a favourable surface chemistry, where it was suggested that the polymer had become organised at the interface with the calcite crystals during polymerisation, such that it presented a low-energy surface to a calcite crystal. Unfortunately, it is not possible to see the resolution of the calcite templates from the SEM imaging of this work, or whether there was any localisation of crystals in the internal angles of the calcite templates.

## 2.2 Methods

### 2.2.1 Cleaning Using Piranha Solution

Piranha solution is a 3:1 mixture of $H_2SO_4$ and $H_2O_2$. The resulting chemical reaction is highly exothermic, and is both highly corrosive and a strong oxidising agent, so must be treated with extreme caution. $H_2SO_4$ (95%, 150 mL) was first added to a 500 mL beaker. $H_2O_2$ (30%, 50 mL) was added slowly, with gentle mixing using a glass rod. Once the liquids were mixed, they were ready for use to clean glassware, which was achieved by immersing glassware in the solution for 2 hours. After glassware was cleaned, the solution was decanted and neutralised with small portions of $Na_2CO_3$ powder. Glassware was rinsed with copious amounts of Milli-Q grade water, and then isopropyl alcohol. Glassware was also stored in isopropyl alcohol until required, where it was dried with a jet of compressed air.

### 2.2.2 Preparing Pristine and Scratched Glass

Pristine, unscratched surfaces were prepared by soaking borosilicate glass slides in a base bath (1M KOH in isopropyl alcohol (IPA)), while scratched surfaces were formed by rubbing borosilicate glass slides with diamond powder (40-60 µm) in a side-to-side motion by a gloved finger with moderate pressure for 20 seconds. Both samples were then cleaned with IPA, then water, then immersed in piranha solution to remove organic residue or diamond powder. Substrates were then washed with copious water and IPA, which was followed by drying with a jet of compressed air.

### 2.2.3 Calcium Carbonate Crystallisation by Direct Mixing

Solutions of $CaCl_2$ (3 mM, 2.5 mL) and $Na_2CO_3$ (3 mM, 2.5 mL) were mixed in a 5 mL square multiwell plate. Substrates were immersed vertically in the solution for 10 minutes, before washing with water and ethanol. They were then dried with a jet of compressed air.

### 2.2.4 Scanning Electron Microscopy (SEM) Imaging

SEM imaging was performed by Dr Alex Kulak. Samples were mounted on aluminium SEM stubs using adhesive copper tape, and inserted into an FEI Nova NanoSEM 450. The chamber pressure was allowed to reach 5 x $10^{-5}$ mbar before imaging, which was performed using voltages of between 3 and 15 kV. Images were taken using circular backscatter (CBS), Everhart-Thornley (ETD) and Through Lens (TLD) detectors.

### 2.2.5 Image Analysis

Three images of each substrate on which crystals had been grown were taken at 10x magnification using a Nikon Eclipse LV100ND microscope, and converted to binary images using ImageJ with appropriate thresholding values. The 'Analyze Particles' feature was used to count the number of crystals and measure their areas, which were averaged and the error was taken as the standard deviation in the three measurements.

### 2.2.6 Atomic Force Microscopy (AFM)

AFM was performed by Dr Simon Connell using a Bruker Dimension Icon atomic force microscope equipped with a Nanoscope V controller. Images were acquired using TESPA-V2 probes (Bruker) in Tapping Mode at a frequency of 335 kHz, scanning at a resolution of 1024 pixels, or 2048 pixels for scans larger than 20 um. NanoScope Analysis v3.0 (Bruker) was used to process the images, image flattening with only a simple 1st order line level, and roughness was measured using the Roughness function.

### 2.2.7 Firing of Ceramic Glazes

Porcelain tiles were cut into ~1 cm squares using tile cutters. Water was added to nepheline syenite to make a thin paste, which was gently brushed onto the tile squares. These were left to air dry for 4 hours, then were heated at 250 $^{o}$C for 3 hours in a convection oven (Memmert UN30). Samples were allowed to cool, then

heated to 1200 $^{o}$C in a tube furnace (Carbolite Gero) at a rate of 3 $^{o}$C/min, and held for 1 hour before cooling to room temperature at a rate of 10 $^{o}$C/min.

### 2.2.8 Monitoring pH Stability of Ceramic Glazes

A pH probe (Mettler-Toledo SevenGo) was calibrated using buffers of pH 4, 7 and 10 and then inserted into a glass vial containing water to take an initial reading. The pH probe was removed, and a glazed ceramic substrate was then placed in this vial, which was sealed and mounted to an agitator (Eppendorf ThermoMixer C), which was set to run at 200 RPM under ambient conditions for 5 hours. The pH probe was re-calibrated, and a final measurement of the water pH was taken.

### 2.2.9 Fabrication of Gold Substrates with Square Pits by Templating with NaCl

A schematic diagram detailing fabrication of the square gold pits is shown in Figure 21. 4-inch (100) orientated silicon wafers were cleaned by rinsing with IPA and then dried. They were then immersed in piranha solution for 2 hours. After washing with copious quantities of Milli-Q grade water, they were placed in a metal deposition system (Cressington 308R), equipped with a thickness monitor (Cressington MTM 10), and a 5 nm film of chromium was deposited by sputtering. A layer of gold (40 nm) was then thermally deposited, and the sample was removed from the chamber (Figure 21).

A solution of NaCl (0.5 M, 5 mL) was prepared, to which IPA (10 mL) was added dropwise with stirring. Once addition was complete, the mixture was pipetted into a small petri dish containing a gold-coated silicon wafer. More IPA (5 mL) was added and the mixture was gently swirled, before leaving it for 10 minutes for crystallisation to occur. The gold substrate was then removed from the petri dish, excess solution was wicked away using a filter paper, and it was washed with copious amounts of IPA. Once dry, the substrates were placed back into the metal deposition system, and a second layer of gold (100 nm) was deposited. The directionality of thermal metal deposition meant that a thick gold layer could be deposited around the edges of the cubic NaCl crystal whilst the edges of the

crystal remained exposed. This allowed the NaCl crystals to be dissolved with water. Substrates were then washed with a strong jet of water from all sides, followed by IPA, and then were dried with a jet of compressed air.

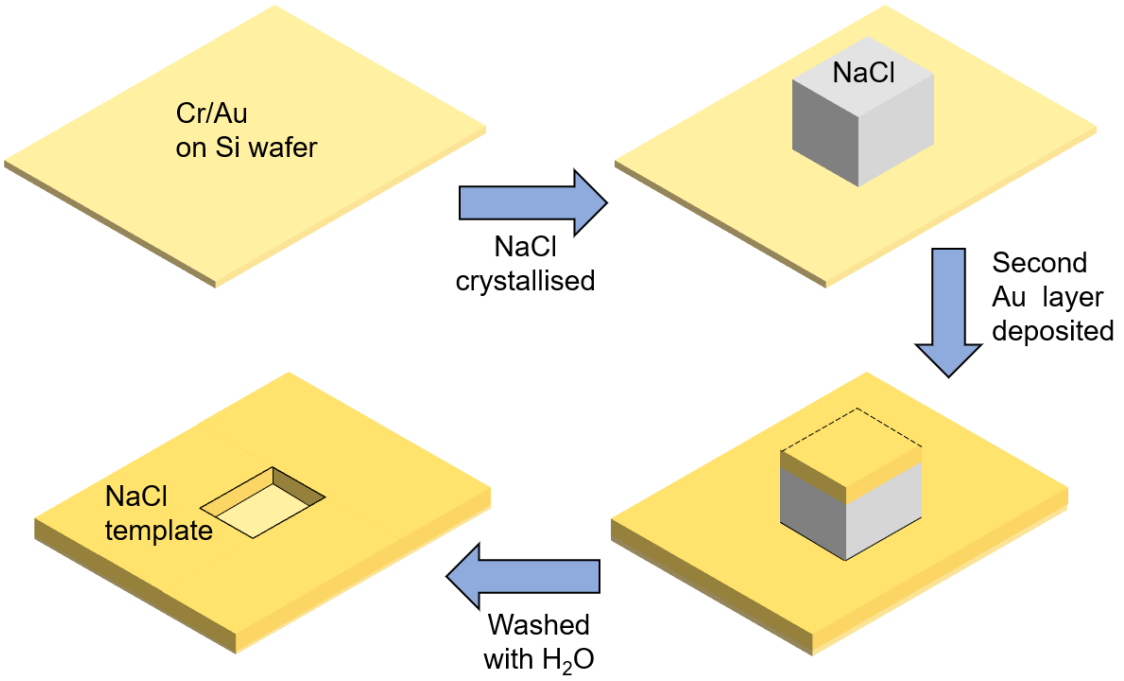


**Figure 21: Schematic diagram showing how square gold pits were fabricated**

### 2.2.10 Crystallisation of $CaF_2$ on Square Gold Pits

Gold substrates with square pits were cut into 1 cm squares, and were placed vertically in a 5 mL multiwell plate. $CaCl_2$ (5 mM, 2.5 mL) was added, followed by $NaF_2$ (10 mM, 2.5 mL) and the solutions were gently mixed by pipetting. After 1 hour, substrates were rinsed with water, and then IPA, and they were finally dried with a jet of compressed air.

### 2.2.11 Crystallisation of $KNO_3$ by Supercooling on Square Gold Pits

A home-built Peltier cooling unit was placed on the sample stage of a Zeiss optical microscope (Axio Scope A1) in reflection mode, equipped with a high speed camera (Phantom Miro M310) imaging at 90 FPS. A gold substrate with square pits was placed on the cooling unit, and a droplet of microfiltered $KNO_3$ solution (saturated at 30$^o$C) was placed on top, followed by a layer of silicone oil.

The substrate was heated to 50 $^{o}$C, then cooled to 0 $^{o}$C at a rate of 1 $^{o}$C / min until $KNO_3$ crystals formed. Substrates were then heated back up to 50 $^{o}$C and held until all the crystals had redissolved, after which they were cooled back down to 0 $^{o}$C at the same rate. 3 cooling cycles were recorded for each substrate.

### 2.2.12 Fabrication of Calcium Carbonate Resin Pits and Calcium Carbonate Crystallisation by ADM

A schematic diagram detailing fabrication of the calcium carbonate resin pits is shown in Figure 22. 4-inch (100) orientated silicon wafers were cut into 1.5 cm squares, and cleaned by rinsing with IPA, then air dried. They were then immersed in piranha solution for 2 hours. Once washed with copious amounts of Milli-Q grade water, substrates were coated with iridium (4 nm) using a Cressington 208HR sputter coater. Iridium coated wafers were then immersed overnight in an ethanolic solution of 16-mercaptohexadecanoic acid (1 mM, 20 mL) containing 1 drop of acetic acid. They were then washed with excess ethanol and dried with a jet of compressed air.

Substrates were then immersed upright in a $CaCl_2$ solution (3 mM, 5 mL) in a square multiwell plate. This was placed in a 5L desiccator chamber along with a covered 20 mL vial containing ammonium carbonate powder (4 g) that had holes pierced in its lid. Crystallisation was allowed to proceed for 16 hours, after which time the substrates were rinsed with water and IPA, and dried with a jet of compressed air.

Conductive carbon resin (Demotec® 70) was prepared by thoroughly mixing a 1:1 weight ratio of the powder and liquid components. Once the viscosity began to increase, 1 mL of the mixture was pipetted onto the calcium carbonate encrusted substrates. The system was covered with a petri dish and left for 24 hours to completely cure. Once cured, the resin was peeled away very carefully using a razor blade, and a jet of compressed air was used to remove debris. Exfoliated resin pieces were placed in dilute HCl (0.01 M, 10 mL) and were lightly agitated for 2 days. They were then rinsed with water and dried with a jet of compressed air.

Calcium carbonate was crystallised on these substrates by placing them vertically in a square multiwell plate containing $CaCl_2$ solution (2 mM, 5 mL). This plate was

placed in a desiccator chamber along with a covered 20 mL vial containing ammonium carbonate powder (4 g) that had holes pierced in its lid, and crystallisation was allowed to proceed for 40 hours. Once complete the substrates were rinsed with water and IPA, and were dried with a jet of compressed air.

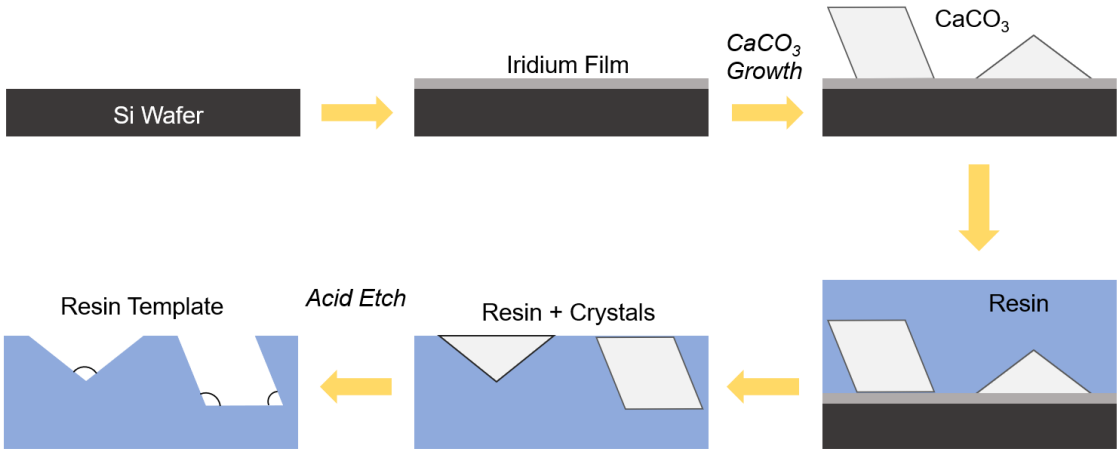


**Figure 22: Schematic showing how calcium carbonate resin templates were prepared.**

## 2.3 Results

### 2.3.1 Calcium Carbonate Crystallisation on Glassy Materials

#### 2.3.1.1 Scratched Glass

The nucleation of calcium carbonate on both pristine and scratched glass was investigated in this set of experiments. Calcium carbonate was crystallised by direct mixing of $CaCl_2$ and $Na_2CO_3$ for 10 minutes (Figure 23), and the numbers of crystals per square millimetre and their average sizes are shown in Figure 23. More than ten times as many crystals were produced on the scratched glass than pristine glass, and the average size of the crystals was reduced by 30%. This reflects the faster depletion of ions in solution when a greater number of nuclei are present, which leads to slower growth rates.

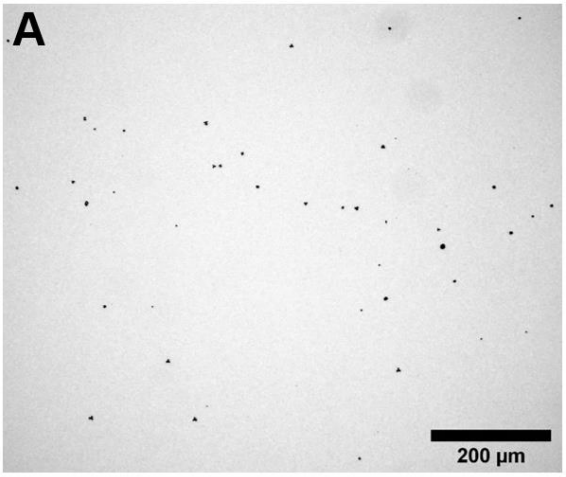


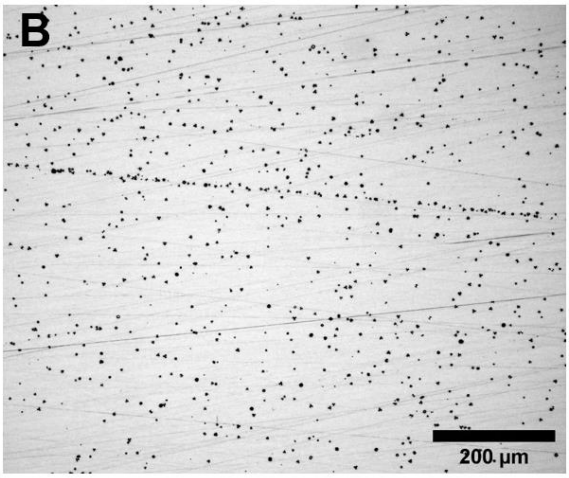


| | |
|---|---|
| Number density = 95 ± 33 crystals / mm$^2$ | Number density = 991 ± 131 crystals / mm$^2$ |
| Average area of a crystal = 12.4 ± 10.0 µm$^2$ | Average area of a crystal = 8.7 ± 7.7 µm$^2$ |

**Figure 23: $CaCO_3$ crystals formed on (A) pristine glass and (B) 40-60 µm diamond powder scratched glass.**

AFM analysis was used to characterise the surfaces of both glass samples, and to find the actual surface area (Figure 24). There were very few surface features on the pristine glass. In contrast, diamond powder abrasion led to the formation of multiple, aligned nano-scale scratches and increased the glass surface area by 0.33%. A corresponding 943% increase in crystal number density was observed.

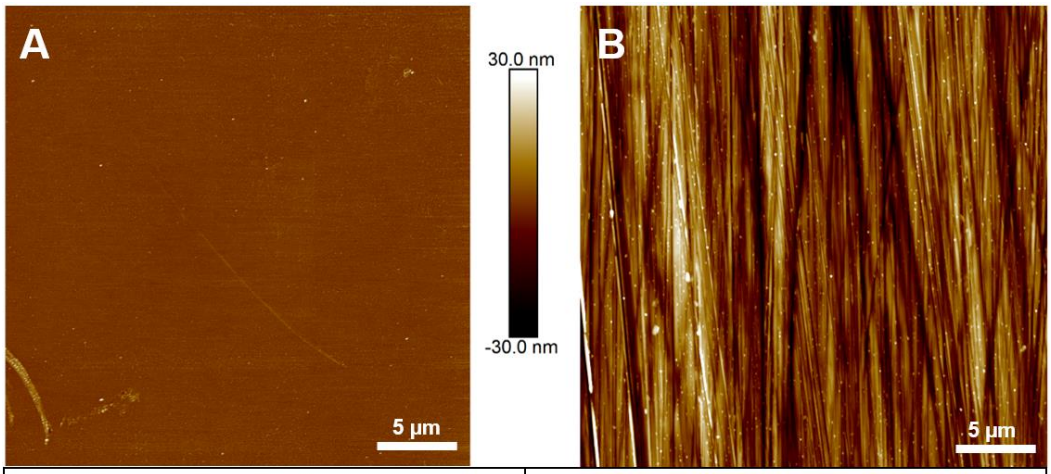


| | |
|---|---|
| Projected area = 900 µm$^2$ | Projected area = 900 µm$^2$ |
| Surface area = 904 µm$^2$ | Surface area = 907 µm$^2$ |
| RMS roughness = 1.68 nm | RMS roughness = 9.30 nm |

**Figure 24: AFM images of (A) pristine glass and (B) 40-60 µm diamond powder scratched glass, showing differences between projected and measured surface areas.**

#### 2.3.1.2 Ceramic Glazes

Under the right conditions, ceramic glazes (Figure 25) form crazes, which feature highly acute angles that can potentially offer highly effective crystal nucleation sites. Therefore crazed ceramic glazes were prepared, and crystallisation of calcium carbonate was explored on these surfaces.

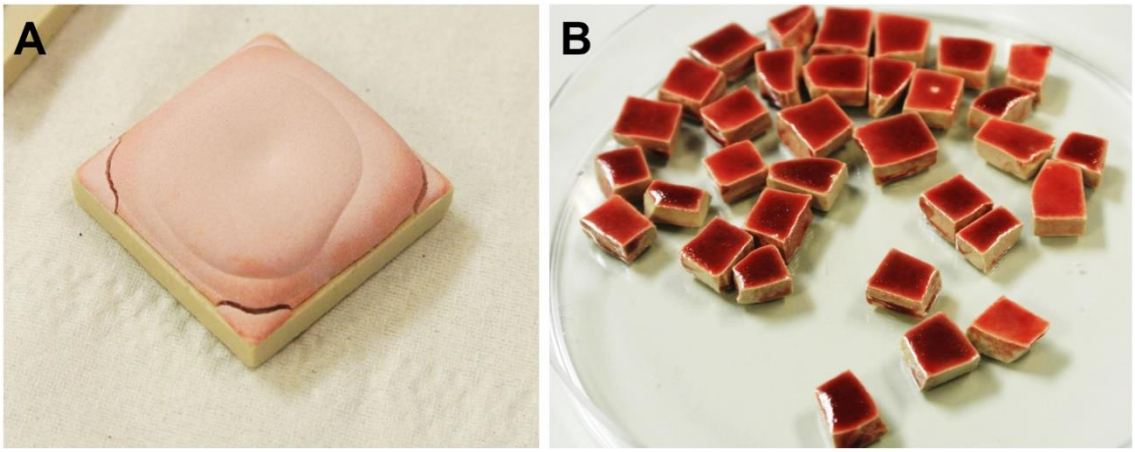


**Figure 25: Pieces of ceramic tile coated with a commercial red glaze (A) before and (B) after firing.**

Nepheline syenite paste was applied to a small piece of ceramic tile which was then fired to produce a uniform glaze. Nepheline syenite was chosen for its high coefficient of thermal expansion (~ 9 x $10^{-7}$ $K^{-1}$), which results from a high alkali metal oxide to $SiO_2$ molar ratio of 1:4.5 [168]. By contrast, conventional craze-free glazes contain lower alkali metal oxide to $SiO_2$ molar ratios of approximately 1:6, and consequently have much lower coefficients of thermal expansion (5-6 x $10^{-7}$ $K^{-1}$). A hard glaze hosting numerous crazes formed spontaneously when nepheline syenite powder was fired and then cooled (Figure 26A). These crazes varied in size and shape, but nearly all were between 1 and 3 µm in width (Figure 26B). Measurement of the angles at their bases was not possible using SEM because they were too acute.

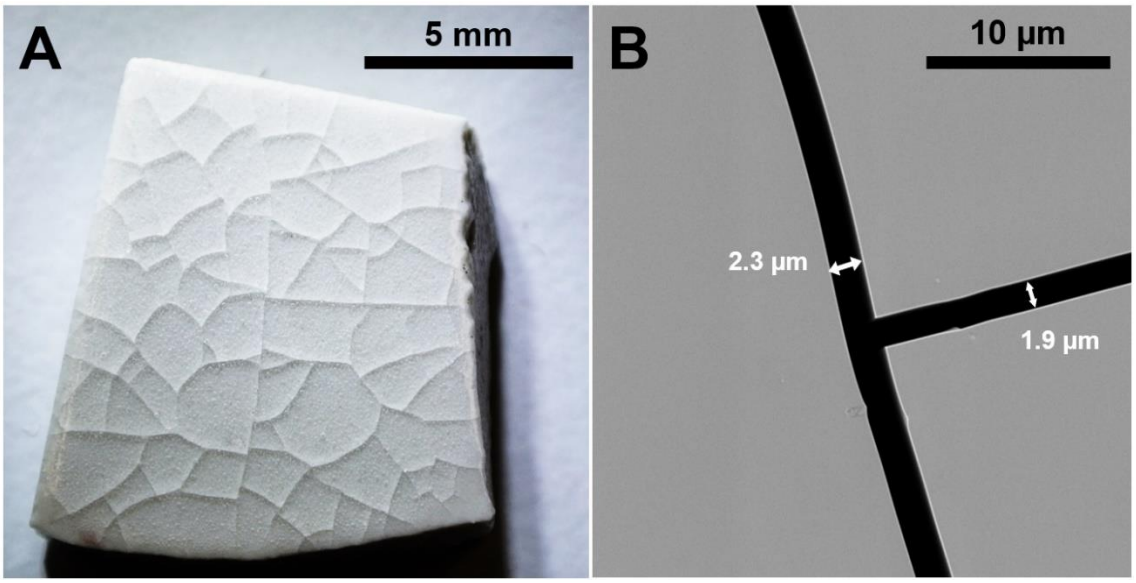


**Figure 26: (A) Photograph of the crazed nepheline syenite glaze. (B) SEM image showing the widths of crazes.**

Since alkali metal oxides typically react strongly with water to liberate hydroxide ions, the stability of the glazes in water was tested. A glazed substrate was stirred in 5 mL deionised water for 5 hours and the pH was monitored. The pH only increased very slightly from 6.55 to 6.57 during this time, which shows that the substrates were sufficiently stable for crystallisation experiments to be run without significant quantities of hydroxide leaching into the mineralisation solution.

$CaCO_3$ was crystallised on the prepared substrates from a solution prepared by direct mixing of $CaCl_2$ and $Na_2CO_3$ (Figure 27). A large number of crystals were

located in several, but not all of the cracks. Calcite was principally formed, in addition to some aragonite crystals in places.

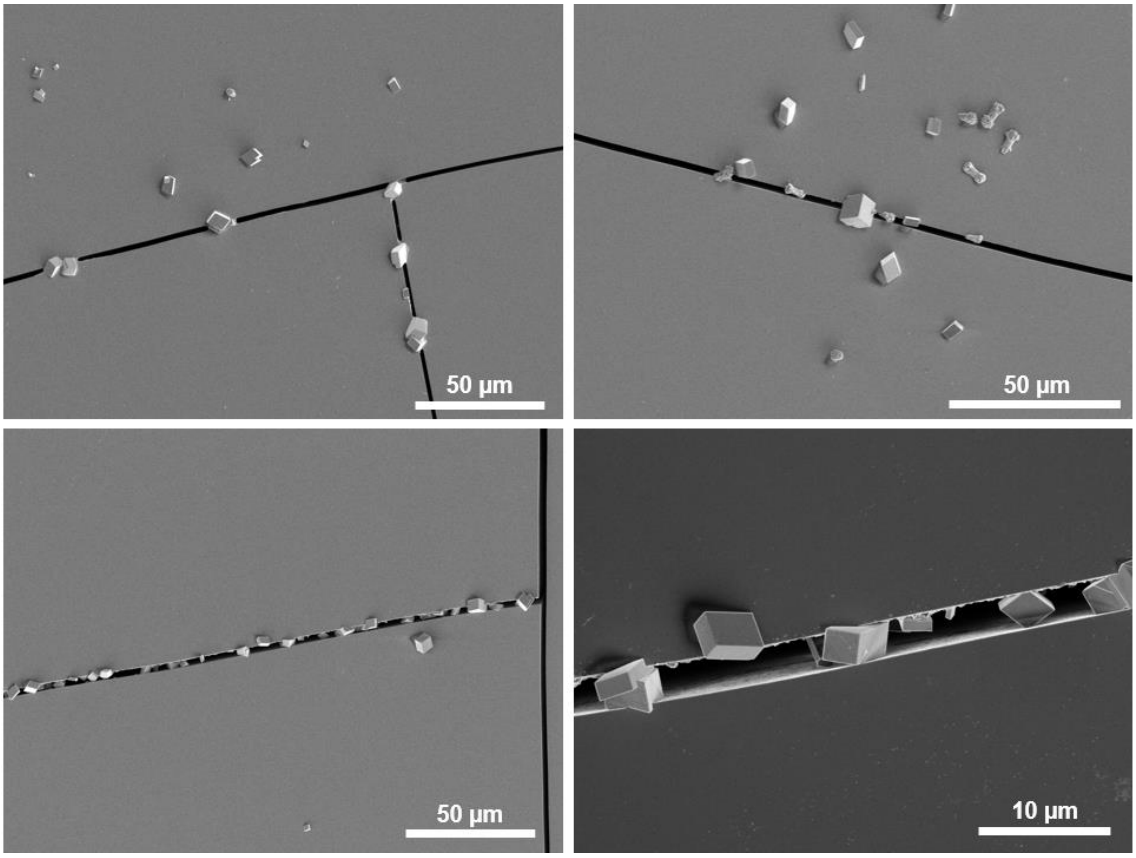


**Figure 27: SEM images showing calcium carbonate crystals grown on crazed nepheline syenite glaze.**

## 2.3.2 Crystal Moulds as Crystallisation Templates

### 2.3.2.1 Square Gold Pits made by NaCl Templating

Here, novel crystal-templated pits with 90$^{o}$ angles at their corners and edges were fabricated by coating cubic NaCl crystals with gold and then removing the NaCl (Figure 21). Crucially, the entire surface of the substrate was chemically-uniform gold, meaning that the effect of topography on crystallisation could be separated from the effects of surface chemistry.

The base substrate for the gold structures was prepared by firstly depositing a smooth layer of gold onto a pristine silicon wafer by thermal deposition. Chromium was used as a eutectic adhesion layer between the silicon and gold,

preventing delamination. When viewed by SEM, the gold appeared flat and smooth, and high-magnification imaging showed the typical film arrangement of sub 100 nm gold ‘islands’ (Figure 28).

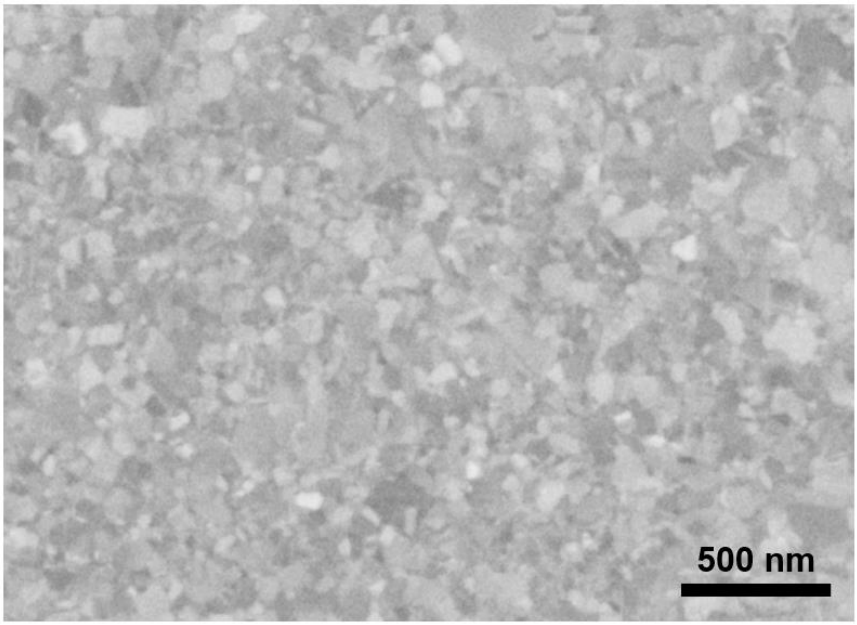


**Figure 28: SEM image showing the ‘island’ structure of a chromium-gold film deposited on a silicon wafer.**

NaCl was then crystallised as 5-10 µm cubes on these substrates. This proved to be highly challenging, since soluble minerals such as NaCl typically grow rapidly, such that a small number of millimetre-scale crystals form within seconds. In order to produce more crystal nuclei – such that the nucleation sites could be identified – the NaCl solution needed to be rapidly taken from an undersaturated to a highly supersaturated state. However, this is not easily achieved when the low growth rates used to give cubic morphologies are employed. Crystal growth in high solution concentrations is often diffusion-limited, meaning that hopper and dendrite morphologies result. Both issues were solved by adding IPA to a 0.5 M NaCl solution (far below its solubility limit of ~5.5 M). In this way, the NaCl concentration was low enough for cubic crystals to form, and IPA behaved as an antisolvent, rapidly driving up the supersaturation and increasing the nucleation

rate. The morphologies were slightly more hopper-shaped than was desirable, but crystals were small and well-distributed across the gold surface.

Samples were washed with IPA and dried, before a much thicker gold layer was thermally deposited (Figure 29A/B). NaCl crystals were then dissolved with water (Figure 29C/D). The corners were slightly rounded, likely as a result of shadowing from the vertices of the slightly hopper-shaped NaCl crystals. The edges of the templates appeared to express 90$^{o}$ angles however.

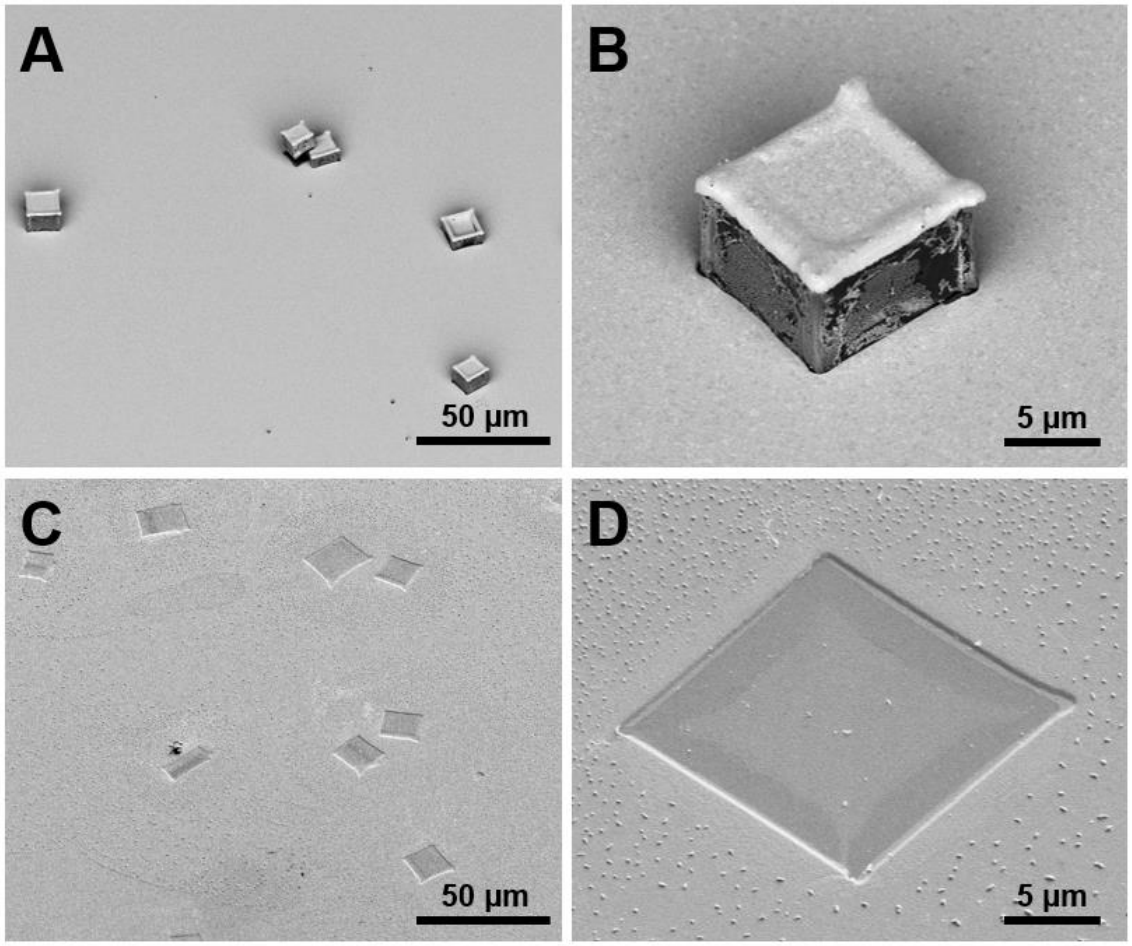


**Figure 29: (A/B)SEM images showing gold deposited on NaCl crystals, which crystallised on top of another gold layer. (C/D) The same samples but following water washing to remove the NaCl and leave templated shapes in gold.**

These substrates were then tested to see whether the crystal templates could enhance nucleation. If the angles expressed were 90$^{o}$ as intended, then according to the principles of angle-directed nucleation, any cubic or

orthorhombic crystal should be preferentially nucleated at the edges of the pits. $CaF_2$ (fluorite) was chosen due to its face-centred cubic (FCC) symmetry and low solubility, meaning that large numbers of $CaF_2$ crystals could be grown to a size similar to the pits.

A slightly greater number of $CaF_2$ crystals formed at the edges of the square pits than on the rest of the gold surface, indicating that there was a slight enhancement of nucleation (Figure 30). Alignment of the morphologies of the crystals with the pit edges was poor however, which suggested that the enhancement of nucleation could not be explained by angle-matching.

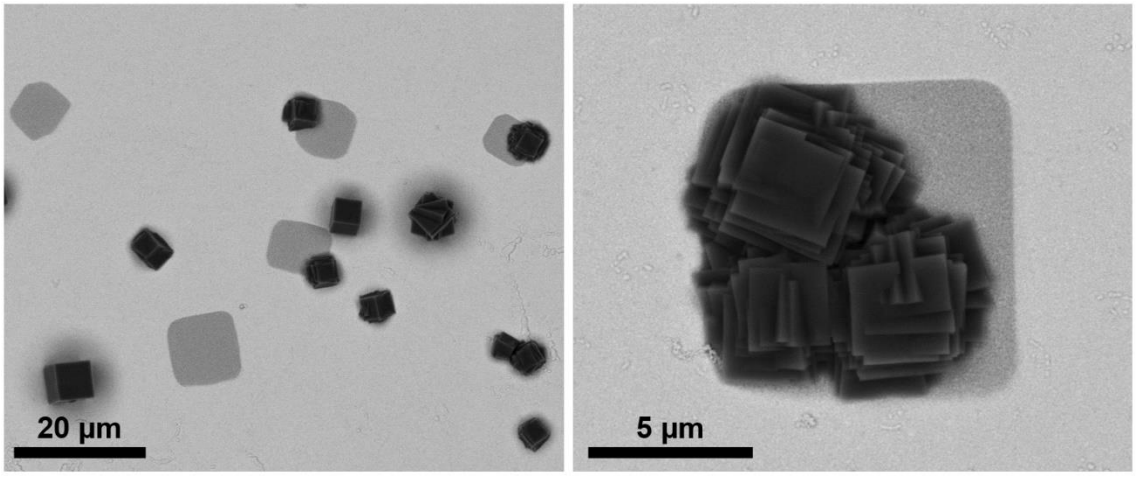


**Figure 30: SEM images showing the results of crystallising $CaF_2$ on NaCl templated gold substrates.**

$KNO_3$ was also crystallised on the gold substrates with square pits, which was achieved by cooling the crystallisation solution. $KNO_3$ has one polymorph with an orthorhombic structure ($\alpha$), and two with rhombohedral structures ($\beta$ and $\gamma$). If the substrate was able to direct polymorph, this would indicate that angle-directed nucleation had occurred. Droplets of $KNO_3$ solution were placed on the gold substrates, and silicone oil was added on top to slow evaporation. Several crystals were produced within each droplet from each cooling cycle, but these were always $\beta$-$KNO_3$ (Figure 31), meaning that polymorph control was not achieved.

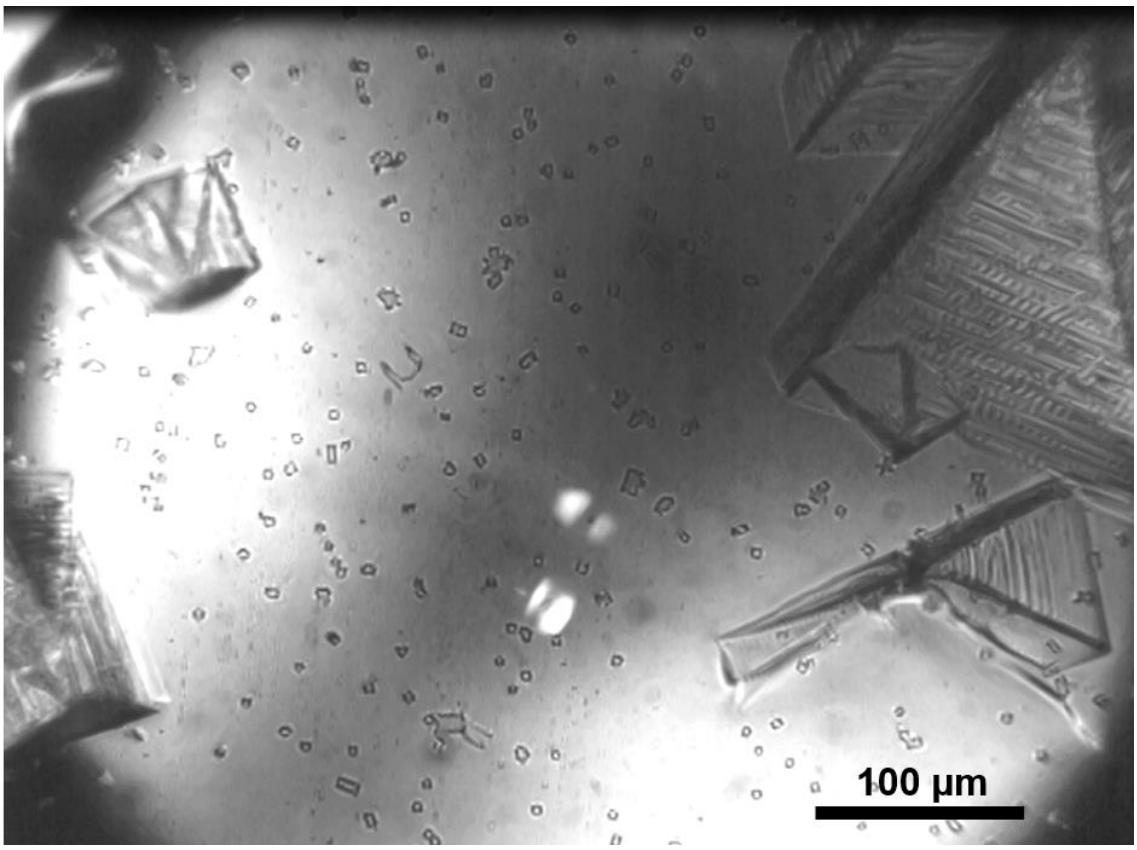


**Figure 31: Optical microscopy images showing $KNO_3$ crystals growing from a supercooled solution on NaCl templated gold substrates.**

Crystallisation on the substrates was also recorded using a high-speed camera, and nucleation events were mapped and counted over three heat/cool cycles, and on two different samples. The numbers in Figure 32 correspond to the number of times nucleation was observed at a nucleation site, with green numbers corresponding to square pits and red numbers corresponding to nucleation events on the planar gold (i.e. not in the pits). Seven out of the twenty total nucleation events occurred in pits (corresponding to 35% of nucleation events). Three pits were responsible for the seven nucleation events at pits, so clearly some were more effective than others at promoting nucleation, perhaps due to their shape. Notably, only 5-10% of the substrate surface was occupied by pits, which shows that they did indeed promote nucleation, albeit only slightly.

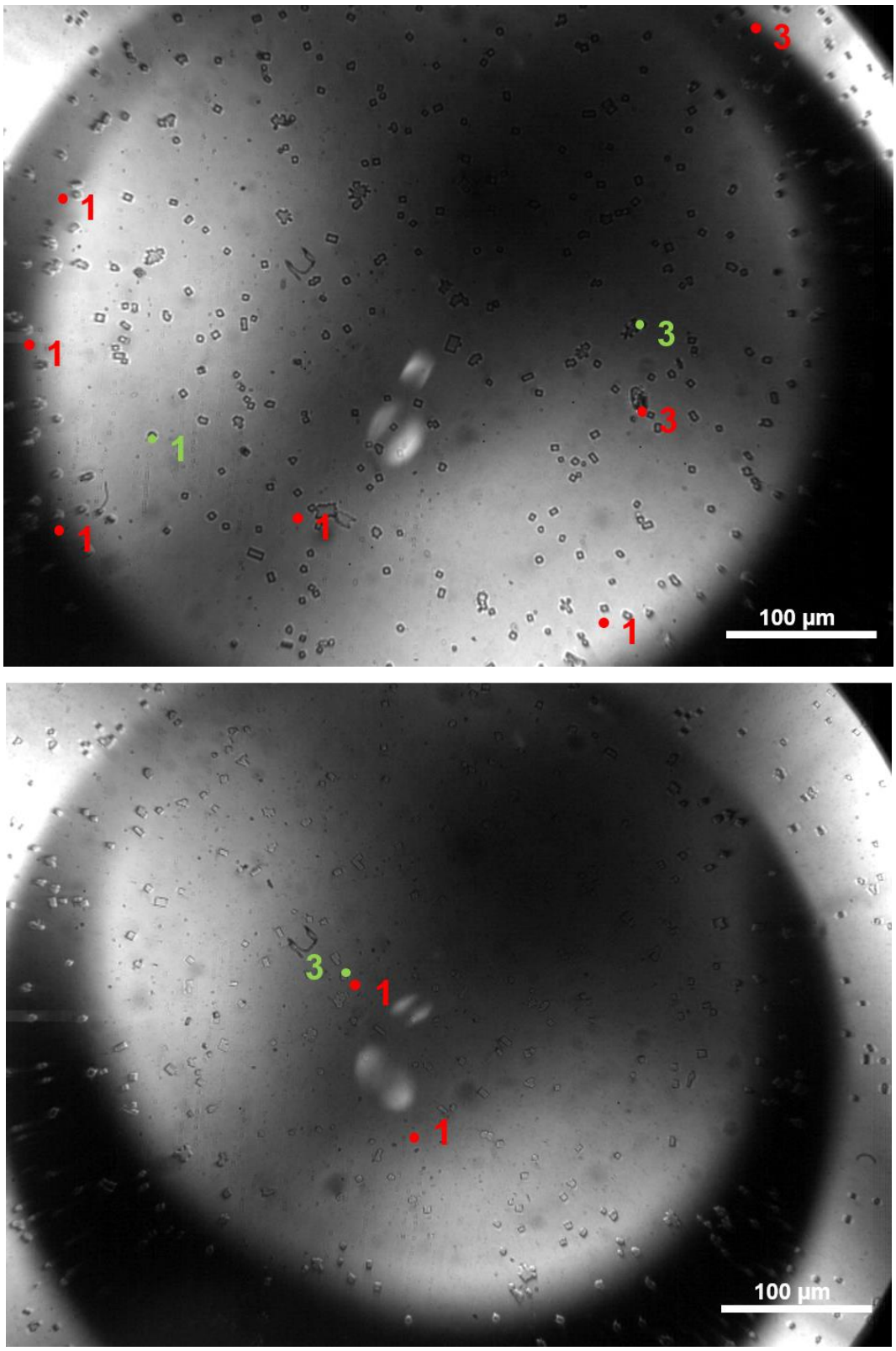


**Figure 32: $KNO_3$ nucleation sites on two separate areas of a gold substrate with square pits. Numbers correspond to the number of times a crystal formed at a site (out of three cooling cycles). Green numbers correspond to crystals which grew on a square pit, and red numbers correspond to crystals which grew on planar gold.**

#### 2.3.2.2 Calcium Carbonate Resin Pits

Calcium carbonate crystals were reverse-moulded to create pits with angles that matched calcite or vaterite (Figure 22), and then calcium carbonate crystals were grown on top. If crystals formed within the templates were morphologically oriented to match the shape of the pit, then this would be strong evidence that angle-directed nucleation had taken place.

A clean Si wafer was coated with iridium, and functionalised with 16-mercaptohexadecanoic acid. Calcium carbonate was then grown via the ammonia diffusion method (ADM). Calcite crystals that lay in various orientations principally formed (Figure 33), together with some vaterite crystals. Resin was then poured on top, cured, and then exfoliated from the surface. This pulled the crystals away with it, exposing their undersides (Figure 34). These crystals were then dissolved by 2 days agitation in HCl, creating resin templates containing calcite-shaped pits (Figure 35).

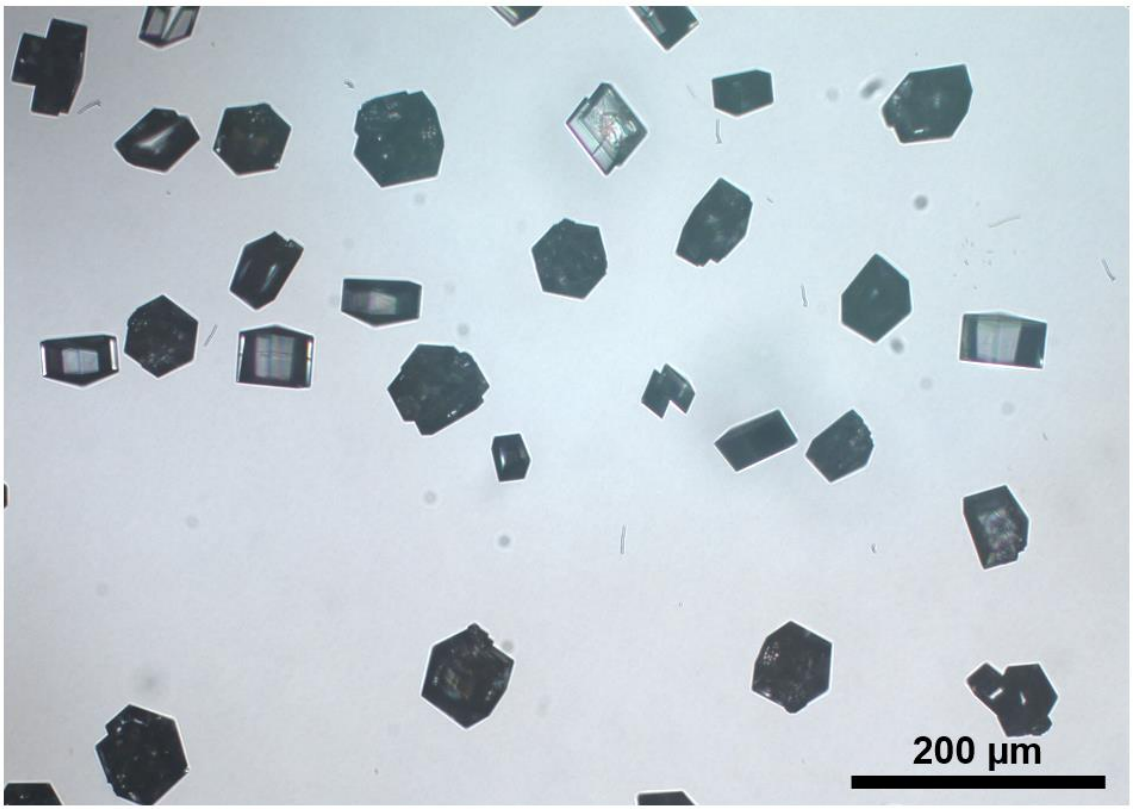


**Figure 33: Optical microscopy image showing calcium carbonate crystals grown by ADM on a 16MHDA-functionalised iridium-coated Si wafer.**

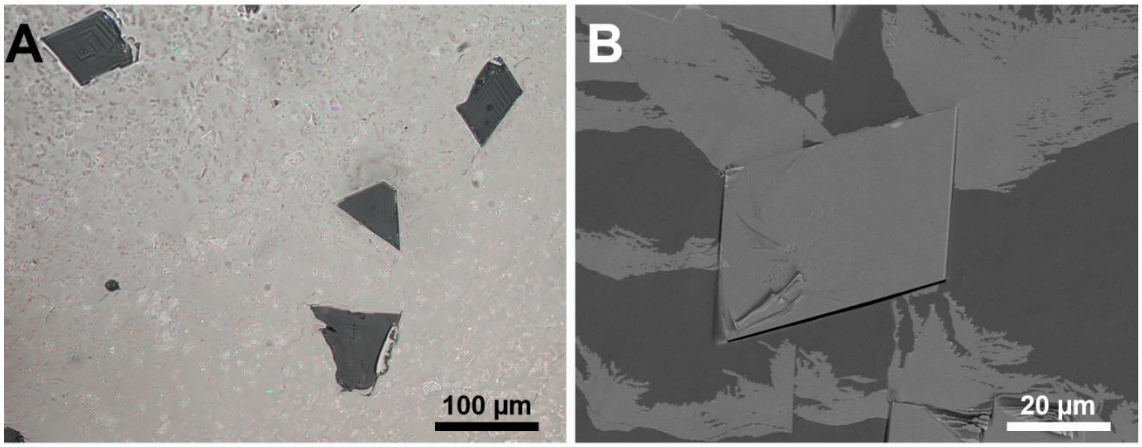


**Figure 34: (A) Optical microscopy and (B) SEM images showing calcium carbonate crystals embedded in resin after exfoliation.**

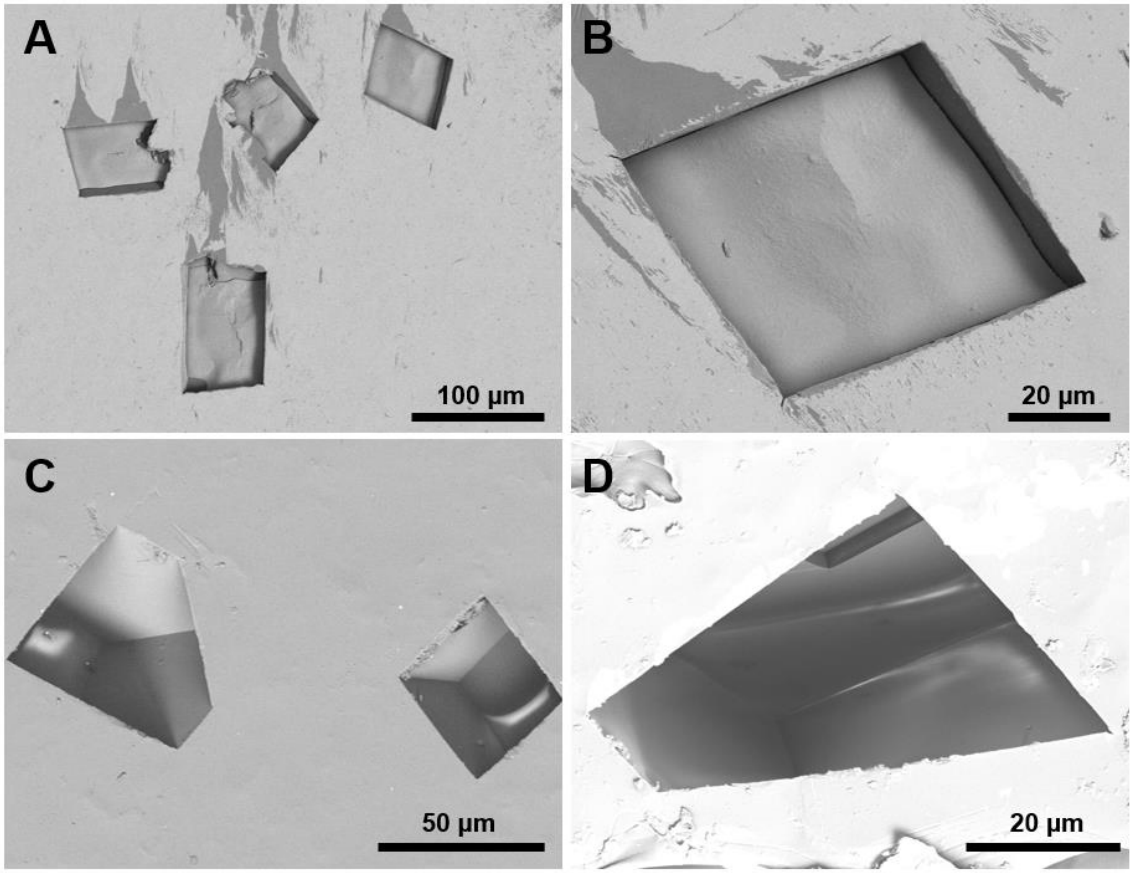


**Figure 35: SEM images showing calcium carbonate crystals embedded in resin (A/B) after partial acid etching and (C/D) after acid etching was complete.**

Visual inspection showed that the pits created in the resin were near-perfect replicas of the calcite crystals from which they had been moulded. Their surfaces

were cleaned using an air jet and some adhesive tape, and calcium carbonate crystals were then grown on the resin surface using the ADM. Analysis by SEM showed that calcite, vaterite and aragonite formed on the substrates (Figure 36), although calcite and vaterite were more abundant than aragonite. Polarised light optical microscopy showed that many of the templates were filled with crystals, however their morphologies were not oriented with respect to the shape of the pits (Figure 37).

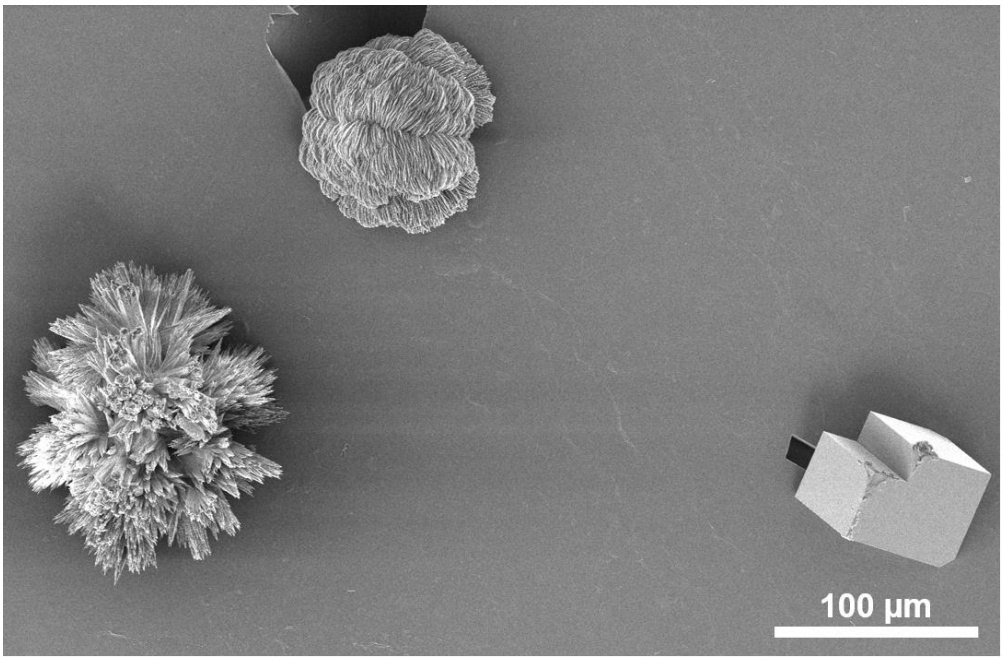


**Figure 36: Calcite, vaterite and aragonite all crystallised on the templated resin surface.**

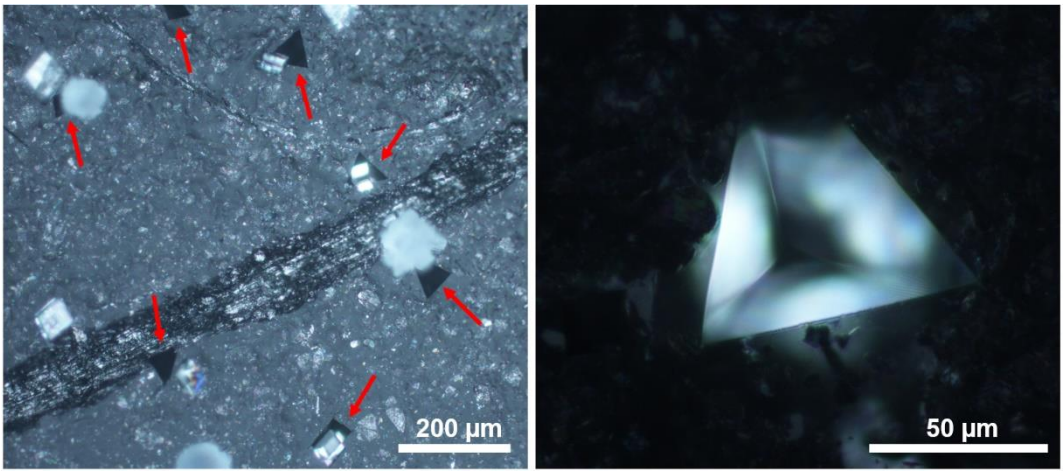


**Figure 37: Polarised optical microscopy images showing calcium carbonate crystals grown on resin substrates. Red arrows show the locations of templates (crystal-shaped pits). The right-hand image shows a template hosting a birefringent calcium carbonate crystal, which illuminates the edges of the template.**

SEM images confirmed that the crystal templates were effective at promoting nucleation. However, the orientation of the calcite templates did not match the orientations of calcite crystals grown on them (Figure 38). The morphologies of reverse-moulded vaterite templates resembled vaterite crystals with astonishingly high resolution, and surprisingly, these were effective at crystallising vaterite (Figure 39).

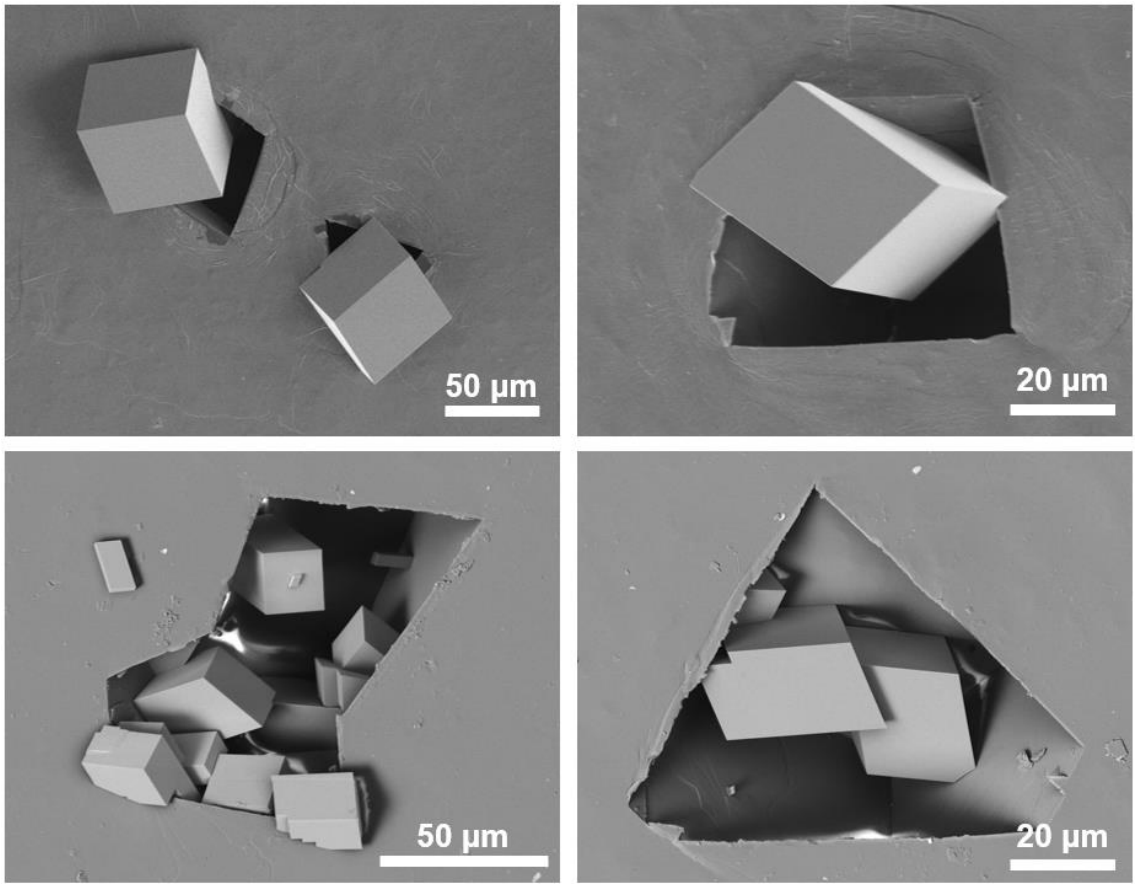


**Figure 38: SEM images showing calcite crystals grown in calcite shaped pits.**

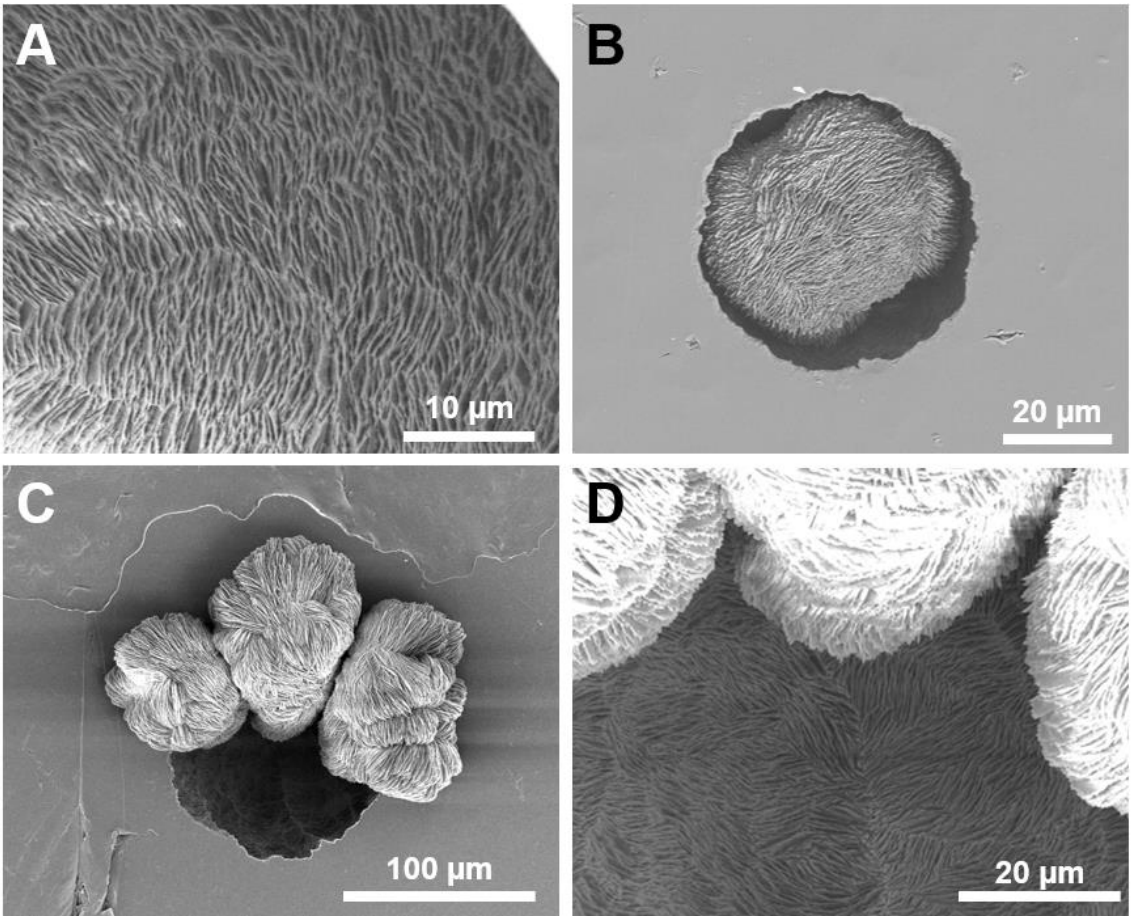


**Figure 39: SEM images of (A) the microstructure of a vaterite shaped pit. (B/C/D) Vaterite crystals selectively grown on vaterite shaped pits.**

## 2.4 Discussion

### 2.4.1 Can Nucleation Sites be Manufactured by Modifying Surface Topography?

Glasses are excellent surfaces with which to explore how surface topography can affect crystallisation. They contain a homogeneous distribution of structural units (such as oxide, silicate and aluminosilicate), but no crystalline order, meaning that the topography of nucleation sites can be studied without considering different surface chemistries or epitaxial matching. The results presented in this chapter show that scratching glass with diamond powder significantly enhances its ability to nucleate calcium carbonate.

The rate of heterogeneous nucleation is related to the substrate surface area as described by Equation 21, where $S$ is supersaturation, and $A_i$ and $B_i$ are the exponential prefactor and exponent respectively.

$$Rate = \sum_{i=1}^{n} A_{\mathrm{i}} S(exp\left(\frac{B_{\mathrm{i}}}{ln^2 S}\right))$$

**Equation 21**

For an ideal flat surface which nucleates homogeneously across its entirety, the number of nucleation sites, $n$, increases linearly with surface area, meaning that the rate of nucleation is also linearly proportional to the area. After scratching glass with diamond powder, the increase in nucleation density of calcium carbonate with increasing surface area was much greater than linear, clearly showing that glass did not behave as an ideal flat surface. Instead, scratched glass exhibited many more nucleation sites than smooth glass, which provides strong evidence that surface topography can enhance crystal nucleation rates. Sharp surface features such as those made by diamond powder abrasion can be effective nucleation sites because nuclei are stabilised by acute features with similar sizes to a critical nucleus[169] (see intro Section 1.8.1).

### 2.4.2 Nucleation in Acute Features

Theoretical work shows that nucleation is enhanced in concave features. Further, when a surface feature contains an angle below 90° and the contact angle between the nucleus and substrate is also below 90°, the barrier to nucleation

can disappear completely[15,16]. These predictions come from simplistic nucleation models however, and do not consider the crystalline structure of a nucleus, or transport of material to the developing nucleus. The crystallinity of nuclei can lead to much higher contact angles than would exist for liquid phases of the same compound[170,171], and highly confined volumes can also physically restrict the formation of a critical nucleus[83,172,173]. Additionally, the transport of material to a concave feature becomes increasingly restricted with a reduction in angle, as there is a narrower aperture for material to diffuse through. In confined solutions there is also an increased presence of dense ordered interfacial liquid (see Section 1.7.2) which can further reduce the diffusion coefficient[71,174–177]. This is highly system dependent however, as there are a multitude of confining feature sizes and geometries which can actually enhance the mobilities of liquids[178].

Crazed ceramic glazes with highly acute cracks were fabricated to explore whether such features can enhance nucleation. The acute bases of the crazes were unfortunately too deep to be visualised by SEM. However, when calcium carbonate was crystallised on the glazes, crystals (mostly calcite with some aragonite) could be seen protruding from some of the crevices. The vast majority of crazes were ineffective at nucleating calcium carbonate however, which suggests that they did not possess the correct sizes or geometries to promote crystallisation. Crazes were between 1 and 3 µm in width at the glaze surface, which is orders of magnitude larger than critical nuclei, and so were unlikely to have restricted their formation. These distances are, however, similar to the confining sizes reported by Stephens *et al.* where calcium carbonate crystallisation was reduced[20]. The crazes were deeper than could be visualised by SEM, which suggests that the acute bases were even more confined than their apertures. There is therefore a trade-off in terms of the nucleation behaviour of acute features and their geometry. Increasing the acuteness of a feature can significantly reduce the free energy of nucleation upon it, but at the cost ease of material transport within this region.

### 2.4.3 How Practically Relevant is Angle-Directed Nucleation?

Angle-directed nucleation has been discussed as a mechanism by which surface topography can enhance heterogeneous nucleation[152,166,179,180]. This theorises that the specific angles expressed by a surface feature can enhance nucleation rates if they match the intrinsic angles of a nucleating crystal. However, there is currently no experimental data to prove that this mechanism operates in real systems, where it is highly challenging to fabricate and characterise suitable structures. Angle-directed nucleation may be highly relevant to situations such as crystallisation on curved features made by conchoidal fractures of glasses. In this case the angles expressed can vary continuously, and hence match crystalline angles perfectly.

In this work, two sets of pits defined by planar faces were fabricated using different materials and methodologies to test the impact of angle-directed nucleation on real systems. Gold templates with 90º edges were made by using NaCl cubes as deposition shadow masks. There was some enhancement of nucleation of $CaF_2$ on the templates, but the lack of control over orientation meant that an angle-directed nucleation mechanism was unlikely. There was also little enhancement of $KNO_3$ nucleation and no polymorph control. The kinetic rhombohedral polymorph *β*-$KNO_3$ always crystallised, meaning that there could no exact matching could occur with the 90º angles of the substrates. The orthorhombic *α* polymorph is more thermodynamically stable than the *β* polymorph and its {1 0 0} planes are separated by 90º angles. This means that an angle-directed nucleation mechanism would have favoured *α*-$KNO_3$ crystallisation. The fact that this did not occur shows that the faster nucleation kinetics of *β*-$KNO_3$ formation dominated over any potential stabilisation of *α*-$KNO_3$ nuclei in the square gold pits.

In contrast, polymorph control did appear to be possible using calcium carbonate shaped resin pits. Calcium carbonate crystals grown on the 16MHDA-functionalised iridium surfaces were predominantly calcite, together with some vaterite. This surface was covered by resin, which was peeled off and the crystals dissolved to give a resin surface containing crystal-shaped pits. Crystallisation of calcium carbonate was generally enhanced at these locations. In general, vaterite-shaped pits produced vaterite, and calcite-shaped pits produced calcite. Calcite and vaterite are both commonly observed in laboratory-scale calcium

carbonate crystallisation experiments, which demonstrates that similar energy barriers exist for both phases. This may explain why polymorph control was achieved in this system. The vaterite pits were highly rough, meaning that many more crevices were present than the few discrete angles expressed by the calcite-shaped pits. This may have significantly increased the likelihood that one of the angles expressed by the vaterite surface perfectly matched vaterite. There was however a possibility that some crystalline material was retained in the shaped pits following the agitation in HCl, particularly given the highly textured appearance of the vaterite-shaped pits. This was thought to be highly unlikely given the excessive time for which the substrates were immersed in acid, but could not be altogether dismissed as a reason for the results obtained without further analysis.

The work described in this chapter suggests that angle-directed nucleation could be responsible for directing the polymorph of calcium carbonate. However, it is not expected to be a dominant mechanism for promoting nucleation in most systems, as more significant enhancement can occur on rough surfaces. This is thought to be a combination of exposed areas with high densities of dangling bonds[150] and also a greater ability to reduce interfacial tension of a nucleus in a more acute crevice[15,16,169].

### 2.4.4 Future Work

Further imaging the ceramic glaze crazes with different techniques would be required to measure the angle at their bases, either using confocal microscopy or by producing a cross section by focused ion-beam (FIB) etching, and imaging it with SEM. The resin templates present results that would also make for an interesting further study. Templates could be made from both NaCl and calcite, and then the effects of the angles on nucleation of both calcium carbonate and $CaF_2$ could be studied, to decouple the classical enhancement of nucleation with surface topography by reduction in interfacial area from an angle-directed nucleation mechanism. Lastly, the absence of residual calcite or vaterite in the resin pits following HCl etching should be confirmed using a high-resolution imaging method such as TEM. This may be challenging however, given that only a tiny cluster of crystalline material in an entire pit may be sufficient to seed crystallisation.

## 2.5 Conclusions

This chapter describes a number of investigations into the effects of surface topography on nucleation. The sharp features created by scratching glass were highly effective at nucleating calcium carbonate. Concave features are generally good at enhancing nucleation[151], and the sizes of these features were shown to be important. When confining dimensions approach nanoscale values, confinement effects can hinder processes involved in nucleation, such as ion and water diffusion, as the diffusion coefficient has units of $m^2\ s^{-1}$.

Angle-directed nucleation might work well in theory, but experimentally it was very challenging to unequivocally state that it occurred in any of the systems investigated, given the many other mechanisms in play. Work described in this chapter showed that $KNO_3$ polymorph control was not possible on square gold templates, but these did enhance the nucleation for $CaF_2$ somewhat. The most convincing evidence for angle-directed nucleation was obtained from a study of calcium carbonate crystallisation on resin templates, where vaterite nucleated in vaterite-shaped pits and calcite nucleated in calcite-shaped pits. It is therefore plausible that angle-directed nucleation promoted nucleation of vaterite in vaterite resin templates, though further experimentation is required to fully confirm this.

# Chapter 3
# Investigation of Nucleating Properties of Functionalised Iridium Cracks

## 3.1 Introduction

### 3.1.1 Overview

This study aimed to investigate the enhanced crystal nucleation behaviour at surface cracks on a novel substrate, which comprises of iridium sputter coated onto PDMS squares. Iridium films are highly brittle, such that any deformation of the underlying PDMS results in the formation of numerous cracks. Following functionalisation with 16-mercaptohexadecanoic acid (16MHDA), numerous calcite crystals form preferentially at the cracks over formation on flat regions. This result presented an exciting opportunity to study how the topography at the cracks promote crystal nucleation.

A series of methodological refinements were made initially to establish a more robust protocol for studying crystallisation on the FC-Ir-PDMS substrates. In the early stages of experimentation, PDMS was plasma treated to form a cracked silica-like surface layer, as it was thought that these features were responsible for the enhanced nucleation. However, it was discovered that crystals were instead localised to iridium cracks, which were numerous within the PDMS cracks. Refinements were also made to the surface functionalisation and washing steps to ensure that results varied little between experiments.

A series of experiments were then conducted to investigate how nucleation of calcium carbonate was promoted at the cracks. *In-situ* microscopy experiments were performed to measure nucleation kinetics and compare these to glass substrates. Cross-sections of crystals grown on cracks were studied using FIB-SEM, which revealed unique insights into how the crystals had formed. TEM analysis of thin sections of crystals in cracks elucidated these insights further, and aided in establishing a mechanism for the nucleation process.

The universality of the substrates for enhancing crystal nucleation was then explored by attempting to crystallise a range of ionic and molecular crystals at the cracks. Commonalities between successful experiments were identified, which enabled the role of surface chemistry to be discussed alongside topography.

## 3.1.2 Background

### 3.1.2.1 Polydimethylsiloxane (PDMS)

PDMS is a widely-used elastomer with tuneable mechanical, optical and chemical properties. It comprises of a repeating silicon-oxygen backbone (Figure 40), which is the second strongest silicon-heteroatom single bond after the silicon-fluorine bond (452 vs 565 kJ $mol^{-1}$ [181]). This makes the backbone highly inert to most chemical environments. The methyl groups decorating the backbone render it hydrophobic and lipophilic, however the silicon-carbon bonds can be oxidised by strong oxidising agents such as hydrogen peroxide[182] or oxygen/air plasma[183]. This replaces -Si-Me moieties with -Si-OH and Si-O-OH moieties[184].

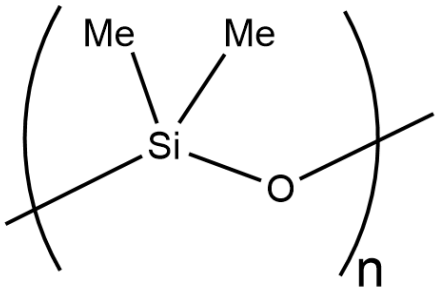


**Figure 40: Structure of a repeat unit of PDMS**

PDMS is used abundantly in microfluidics[185–187], sensing[163,188] and soft robotics[189,190] applications due to its flexibility, optical transparency, ease of moulding and tuneable stiffness achieved by varying the degree of crosslinking[191]. The oxidation of PDMS by oxygen/air plasma has been well-documented to increase its hydrophilicity, enabling separate pieces of PDMS to be covalently bonded together[192] or to other hydrophilic surfaces such as glass without the use of adhesives.

Under high oxygen/air plasma dosages, a brittle silica-like crust is produced, which, under excessive intrinsic or applied stress, can produce micro-cracks[183] (Figure 41). These are generally undesirable for most applications, because the silica layer does not possess the elastomeric properties of bulk PDMS, thus preventing it from producing a properly sealed bond. However, the micro-cracks have an acute geometry, making them attractive as potential crystal nucleants.

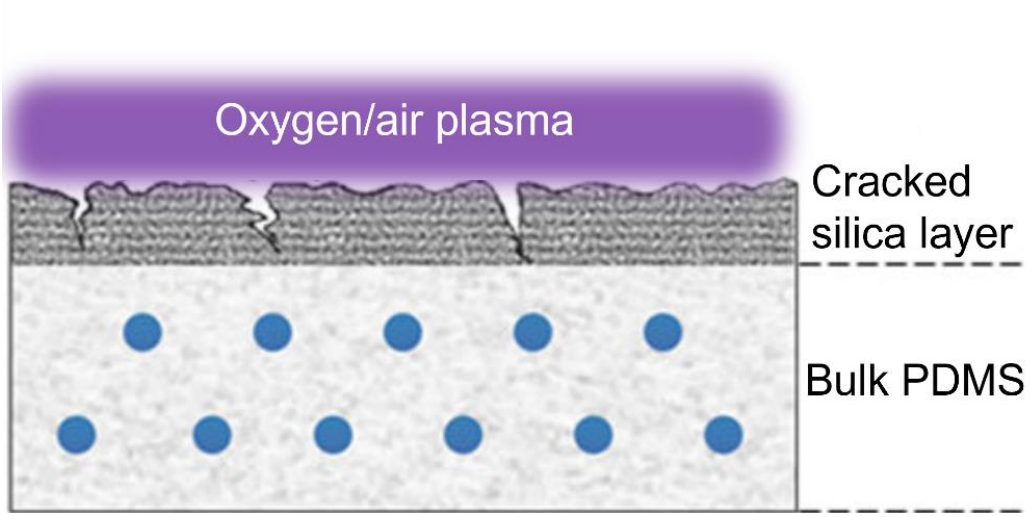


**Figure 41: Schematic showing the generation of a cracked silica-like layer on PDMS by oxygen plasma.**

#### 3.1.2.2 Structure and Surface Chemistry of Self-Assembled Monolayers

Self-assembled monolayers (SAMs) are constructed from a series of molecules which spontaneously organise into a highly ordered arrangement upon a surface. Typically, the enthalpic gain from bonding with the surface in a tightly-packed arrangement is enough to offset the concomitant loss of entropy, although some self-assembly processes are also entropically driven[193,194].

SAM-forming molecules typically contain a 'tail', and a 'head', which are connected by a carbon chain. The chemistry of the tail group can be tailored to facilitate covalent bonding with a specific substrate surface. Most commonly used tail groups are thiols, which are tailored towards noble metals (Figure 42A), and silanes, which are tailored towards a range of hydroxylated surfaces (Figure 42B). High-quality silane monolayers are typically more challenging to deposit than thiols, because the amount of water present needs to be tightly controlled[195]. Too little water restricts the bonding condensation reaction, producing an incomplete monolayer, whereas too much water causes silanes to polymerise, producing a highly disordered surface.

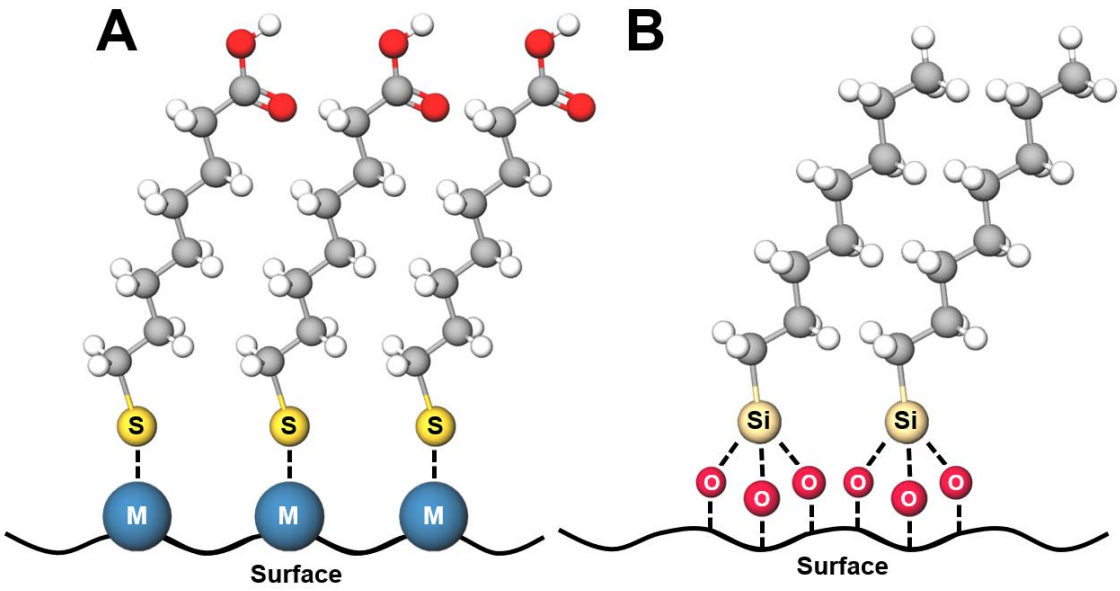


**Figure 42: Schematic showing the structure of (A) carboxylated alkanethiol and (B) alkylsilane self-assembled monolayers. M represents a noble metal atom.**

Alkyl chains of neighbouring SAM molecules interact with one another by dispersion forces, enhancing the ordering of the SAM group (often referred to as its crystallinity). SAMs with longer alkyl chains are generally more crystalline, but when alkyl chains are too lengthy they can hinder the kinetics of SAM formation[195]. A range of surface chemistries can be explored for the head group, limited only by general rules regarding chemical compatibilities. In cases where unwanted chemical reactions can occur between head and tail groups, such as the autopolymerisation of molecules with –COOH head groups and $–Si(OMe)_3$ tail groups, additional synthesis steps can help to circumvent the problem. In the case above, starting with a succinic acid head group instead of a carboxylic acid prevents autopolymerisation, and once monolayer assembly is complete, the succinic acid groups can be converted to two –COOH groups by immersion in water[196]. The design of these individual components is therefore highly flexible, and can facilitate exploration of a wide range of surface chemical modifications on a variety of surfaces.

### 3.1.2.3 Using SAMs to Control Inorganic Crystallisation on Flat Surfaces

SAMs form on crystalline substrates as a 2D crystal layer, the spacing and symmetry of which is determined by several variables. The angle expressed between the substrate and SAM chains is chiefly dependent on the underlying substrate. Similar angles of SAM chains have been reported for alkanethiols containing different head groups formed on Au(111) surfaces, whereas SAMs on Ag(111) surfaces have entirely different chain angles[197]. The position of SAM head groups is determined partly by the chain orientation with respect to the surface, but also by the carbon chain length and identity of the head groups.

These structural properties are capable of controlling crystallisation, such as the different orientations of calcite crystals formed on SAMs with -COOH, -$SO_3H$ and -OH terminal groups[197,198]. SAM chain length is also crucial, with even-numbered carbon chains showing greater chain alignment than odd-numbered chains, and providing a more favourable surface for calcite formation[23,199]. 16-mercaptohexadecanoic acid, a widely explored SAM-forming molecule contains a long even-numbered alkyl chain with a thiol tail group and a carboxylic acid head group. When assembled on noble metal surfaces, this produces highly-ordered, highly crystalline SAMs which effectively nucleate calcite[197].

It is generally accepted that epitaxial matching occurs between specific calcite crystal faces and the structurally ordered SAM head groups[197], but the flexibility of the SAM can further impact nucleation rates. As mentioned in Section 1.3.4, structural mismatch between two solid materials leads to a high interfacial energy. Thus, where there is slight structural mismatch between a growing crystal nucleus and SAM head groups, movement of the SAM chains can reduce interfacial energy, particularly in regions where defects are present[200].

### 3.1.2.4 Using SAMs Alongside Surface Topography Engineering to Control Inorganic Crystallisation

Use of SAMs can be a highly versatile method of achieving control of surface chemistry whilst retaining the nanoscale topography of a surface. In this way, SAMs can be used to directly compare crystallisation processes on substrates with a common topography but different surface chemistries[201].

The effect of a SAM on crystallisation can also be influenced by the surface topography of a substrate, which affects how the SAM is able to organise. Many key experiments using SAMs to control inorganic crystallisation employed smooth surfaces, as these offer remarkable control over crystal orientation. Aizenberg *et al.* showed that by depositing SAMs on metal supports with angular topographies (Figure 43A), the SAMs become disordered (Figure 43B), and calcite nucleation rates can be significantly increased here (Figure 43C & D) [202,203]. Ag was micropatterned onto Au substrates, forming a right-angular feature at the transition region between the two metals. It was suggested that structural mismatch between the Au and Ag regions along with the right-angle feature caused the alkanethiol SAMs to be disordered in this region. Nucleation of $CaCO_3$ was rapid on these substrates and occurred on the regions of disordered SAM.

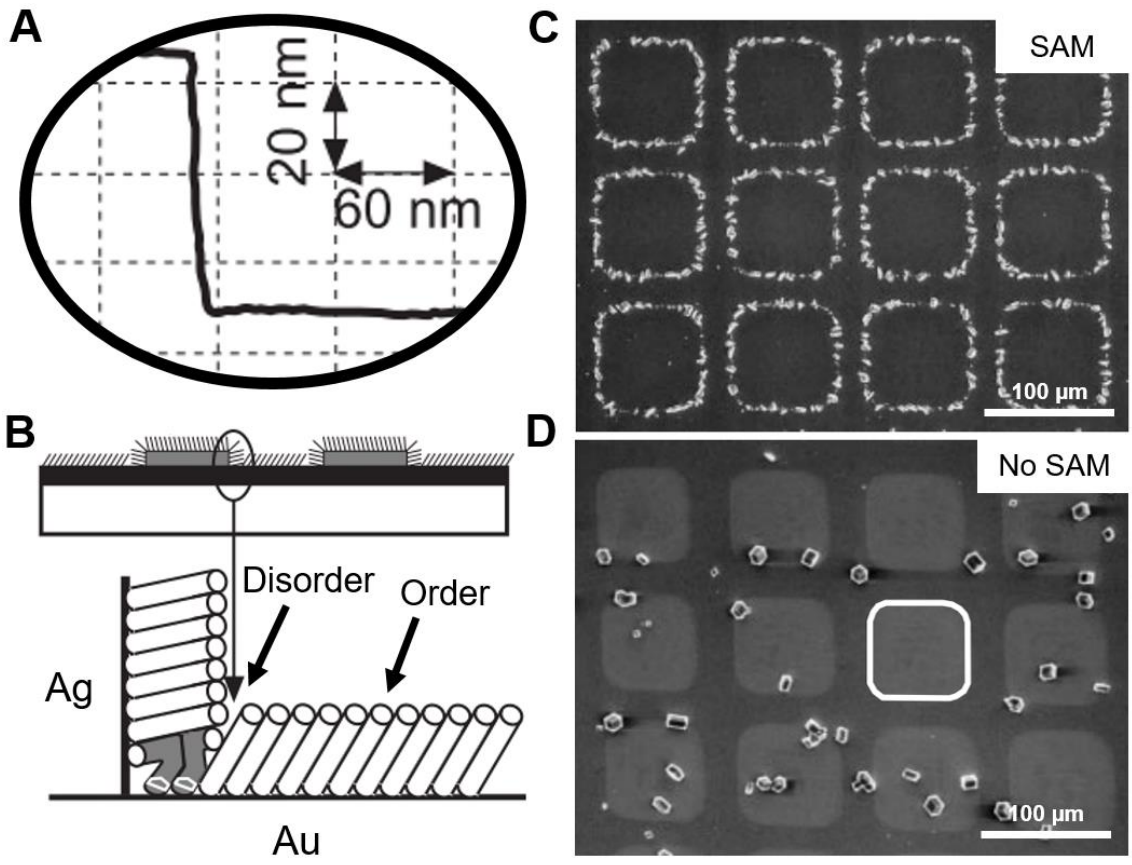


**Figure 43: Work by Aizenberg *et al.* showing (A) the near-vertical topography of as-produced Ag on Au films measured by AFM. (B) Schematic showing disordered regions in SAMs patterned on these substrates. (C) and (D) show the results of crystallisation of $CaCO_3$ on these substrates with and without a 16-mercaptohexadecanoic acid (16MHDA) self-assembled monolayer (SAM). *Reproduced with permission from Springer Nature* [202].**

Recently, molecular dynamics simulations by Marinova *et al*. have revealed new mechanistic insights into calcium carbonate crystallisation on 16MHDA SAMs. It was shown that mobility of individual molecules within the SAM can be enhanced at topographical defects on a Au(111) surface such as steps, groups of steps or vacancies[204]. These defects behaved as anchoring sites for clusters of $Ca^{2+}$ and $CO_3^{2-}$ ions. Not only were concentrations of ions significantly higher at defects than on a defect-free terrace, but the diffusion of both water and ions was also significantly hindered (Figure 44). In practice, this may allow a growing cluster to spend more time at the surface and approach criticality, which could be kinetic

component for why high nucleation rates are observed for calcite on 16MHDA-functionalised gold surfaces. Studies involving defects such as these are of great relevance to real-world systems, since the highest-quality achievable gold surfaces are typically rife with nanoscale surface defects.

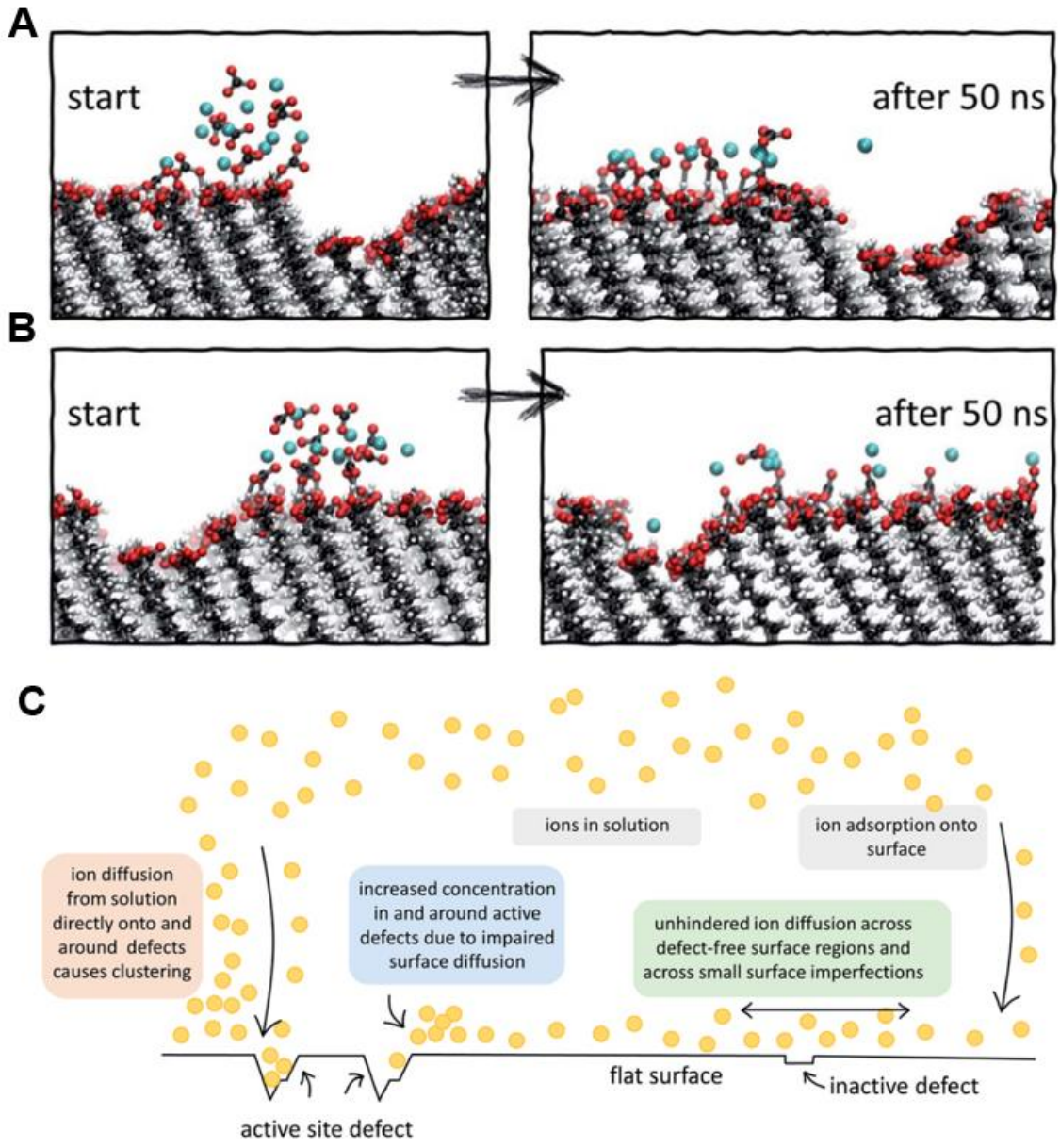


**Figure 44: Simulations performed by Marinova *et al*. of aqueous $Ca^{2+}$ and $CO_3^{2-}$ ions diffusing across (A) hindered and (B) unhindered regions of a 16MHDA SAM on a defect site of a Au(111) surface[204]. (C) A schematic detailing the diffusion and accumulation of ions across the surface. *Reproduced with permission from the Faraday Division, Royal Society of Chemistry.***

## 3.2 Methods

### 3.2.1 Fabrication of 16MHDA Functionalised Cracked Iridium Substrates (FC-Ir-PDMS)

#### 3.2.1.1 Polydimethylsiloxane (PDMS) Mixing and Curing

Sylgard™ 184 silicone elastomer base (18 g) was added to a plastic cup, and the associated crosslinker (1.8 g) was added to produce a mixture with a 10:1 ratio of elastomer to crosslinker. The contents were thoroughly stirred and degassed until no bubbles remained using a vacuum desiccator. The mixture was poured into a square 100 x 100 mm polystyrene petri dish. A second degassing step was performed, and the mixture was cured in a levelled oven at 60$^{o}$C for at least 2 hours. Once removed and cooled to room temperature, the cured PDMS was cut into squares with dimensions of 10 mm (W) x 10 mm (L) x 3 mm (H). These were placed onto Scotch® Magic™ tape until required, where the tape-protected surface would become the active surface for further use once the tape was removed.

#### 3.2.1.2 Plasma Treatment – Preparation for Metal Coating

PDMS squares were removed from the sealing tape and placed on a clean borosilicate microscopy glass slide with their clean faces pointing up. The glass slide was placed in a Diener Atto plasma cleaner set to 200 W, the chamber pressure allowed to reach ≈1 mbar and the air inflow rate to 0.5 Nl/h. The samples were exposed to plasma for 30 seconds, after which the chamber was ventilated, and the samples removed. After this amount of plasma exposure, no cracks were produced but the hydrophilicity of the surface was increased. Samples were used within 15 minutes of plasma treatment to avoid hydrophobic recovery of the PDMS[183].

#### 3.2.1.3 Plasma Treatment to Produce PDMS Cracks

PDMS squares were removed from the sealing tape and placed on a clean borosilicate microscopy glass slide. The glass slide was placed in a Diener Atto plasma cleaner set to 200 W, the chamber pressure was allowed to reach

≈0.1 mbar and the air inflow rate was set to 0.1 Nl/h. The samples were exposed to plasma for 7 minutes, after which the chamber was ventilated, and the samples removed.

#### 3.2.1.4 Plasma Treatment to Increase PDMS Hydrophilicity – Preparation for Metal Coating

PDMS squares were removed from the sealing tape and placed on a clean borosilicate microscopy glass slide with their clean faces pointing up. The glass slide was placed in a Diener Atto plasma cleaner set to 200 W, the chamber pressure allowed to reach ≈1 mbar and the air inflow rate 0.5 Nl/h. The samples were exposed to plasma for 30 seconds, after which the chamber was ventilated, and the samples removed. After this amount of plasma exposure, no cracks were produced but the hydrophilicity of the surface was increased. Samples were used within 15 minutes of plasma treatment to avoid hydrophobic recovery of the PDMS[183].

#### 3.2.1.5 Iridium Coating to Produce Ir-PDMS

Super Glue was used to stick a layer of greaseproof weighing paper at the bottom of a large circular polystyrene petri dish to prevent the PDMS from sticking to the dish. Hydrophilic plasma-treated PDMS substrates prepared as detailed in Section 3.2.1.2 were placed upon the greaseproof paper, and the uncovered petri dish was placed in the chamber of a Cressington 208HR sputter coater equipped with an iridium target and built-in quartz crystal thickness monitor. Iridium was deposited in argon at a pressure of approximately $8 \times 10^{-2}$ mbar, until the thickness monitor read 5 nm, after which the chamber was repressurised and the samples removed. Ir-PDMS substrates were used within 1 day of coating. Picking the samples up and gently squeezing with tweezers would produce numerous cracks. If patterned cracks were desired, samples needed to be gently lifted from below without disturbing the surface so that they could be further processed without adventitious crack formation.

#### 3.2.1.6 Functionalisation and Washing to Produce FC-Ir-PDMS

Cracked Ir-PDMS substrates were immersed in an ethanolic solution of 16MHDA (5 mM, 20 mL) containing one drop of acetic acid for 10 minutes. The substrates were then gently rinsed with ethanol, then were placed in fresh ethanol for a further 10 minutes, after which they were gently rinsed with more ethanol, then with water, producing the cracked and -COOH functionalised FC-Ir-PDMS substrates. These were kept in water for up to 1 hour until required.

### 3.2.2 Crystallisation on Substrates

All crystallisation experiments were carried out by immersing substrates in a solution in an upright position in a 5 mL square multiwell plate, to ensure that crystals forming in solution did not fall down onto substrate surfaces (Figure 45).

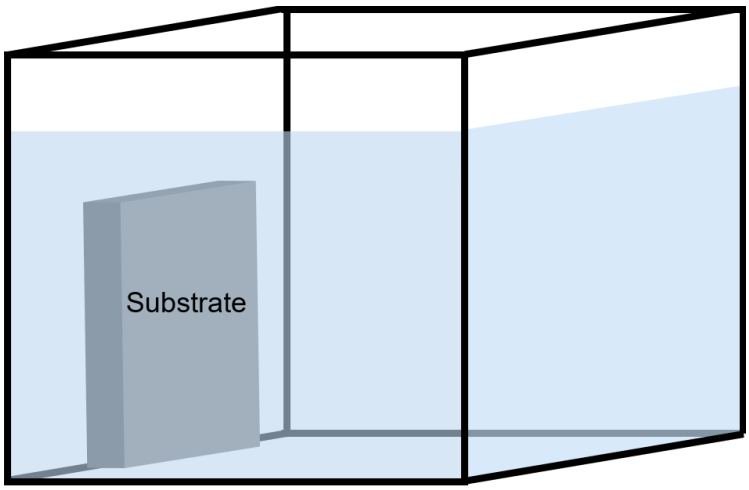


**Figure 45: Schematic showing how substrates were immersed upright in 5 mL square wells during crystallisation.**

#### 3.2.2.1 Precipitation by Direct Mixing of Solutions

Direct mixing was used to crystallise $CaCO_3$, $BaCO_3$, calcium oxalate, and ZIF-8. As a general rule, substrates were immersed in a primary solution in a polystyrene 5 mL square multiwell plate, then a second solution was added without mixing, and substrates were left for a defined period of time to crystallise.

After crystals were formed, substrates were washed gently with water, then ethanol, and then were air dried.

The identities and concentrations of the primary and secondary solutions are shown in Table 3. All aqueous solutions were passed through a Millex® cellulose ester syringe filter (pore size 0.22 µm).

| Compound | Solution 1 | Solution 2 | Incubation time |
|---|---|---|---|
| **$CaCO_3$** | $CaCl_2$ (5 mL, 2 mM) | $Na_2CO_3$ (100 µL, 100 mM) | 20 minutes |
| **$BaCO_3$** | $BaCl_2$ (5 mL, 2.5 mM) | $Na_2CO_3$ (62.5 µL, 100 mM) | 5 minutes |
| **Calcium oxalate** | $CaCl_2$ (5 mL, 2 mM) | $(NH_4)_2C_2O_4$ (40 µL, 100 mM) | 30 minutes |
| **ZIF** | $Zn(NO_3)_2$ (2.5 mL, 1 mM) | 2-methylimidazole (2.5 mL, 60 mM) | 72 hours |

**Table 3: Solution compositions and incubation times used for direct mixing experiments to produce the crystals listed.**

### 3.2.2.2 Precipitation by Acidification

Ibuprofen and benzoic acid were precipitated by acidification using the concentrations and crystallisation times specified in Table 4. Substrates were washed in water and air dried following crystallisation.

| Compound | Solution 1 | Solution 2 | Incubation time |
|---|---|---|---|
| **Ibuprofen** | Ibuprofen (sodium salt) (3 mL, 0.8 mM) | HCl (1 mL, 2 mM) | 1 week |
| **Benzoic acid** | Sodium benzoate (4 mL, 30 mM) | HCl (1 mL, 5 mM) | 1 week |

**Table 4: Solution compositions and incubation times used for acidification experiments to produce the crystals listed.**

#### 3.2.2.3 Precipitation by Antisolvent

Glycine was precipitated by mixing an aqueous glycine solution with ethanol, which acted as an antisolvent. Glycine was dissolved in water to a concentration of 250 mM, and 2 mL of this solution was added to a 5 mL square multiwall plate. Ethanol (3mL) was quickly added, crystallisation was allowed to proceed for 20 seconds, and substrates were washed with ethanol and air dried.

#### 3.2.2.4 Crystallisation of Guanine

A Gomori buffer (50 mM, pH 7.2) was prepared by dissolution of $KH_2PO_4$ (130 mg) and $K_2HPO_4$ (270 mg) in water (40 mL). Guanosine (25 mg) was fully dissolved in this solution and water was added to make a total volume of 50 mL. It was the filtered through a syringe filter. Purine nucleotide phosphorylase (1U) was added, and the solution was left to crystallise for 3 days. Substrates were washed in water and air dried following crystallisation.

### 3.2.3 Raman Spectroscopy

Raman spectra were collected using a Horiba LabRAM HR Evolution Raman microscope running LabSpec 6 software using a 50 W 532 nm (green) laser passing through an edge filter. A hole size of 50 and laser powers of 1-10% were used. Spectra were exported from the software and replotted using Origin.

#### 3.2.3.1 Raman Spectroscopic Mapping

Point-by-point Raman spectroscopic mapping on $CaCO_3$ crystals embedded in FC-Ir-PDMS cracks were collected from air dried samples using a Horiba LabRAM HR Evolution Raman microscope using a 50 W 532 nm (green) laser passing through an edge filter. A hole size of 50 and laser powers of 1-10% were used. The spectrometer was positioned at 1085 $cm^{-1}$, acquisition time was set to 1s and 3 spectra were accumulated per image. The spacing between scan points was 2 µm.

### 3.2.4 *In-situ* Video Recording of Crystallisation

Figure 46 shows a diagram of the setup used for *in-situ* video recordings. PDMS was mixed and cured as detailed by section 3.2.1, then cut into a rectangle with dimensions of 20 mm (W) x 40 mm (L) x 2 mm (H) and another 2 of sizes 5 mm (W) x 20 mm (L) x 5 mm (H). A large thin piece was placed on a borosilicate glass slide, and two of the thicker pieces, placed parallel to the length of the glass slide and 8 mm apart. These pieces acted as supports for a sample, which was placed upside-down on top to prevent crystals from falling onto the surface. The whole glass slide was placed on the stage of a Zeiss Axio Observer 7 inverted light microscope set to reflection mode. $CaCl_2$ (2 mM, 150 µL) was injected as a droplet in the channel underneath the sample, and when the video recording was started, $Na_2CO_3$ (100 mM, 20 µL) was injected at the edge of the $CaCl_2$ droplet.

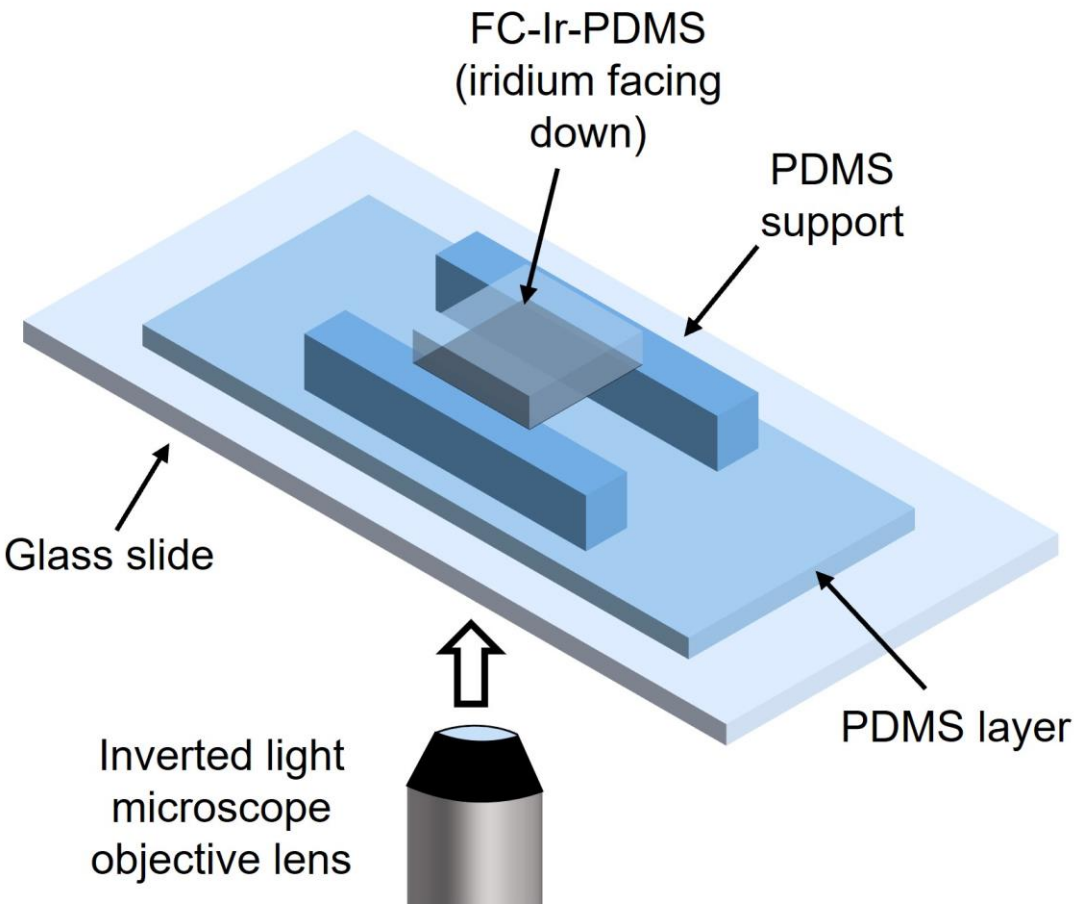


**Figure 46: Diagram showing the setup required for *in-situ* video recordings of crystallisation on FC-Ir-PDMS.**

#### 3.2.4.1 Measuring Nucleation Rates and Particle Growth From *In-Situ* Video Recordings

Video recordings of experiments were imported to ImageJ as 8-bit image stacks. The image stack was converted to a binary format, ensuring that thresholding was set to an appropriate value to identify particles (dark) but exclude background pixels (lighter). The 'analyze particles' feature was then used to measure the area of each particle in each frame, and this data was exported to Microsoft Excel. This was used to calculate the number of particles and average particle area per frame (each frame corresponded to 1 second), both of which were plotted using Origin. From plotted curves, the gradients were measured at their steepest points, which represented the steady state nucleation rates.

#### 3.2.4.2 Determining Induction Times From *In-Situ* Video Recordings

Video recordings of experiments were imported to ImageJ as 8-bit image stacks. The time when the first particle appeared was recorded (each frame corresponded to 1 second) and tabulated.

### 3.2.5 Resin Exfoliation

Demotec® 70 conductive carbon resin was prepared by thoroughly mixing a 1:1 weight ratio of the powder and liquid components. Once the viscosity began to increase, the mixture was poured into a 20 mm diameter cylindrical silicone mould to a depth of 5 mm. A FC-Ir-PDMS substrate with crystals grown on top was gently floated face-down on the liquid resin mixture, then the system was covered with a petri dish and left for 24 hours to completely cure. Once cured, the FC-Ir-PDMS substrate was gently peeled away, and the excess resin was trimmed away from the imprinted resin surface using a razor blade. Finally, an air jet was used to clean the surface ready for analysis by scanning electron microscopy (SEM).

### 3.2.6 Atomic Force Microscopy (AFM)

AFM was performed by Dr Mark Holden using a Multimode 8 atomic force microscope (Bruker). Images were acquired using TESPA-V2 probes (Bruker) in Tapping Mode at a frequency of 297 kHz and resolution of 4096 pixels. NanoScope Analysis v3.0 (Bruker) was used to process the images, image flattening with only a simple 1st order line level.

### 3.2.7 Focused Ion Beam Scanning Electron Microscopy (FIB-SEM)

An Helios G4 CX DualBeam FIB-SEM (FEI) was used for both imaging and fabrication of lamellae for TEM, and Mr. Stuart Micklethwaite offered guidance and practical assistance. Substrates were mounted on an SEM stub with conductive carbon resin and plunge-frozen in liquid nitrogen, then placed in the SEM chamber. Once a stable vacuum of below 5 x $10^{-5}$ mbar was achieved, images were taken of the crystals using the electron beam, and when a suitable crystal was found, a gas injection system (GIS) needle was used to deposit platinum atop calcite crystals to protect their top surfaces from 'curtaining' and beam damaging during ion-beam milling[205].

To prepare a lamella for transmission electron microscopy (TEM), the sample stage was orientated to view a crystal down the length of a crack. From this orientation, the front and back of the crystal were milled away using a gallium ion beam, and an undercut was also made. One edge was also milled away, and the crystal was held by cryo-tweezers (Kleindiek Nanotechnik). The final edge was milled away and the crystal removed from the surface and mounted to a copper TEM slot grid. The crystal was thinned by FIB milling to the desired thickness, and held in a vacuum desiccator until TEM imaging.

### 3.2.8 Transmission Electron Microscopy (TEM) Imaging

TEM imaging was performed with guidance and practical assistance from Dr. Zabeada Aslam using a Titan3 Themis 300 (FEI) operating at 300 keV. Energy dispersive x-ray (EDX) spectra and elemental maps were collected using a Super-X EDX system (FEI). The electron dose was calculated to be ~500 $e^{-}$ $Å^{-2}$ per image. Selected area electron diffraction (SAED) imaging used an electron

dose of ~2000 $e^{-}$ $Å^{-2}$ per image. SAED patterns were indexed to calcite using CrystalMaker Single Crystal and reference [206]. High-resolution TEM images were processed using ImageJ and Gatan GMS 3, and powder rings were indexed to CaO using reference [207].

## 3.3 Results

### 3.3.1 Initial Experiments for Development of a Robust Methodology for Crystallisation on Cracked Substrates

A general investigation was conducted into each stage of fabricating functionalised iridium-coated cracked PDMS substrates, and crystallisation upon them. Emphasis was placed on optimising the procedure to establish a robust methodology which reduced variability between experiments.

#### 3.3.1.1 Producing and Characterising PDMS Cracks

The production of cracks on air plasma treated PDMS was investigated first. The most reliable indicator for an air plasma that would produce cracks was found to be visual. A high air inflow rate produced a magenta plasma (Figure 47), and this took around 30 minutes to crack PDMS. On the other hand, a low air inflow rate produced a lilac plasma, which took only 3 minutes to crack PDMS. Lower pressure plasmas are more energetic than high pressure plasmas at the same power, so are more reactive towards the PDMS surface.

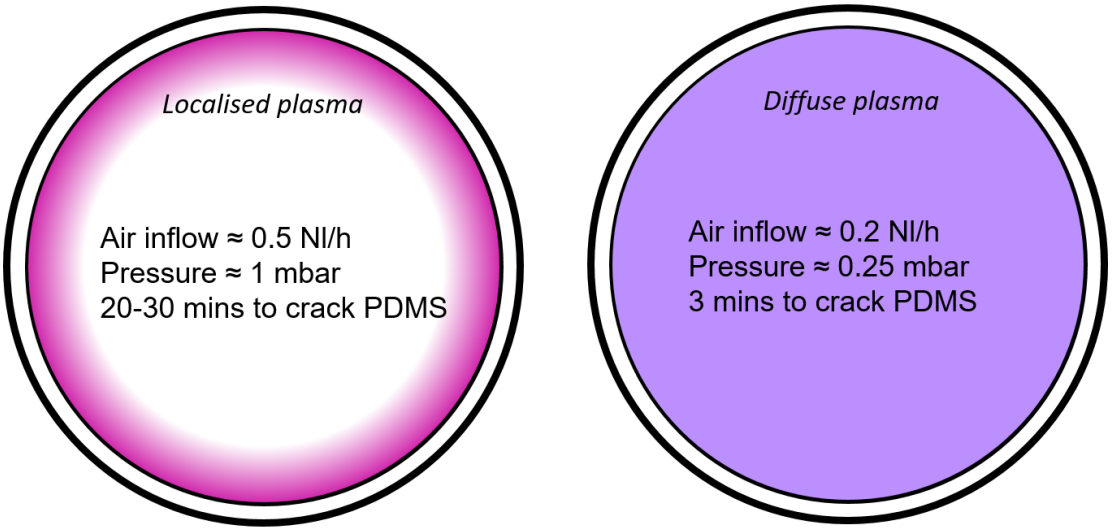


**Figure 47: Diagram showing how plasma quality was visually assessed to reproducibly form surface cracks in PDMS**

Varying the plasma exposure time could be used to control the degree of cracking (Figure 48). Cracks began to form between 1 and 3 minutes of exposure, and

became wider and more numerous with increasing exposure time. From the times tested, 7 minutes was deemed sufficient to produce a moderate number of cracks.

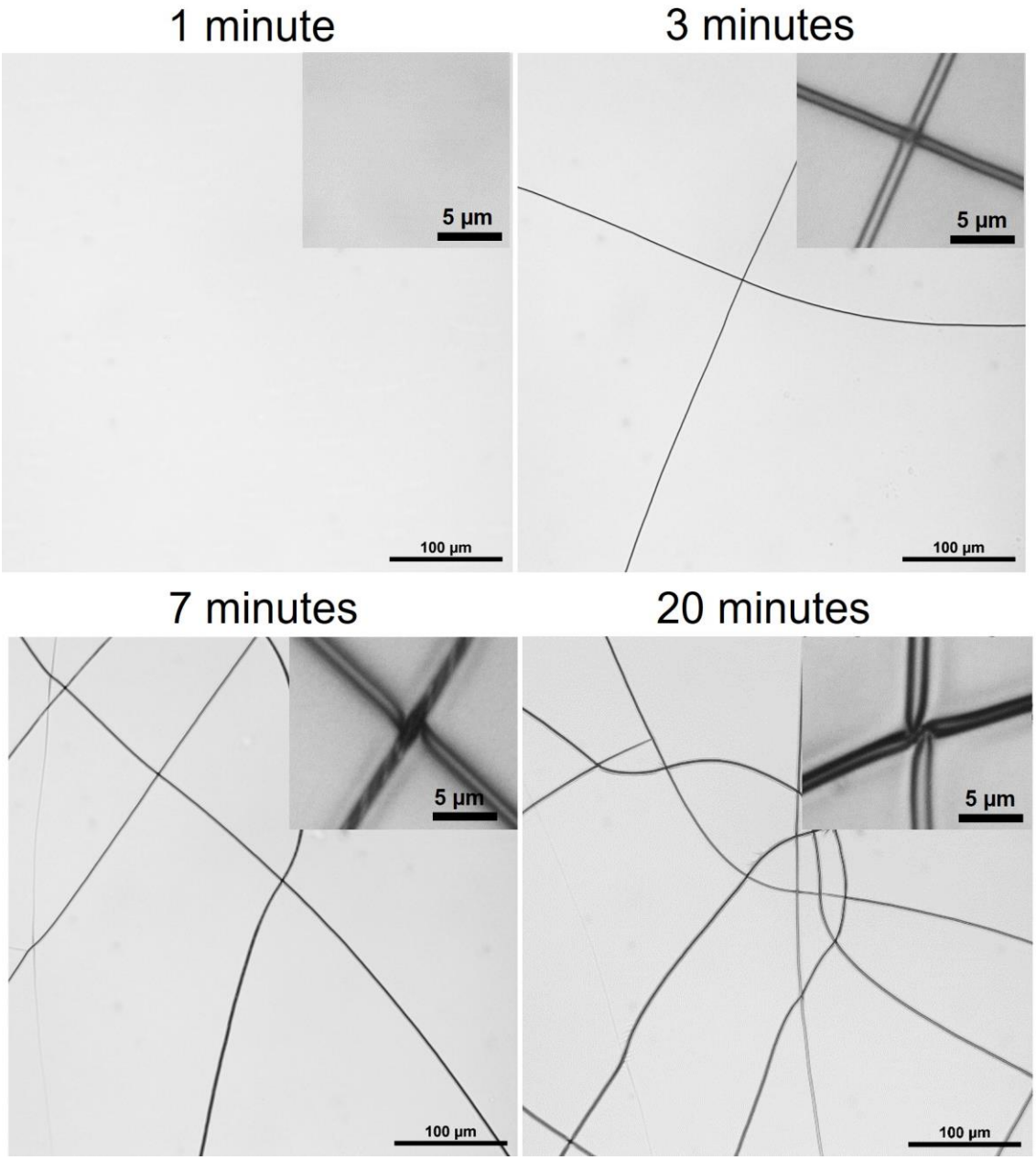


**Figure 48: Varying degrees of cracks formed in PDMS as a result of varying the exposure time to air plasma.**

Atomic force microscopy (AFM) was used to study the topography of these surfaces. The PDMS surface was highly smooth away from the cracks (Figure 49A). The cracks themselves were ≈1.5 µm wide (Figure 49B) and ≈100 nm deep, which is assumed to correspond to the depth of the brittle glassy layer. This

compares well with literature, which reports depths of 91 nm following similar plasma dosages[183]. Additionally, it was found that the edges of the crack were raised, suggesting that they had buckled slightly.

Pressing the surface with the AFM tip also produced a set of web-shaped cracks, which were rougher in profile and varied in width and depth (Figure 49C). Interestingly, these cracks did not exhibit the raised edges of the natural cracks.

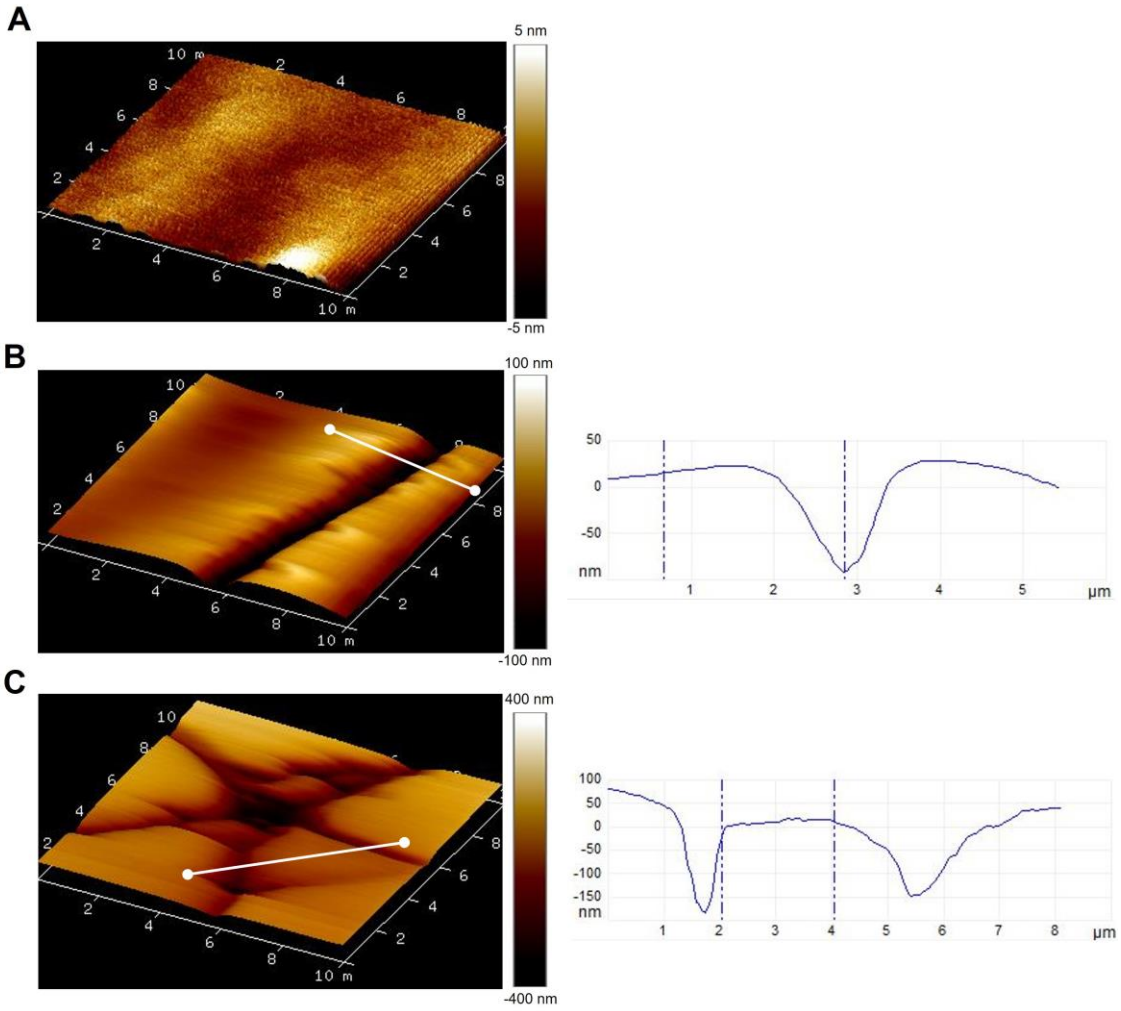


**Figure 49: Atomic force microscopy (AFM) maps and line profiles for PDMS exposed to 7 minutes of air plasma. The surface away from a crack is shown in (A), a natural crack is shown in (B) and a crack produced by pressing the surface with the AFM tip is shown in (C).**

### 3.3.1.2 The Role of PDMS Cracks and Iridium Cracks

Air plasma cracked PDMS samples were sputter coated with a 5 nm layer of iridium. This enabled 16MDHA to form a SAM on the surface following immersion

in an ethanolic solution of 16MHDA with a very small amount of acetic acid (to ensure the full protonation of 16MHDA[208]). After washing with ethanol and water and drying, $CaCO_3$ was crystallised by direct mixing of $CaCl_2$ (2 mM, 5 mL) with $Na_2CO_3$ (100 mM, 100 µL). As previously reported, $CaCO_3$ crystallised abundantly and selectively within the cracks (Figure 50A & B). The rhombohedral crystals were confirmed to be calcite using Raman spectroscopy of individual crystals and mapping of larger areas (Figure 50C & D).

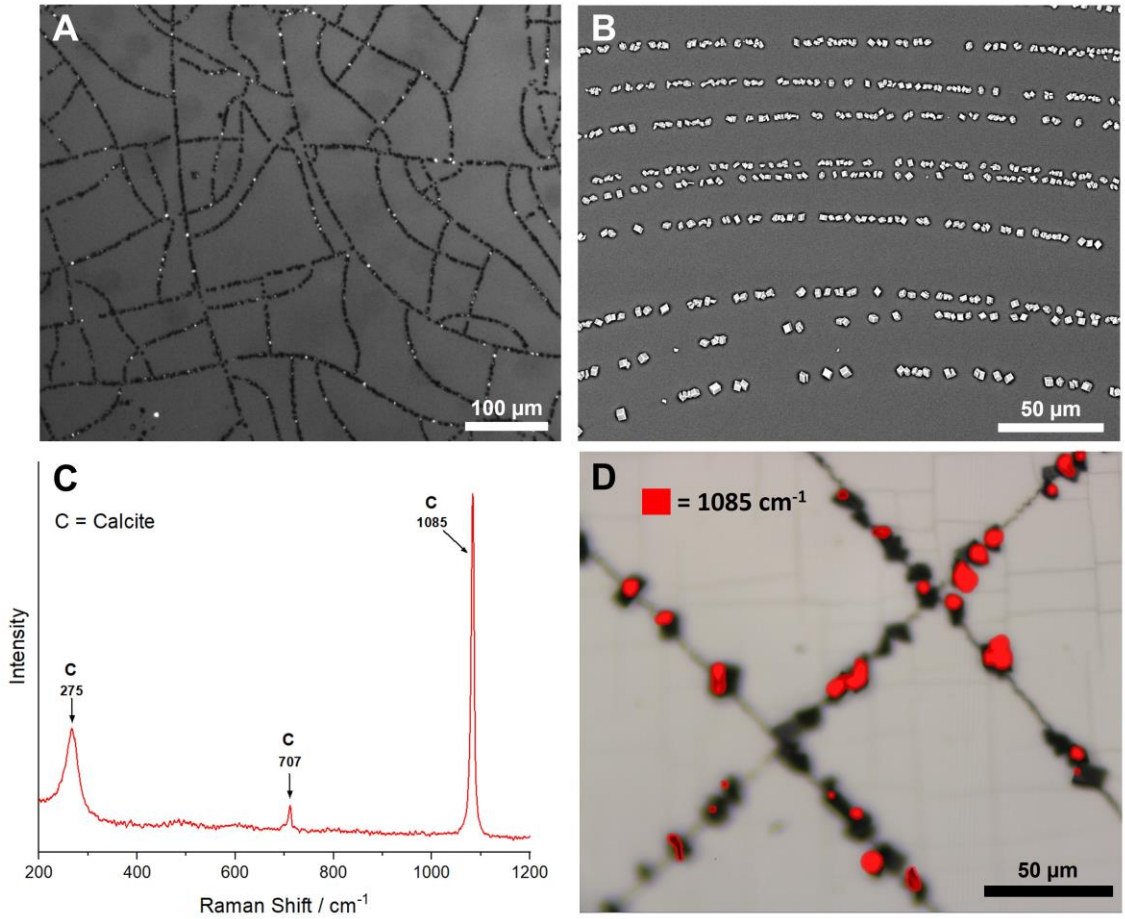


**Figure 50: (A) Optical microscopy (OM) and (B) scanning electron microscopy (SEM) images of $CaCO_3$ grown on cracked PDMS substrates. (C) Raman spectroscopy point spectrum and (D) Raman spectroscopic mapping of the rhombohedral crystals in cracks.**

Further inspection of SEM images showed that many of the crystal-filled PDMS cracks contained micro-cracks in the iridium (Figure 51).

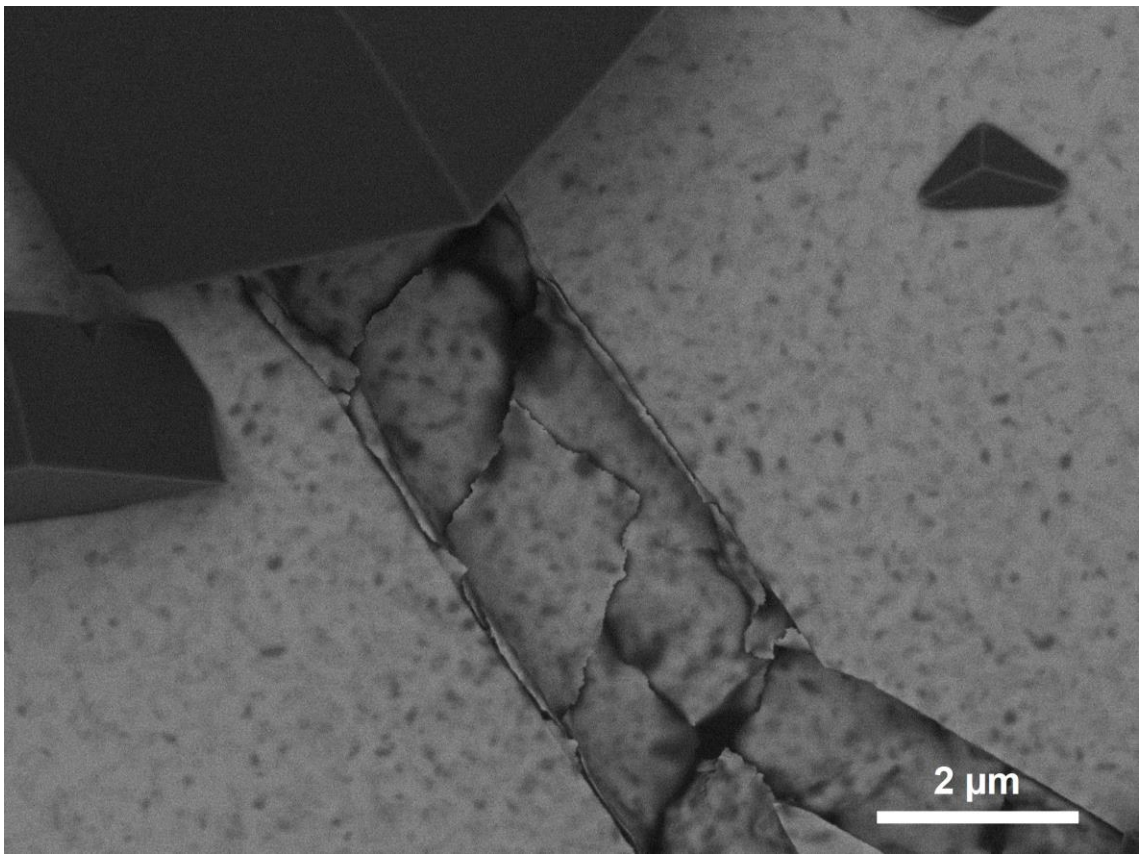


**Figure 51: SEM image showing the iridium micro-cracks within a larger PDMS crack**

Focused ion-beam scanning electron microscopy (FIB-SEM) was performed under cryogenic (liquid $N_2$) conditions to further characterise these micro-cracks. Under standard non-cryogenic conditions, the underlying PDMS tended to melt instead of cleanly milling under the FIB. However, liquid $N_2$ rapidly cooled the substrate to below its glass transition temperature of 150 $^{o}$C, vastly improving the results of the FIB milling process. Two types of cracks were present, namely smooth-looking PDMS cracks which had been evenly coated in iridium (Figure 52A & B), and PDMS cracks in which the iridium surface layer had also split, producing a jagged edge (Figure 52C). Precipitation of $CaCO_3$ was only observed at the jagged edged cracks (Figure 52D). FIB cross-sections of calcite crystals formed in cracks showed that the iridium layer underneath the crystals was itself very cracked (Figure 52E & F). This indicated that the iridium cracks were essential for enhancing $CaCO_3$ crystallisation, and suggested that the PDMS cracks alone were not active.

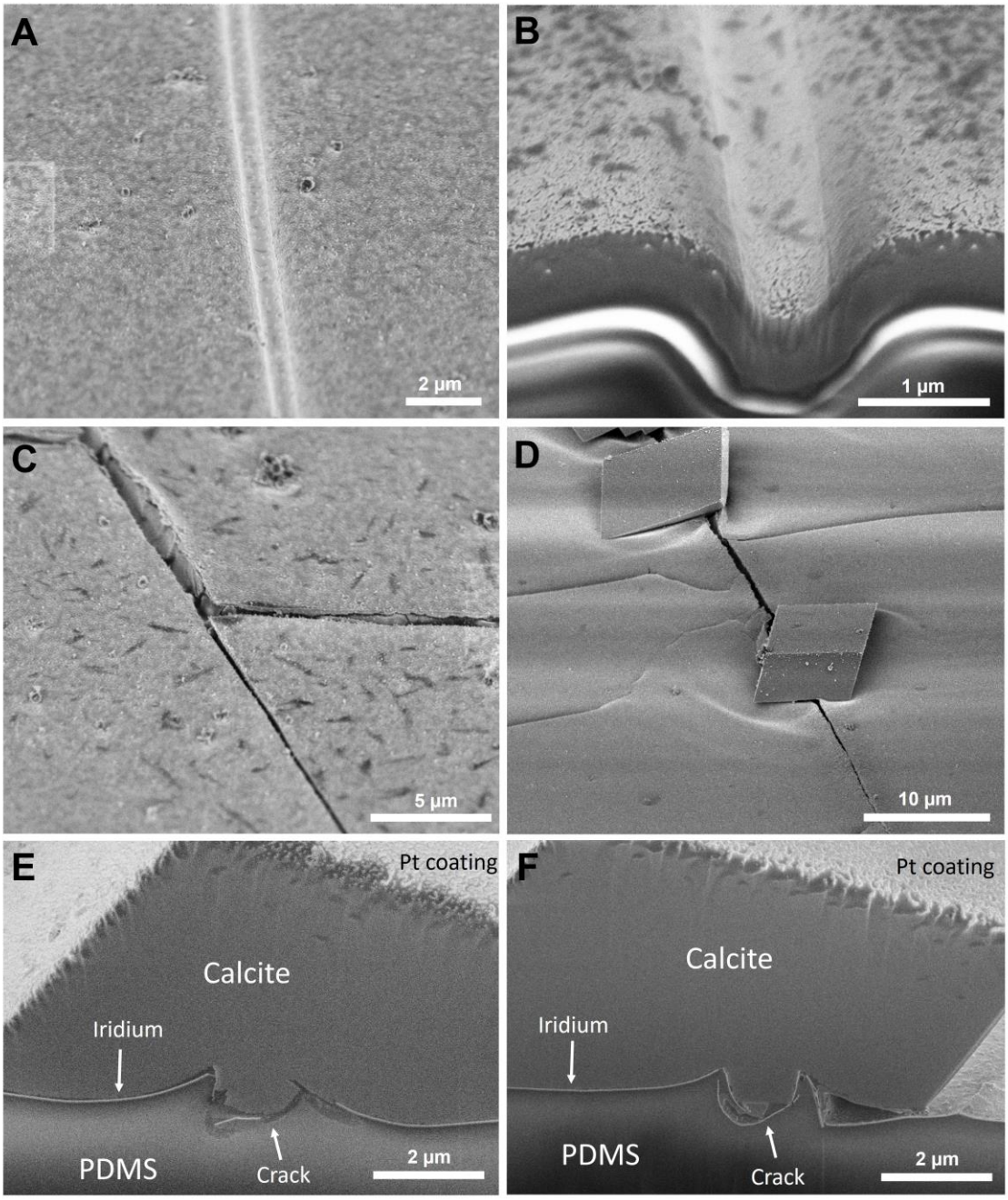


**Figure 52: (A) SEM and (B) focused-ion beam SEM (FIB-SEM) of a smooth iridium-coated PDMS crack. (C) and (D) show two examples of a jagged PDMS crack (C) before and (D) after $CaCO_3$ was crystallised on the substrates. (E) and (F) show FIB cross-sections of calcite crystals embedded in PDMS cracks.**

To investigate whether the PDMS cracks contributed to the enhanced nucleation, PDMS substrates were exposed to a much lower dose of air plasma prior to iridium coating, such that the PDMS was hydrophilic enough to accommodate a stable iridium coating but was not covered with cracks. 30s exposure to a higher pressure, magenta-coloured air plasma (see Figure 47) was found to be optimal, and iridium coating was performed immediately afterwards to avoid hydrophobic recovery of the PDMS surface[183]. Surfaces produced by this method were uniform and flat under SEM imaging, but were extremely fragile, and formed an expansive array of surface cracks after being gently picked up with tweezers (Figure 53A & B). These surfaces were then functionalised with 16MHDA and used in crystallisation assays. The $CaCO_3$ crystals again showed strong fidelity for the cracks (Figure 53C & D), confirming that the iridium cracks were responsible for enhancement of nucleation. On some substrates, nearly all crystals were observed to have crystallised in the {012} orientation[209], indicating an oriented growth mechanism had taken place (Figure 53E & F).

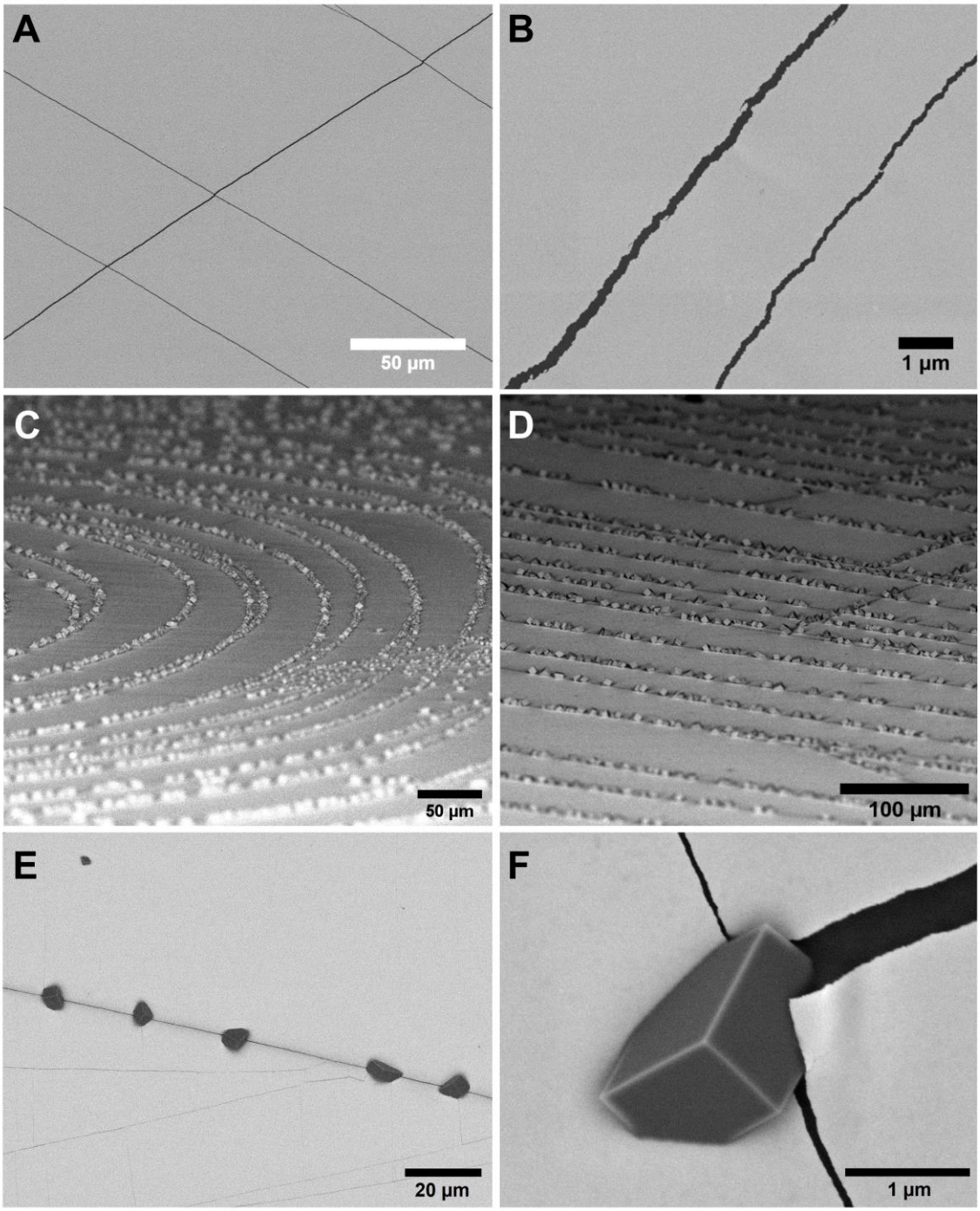


**Figure 53: (A & B) Iridium cracks formed by handling iridium-coated PDMS with tweezers. (C & D) SEM images of calcite showing a strong preference for formation at the iridium cracks. (E & F) Crystal growth selectively from the {012} orientation[209] on some samples.**

#### 3.3.1.3 Iridium Cracking and Functionalisation

Functionalisation of the cracked substrates was initially achieved by overnight immersion of iridium-coated substrates in a 1 mM ethanolic solution of 16MHDA. This procedure reproducibly produced the desired results of crystallisation localised in cracks. However, it was often observed that a series of large concentric ring-shaped cracks would form around the edge of the substrates after this step (Figure 54A-C). The concentricity of the cracks suggested that they had formed by stress applied radially to the iridium layer and from the outside-in, which strongly implied that the PDMS support had swelled in the ethanolic solution. Additionally, when the samples were moved between ethanol and water washing steps, rapid de-swelling of the PDMS produced additional cracks (Figure 54D). Whilst this did not affect the efficacy of the surface as a whole and in fact the concentric cracks were themselves effective at nucleating $CaCO_3$ (Figure 54E), uncontrolled crack formation presents several issues which are discussed in the next chapter (Section 4.3.2).

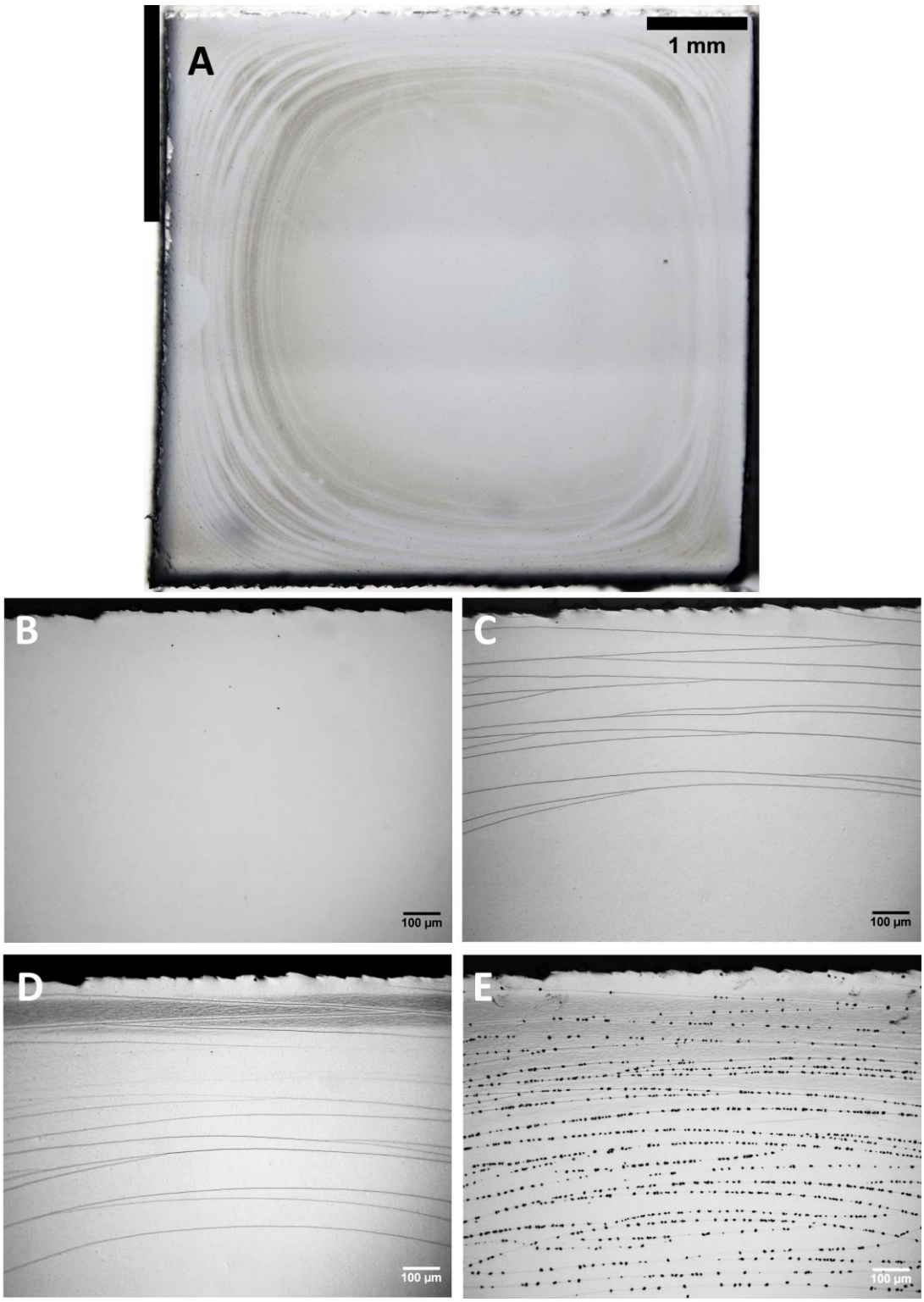


**Figure 54: (A) The concentric rings of iridium cracks resulting from overnight immersion in ethanolic 16MHDA followed by ethanol and water washing. (B-E) Imaging the same position on iridium coated PDMS (B) after iridium coating, (C) after overnight 16MHDA immersion, (D) after ethanol and water washing and (E) after crystallisation of $CaCO_3$ by direct mixing of $CaCl_2$ (2 mM, 5 mL) and $Na_2CO_3$ (100 mM, 100 µL).**

The procedure was therefore modified to avoid unintentional crack formation from swelling and de-swelling. Ir-PDMS substrates were immersed in both 1 mM and 5 mM solutions of 16MHDA for varying lengths of time and the results of crystallisation of $CaCO_3$ are shown in Figure 55 and Figure 56. In these experiments, cracks were observed in the samples immersed for 1 hour and 24 hours but not for 1 minute or 10 minutes. Therefore, although some of the longer immersion times produced impressive results, the uncontrolled crack formation resulting from swelling in ethanol meant that only the 1 and 10 minute immersion times were pursued further.

Samples immersed for 1 or 10 minutes needed to be picked up with tweezers prior to functionalisation to form cracks and test their nucleation efficacy, since without this step there was very little nucleation anywhere at the surface. Of the cracked samples immersed for 1 or 10 minutes, immersion in 5mM 16MHDA for 10 minutes led to the most effective cracks at forming crystals, so this condition was carried forward for future experiments.

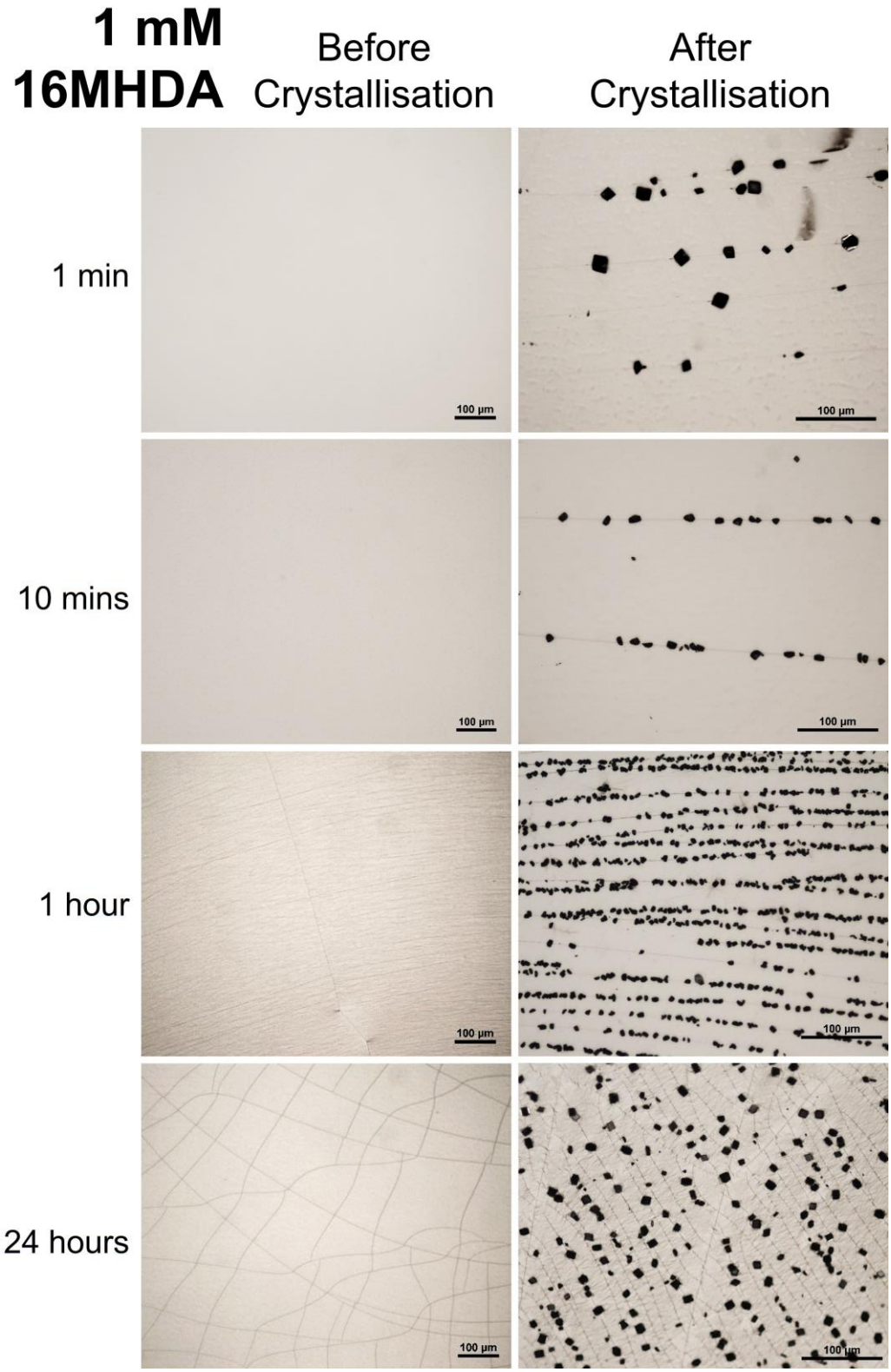


**Figure 55: Cracking patterns formed by immersing Ir-PDMS in 1mM 16MHDA for time lengths ranging from 1 minute up to 24 hours, and the subsequent results of $CaCO_3$ crystallisation upon them. NOTE: For samples where cracks did not form from swelling, substrates were lightly squeezed to produce cracks before $CaCO_3$ was crystallised.**

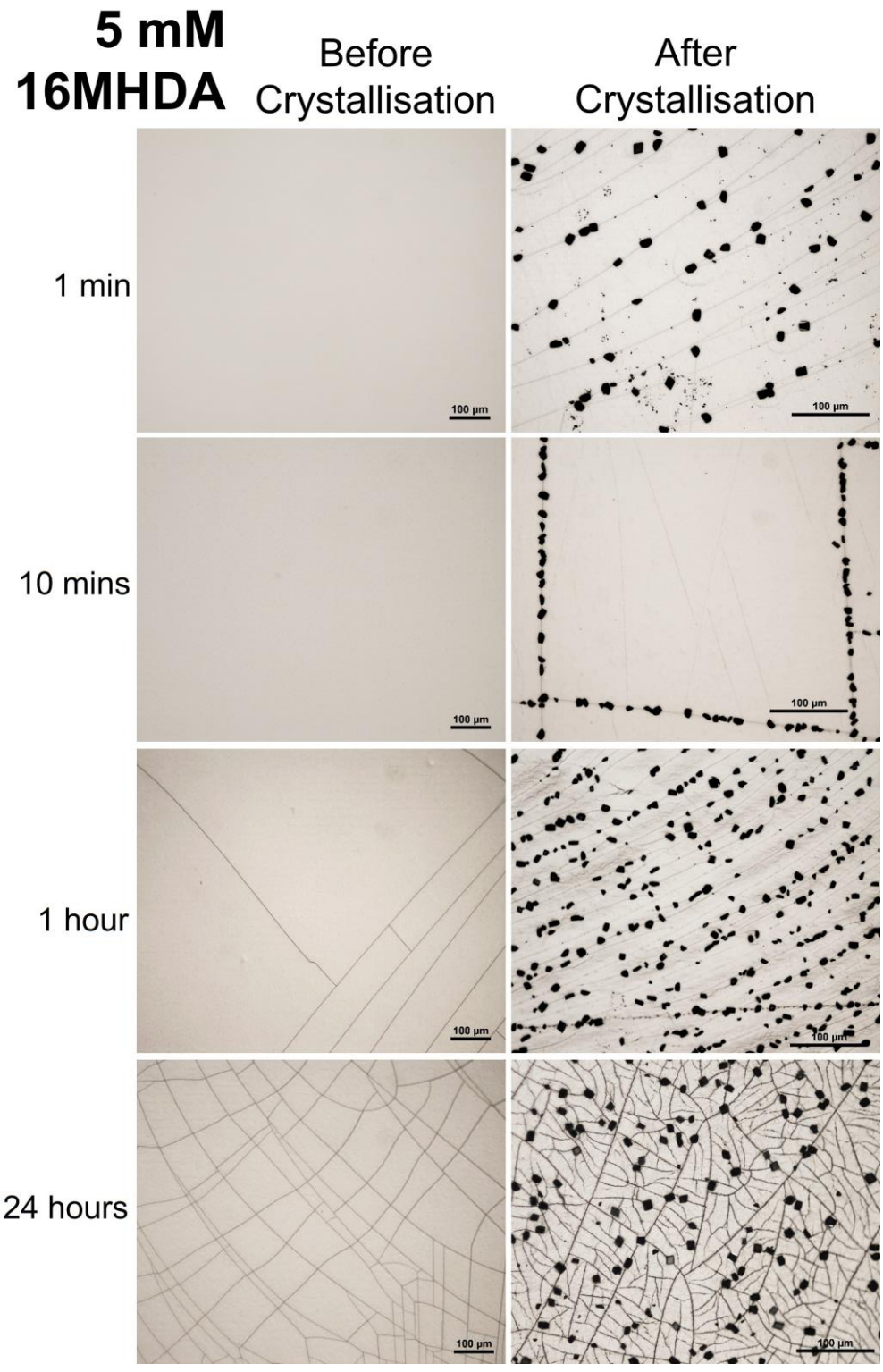


**Figure 56: Cracking patterns formed by immersing Ir-PDMS in 5mM 16MHDA for time lengths ranging from 1 minute up to 24 hours, and the subsequent results of $CaCO_3$ crystallisation on these substrates. Note that for samples where cracks did not form from swelling, substrates were lightly squeezed to produce cracks before $CaCO_3$ was crystallised.**

### 3.3.1.4 Washing Cracked Substrates

The washing step was investigated next. A low-electron density residue was observed in and around the cracks using SEM after crystals had formed. This was likely of organic origin due to its dark appearance as compared to the bright, electron-dense iridium layer (Figure 57).

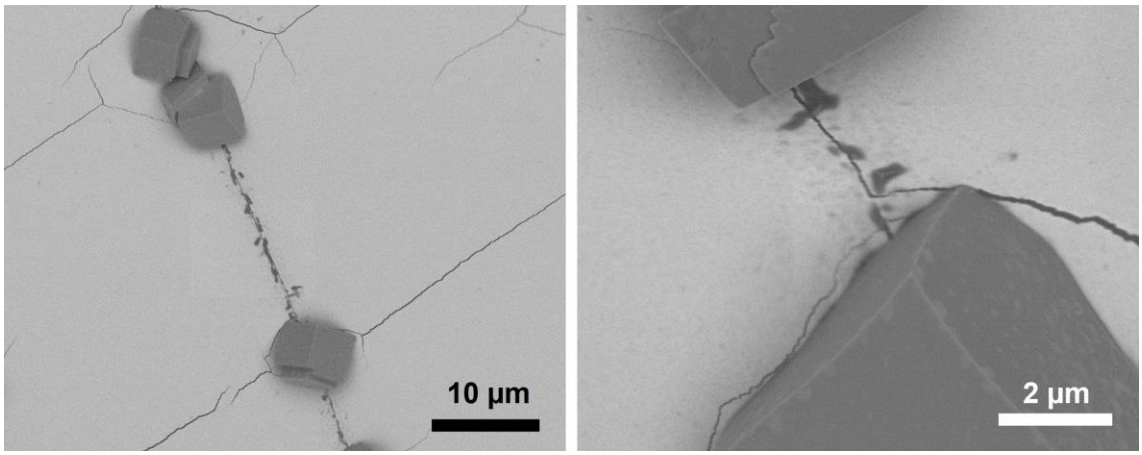


**Figure 57: SEM image showing organic residue surrounding iridium cracks with $CaCO_3$ crystals in.**

Imaging of the cracks before and after 16MHDA functionalisation revealed that this residue only appeared after the functionalisation step (Figure 58A & B). This strongly suggested that the residue was excess 16MHDA, even though it remained after washing with copious ethanol. One possible explanation is that both 16MHDA and ethanol partially infiltrated the PDMS that was exposed at the iridium cracks, a highly documented process[210]. Water is miscible with ethanol but is an effective antisolvent for 16MHDA. This means that the infiltrated ethanol and dissolved 16MHDA may have been washed from the substrates during the ethanol washing, and the 16MHDA deposited in the immediate vicinity of the crack. With this in mind, it was found that the only way to fully remove the residue was by washing with copious ethanol, then immersing in ethanol for at least 10 minutes, followed by more ethanol washing (Figure 58C). $CaCO_3$ crystals still formed in the cracks on surfaces in which the 16MHDA residue had been fully removed, demonstrating that the residue was not responsible for the enhanced nucleation of $CaCO_3$ at the cracks (Figure 58D). This was also confirmed by crystallising $CaCO_3$ on PDMS that was not iridium coated but was subjected to

the same 16MHDA functionalisation procedure; very little crystallisation occurred anywhere on the surface (Figure 59).

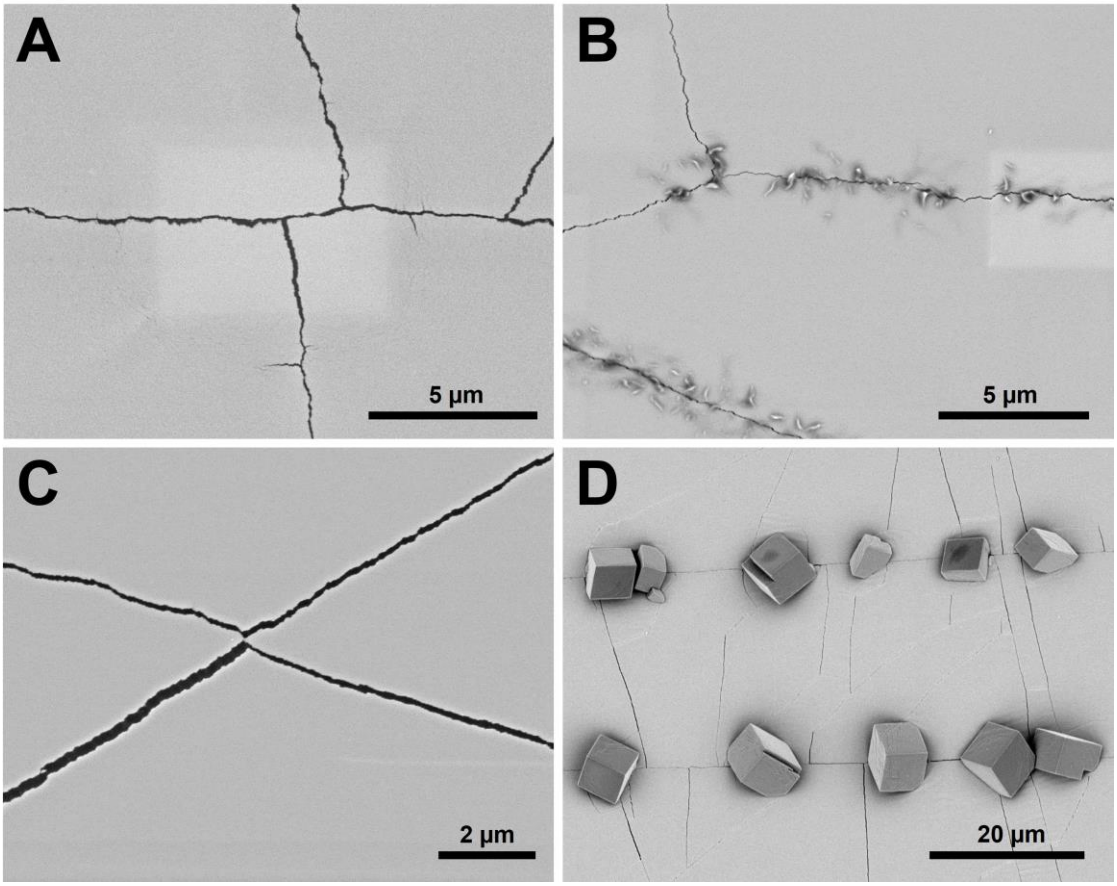


**Figure 58: SEM images showing (A) iridium cracks resulting from mechanical squeezing of Ir-PDMS substrates. (B) Persistence of organic material at cracks after a normal degree of ethanol washing. (C) Full removal of organic material following ethanol immersion washing step. (D) Preferential $CaCO_3$ crystallisation in cracks after organic material was removed by ethanol immersion washing.**

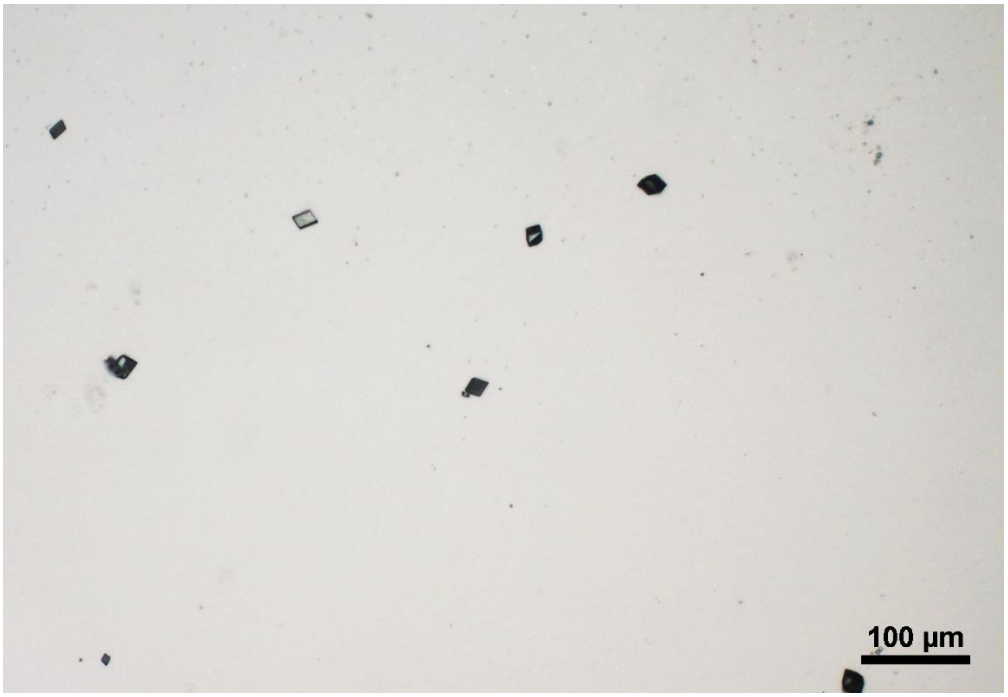


**Figure 59: $CaCO_3$ crystals grown on uncoated PDMS after 10 minutes of immersion in 5mM 16MHDA followed by ethanol washing.**

### 3.3.1.5 Crystallisation of $CaCO_3$ on Cracked Substrates

$CaCO_3$ was precipitated by (i) immersing FC-Ir-PDMS substrates in $CaCl_2$ solution (2 mM, 4.9 mL), (ii) adding $Na_2CO_3$ (100 mM, 100 µL) without mixing, (iii) leaving the solutions to crystallise for 1 hour, (iv) washing with water and ethanol, and (v) air drying. Substrates were placed upright in solutions to stop any crystals formed in the bulk solution from falling onto the surfaces in random locations. Since this method of mixing solutions had not been reported elsewhere, the results obtained from this technique (termed 'slow diffusion') were compared to a more standard approach, whereby equimolar $CaCl_2$ (4 or 8 mM, 2.5 mL) and $Na_2CO_3$ (4 or 8 mM, 2.5 mL) were thoroughly mixed by a vortex mixer, and then FC-Ir-PDMS substrates were quickly immersed, again in an upright position. These standardly-mixed solutions had supersaturation indices of 2 and 2.39 respectively.

The results are shown in Figure 60 and demonstrate that the results from the 4 mM solutions were very similar to those from the slow diffusion method. Using 8 mM solutions, however, there were two sets of crystal sizes, corresponding to two sets of nucleation events. Crystals localised at the cracks were larger than

those formed elsewhere, suggesting that they formed first. A high number of crystals formed away from the cracks, and these again formed later on as indicated by their small size. This shows that the solution supersaturation was too high to give selectivity for crystallisation in the cracks.

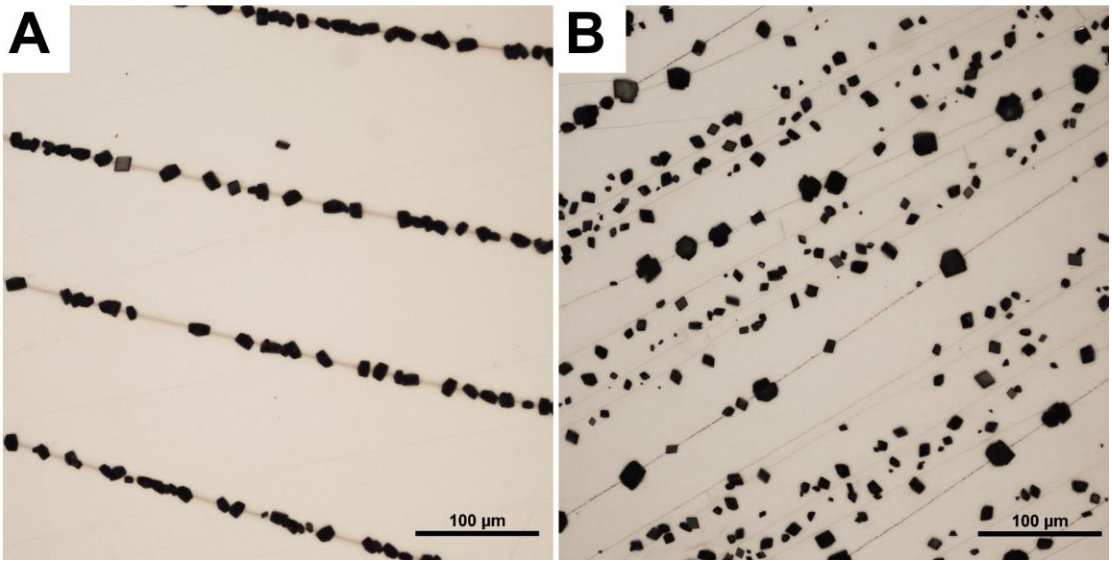


**Figure 60: $CaCO_3$ crystallised on FC-Ir-PDMS by direct mixing of equal volumes of $CaCl_2$ and $Na_2CO_3$ with initial (i.e. before mixing) concentrations of (A) 4mM and (B) 8mM.**

A set of rough supersaturation calculations for the slow diffusion method crystallisation conditions are shown in Figure 61. This figure shows that a region exists close to the diffusion front of the $Na_2CO_3$ solution where the supersaturation climbs above 2, up to a maximum of around 2.4. Due to the small volume of the $Na_2CO_3$ droplet (100 µL) compared to the volume of $CaCl_2$ solution (5 mL), this region is expected to be very small and so a substrate immersed in this solution is only expected to be exposed to the highly supersaturated conditions for a short time. This is likely to stimulate the formation of amorphous calcium carbonate on the surface, before exposing the resulting crystals to a much lower supersaturation. The crystals that have nucleated already can therefore grow, but the probability of further nucleation is significantly reduced.

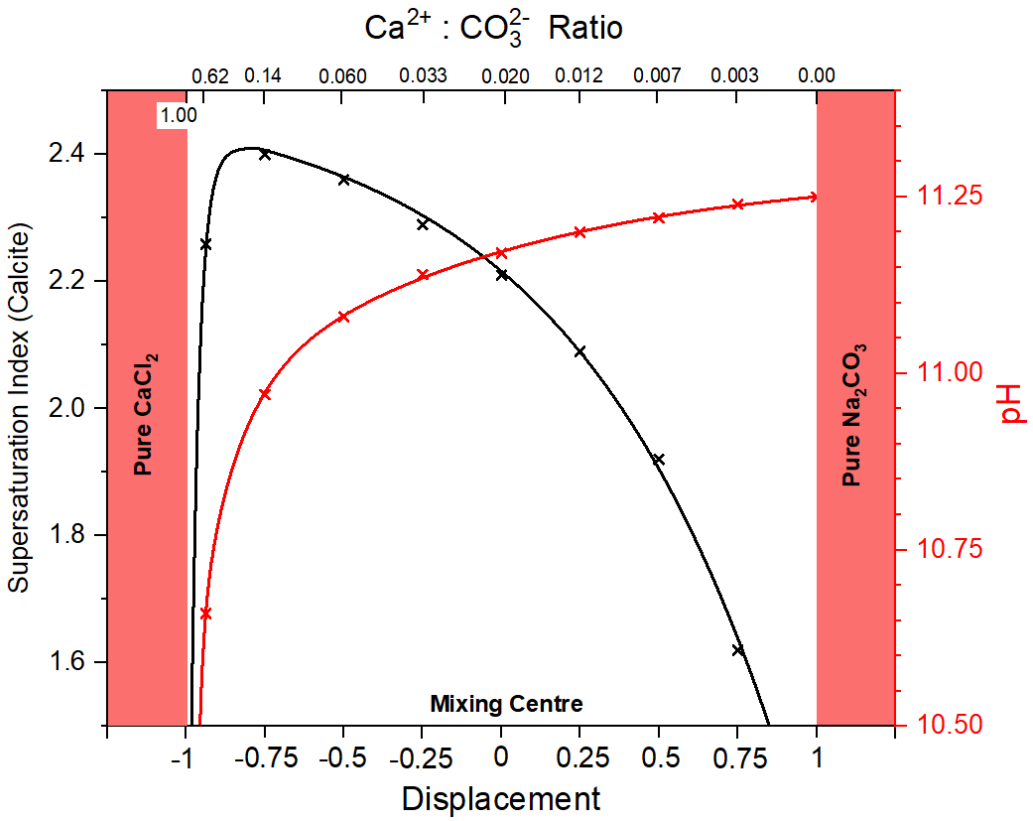


**Figure 61: Supersaturation and pH calculations at varying displacements from the mixing centre, based on mixing of 2 mM $CaCl_2$ and 100 mM $Na_2CO_3$.**

The slow diffusion method was used in all experiments from hereon (unless specified) due its convenience and reproducibility. Occasionally, large amounts of vaterite were formed by direct mixing, which was never observed using the slow diffusion method. Additionally, it was easier to gently position the FC-Ir-PDMS upright in a $CaCl_2$ solution and then add a small amount of $Na_2CO_3$ than to mix the solutions and then quickly immerse the substrate.

### 3.3.2 Investigation of Mechanism of Enhanced Nucleation

With a robust methodology for fabricating and crystallising $CaCO_3$ on FC-Ir-PDMS, the activity of the cracks and the mechanism by which nucleation was promoted could be investigated.

#### 3.3.2.1 Crystal Nucleation and Growth Rates on Surfaces Measured by Analysis of Optical Microscopy Images

*In-situ* experiments were performed to establish how the nucleation rates of crystals varies on FC-Ir-PDMS as compared to glass surfaces, both scratched and pristine. A time lapse was set up using the configuration shown in Figure 46. This mimicked the standard method used for $CaCO_3$ crystallisation on cracked substrates but enabled monitoring by inverted light microscopy. Once experiments were run, the full image stacks were processed using ImageJ with the 'Analyze Particles' feature, which outputted the areas of each particle detected in each frame. The numbers of particles in each frame and the average area of a particle in the frame were calculated using Excel, and the resulting plots are shown in Figure 62. The gradients of the steep, straight part of the plots shown in Figure 62A were used to estimate the steady state nucleation rate on each surface. Gradients of the plots in Figure 62B cannot be considered measures of growth rate since they do not consider the z component of the growth rate. The plot does, however, show a sharp increase in gradient where nucleation stopped and only growth could continue.

Similarly to the results shown in Section 2.3.1, scratched glass produced more crystals than pristine glass, and this was reflected by a 103% increase in nucleation rate from 0.971 to 1.97 particles per $mm^2$ per second (Figure 62A). FC-Ir-PDMS was much less effective, giving nucleation rates nearly an order of magnitude lower than the scratched glass. This produced fewer crystals that grew to much larger sizes in the more ion-rich solution.

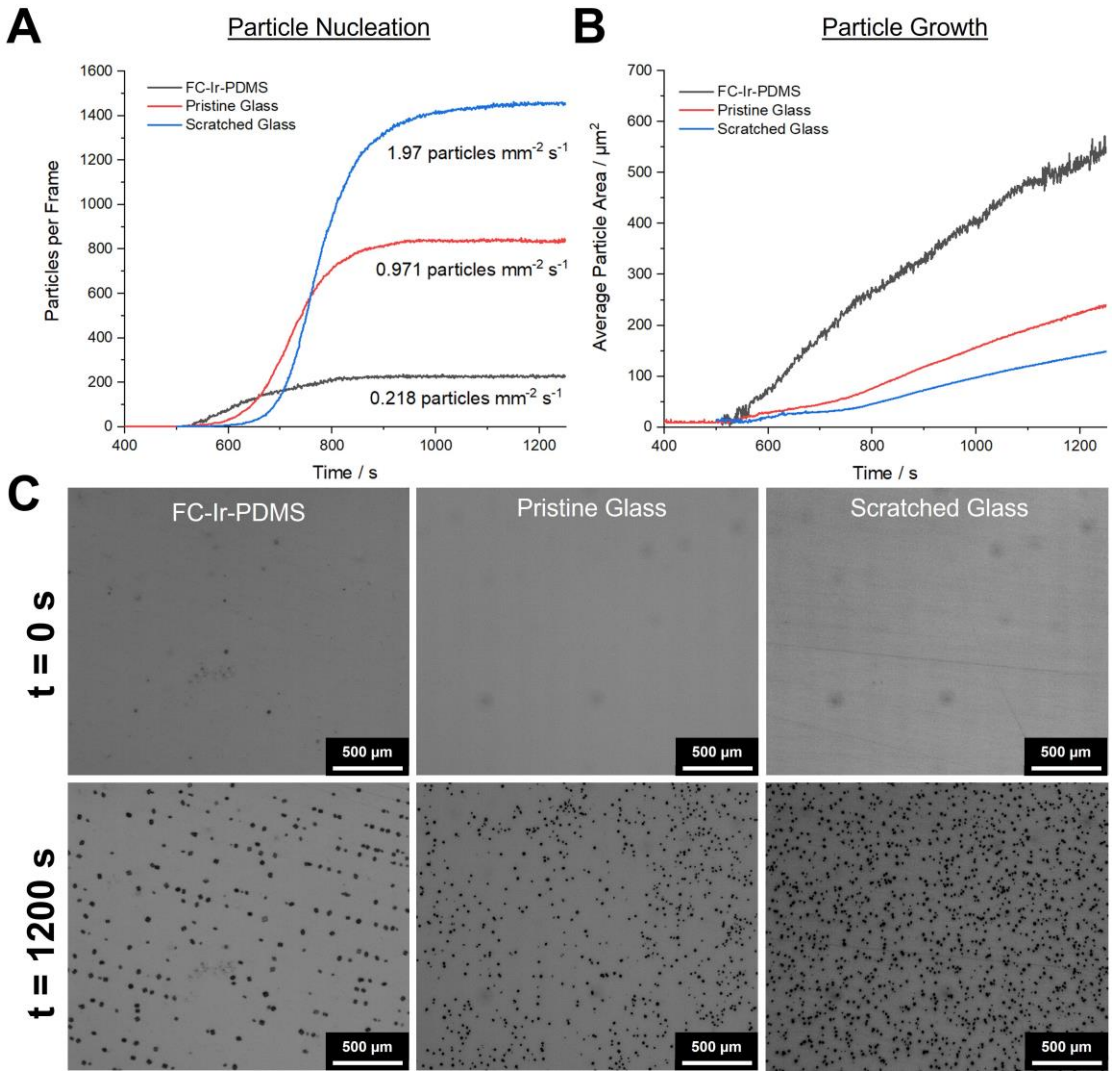


**Figure 62: (A) Frame-by frame numbers of particles counted by the 'Analyze Particles' feature in ImageJ for FC-Ir-PDMS, pristine glass and scratched glass. (B) Average particle area per frame from the same feature within ImageJ. (C) Images of crystals growing on the substrates at time t = 0 s and t = 1200 s.**

The total area occupied by cracks was only a fraction of the full surface area, but these were responsible for nucleating every crystal observed. Comparing the total number of crystals formed in the entire field of view on each substrate was therefore not suitable for comparing the nucleating efficacies of glass and the FC-Ir-PDMS cracks. Image analysis was used to estimate the fraction of the surface area occupied by cracks. Lines of thickness 50 µm were drawn over each visible crack, which was an over-estimation of their real width, but was adopted to

account for the possibilities of undetectable cracks radiating away from the larger visible cracks. Altogether, the areas of these lines represented only 17% of the full frame, so the surface area used to calculate the nucleation rate for FC-Ir-PDMS was multiplied by 0.17. This allowed for a more realistic comparison between the nucleation efficacies of the active surface area of the substrates (Figure 63). This adjustment to the calculation showed that the nucleation rate on FC-Ir-PDMS was greater than on pristine glass, but slightly less than on scratched glass. This nucleation rate is also a low estimate due to the generous width assumed for each crack, and real values are likely considerably higher.

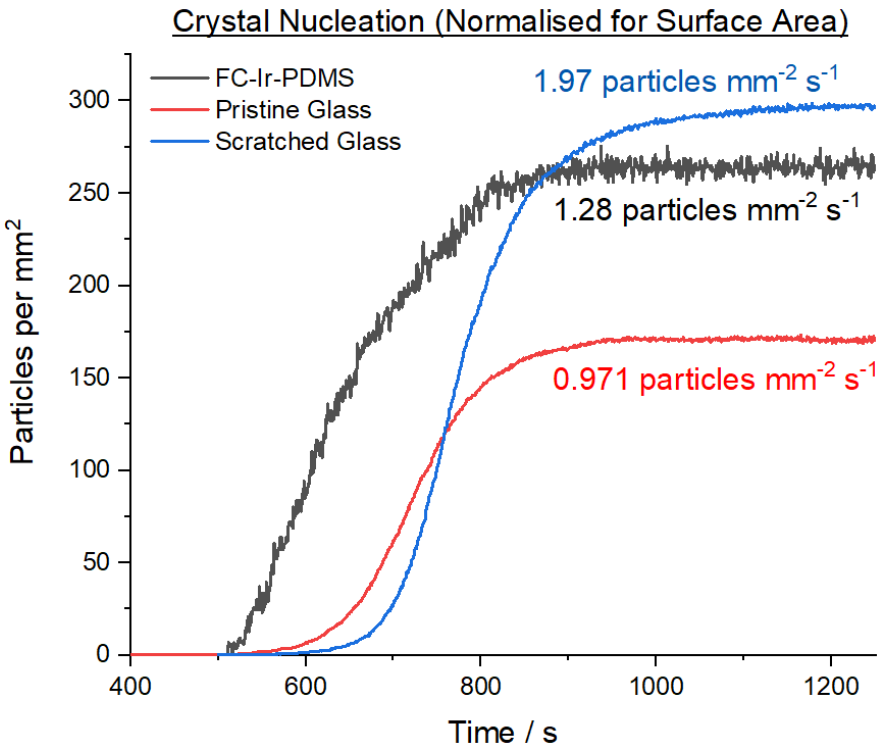


**Figure 63: Number of particles per frame normalised by active nucleant surface area. This was estimated from the observation that only 17% of the area of the FC-Ir-PDMS image frame could be considered a crack site, but all the nucleation happened at the cracks.**

### 3.3.2.2 Effect of Addition of Magnesium Ions on Crystallisation of Calcium Carbonate on Cracks

The effect of magnesium ions on the crystallisation of $CaCO_3$ was explored. FC-Ir-PDMS was immersed in $CaCl_2$ solutions (2 mM, 4.9 mL) with varying concentrations of $MgCl_2$ (0 mM, 5mM, 10 mM). $Na_2CO_3$ (100 mM, 100 µL) was then added, and the solutions were left to crystallise for 3 days. Addition of $Mg^{2+}$ modified the morphology of the calcite crystals and resulted in the formation of some aragonite crystals. The number density of crystals in cracks also increased with increasing $Mg^{2+}$ concentration (Figure 64). $Mg^{2+}$ ions are known to suppress both the nucleation and growth of $CaCO_3$, and in this case growth was suppressed more than nucleation.

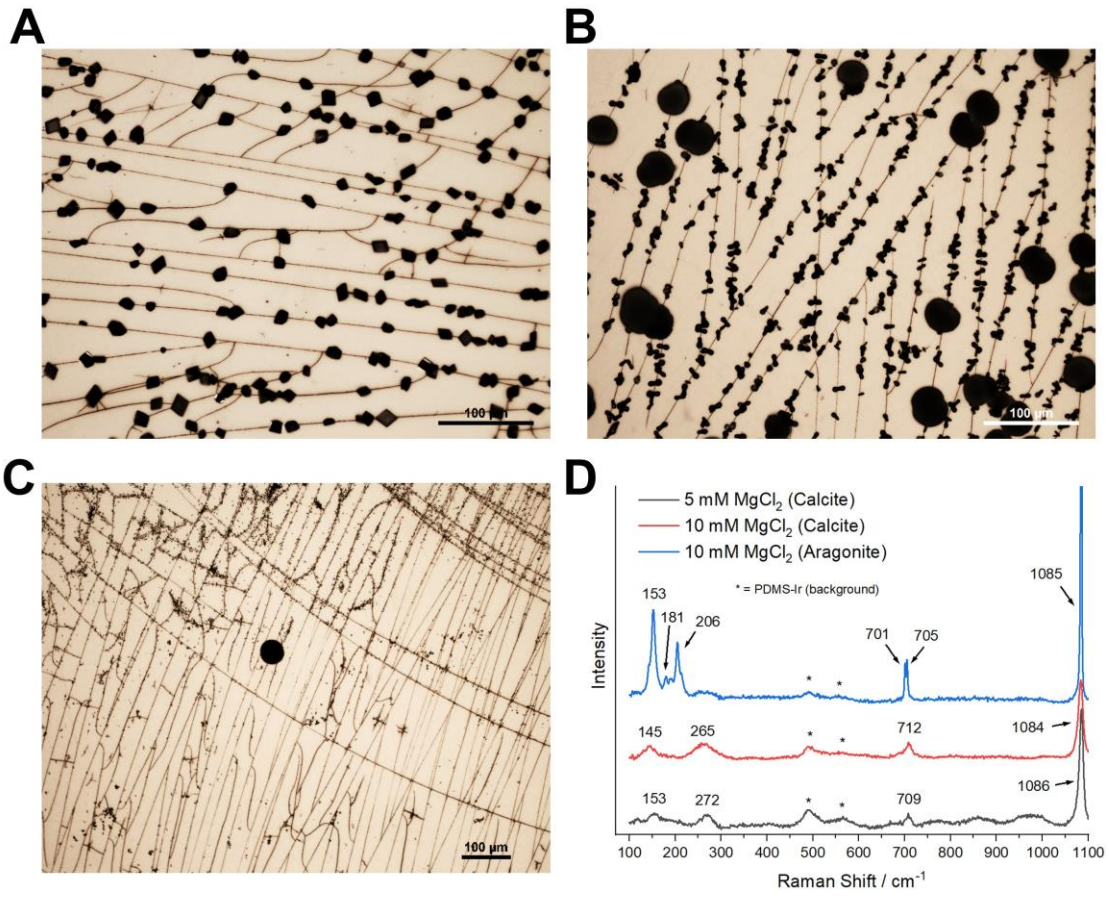


**Figure 64: (A-C) OM images showing $CaCO_3$ crystals grown after 3 days on FC-Ir-PDMS with (A) 0 mM $MgCl_2$, (B) 5 mM $MgCl_2$ and (C) 10 mM $MgCl_2$. (D) Raman spectra of the morphologically altered calcite and aragonite crystals shown in (C & D).**

#### 3.3.2.3 Electron Microscopy of Crystal Nucleation Sites

The locations of the nucleation sites on the substrates was investigated using FIB-SEM and TEM to determine exactly where the nuclei formed on the surface, and if any morphological features of the nucleating crack carried through to the resulting bulk crystal.

Samples were prepared for FIB-SEM by crystallising $CaCO_3$ for only 10 minutes, as compared to the usual 20 minutes, to capture the earlier stages of the crystallisation process. FIB-SEM was used to produce cross-sections of a calcite crystals formed on the cracks (Figure 65). The crack appeared in these images as a small discontinuity in the bright electron-dense iridium layer. These sections showed that the centres of the crystals were coincident with the crack. Most interestingly, the calcite crystals appeared to contain a zone of low density material centred around the crack, appearing in SEM as a dark region surrounded by brighter, more electron dense crystalline material. Sequential milling to expose cross sections along the length of the crack showed that the low-density zone was localised to the approximate centre of the crystal, and did not extend along the full length of the crystal following the crack. There was some variation in the size of this low-density zone, where it was highly prominent in some samples (Figure 65C) and much smaller in others (Figure 65B).

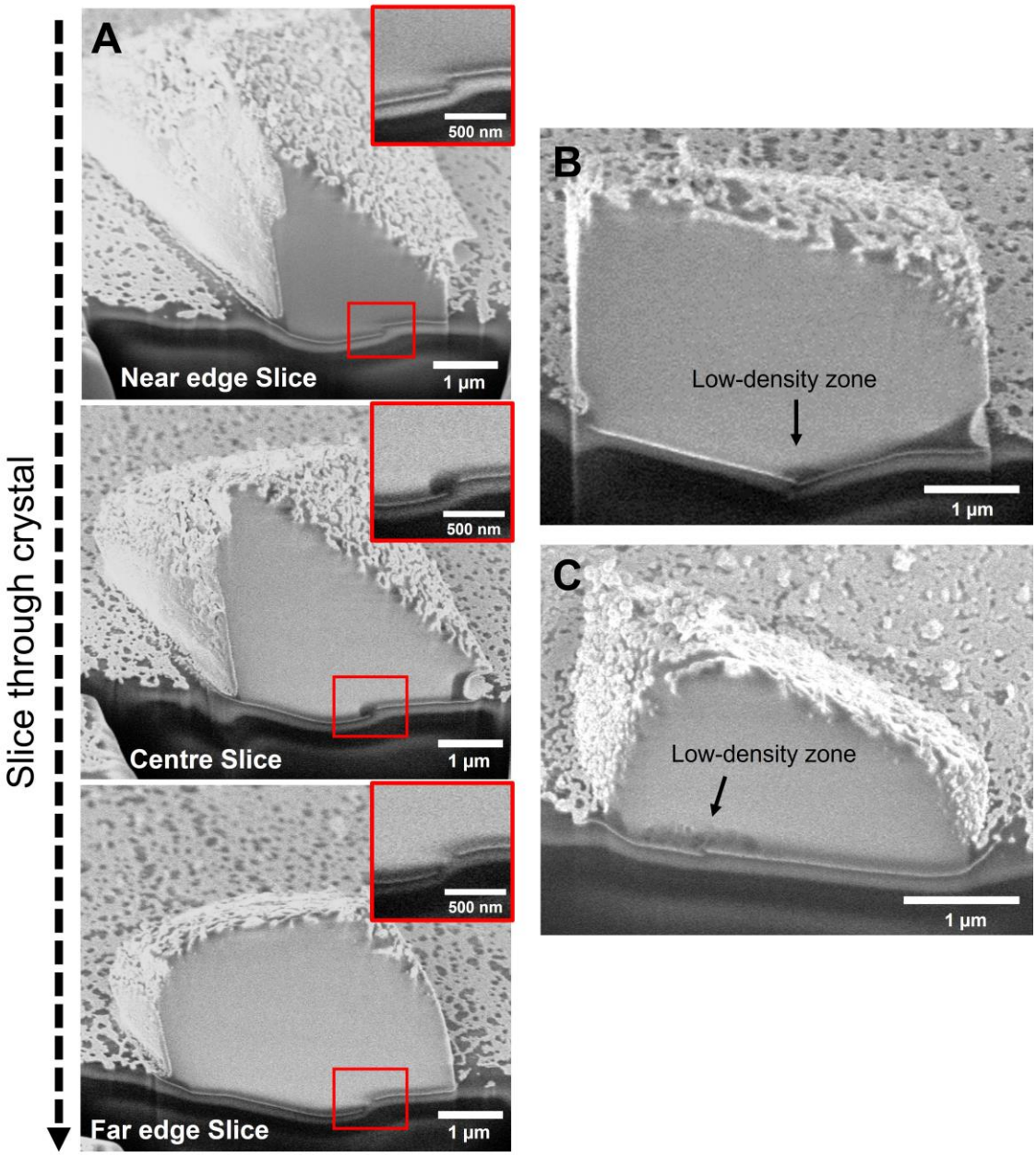


**Figure 65: SEM images showing (A) FIB slice-and-view cross-sectional images of a calcite crystal upon 16MHDA-functionalised cracked iridium surfaces both at its centre and near its edge. (B & C) SEM images of FIB cross-sections of the centres of two more calcite crystals, showing the various appearances of the low-density zone localised at the crack.**

This low-density region of the crystal was further explored by preparing a lamella of the crystal-crack composite using FIB-milling under cryogenic conditions (Figure 66). The final thickness of the lamella after thinning was 130 nm, which was suitable for TEM to be performed.

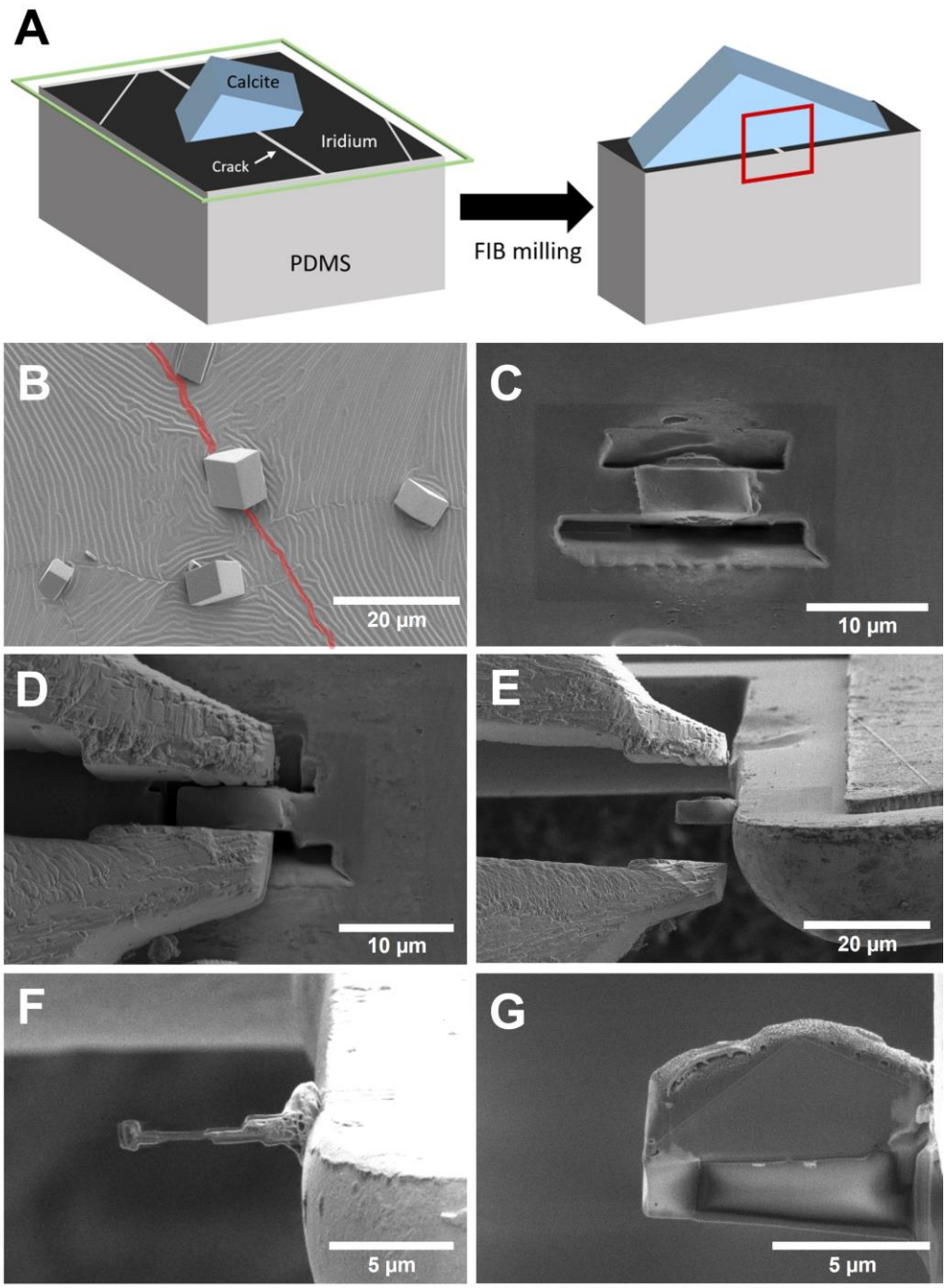


**Figure 66: (A) A schematic overview of the FIB-milling process to produce a lamella for TEM. (B-G) show the individual stages of the process: (B) The crystal in a crack, which is highlighted in red for clarity. (C) The sides of the crystal are milled by the FIB and undercut at the base. (D) Cryo-grippers are latched on to the crystal, and the last remaining side is milled through. (E) The crystal is placed aside a TEM grid and the FIB is used to sinter the crystal to the grid. (F) The FIB is used to thin the crystal until it reaches the desired thickness. (G) A cross-sectional view of the finished lamella ready for TEM.**

The lamella was imaged using TEM (Figure 67A). The aspect ratio of the width/height of the lamella compared to its thickness caused bend contours to appear as curved lines in the single crystal, but these did not significantly affect imaging. Selected area electron diffraction (SAED) near the centre of the crystal confirmed the presence of single crystalline calcite (Figure 67B) and that the zone axis was [4 -7 -1].

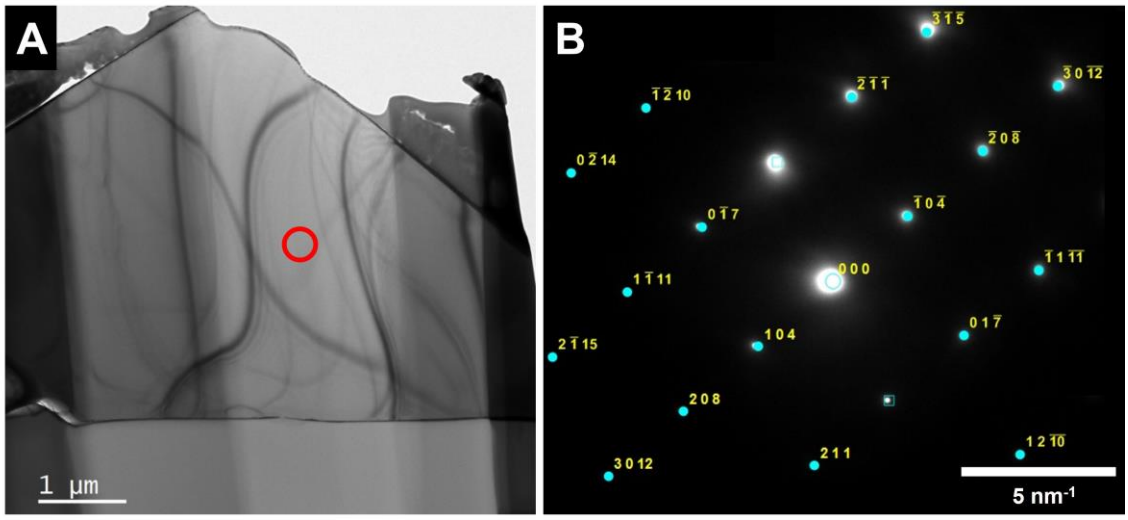


**Figure 67: (A) Low-magnification TEM image of the crystal lamella. The red circle corresponds to the location of SAED measurement. (B) Selected area electron diffraction pattern of the bulk crystal indexed to calcite (zone axis [4 -7 -1]).**

High-resolution images were then taken of different regions of the low-density zone at the crack. Figure 68 shows three selected regions – the bulk crystalline calcite above the low-density zone, the centre of the low density zone, and the interface between the crystal and PDMS. Fast Fourier transform (FFT) images showed diffraction patterns corresponding to single crystalline calcite far from the low density region. Within the region, which extended about 100 nm from the crack, a series of powder diffraction rings were observed together with the diffraction spots corresponding to single crystals of calcite. These were indexed to polycrystalline CaO, a common product resulting from electron beam damage or heat-induced calcination of $CaCO_3$. The intensity of these rings increased with increasing proximity to the crack, as shown in a plot of the radial intensity plots of FFTs shown in Figure 69. No CaO was observed at the calcite-PDMS interfacial region, but a diffuse ring-shaped amorphous diffraction signal was produced by the PDMS.

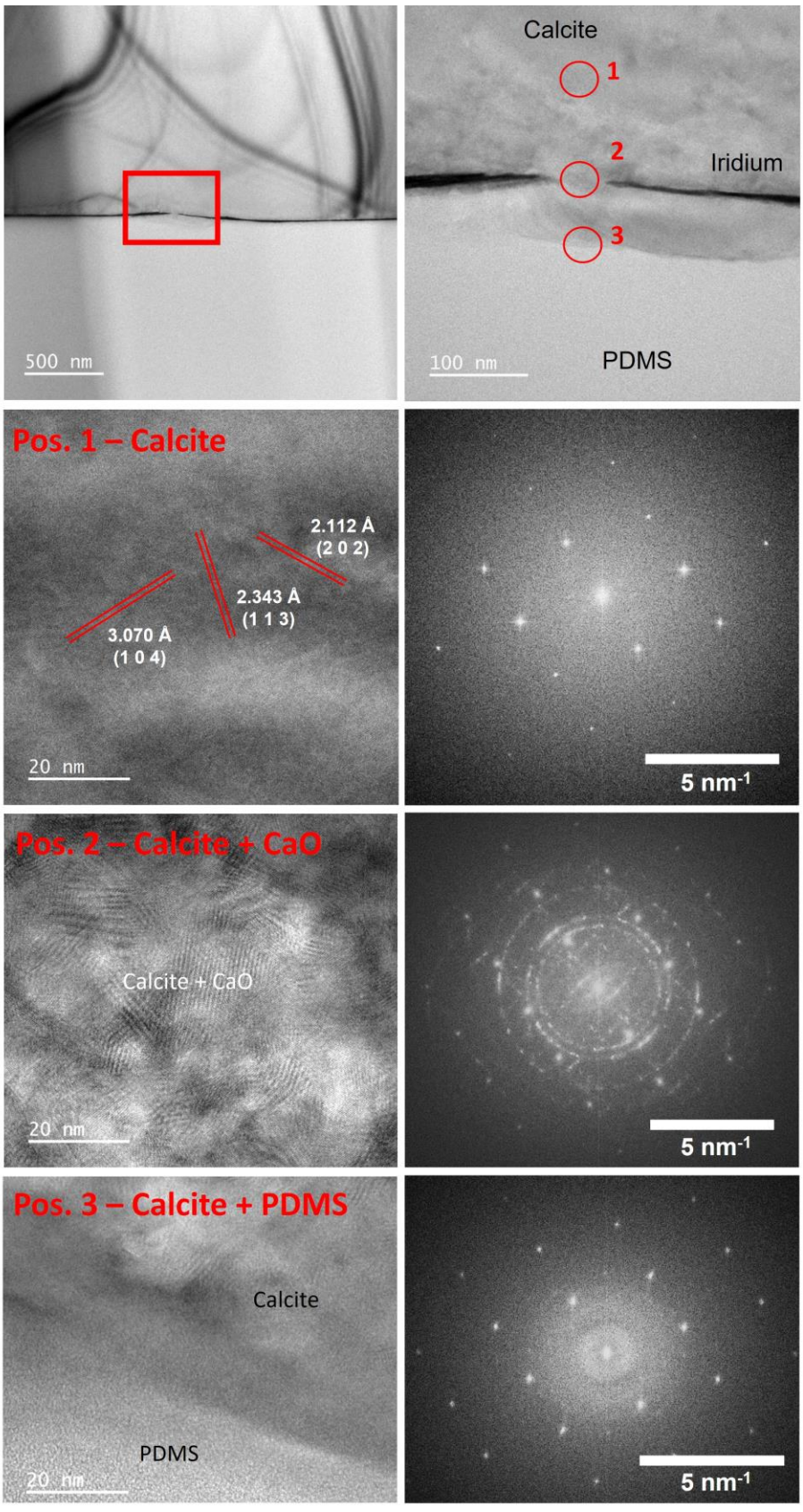


**Figure 68: TEM images of varying magnification showing the calcite crystal on the crack, focusing on the interface between the two regions. Fast Fourier transform images of the HRTEM images are shown on the right.**

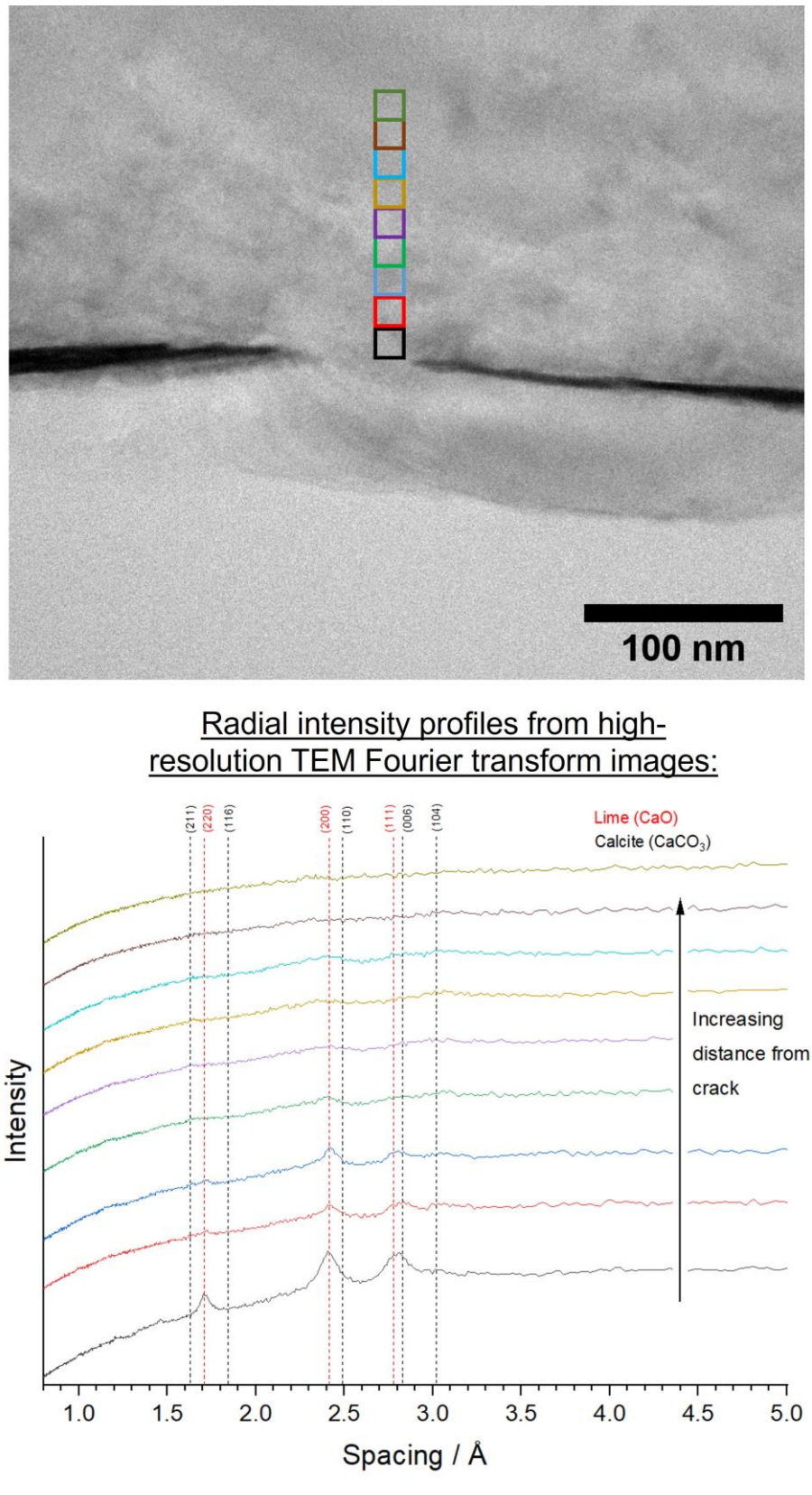


**Figure 69: TEM image of the region surrounding the crack, with associated radial intensities plotted from Fourier transforms of high-resolution TEM images.**

#### 3.3.2.4 Resin Exfoliation to Show Crystal Nucleation Sites in Cracks

The labour-intensive nature of using FIB to create a lamella for TEM made it challenging to view the crack-crystal interface of many crystals. A novel method was therefore developed to image the crack-crystal interfaces of many crystals in a time and cost-efficient way. A conductive carbon and polymethyl methacrylate-based resin kit (Demotec® 70) was poured onto the crystal covered FC-Ir-PDMS, cured, and exfoliated. This left the iridium coating still attached to the PDMS, but removed the crystals. The tops were embedded in the resin but the bottoms, where iridium had been in contact, became exposed. SEM was then used to image the crystals and the iridium cracks from which the crystals had been plucked (Figure 70). Figure 70B shows a faint remaining outline of the crystals shown in Figure 70A, caused by pressure on the iridium surface resulting from the calcite growth.

There was no trace of organic material in the regions underneath the crystals, and the undersides of the two exfoliated crystals shown in Figure 70C & D confirm the absence of organic material, but reveal the identity of the low-density region as a void centred at the iridium cracks. The size of this void varied considerably between crystals, and was absent at the bases of some crystals.

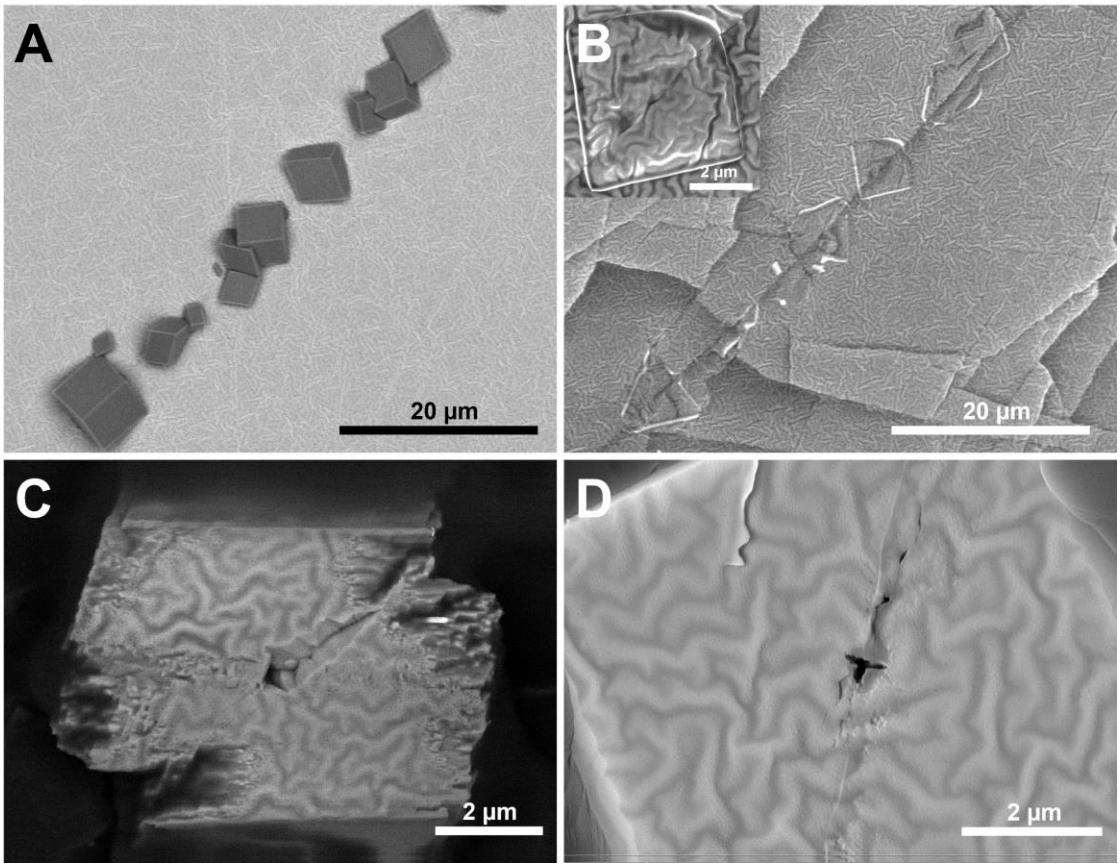


**Figure 70: (A) Calcite crystals grown on FC-Ir-PDMS. (B) The intact iridium substrate underneath the crystals shown in (A), exposed by exfoliating crystals from the surface with resin. (C & D) The undersides of two calcite crystals exposed by resin embedding and exfoliation.**

A second TEM lamella (thickness = 74 nm) was prepared using cryo-FIB, this time using a crystal which had been exfoliated by resin. Unfortunately, this crystal did not contain a void such as those seen in Figure 70C & D. However, when this crystal was imaged, the results were very similar to those of the previous TEM lamella. Powder diffraction rings indexed to CaO were present along the length of the iridium layer in close proximity to it (Figure 71).

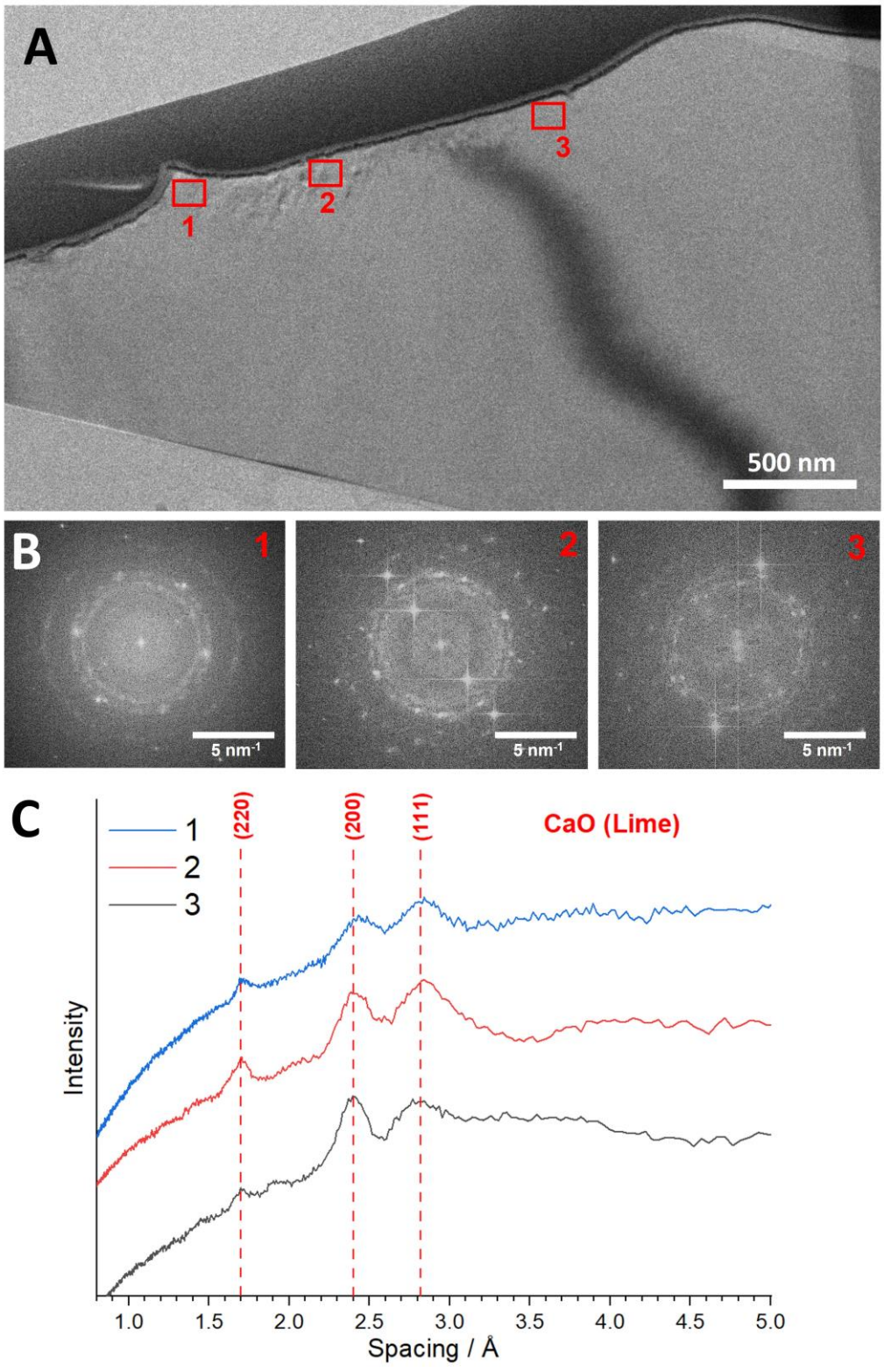


**Figure 71: (A) Low magnification TEM image of a FIB-milled thin section of resin-exfoliated $CaCO_3$ grown in a crack, showing positions from which high resolution images were taken. (B) FFTs of the HRTEM images taken at these positions. (C) Radial intensity profiles of these FFTs, with powder diffraction rings indexed to CaO.**

Energy-dispersive x-ray (EDX) spectroscopic mapping was also used to determine the distribution of carbon, calcium and oxygen at varying distance from the iridium layer in TEM (Figure 72). The calcium signal was consistently high across the entire crystal, but the oxygen signal dropped considerably within 200 nm of the iridium layer.

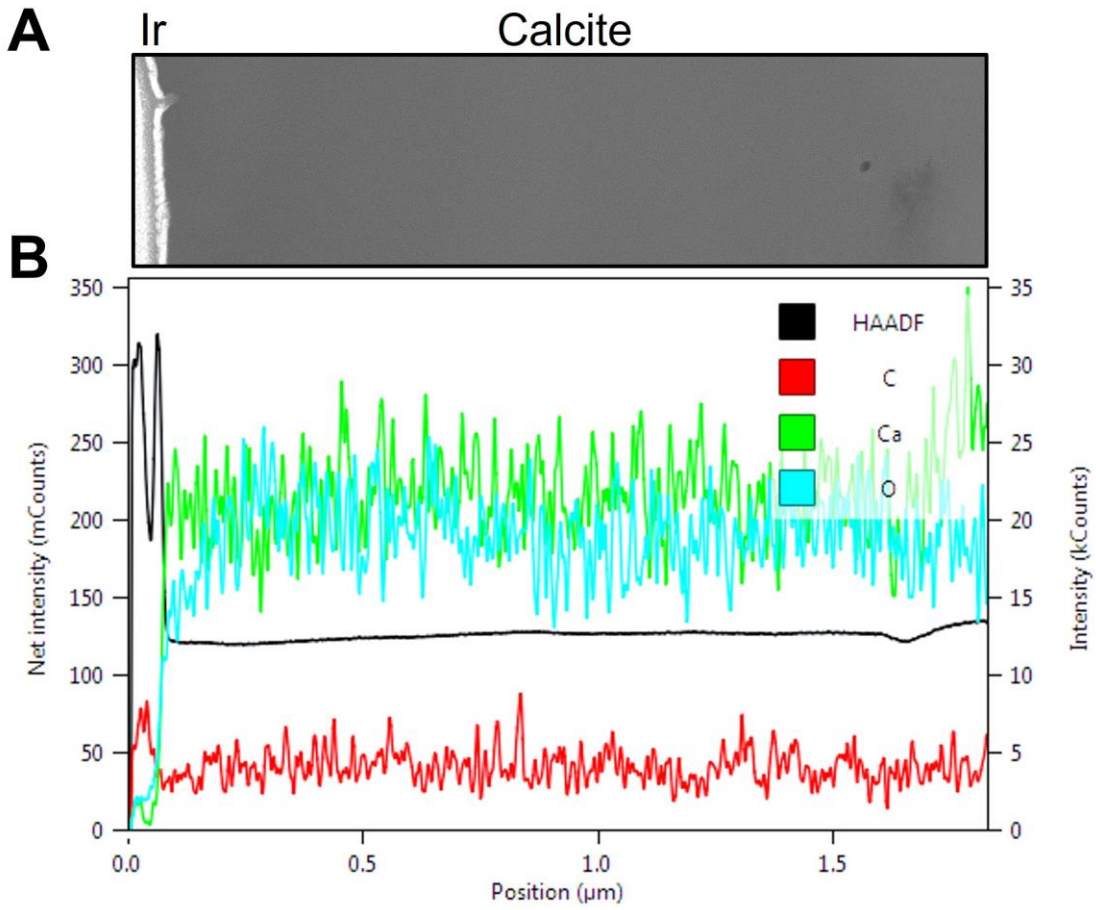


**Figure 72: (A) TEM image and (B) EDX line-scan showing elemental analysis at increasing distance from the iridium layer. NOTE: HAADF signal corresponds to heavy metal signal i.e. iridium.**

### 3.3.3 Investigation of Nucleant Behaviour for Alternative Crystals

In this section, the generality of FC-Ir-PDMS towards nucleation of a range of other types of crystals was explored.

#### 3.3.3.1 Barium Carbonate and Calcium Oxalate on Cracks

Barium carbonate contains a carbonate anion, and calcium oxalate contains two carboxylate groups (Figure 73), so the compounds bear some similarities in their chemical functionalities.

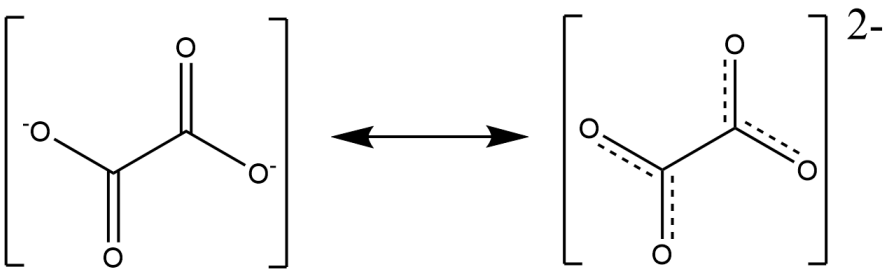


**Figure 73: The resonance structure of the oxalate anion.**

These compounds were crystallised in a similar way to calcium carbonate, whereby substrates were immersed in a solution of either barium chloride or calcium chloride, and then a small quantity of much more concentrated sodium carbonate or ammonium oxalate was added without stirring. Similarly to the results of $CaCO_3$ crystallisation, these compounds both crystallised abundantly at the cracks (Figure 74).

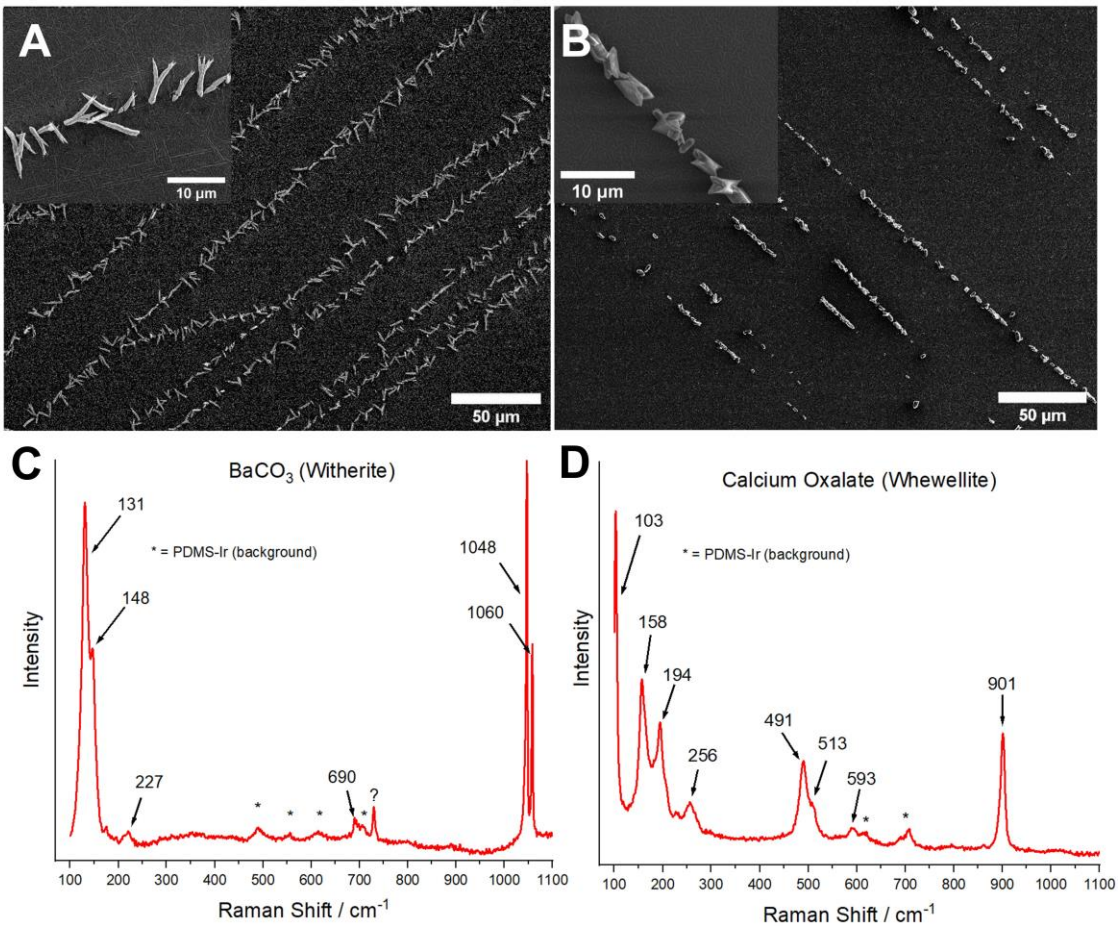


**Figure 74: SEM images of (A) barium carbonate and (B) calcium oxalate crystallised on FC-Ir-PDMS. (C & D) Raman spectra of the crystals shown[211,212]. Asterisks denote peaks deriving from the FC-Ir-PDMS background.**

### 3.3.3.2 Sulfate Crystallisation on Cracks

Calcium, strontium, and barium sulfates were also crystallised by direct mixing on FC-Ir-PDMS. The concentrations of $CaCl_2$, $SrCl_2$, $BaCl_2$ and $Na_2SO_4$ were chosen such that the supersaturation indices of the sulfate minerals would be close to 2. All three minerals are sparingly soluble in water, with room-temperature solubilities of 19.1 mM ($CaSO_4$[213]), 135 mM ($SrSO_4$[214]) and 0.0105 mM ($BaSO_4$[214]). No enhancement of nucleation in the cracks was observed for any of these (Figure 75), and no calcium sulfate crystals were observed on the surface apart from a small cluster at the edge.

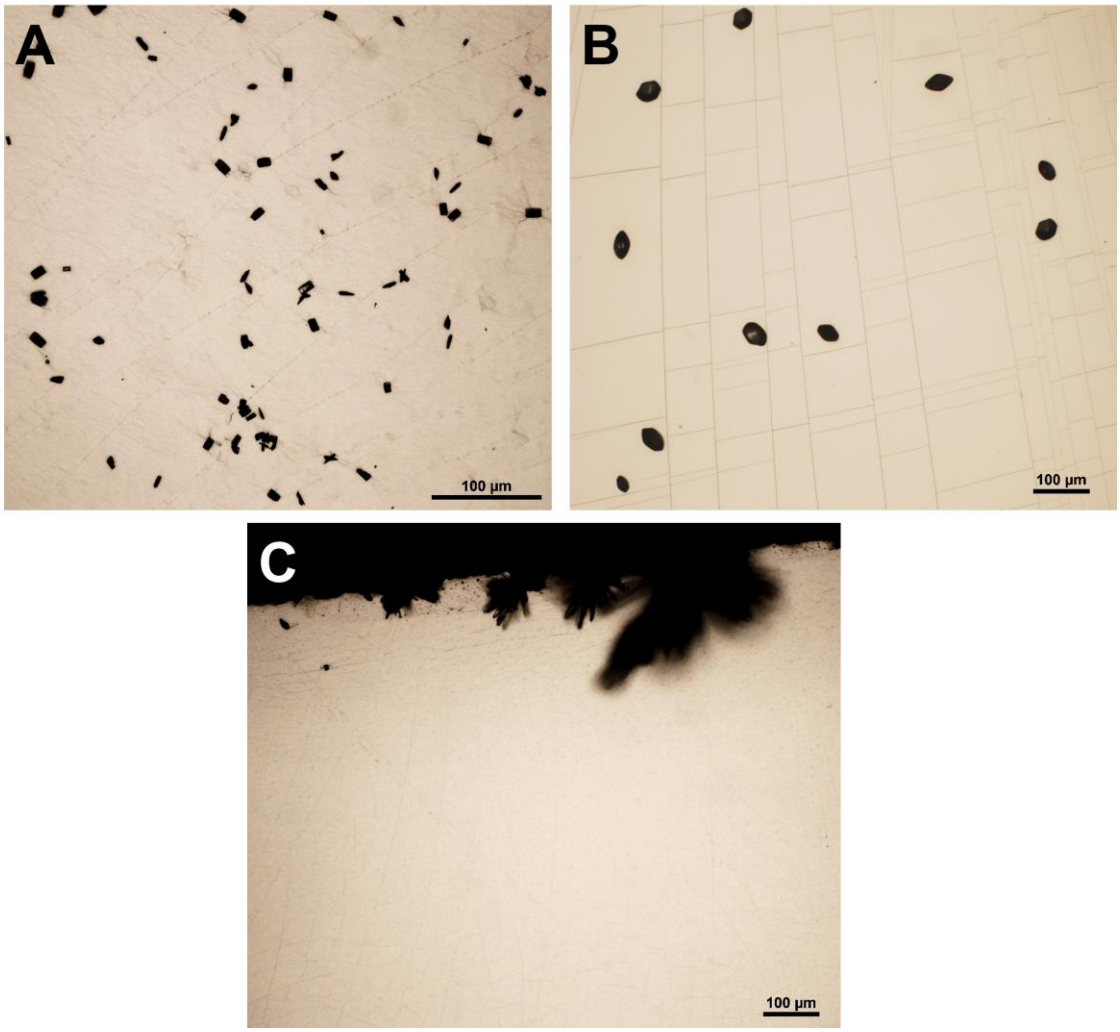


**Figure 75: OM images showing (A) $BaSO_4$, (B) $SrSO_4$ and (C) $CaSO_4$ crystallised on FC-Ir-PDMS.**

### 3.3.3.3 Crystallisation of Organic Compounds on Cracks

Guanine, ibuprofen benzoic acid and glycine were also crystallised on the cracked substrates using a range of methods (Figure 76).

Solutions of guanosine in Gomori buffer were prepared with added purine nucleotide phosphorylase enzyme, which slowly produced highly insoluble guanine crystals. Whilst β-guanine deposits formed in small quantities across the substrate, small cubic crystals presumed to be guanosine were deposited in a few of the cracks (Figure 77A). Due to their extremely small size, however, they could not be further characterised by XRD or Raman spectroscopy.

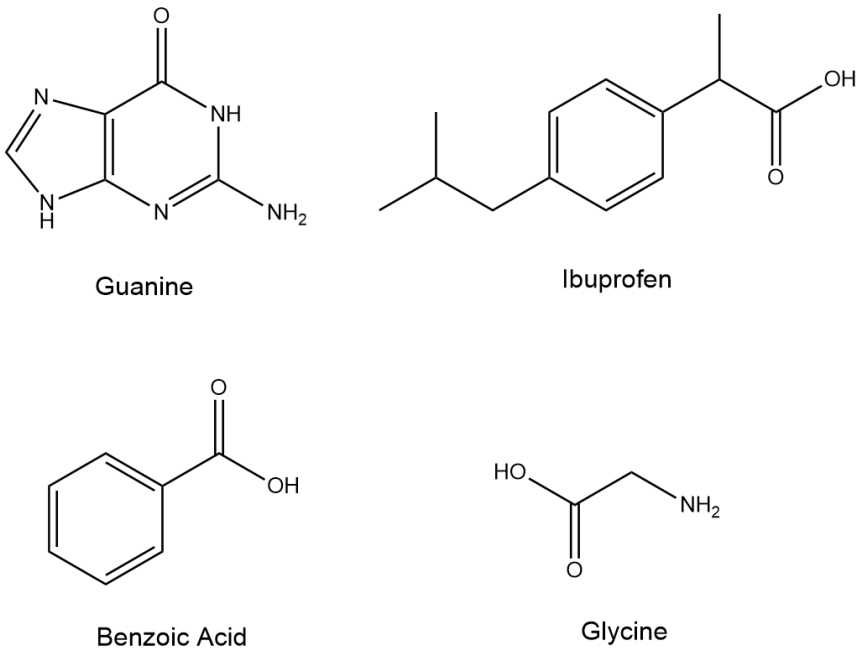


**Figure 76: Structures of guanine, ibuprofen, benzoic acid and glycine.**

A method was also developed for the crystallisation of ibuprofen from its water-soluble sodium salt form, in which an excess of acid would be added to convert it to its insoluble protonated form (Equation 22).

$$\mathrm{Ibu}^-_{(aq)} + \mathrm{H_3O^+} \rightleftharpoons \mathrm{Ibu}_{(l)} + \mathrm{H_2O}_{(l)}$$

**Equation 22**

Instead of crystallising as intended, ibuprofen underwent liquid-liquid phase separation. Even after incubation for 1 week at room temperature, only very small spherical precipitates were observed at the cracks by SEM (Figure 77B). Due to their small sizes, further characterisation was not possible. Attempts were also made to crystallise benzoic acid by this method, but again no crystals were observed on cracks.

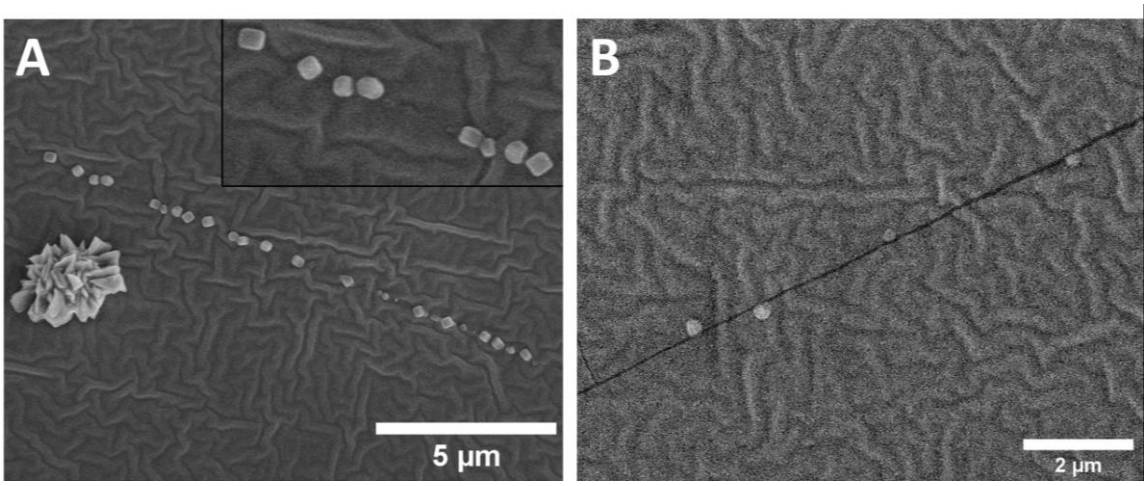


**Figure 77: SEM images showing results of crystallisation of (A) guanine and (B) ibuprofen on FC-Ir-PDMS.**

Far greater success was achieved by crystallising glycine on the FC-Ir-PDMS substrates. Glycine was precipitated by mixing an aqueous glycine solution with ethanol as an antisolvent. Large numbers of crystals formed at the crack sites (Figure 78A & B). These were needle-like in shape, which is characteristic of the β-phase[215], and the presence of this polymorph was confirmed by Raman spectroscopy (Figure 78C). This demonstrates that highly soluble crystals could also preferentially form at the cracks.

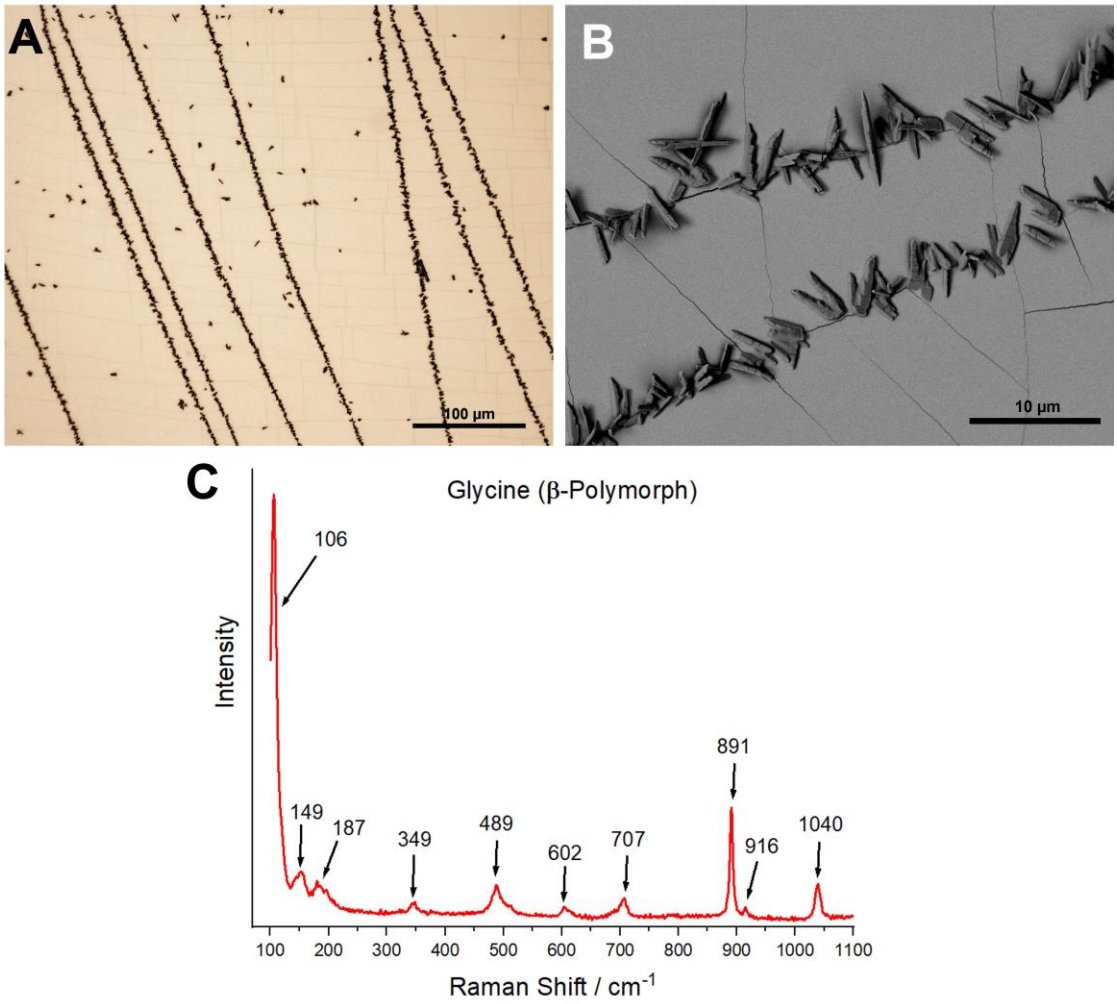


**Figure 78: (A) OM and (B) SEM images of glycine crystallised by ethanol addition on FC-Ir-PDMS. (C) Raman spectrum showing that crystals formed were exclusively β-glycine[216].**

### 3.3.3.4 Crystallisation of a Zeolitic Imidazolate Framework (ZIF) on Cracks

Crystallisation of a zeolitic imidazolate framework (ZIF) was also investigated. ZIFs are a class of metal-organic framework (MOF) which form structures based on tetrahedral units, and that resemble zeolites[217]. Their high internal porosity and thermal/ chemical stability makes them of enduring interest for $CO_2$ or $H_2$ storage applications[218]. The ZIF system adopted in this experiment comprised of $Zn^{2+}$ with a 2-methylimidazole precursor, which typically crystallises as either ZIF-8 (Figure 79A) or ZIF-L (Figure 79B) depending on the stoichiometric ratio of $Zn^{2+}$ to 2-methylimidazole used.

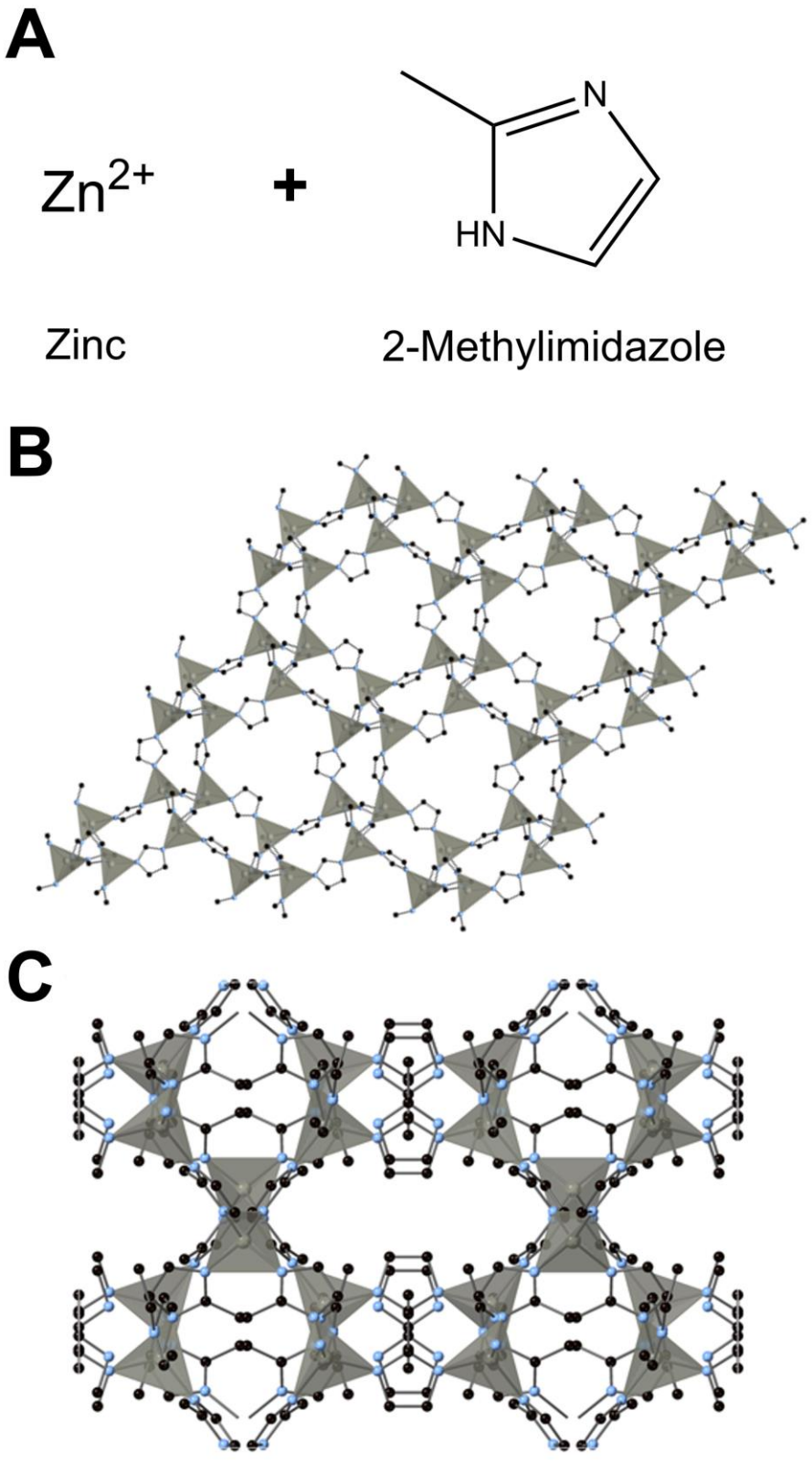


**Figure 79: (A) Precursors used to crystallise ZIFs. (B and C) Structural units of (B) ZIF-8 and (C) ZIF-L [219]. *Reproduced with permission from Springer Nature.***

Stock solutions of zinc nitrate (metal) and 2-methylimidazole (linker) were mixed to prepare a solution containing 1 mM zinc and 60 mM 2-methylimidazole. After 72 hours of immersion of the FC-Ir-PDMS, the samples were washed with water and ethanol, then were air-dried. Crystals were produced in abundance at the cracks (Figure 80A), and SEM showed that their morphologies were more similar to typical leaf-shaped crystals of ZIF-L (Figure 80B). Raman spectra of these crystals showed a distinct peak at 3167 $cm^{-1}$, confirming that ZIF-L had been produced[220], despite the fact that ZIF-8 is typically produced at the high metal:linker ratios used in this experiment [221,222].

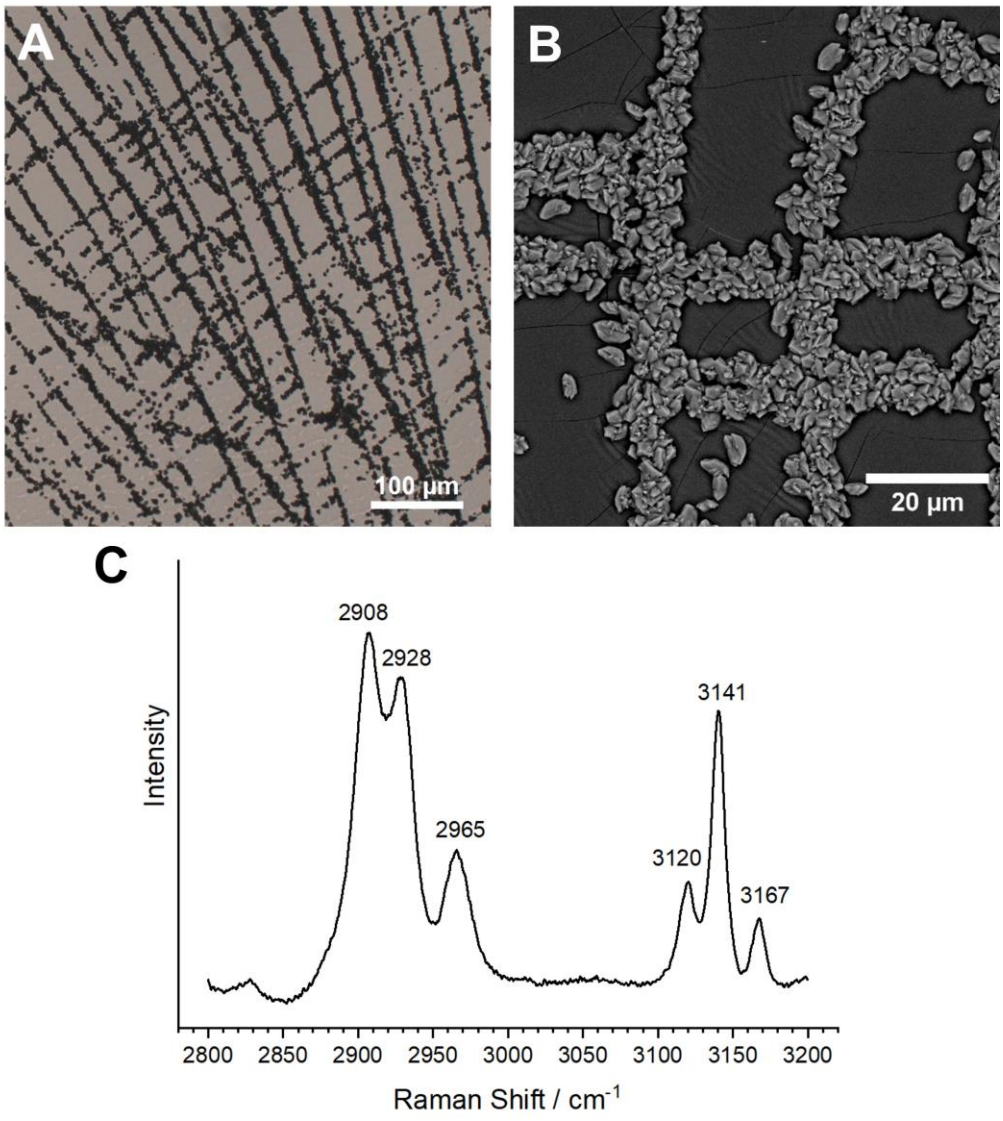


**Figure 80: (A) Optical microscopy and (B) SEM images of ZIFs crystallised on FC-Ir-PDMS. (C) Raman spectrum of the crystals formed at the cracks. The peak at 3167 $cm^{-1}$ confirms the presence of ZIF-L instead of the expected ZIF-8.**

## 3.3.4 Discussion

### 3.3.4.1 The Role of Surface Topography

Classical nucleation theory (CNT) predicts that energy barriers to nucleation are reduced when the interfacial areas of a sub-critical nuclei are reduced. This not only leads to the prediction that growing nuclei should be spherical in shape, but also that heterogeneous nucleation proceeds with a lower energy barrier than homogeneous nucleation as long as the nucleus-surface contact angle is below 180$^{o}$. Further evaluation of CNT for nucleation on non-flat surfaces shows that nucleation can be particularly enhanced at nanoscale topographical features [15,16] (see Section 1.3.5).

In the last two decades, a growing body of experiments and simulations have verified that surface topography is a vital component in determining how surfaces promote nucleation. Crystallisation from vapour has been shown to be highly enhanced at concave surface features[94,99,223], where a two-step condensation and freezing mechanism[72,224] allows nuclei to form with low contact angles, in some cases below saturation vapour pressure[17]. On the other hand, crystal nucleation from the melt phase has been suggested to be indifferent to the topography of a surface due to high nucleus-substrate contact angles[170]. Crystallisation from solution is anticipated to provide an intermediate but highly system-dependent case, as the interfacial energies between the solution, surface and nucleus cannot be as readily generalised as for nucleation from vapour or melt.

Calcium carbonate crystallisation has been previously shown to be enhanced at nanoscale topographical features. Additionally, where highly acute features with attractive surface chemistries are presented, amorphous calcium carbonate (ACC) can precipitate and persist for days without redissolving[20]. The iridium cracks of the FC-Ir-PDMS substrates used in this work were highly jagged (Figure 81), and a wide range of surface geometries were present with varying degrees of acuteness.

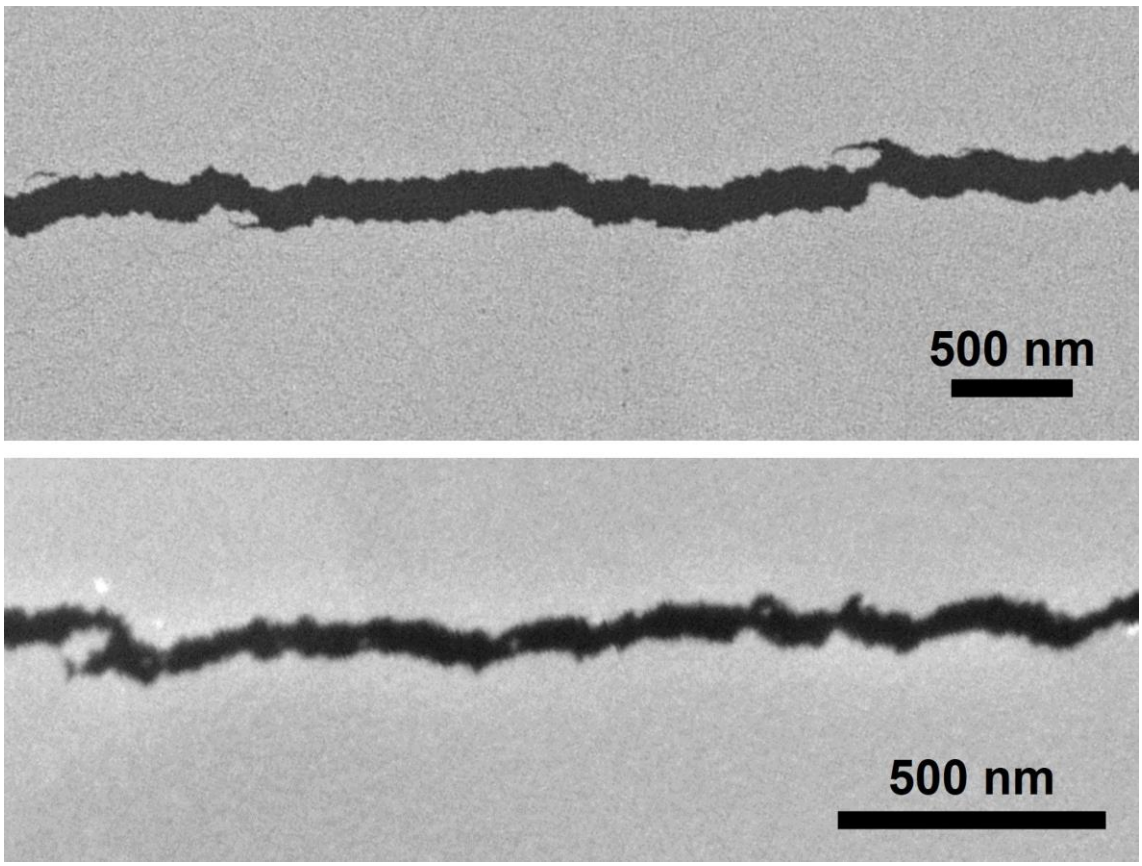


**Figure 81: SEM images showing the jagged profile of iridium cracks.**

With the variation in topography presented across the length of the cracks, there is a strong possibility that nucleation at the cracks was promoted by highly active sites where the topography improved conditions for nucleation. Experimental evidence shows that strong nucleating properties of a surface can be the result of a select few nucleation sites. Freeze/thaw cycling experiments of millimetre-sized water droplets on polished feldspar and quartz surfaces showed that nucleation occurred at a handful of sites – each associated with a pit/ surface defect[225].

### 3.3.4.2 The Role of Surface Structure and Chemistry

One key question regarding the mechanism by which the cracks enhance nucleation is whether they can promote ordering of calcium carbonate clusters (increasing the kinetic prefactor for nucleation), or by a more general mechanism where solute concentration was increased at or adjacent to the surface (increasing the thermodynamic driving force)[226]. Crystalline surfaces which

promote ordering of solids can do so via epitaxial matching, which has been shown to be a highly effective strategy for promoting nucleation[50,227–229]. For a high number density of crystals to be produced, the crystalline surface should express lots of epitaxial nucleation sites, which would be the case if the sites were formed as an intersection between low-index facets. However due to the well-defined nature of these types of features, the crystalline surface is likely to effectively nucleate only a limited number of crystals. In contrast, increase in local solute concentration as a result of charge[230], chemistry[96] or topography[89,231] can promote nucleation of a wider range of compounds[232].

The role of structural matching in promoting nucleation is first considered. When calcite is crystallised on various SAMs, structural/ epitaxial matching between calcite and the arrangement of monolayer head groups is indisputably responsible for the orientation of crystals frequently reported throughout literature[197,198,209,233,234]. However this epitaxial relationship is also often used to rationalise why calcite crystallisation is promoted on alkanethiol SAMs. Indeed an epitaxial relationship between a surface and crystal may increase nucleation rates, however evidence revealed in this work suggests that this may not always be the dominant driving force. When calcite was crystallised on the cracks, in some cases, there was no discernible orientation of calcite crystals, whilst at other times the calcite orientations were almost exclusively {012}. This orientation of calcite on 16MHDA SAMs has been previously reported[233,234], albeit using Au and Ag substrates instead of Ir. When orientation control was observed, this implied that crystals had adopted the lowest-energy configuration based on the head group geometry of the SAM, but due to the fact that orientation control was only occasionally observed, this was evidently not the driving force for nucleation. The source of this inconsistency was likely related to the uniformity of the sputter coated iridium films. As the iridium sputter target was frequently used, its performance varied over time. Some iridium films had visibly rougher grain structures, which may have affected the arrangement of a SAM at its surface.

A range of compounds nucleated abundantly at the cracks, despite the fact that it is highly unlikely for strong epitaxial matches to exist for each compound. A more clear trend in whether or not a compound would crystallise at the cracks can be established by considering the role of chemical interactions. Both barium and calcium carbonate formed selectively at the cracks but calcium, strontium

and barium sulfates did not. This suggests that compounds containing carbonate ions were more readily crystallised than those containing sulfate ions. It also suggests that the identity of the cations was of lesser importance than the identity of the anions, although a greater range should be tested to make this assertion confidently. The presence of carbonate ions for enhanced nucleation was not always necessary however, as shown by the enhanced crystallisation of ZIF-L in cracks. Glycine crystallisation was also strongly promoted, suggesting that in this case either the carboxylic acid or amine moieties were able to bind to the SAM surface. Similarly, calcium oxalate also crystallised abundantly at the cracks and contains two carboxylate groups. I therefore propose that strong interactions between ions and the surface promote nucleation, and that a structural match is not always required. It is however unclear why sulfate ions could not interact with the SAM surface as strongly as the other anions tested.

#### 3.3.4.3 Activity and Mechanism of Crystallisation at Cracks

The nucleation rate at the cracks was found to be similar to that for scratched glass. However, the localisation of crystals to cracks was nearly 100% compared with the flat areas of iridium. This meant that the key to producing such impressive numbers of crystals located in cracks lay in large differences in nucleation rates at the cracks and away from them. Equation 23 expresses nucleation rate in terms of the kinetic prefactor A, exponent B and supersaturation.

$$J = A\exp(\frac{-B}{\ln^2 S}) \qquad \textbf{Equation 23}$$

It is assumed that both regions would promote nucleation by the same mechanism, but with different values of A and B. Ideally, experiments would have been run at a variety of supersaturations and the nucleation rates measured. These experiments would have been extremely challenging to perform however, as they would have required the use of controlled flow apparatus to keep supersaturation constant throughout. If this experimental data was obtained, plotting ln(J) against $1/\ln^2 S$ would have enabled the prefactor and exponential terms to be calculated from the y intercept and gradient, and compared with other nucleants. Although these experiments were not run, the aspects of the

nucleation rate equation expected to be affected by features of the FC-Ir-PDMS are discussed nevertheless.

The exponent B is the barrier height for nucleation, and is considered first. Equation 24 expresses B in terms of the shape factor c, the molar volume v and the effective interfacial energy $\gamma_{eff}$. Equation 25 shows how $\gamma_{eff}$ is calculated from the nucleus-substrate contact angle[235], which relates to the interfacial energy between the nucleus, substrate and liquid by Young's relation (Equation 26).

$$B = \frac{4}{27} c^3 v^2 \left(\frac{\gamma_{eff}}{kT}\right)^3 \quad \textbf{Equation 24}$$

$$\gamma_{eff} = \left(\frac{(2+\cos\theta)(1-\cos\theta)^2}{4}\right)^{\frac{1}{3}} \gamma_{nl} \quad \textbf{Equation 25}$$

$$\cos\theta = \frac{\gamma_{sl} - \gamma_{ns}}{\gamma_{nl}} \quad \textbf{Equation 26}$$

To reduce B as much as possible and improve the nucleation rate, there are two options. Firstly, c can be reduced by improving the wettability of the nucleus on the substrate, either by reducing its contact angle, or by introducing an acute surface topography (as discussed in Section 1.3.5) which reduces the interfacial area between the nucleus and liquid phases. This is likely to be highly relevant at the cracks, given their jagged profile as shown in Figure 81. The exponent B can also be reduced by reducing $\gamma_{eff}$, which varies between 0 and $\gamma_{nl}$ (implying that homogeneous nucleation takes place) as θ varies between 0 and 180° [235]. To achieve this, either the nucleus-liquid interfacial energy must be reduced, or the nucleus-substrate interfacial energy must be reduced relative to the substrate-liquid interfacial energy. The latter case is interesting because it predicts that a hydrophobic surface may make an effective nucleant, as long as the nucleus-substrate interfacial energy is low enough. The water contact angle of the FC-Ir-PDMS substrates was not measured, as the cracks were both topographically and chemically non-uniform, meaning that a macroscopic measurement would not suffice. There exist techniques for measuring microscale water contact angles however[236], which would be useful to perform to determine whether hydrophobicity could play a role in the highly spatially selective crystallisation observed at the cracks.

The kinetic prefactor A at the cracks is considered next. Equation 27 expresses A in terms of the number of nucleation sites $N_s$, the Zeldovich factor Z and the attachment frequency v* [237].

$$A = N_s Z \nu^* \qquad \textbf{Equation 27}$$

Attachment of material to a nucleus is in many cases the rate-limiting step of nucleation[237], and therefore v* is where much of the potential for an effective nucleant lies. It incorporates the diffusion coefficient, along with the sticking coefficient (which describes the likelihood of successful attachment of a unit) and the molecular volume[237]. In the case of the cracks, the geometry of the features is unlikely to have significant implications for the diffusion coefficient, however the surface chemistry of the cracks likely increases the sticking coefficient by improving the chemical interactions with the surface, thereby increasing the attachment frequency.

The topography of the jagged crack may affect $N_s$ by increasing the available surface area for crystal nuclei to interact with[169]. More complex kinetic phenomena may also be relevant as a result of the surface topography, such as the increased nucleation rate at jagged features as compared to those with a smoother profile[169]. Additionally, the rate of nucleation may be dramatically increased at topographical sites which host regions of disorder in SAMs[202,203]. In terms of the molecular dynamics of the SAM, which is not a rigid entity, defects may play more of a role than previously anticipated. As proposed by Marinova *et al*., the lateral movement of nanoscale ion clusters is also hindered in defect regions[204], due to increased flexibility of the SAM molecular chains. This may positively affect the Zeldovich factor in the nucleation kinetic prefactor, as growing clusters become less likely to dissolve back into bulk solution. Additionally, with an increased flexibility, SAM head groups can better accommodate any lattice mismatch with a growing crystal nucleus, greatly reducing the substrate-nucleus interfacial energy and hence the free energy barrier to its formation. The cracks may behave as highly concentrated regions of disorder, offering much increased nucleation rates compared with the flat iridium surface. The ability of the flexible SAM chains to rearrange at defect sites may also explain why nucleation of a range of crystals with dissimilar structures was enhanced by the cracks.

### 3.3.4.4 The Role of Amorphous Calcium Carbonate (ACC)

To better understand how calcite crystallisation proceeded at the cracks, it is crucial to identify whether calcite nucleated directly at the surface or via an amorphous precursor phase. The presence or absence of ACC and its role in the crystallisation process of calcite on carboxylate SAMs is debated. Based on free-energy calculations, it has been suggested that calcite crystallises directly from solution on carboxylate SAMs without forming an amorphous precursor phase, as there is no reduction in the free energy barrier by forming an amorphous precursor[23]. Additionally, kinetics of calcite on 16MHDA SAMs have been found to compare well with classical models of a single nucleation step[238]. However, separate experimental evidence has shown that ACC can be directly observed for up to 72 hours in a gold coated crossed-cylinder geometry functionalised with a carboxylate SAM[20]. Confinement was assumed to be responsible for the stabilisation of ACC in this case. However the fact that it formed in the first place instead of calcite suggests that appreciable quantities of ACC may also form in non-confined systems. At the conditions used for crystallisation on FC-Ir-PDMS, supersaturation calculations using different mixing ratios of $CaCl_2$ and $Na_2CO_3$ showed that a small area of the crystallisation solution at the diffusion front of the highly concentrated carbonate solution may have reached supersaturation index of around 2.4. This is greater than some supersaturations at which ACC has been previously observed[239,240], and it is therefore thought to be feasible that ACC may have formed in this system.

Although no direct evidence for an ACC precursor phase was found in my experiments, unusual features at the cores of calcite crystals precipitated on cracks are consistent with its presence. By exfoliating calcite crystals and imaging their undersides with SEM, it was found that the cores of many crystals grown at cracks had voids that extended along the length of the cracks in which they had formed. These voids did not originate from a substrate templating effect, as no corresponding structures were found on the iridium surface after the crystals had been extracted. It is possible that they originated from transformation of ACC to calcite at the cracks. Aggregates of ACC particles present at the crack may have transformed rapidly to calcite at the jagged iridium crack edge, if indeed these were the nucleation sites. If the outside of the aggregate in contact with a jagged

iridium edge crystallised before the core, a volume contraction associated with the transformation process from ACC to calcite may have created the void.

The appearance of these features and proposed mechanism is remarkably similar to buried voids (Figure 82), a well-documented class of interfacial defect in the field of solar cells and semiconductors[241]. Formation of buried voids occurs when crystals nucleate away from a surface, and two crystal growth fronts reach the solid surface, trapping a region in-between[241]. If true, these data provide some evidence that the functionalised iridium was the location of the nucleation site, and that a transformation process from ACC to calcite took place around these localities.

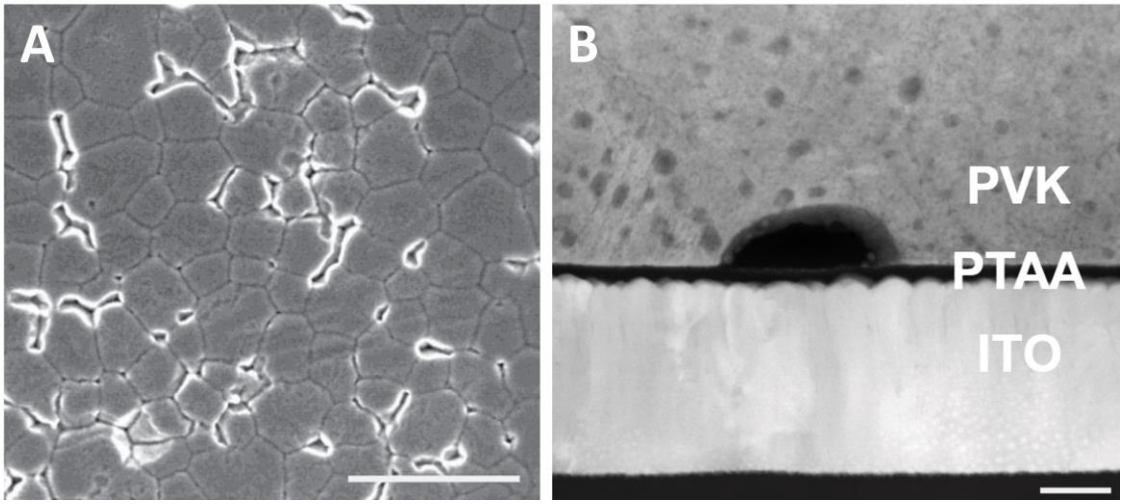


**Figure 82: (A) Top view and (B) side view of an exfoliated perovskite (PVK) film produced by Zhang and co-workers[241], showing the buried void defects formed at the interface between the film and polytriarylamine (PTAA) coated indium tin oxide (ITO).** ***Reproduced with permission from the American Association for the Advancement of Science (AAAS).***

Whilst a potential mechanism could be proposed which explained the presence of the voids, there was no direct evidence that ACC formed as a precursor to calcite. Two lamellae of calcite crystals in cracks were prepared and investigated by TEM, however these also showed no evidence of ACC having formed during the crystallisation process. The role of ACC in the crystallisation process of calcite at the cracks is therefore still not known. Notably, however, preferential nucleation at the cracks occurs for a number of systems such as $BaCO_3$, where there is no

documented amorphous precursor phase. The formation of a macroscopic amorphous precursor phase is therefore not required for crystallisation to be enhanced at the cracks.

#### 3.3.4.5 Future Work

More work should be carried out to gain insights into the role of chemical interactions on the promotion of nucleation. Measuring the protonation state of the surface would provide important mechanistic insights, and could help to rationalise the {012} orientation of calcite crystals. Accurate and representative contact angle measurements would be challenging to obtain given the heterogeneity of the surface, so a scanning probe measurement of surface charge such as scanning ion-conductance microscopy (SICM) could be used instead to investigate the surface protonation state.

Only 16MHDA was investigated in this work. Therefore, it would be interesting to explore the behaviour of other SAMs to determine whether these could enhance nucleation of different compounds, particularly if the head group chemistry was tailored to promote different chemical interactions. Using the same logic that carboxylate SAMs promote carbonate formation, perhaps sulfonic acid ($-SO_3H$) terminated SAMs would promote formation of calcium, strontium or barium sulfates.

Lastly, the presence or absence of ACC as a precursor to calcite at the cracks could not be directly verified by the experimental and analytical techniques used. Stronger evidence could be obtained by directly mixing equimolar $CaCl_2$ and $Na_2CO_3$ on the FC-Ir-PDMS substrates, then quenching them with ethanol to arrest crystallisation at various time points and imaging with SEM. Comparing these images with an analogous experiment involving $BaCO_3$ crystallisation (which has no known amorphous precursor phase) would show whether an appreciable quantity of ACC formed in the $CaCO_3$ experiment, and if so, verify that this was not present in the case of $BaCO_3$ crystallisation.

## 3.4 Conclusions

Several compounds with different compositions and crystal structures crystallised in large quantities on the cracked substrates, therefore it was evident that crystallisation was not epitaxially driven. A trend was established between crystals which were nucleated preferentially at the cracks, and those which did not. Compounds containing carbonate, carboxylic acid and imidazole groups were selectively crystallised at the cracks, whilst sulfates were not. This suggests that the promotion of crystallisation was linked to chemistry and not structural matching. That is, the chemical interactions increased local concentration at the surface, creating a solution environment that was favourable for nucleation[226]. Based on these results, it is likely that alternative functional groups would also promote nucleation at FC-Ir-PDMS cracks, in particular those which are weakly acidic.

When $Zn^{2+}$ and 2-methylimidazole were mixed, ZIF-L crystallised preferentially instead of ZIF-8, despite conditions favouring formation of the latter phase. Therefore, whilst chemistry appeared to be the dominant influence on nucleation rate at the cracks, some polymorphic selectivity is clearly achievable using the cracks. Multiple polymorphs of the same compound can also be formed however, as shown by the crystallisation of aragonite instead of calcite following addition of $Mg^{2+}$ ions.

In the case of $CaCO_3$, experimental evidence suggested that an amorphous precursor phase may have formed, though it was not directly observed. Notably, several other compounds without documented amorphous phases also preferentially crystallised at the cracks, therefore 1-step crystal nucleation could also occur in these cases.

The results presented show that the cracks were the preferred crystal nucleation sites compared to the flat iridium surface. This was thought to be a combination of the classical argument for heterogeneous nucleation of a reduction in interfacial tension, along with its ability to support a highly disordered film. Work by Aizenberg *et al*. has shown that near-right-angle topographies made by shadow masked metal deposition can support disordered SAMs which can significantly enhance nucleation rates of calcite[202,203], although these topographical features are nowhere near as atomically sharp as those which can

be created by brittle fracture. Crystallisation on SAMs assembled on highly jagged surface features has never been explored, and results show that with the right topography, these make remarkably effective and regioselective nucleants for a range of crystals.

# Chapter 4
# Patterning Functionalised Iridium Cracks to Pattern Crystallisation

## 4.1 Introduction

### 4.1.1 Overview

This chapter focused on patterning FC-Ir-PDMS cracks, and using these substrates to pattern the crystallisation of calcium carbonate. Three different methods of patterning cracks were explored: pressing the surface with a needle tip, shadow masking the iridium deposition into a series of stretchable parallel lines, and a photolithography assisted process where cracks could be induced between patterned 'nodes' by heating.

## 4.2 Methods

### 4.2.1 Forming Cracks on Ir-PDMS

#### 4.2.1.1 Cracking Ir-PDMS by Mechanical Stressing

Ir-PDMS substrates were fabricated using the procedure detailed in Section 3.2.1.5. Substrates were placed on a borosilicate glass microscope slide under observation with a Nikon Eclipse LV100ND microscope and squeezed gently with tweezers. The resulting mechanical Poisson effect produced anisotropic stress which led to formation of a series of cracks perpendicular to the edges that had been squeezed.

#### 4.2.1.2 Cracking Ir-PDMS by Air Plasma

Ir-PDMS substrates were fabricated using the procedure detailed in Section 3.2.1.5, and were placed in a plasma chamber. The plasma power was set to 200 W, the chamber pressure was allowed to reach ≈1 mbar and the air inflow rate was adjusted to 0.5 Nl/h. PDMS squares were exposed for 1 minute, after which time the chamber was ventilated, and the samples removed.

#### 4.2.1.3 Cracking Ir-PDMS by Ethanol Swelling

Ir-PDMS substrates were fabricated using the procedure detailed in Section 3.2.1.5, and were then placed in a petri dish containing ethanol for 16 hours, before gently air drying.

#### 4.2.1.4 Cracking Ir-PDMS by Heating

Ir-PDMS substrates were fabricated using the procedure described in Section 3.2.1.5, and were placed on a borosilicate glass microscope slide under observation with a Nikon Eclipse LV100ND microscope. A heat gun was held ≈70 cm from the substrates and heat was gently applied for 10-30 s until the desired degree of cracking was achieved.

### 4.2.2 Patterning Ir-PDMS Cracks

#### 4.2.2.1 Patterning Ir-PDMS Cracks – Needle Tip Pressing

Iridium-coated substrates were placed on a glass slide mounted on a Nikon Eclipse LV100ND microscope (Figure 83). A bent needle was mounted on a Sutter MP285/M-24657 micromanipulator using a custom-made steel rod attached with a Luer-lock. The micromanipulator allowed the bent needle to slowly approach the surface and press gently. Once the desired degree of cracking was achieved, the needle was retracted.

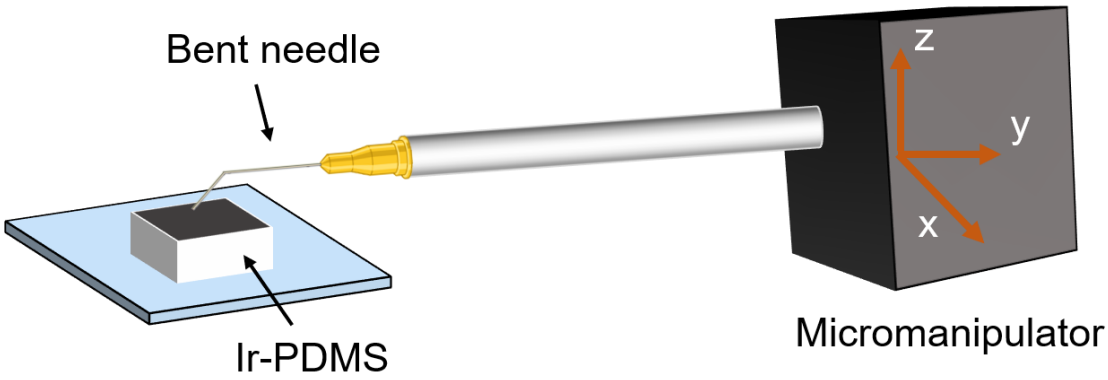


**Figure 83: Diagram showing how a needle tip was used to pattern iridium cracks.**

#### 4.2.2.2 Patterning Ir-PDMS Cracks – TEM Grid Shadow Masking

A copper TEM grid with parallel bars (G200PB-Cu, Electron Microscopy Services) was placed at the centre of the surface of plasma-treated PDMS pieces (Figure 84). These were then coated with 5 nm iridium as detailed in Section 3.2.1.5. The resulting substrates with shadow masked lines of iridium were then placed on a glass slide mounted on a Nikon Eclipse LV100ND microscope, and squeezed gently with tweezers from the edges parallel to the long axis of the lines until the desired degree of cracking was achieved. The pressure was then released.

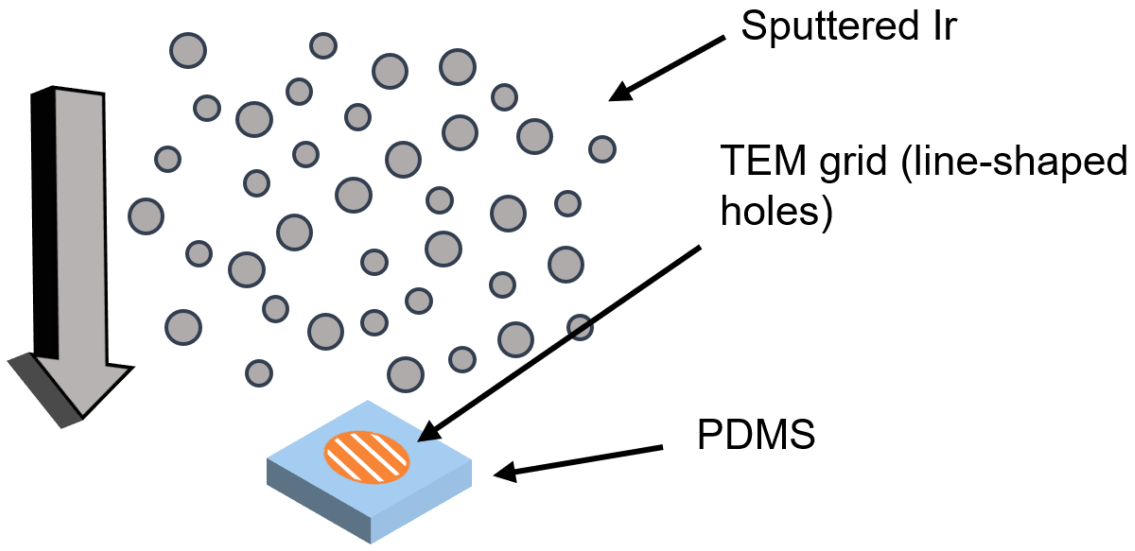


**Figure 84: Diagram showing the configuration for producing line shaped Ir films on PDMS.**

#### 4.2.2.3 Patterning Ir-PDMS Cracks – Photolithography, PDMS Moulding and Cracking

Autodesk® AutoCAD® was used to design arrays of nodes in a series of shapes. These designs were sent to Micro Lithography Services Limited to be turned into photomasks, ensuring that the patterned shapes were transparent holes for UV light to travel through in the final designs. Fabrication of SU-8 masters was performed by Dr Liam Hunter in clean-room facilities to avoid exposure to adventitious particles, which would significantly reduce the quality of the photoresist layer. 4 inch silicon wafers (100 orientation) were cleaned with acetone and isopropanol, then heated in an oven to 150 $^{o}$C for 15 minutes to remove solvent residue (Figure 85A). Wafers were mounted on a spin coater,

and a few drops of SU-8 2005 photoresist were placed in the centre. The wafer was spun at 1000 RPM for 30s, and then heated to 55 $^{o}$C on a hotplate for 30 minutes to partially cure the spin-coated film (Figure 85B). The photomask with the array design and the SU-8 coated Si wafer were both mounted in a mask aligner (Model 200, OAI). The coated Si wafer was exposed to 100 mJ cm$^{-2}$ of 365 nm UV light through the photomask (Figure 85C). After exposure, the patterned wafer was then again heated to 55 $^{o}$C for 30 minutes to enhance the UV-induced crosslinking (Figure 85D). The photoresist-covered wafer was developed by immersion in EC solvent to remove the light-masked areas of SU-8, then washed with deionised water and heated to 210 $^{o}$C to fully cure, producing the finished SU-8 master (Figure 85E). The feature height was determined to be 7 µm by Dektak XT surface profilometer.

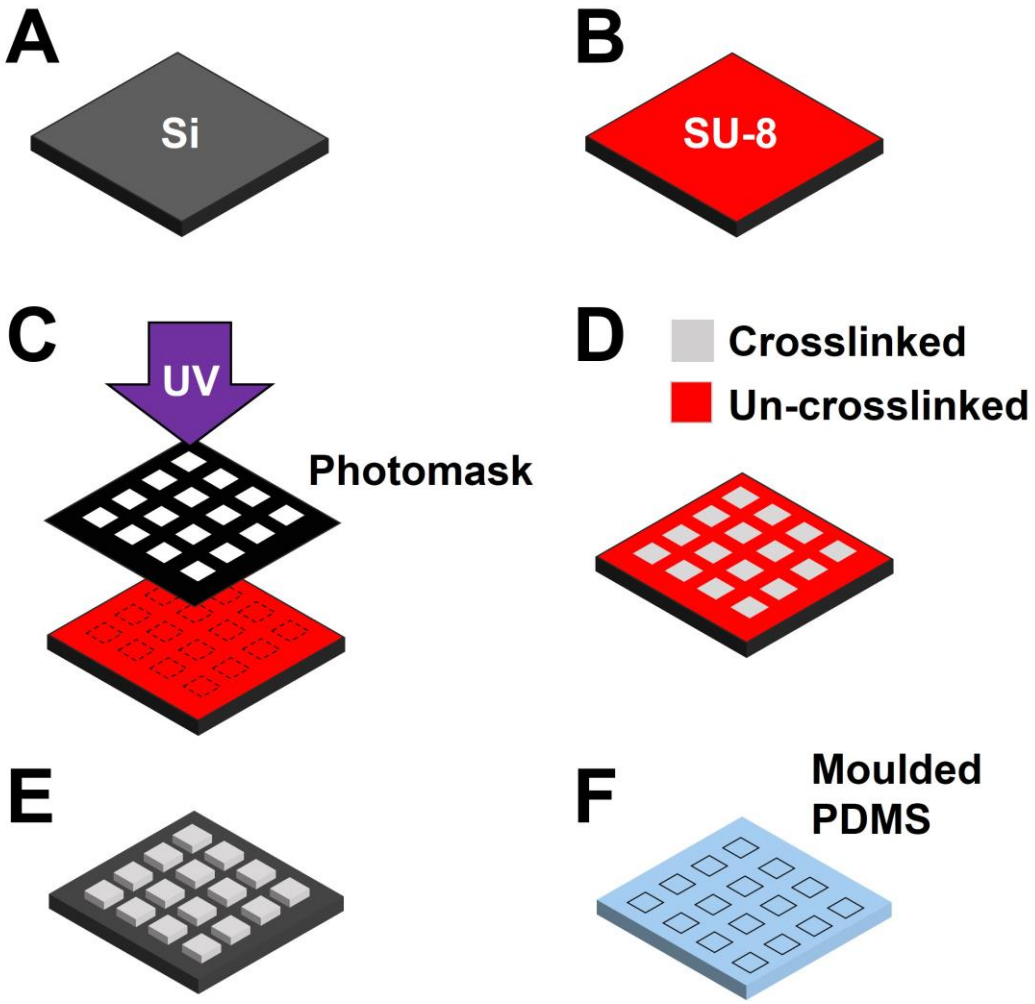


**Figure 85: Schematic showing how photolithographically patterned PDMS was fabricated. (A) A silicon wafer was cleaned. (B) The wafer was spin coated with SU-8 photoresist and heat-cured. (C) The coated wafer was regioselectively exposed to UV light through a photomask. (D) The coated wafer was baked, and now contained crosslinked UV-exposed regions and un-crosslinked masked regions. (E) The coated wafer was immersed in EC solvent to selectively remove un-crosslinked areas, producing an SU-8 master. (F) PDMS was mixed, poured, degassed, cured and peeled from the SU-8 master to produce patterned moulded PDMS.**

From this point, cleanroom facilities were no longer required. PDMS was mixed and cured on top of the SU-8 master as detailed in Section 3.2.1.1, and then cut into squares of dimensions 10 mm (W) x 10 mm (L) x 3 mm (H) with one patterned face (Figure 85F). Figure 86 shows how the patterned PDMS was bonded to a

PDMS support and prepared for iridium coating. The patterned PDMS squares were placed on a glass slide with their patterned sides facing down in the plasma cleaner, along with larger squares of PDMS with dimensions of 15 mm (W) x 15 mm (L) x 3 mm (H). The plasma power was set to 200 W, the chamber pressure was allowed to reach ~ 1 mbar and the air inflow rate was set to 0.5 Nl/h. PDMS squares were exposed for 30 seconds, after which time the chamber was ventilated, and the samples removed. The exposed faces of small squares were bonded to the top faces of large squares, which would act as supports. The supported PDMS squares were then re-exposed to air plasma on their patterned top faces using the same method, before iridium coating using the method described in Section 3.2.1.5. From this point, extreme care was taken to avoid touching the central PDMS square, only holding the supporting PDMS.

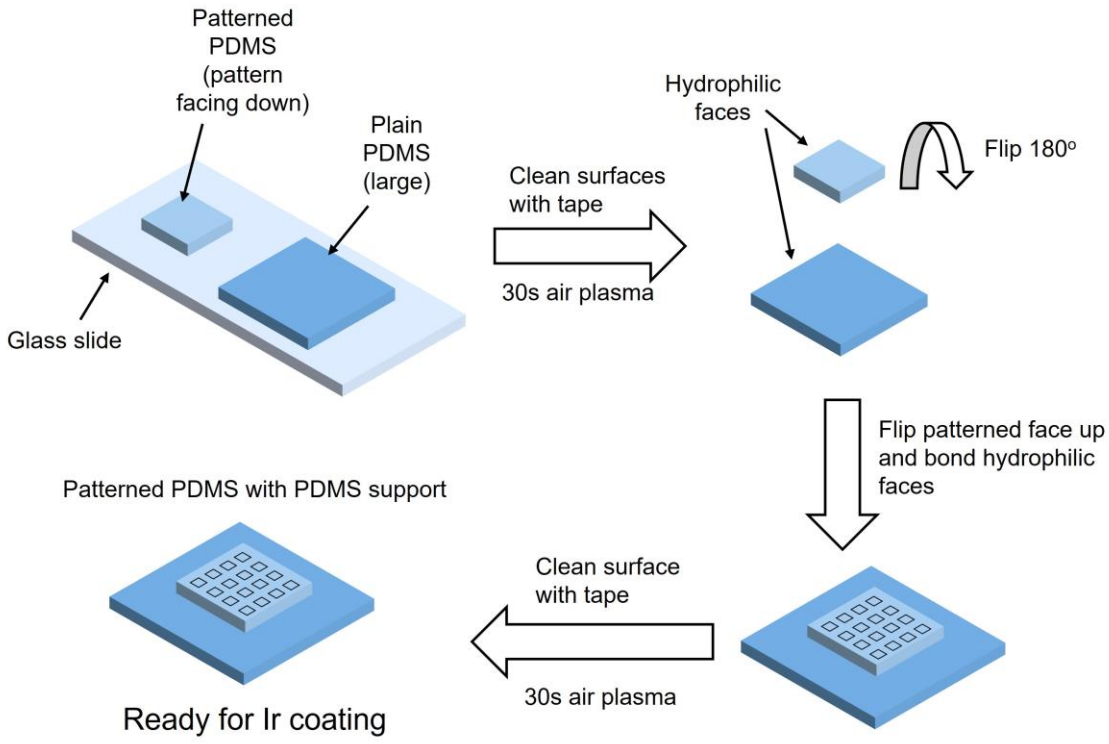


**Figure 86: Diagram detailing how to bond patterned PDMS to a PDMS support and prepare it for iridium coating.**

Iridium crack patterning was then achieved by following the procedure reported in Section 4.2.1.4.

#### 4.2.2.4 Chromium / Gold Coating

Plasma-treated PDMS substrates were prepared as detailed by Section 3.2.1.2, and placed on a glass slide without plasma bonding. Glass-supported substrates were then mounted upside-down at the top of a Cressington 308R coating system. Chromium was sputter coated from a target to a thickness of 5 nm, and then gold (99.999%, Kurt J. Lesker) was thermally deposited to a thickness of 20 nm, as determined *in-situ* by a built-in quartz crystal thickness monitor. The chamber was repressurised, the substrates were removed and were used within 1 day of coating.

### 4.2.3 16MHDA Functionalisation of Substrates with Patterned Cracks

Substrates were placed in a petri dish, ensuring that only the PDMS support was touched to avoid unintentional crack formation. Substrates with patterned cracks were immersed in an ethanolic solution of 16MHDA (5 mM, 20 mL) with one drop of acetic acid added. After 10 minutes had elapsed, substrates were gently rinsed with ethanol, then were placed in fresh ethanol. Water was slowly added to the ethanol-immersed substrates over the course of 5 minutes, occasionally draining some of the mixture, until the mixture was completely replaced with water. Substrates were kept in water for up to 1 hour until required.

### 4.2.4 Crystallisation of $CaCO_3$ on Patterned Substrates by Direct Mixing

Crystals were grown on the substrates by immersing them in an upright position in the solution, to ensure that crystals forming in solution did not fall down onto substrate surfaces. All aqueous solutions were passed through a syringe filter. $CaCO_3$ was crystallised by direct mixing of $CaCl_2$ (5 mL, 2 mM) and $Na_2CO_3$ (100 µL, 100 mM). After crystals were formed, substrates were washed gently with water, then ethanol, and then were air dried.

## 4.3 Results

### 4.3.1 Investigating Methods of Producing Cracks

Crack formation on iridium coated PDMS resulted from stress building up in the iridium film. However, there are several ways in which stress can be introduced. In this section, four different ways to introduce stress were explored – solvent-induced swelling, air plasma, thermal, and mechanical.

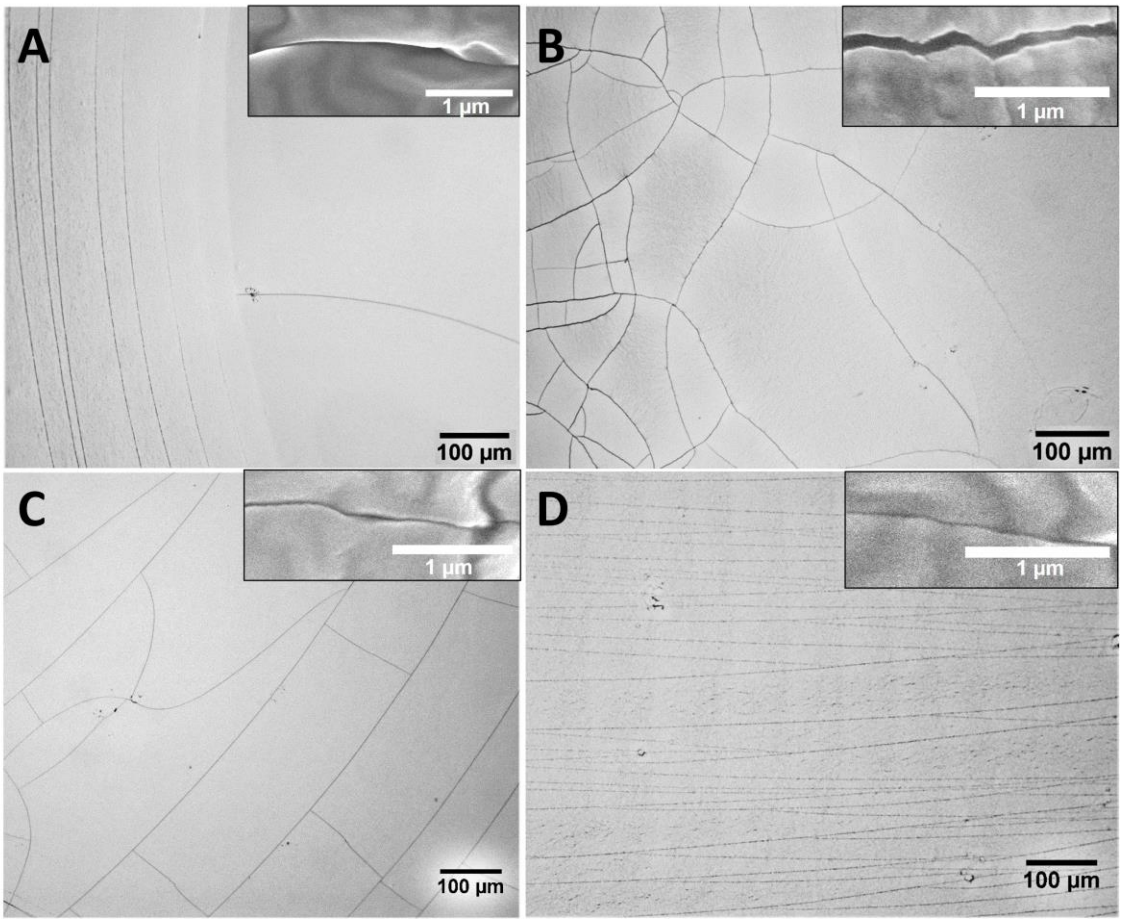


**Figure 87: OM images with inset SEM images of iridium cracks formed by (A) swelling after 18 hours immersion in ethanol, (B) 1 minute of air plasma exposure, (C) heating gently with a heat gun and (D) mechanical stress applied by squeezing.**

PDMS was sputter coated with iridium, which was initially crack-free. Solvent-induced swelling was achieved by immersing the substrate in ethanol for 18 hours, and this produced a series of concentric ring-shaped cracks around the outer edge of the substrate (Figure 87A). After 1 minute of air plasma exposure,

a random array of iridium cracks formed, where these were slightly wider than those made by other means (Figure 87B). A random array of cracks was also formed by gently heating the surface using a heat gun. It was additionally found that the degree of cracking could be easily controlled by mounting the substrate on an optical microscope stage and stopping heating at any point (Figure 87C). Lastly, mechanical stressing was achieved by squeezing the square substrate from parallel edges with tweezers, which produced an array of cracks roughly perpendicular to the edges that were squeezed (Figure 87D).

When these substrates were functionalised with 16MHDA and $CaCO_3$ was crystallised, it was found that crystals were located in all types of cracks except for those made using air plasma.

### 4.3.2 Crack Patterning

This section is focused on developing a methodology by which cracks, and hence crystals, could be patterned upon FC-Ir-PDMS. Initial experiments had showed that iridium-coated PDMS was extremely fragile, so needed to be handled carefully to avoid unintentional formation of cracks. Several procedures were explored with varying degrees of success, and are documented here.

#### 4.3.2.1 Needle Tip Pressing

Here, a needle tip was used to mechanically press the iridium surface and create localised cracks, which would in turn nucleate a large number of crystals. Ir-PDMS was prepared according to the methodology described in Section 3.2.1.5, and extreme care was taken to ensure that the iridium did not crack prior to the intentional formation of patterned cracks. Initially, the needle tip was held manually. However, it was very challenging to apply a sufficiently light pressure to the iridium surface. To improve this, a bent needle was attached to a micromanipulator, allowing for precise movement and monitoring of the process by optical microscopy. This worked very well, producing a web-shaped set of cracks surrounding the needle tip (Figure 88A), which, when functionalised, selectively crystallised $CaCO_3$ as intended (Figure 88B).

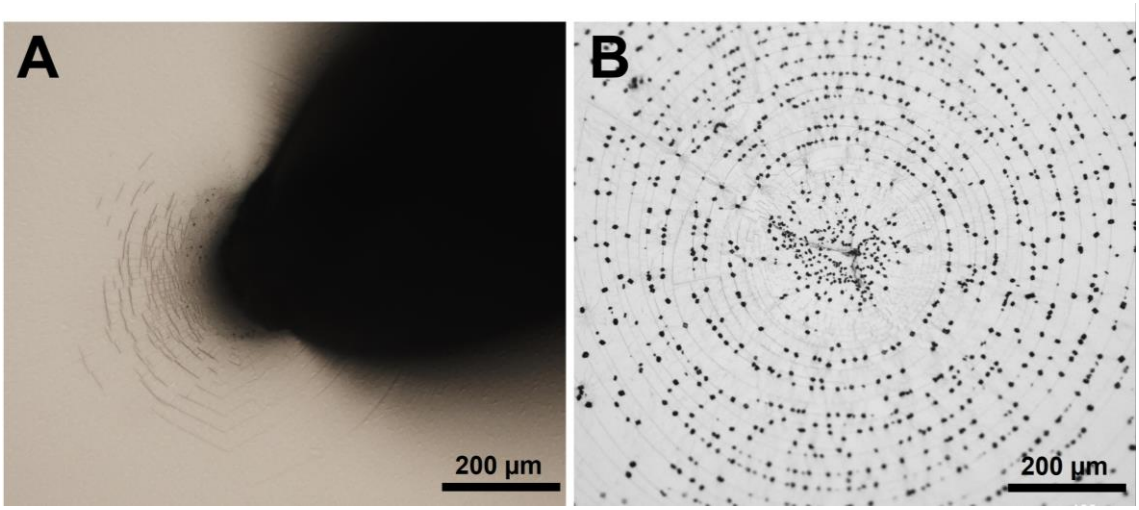


**Figure 88: (A) Schematic showing needle tip pressing was used to produce patterned iridium cracks. (B) The formation of concentric circular cracks during needle tip pressing (C) The results of crystallising $CaCO_3$ on these patterned FC-Ir-PDMS substrates.**

It was clear, however, that the needle-tip methodology was not capable of producing entirely localised cracks, as some long cracks were produced that radiated across the sample, and the degree of cracking in the central area was uncontrollable. It was also quite laborious to form cracks in this way. Whilst movement of the micromanipulator could have been controlled by a computer script to reduce the necessity for manual operation, development of a more rapid and robust methodology reliant on self-organisation processes was explored. However, these needle tip pressing experiments did succeed in proving the viability of the basic concept of patterning cracks to pattern crystallisation.

#### 4.3.2.2 Stretchable Shadow-Masked Lines

In this section, a procedure reported by Baëtens *et al*. was followed[242] and adapted to form a series of line-shaped metal films on PDMS, which could be mechanically squeezed to produce evenly-spaced cracks. The procedure also detailed how application of different amounts of stress would produce cracks of varying widths, which was attractive since it would illuminate whether there was an ideal crack width for promoting crystallisation. This involved using line-shaped transmission electron microscopy (TEM) grids as masks for metal deposition

instead of custom-made shadow masks (Figure 91). The reported methodology utilised chromium-gold films instead of iridium, and since alkanethiol SAMs form on a wide variety of noble metal surfaces, following this procedure presented a good opportunity to also study the nucleating properties of functionalised and cracked Cr-Au films.

PDMS was mixed, cured, cut into squares and plasma-treated following the same protocol used for the iridium coated samples. At this stage, the iridium sputter coating step was replaced by sputter coating of 5 nm of Cr followed by thermal evaporative deposition of 20 nm of Au. The increased malleability of these films meant that they tended to wrinkle under intrinsic and applied stress instead of cracking as did the highly brittle iridium (Figure 89A & B). This made them much easier to handle without unintentionally forming cracks than the iridium coated PDMS. Significant build of strain in caused cracks to form, which resulted in film wrinkling and the production of a smoother metal film (Figure 89C).

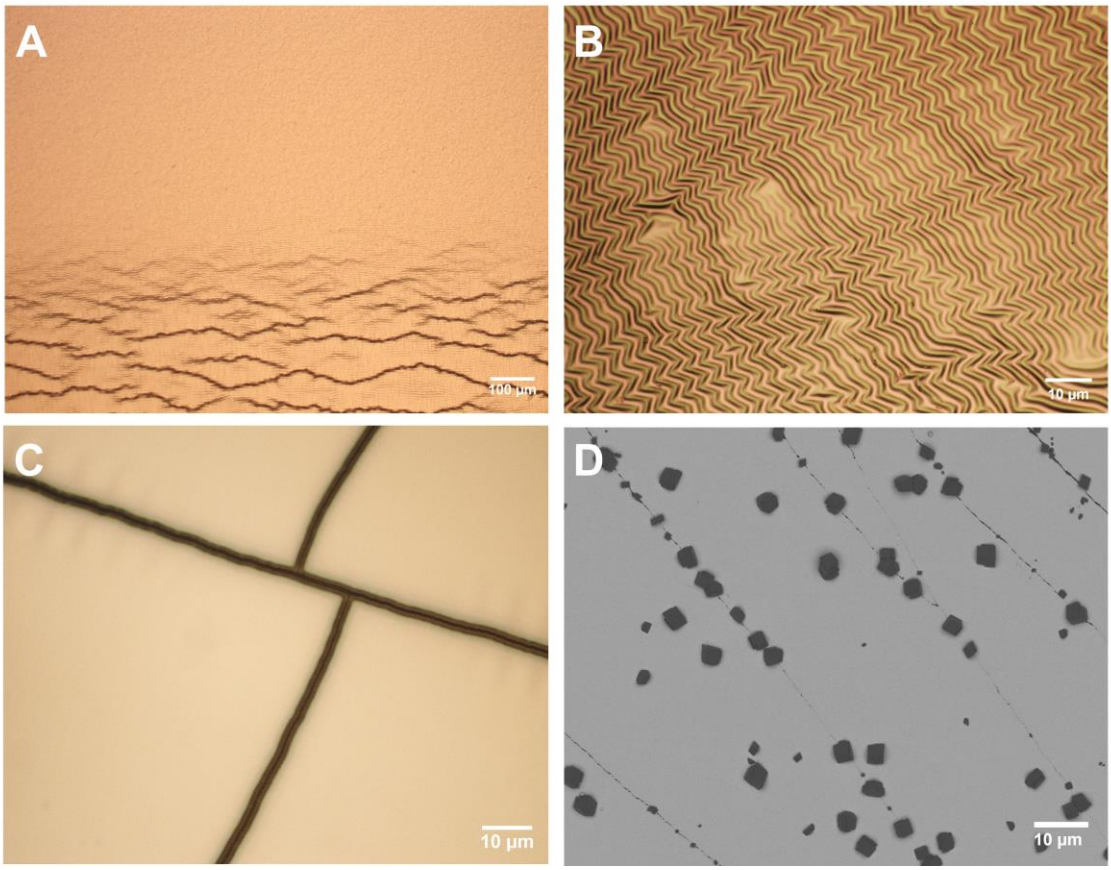


**Figure 89: (A/B) Wrinkling in as-deposited Cr/Au films as a result of intrinsic stress in the film. (C) The degree of wrinkling subsides as cracks form in the films. (D) SEM image showing $CaCO_3$ grown in 16MHDA-functionalised cracks of Cr/Au films.**

Crystallisation in the cracks was occasionally successful upon Cr-Au films, however the results were less impressive than for Ir films (Figure 89D). Often, many crystals formed on the uncracked regions of the film, and due to wide variation in the quality of the deposited Cr and Au, a plethora of issues such as film delamination and film disintegration were encountered often (Figure 90).

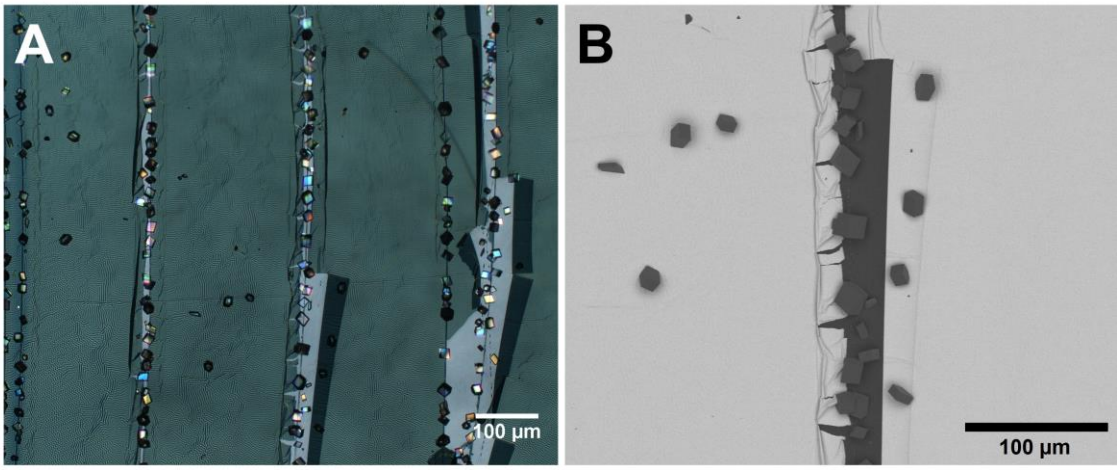


**Figure 90: (A) Cross-polarised light microscopy and (B) SEM images showing delaminating chromium/gold following water and ethanol washing after $CaCO_3$ was crystallised.**

Despite the mixed results, the shadow-masking procedure reported by Baëtens was followed[242] (Figure 91).

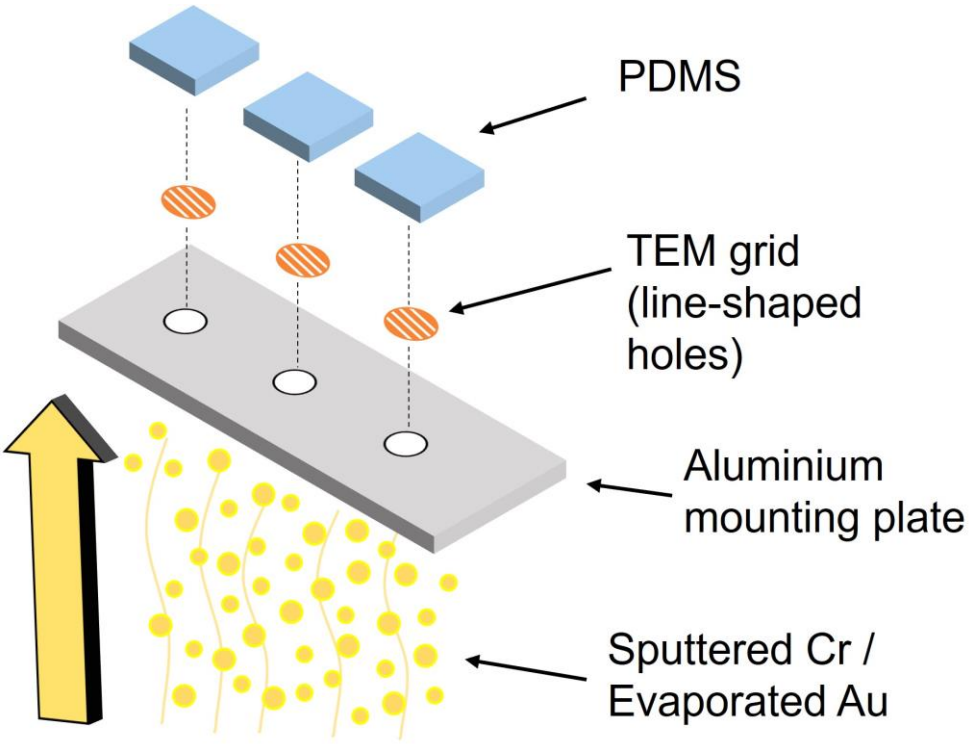


**Figure 91: Schematic showing the adapted procedure for depositing line-shaped Cr/Au films on PDMS**

After Cr-Au was evaporated through the TEM grid masks, many of the samples were heavily wrinkled and suffered delamination. However, some were of sufficient quality to process further (Figure 92A & B). These samples were squeezed gently with tweezers from the edges parallel to the long axes of the deposited lines, which produced a series of cracks perpendicular to the long axis of the films (Figure 92C). When these substrates were functionalised and $CaCO_3$ was crystallised, many crystals formed in the cracks. However a large number of crystals were located away from the cracks (Figure 92D).

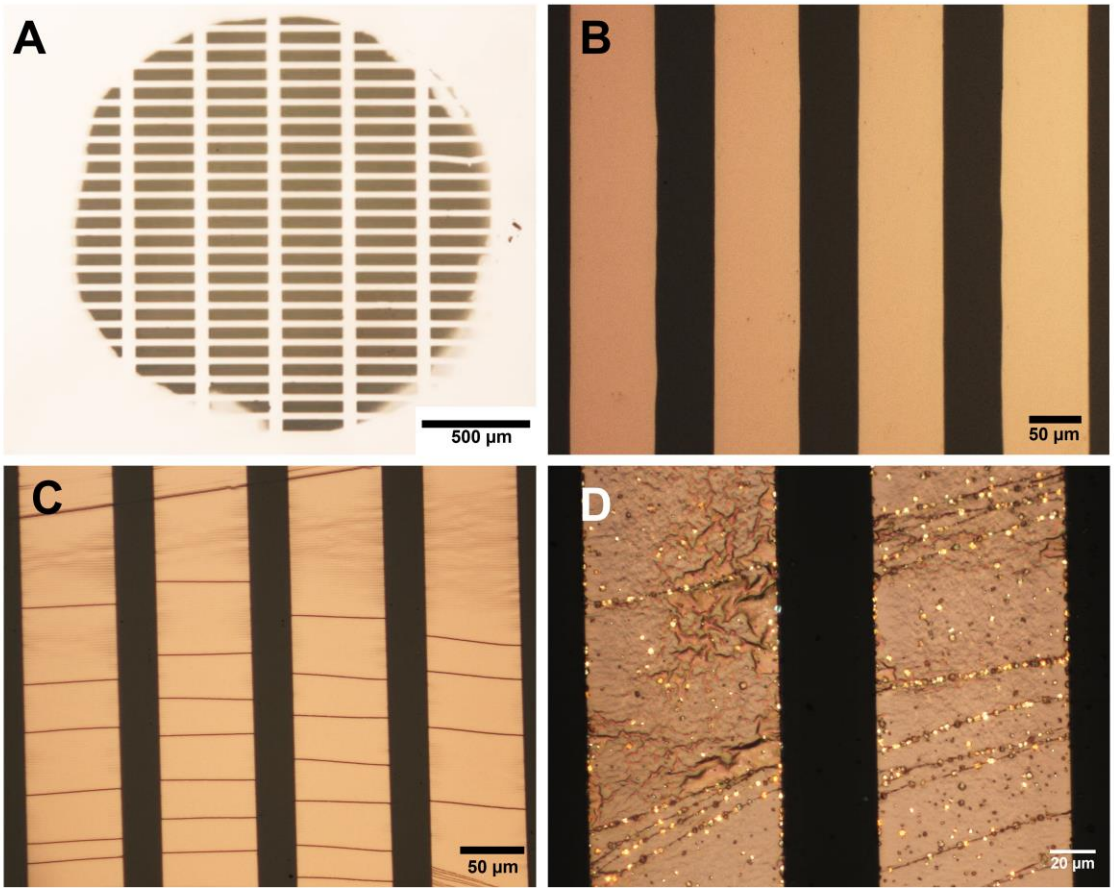


**Figure 92: (A/B) As-deposited crack-free lines of Cr/Au films. (C) Cracks formed by mechanically squeezing the substrates. (D) Cross-polarised optical microscopy image showing $CaCO_3$ crystallised on these substrates after functionalisation with 16MHDA.**

This procedure was also adapted to produce iridium-coated samples by sputter coating. This produced a set of line-shaped Ir films on the PDMS substrates

(Figure 93A). As before, squeezing the substrates to apply Poisson effect-induced stress on the patterned iridium lines produced cracks perpendicular to the long axis of the lines (Figure 93B). When these substrates were functionalised with 16MHDA and $CaCO_3$ was crystallised, crystallisation selectively occurred at the patterned cracks (Figure 93C & D). This suggests that either the iridium cracks were more effective nucleants, or that the flat iridium surface away from the cracks was a poorer nucleant than the flat gold surface.

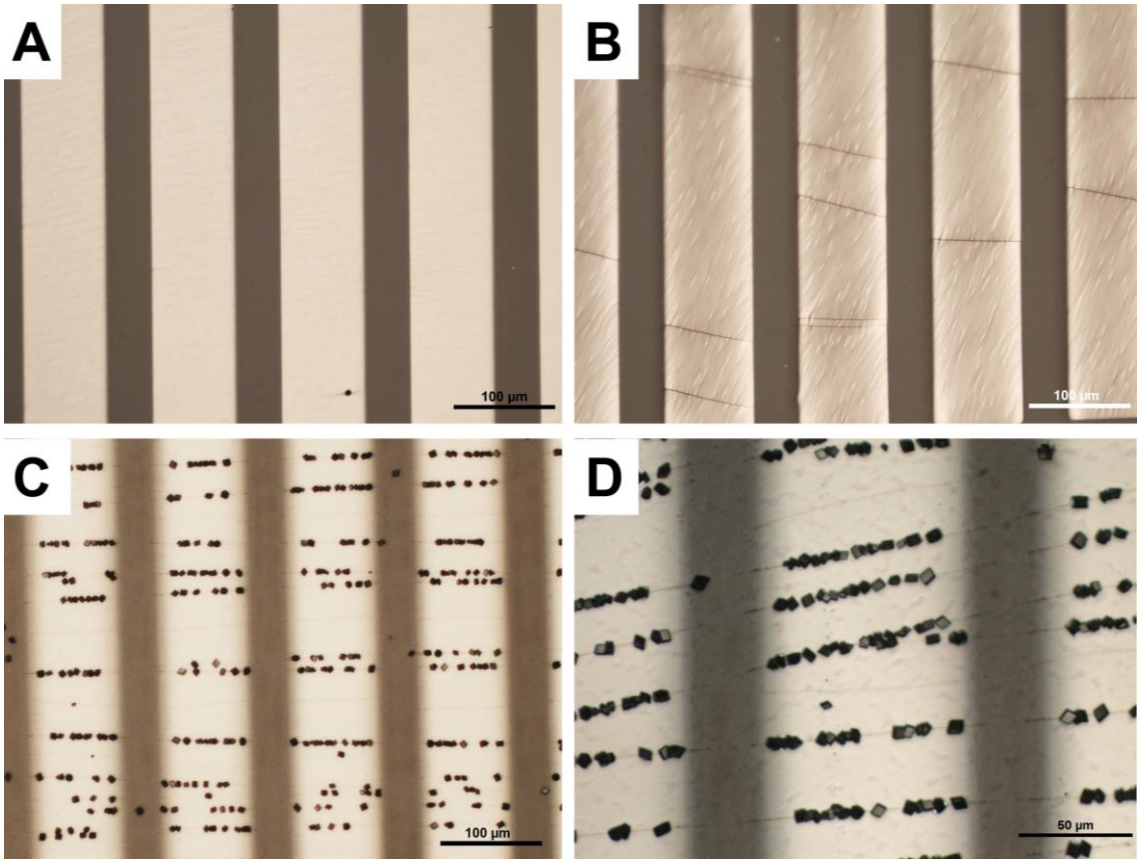


**Figure 93: (A) OM images of line-masked sputter-coated iridium films (B) under mechanical strain, causing cracks to form. (C/D) $CaCO_3$ grown on the shadow mask patterned FC-Ir-PDMS.**

As a final point of note from a separate experiment, it was found that line-masked Cr/Au films deposited on a pristine Si wafer produced an effect very similar to that reported by Aizenberg and co-workers[202]; increased $CaCO_3$ nucleation occurred on just one edge of the metal film. This was likely due to the way that Au was thermally evaporated through the small aperture of the TEM grids (Figure 91). Au evaporative deposition is typically carried out at pressures of $10^{-6}$ – $10^{-7}$ mbar,

where its mean free path is in the order of tens of metres. Without collisions to change the trajectory of the gaseous gold, its flight through the chamber is highly directional. Off-centred samples therefore experienced a shadowing effect from the TEM grids, where one edge received a thicker layer of metal than the other. This generates one edge with a smoother topography (bottom edge shown in Figure 94) and the other with a much sharper topography (top edge). Once functionalised with 16MHDA, the difference in topographies resulted in marked differences in the numbers of crystals at the two edge types in the Au film.

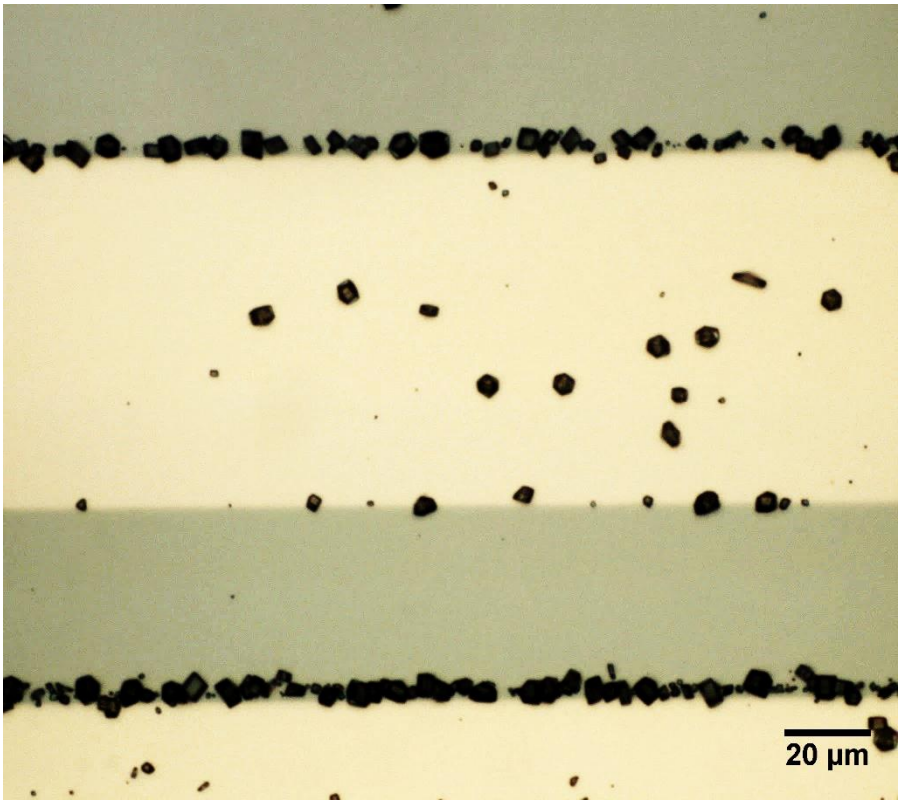


**Figure 94: OM image showing $CaCO_3$ crystals grown on a 16MHDA functionalised shadow masked Cr/Au film on a Si wafer. Selective crystallisation at one edge results from the more acute topography at this region as a result of the TEM grid shadow mask being off-centre from the evaporation source.**

Whilst some success was achieved using this method with iridium films, there was little control over how many cracks formed, or where exactly along the metal film the cracks would form. An alternative, more controllable methodology was

therefore sought that would give greater control over the metal film cracking process.

#### 4.3.2.3 Photolithographic Patterning for Crack Patterning

A series of experiments was performed that patterned the PDMS substrates using photolithographic methods prior to metal deposition as a means of directing crack propagation through structural weak points, termed ‘active nodes’. This was inspired by a publication by Kim and co-workers[243], where photolithographic patterning of sharp features into SU-8 substrates meant that the isotropic strain caused by swelling these substrates in solvent caused cracks to form between these active nodes (Figure 95).

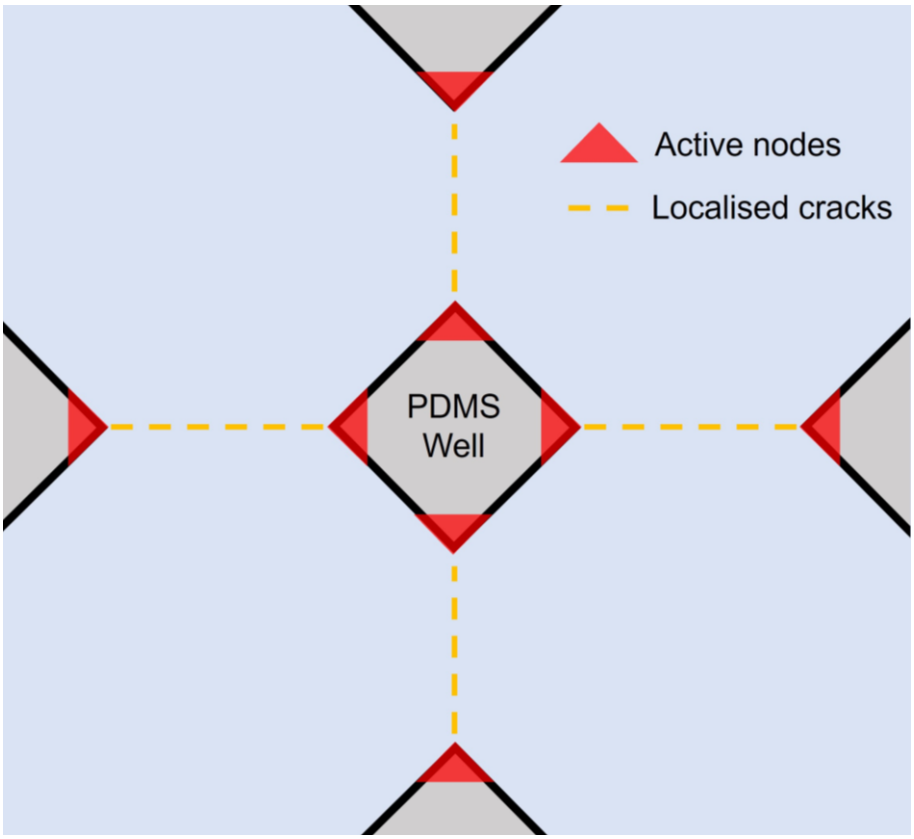


**Figure 95: Diagram showing how PDMS wells could be fabricated with ‘active nodes’, to produce localised cracks when stress was applied, inspired by work by Kim *et al*.** [243]**.**

The method reported by Kim *et al*. required use of cleanroom facilities for photolithography processing to make each substrate[243]. The method was

therefore adapted here to create a single SU-8 master mould from which patterned PDMS could be repeatedly cast. This meant that the expensive and labour intensive cleanroom fabrication steps only needed to be performed once.

Several different designs were created using Autodesk® AutoCAD®, and sent to Micro Lithography Services Limited for photomask fabrication. SU-8 coated Si wafers were used to create moulds with height 7.5 µm (Figure 96). Several variations of the same designs were produced to determine optimal feature shapes and spacings.

PDMS was cast onto these SU-8 moulds, and once cured and peeled away, it was plasma bonded to an underlying support. This mechanical support could be held by tweezers instead of the crack-prone surface, which was necessary to protect it from unintentional crack formation. This was initially a small piece of clean glass, however glass was later substituted for a PDMS support (Figure 86), reasons for which are discussed later in this section.

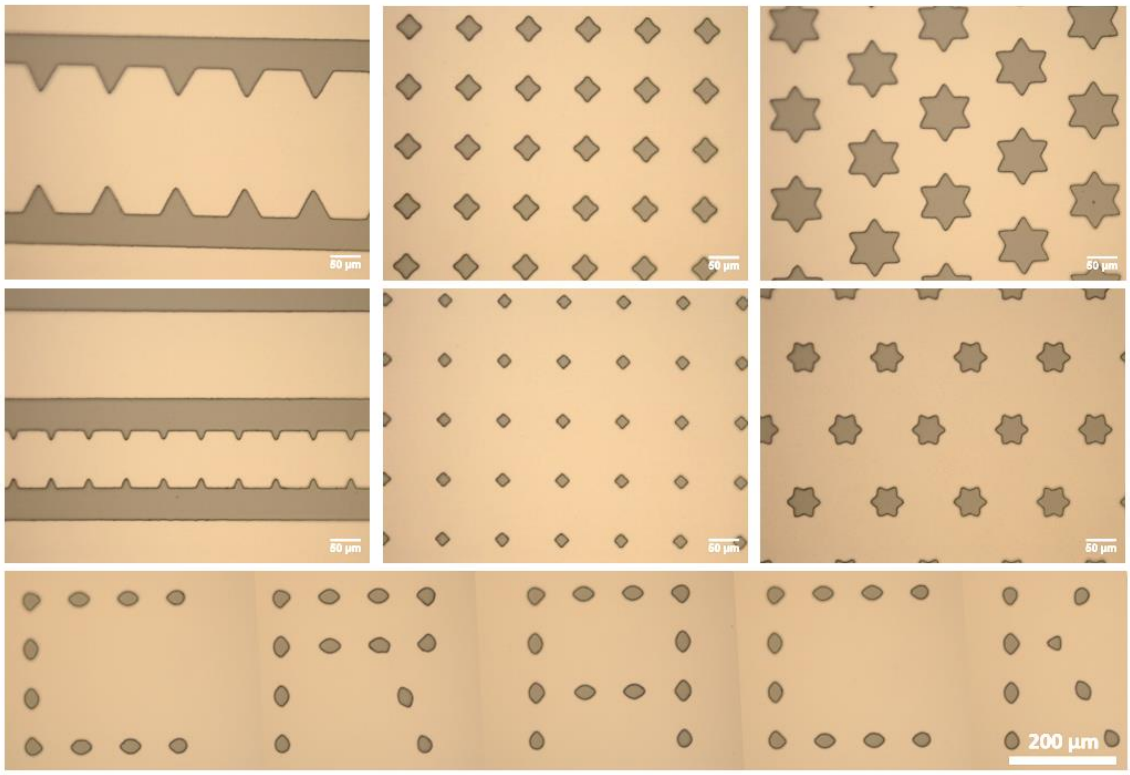


**Figure 96: Photolithographically-patterned SU-8 moulds used for patterning PDMS. Dark patches indicate raised features intended to become wells in the finished PDMS.**

Whilst Kim *et al*. had only investigated swelling-induced crack formation in their work[243], heating was also explored here to induce cracking of the iridium coated patterned substrates, and offered more control over the degree of cracking. A set of 'teeth' designs with varying dimensions was used to optimise the feature spacings (Figure 98). The crucial dimensions varied were distance between active nodes *D*, lateral spacing between nodes *S* and node height *H*.

This set of experiments showed that the cracks failed to propagate in a straight line and would sometimes travel to adjacent nodes or cracks if the spacing between active nodes was too large (Figure 98). A spacing that was too small would require larger amounts of applied strain, and would produce a smaller crack that would host fewer crystals. Only some of the expected cracks formed if the nodes were too close together, and curved cracks formed if nodes were too small as insufficient directional strain was generated. Of the dimensions tested, it was found that the ideal node height was 45 µm, the ideal spacing was 115 µm and the ideal spacing between nodes was 105 µm.

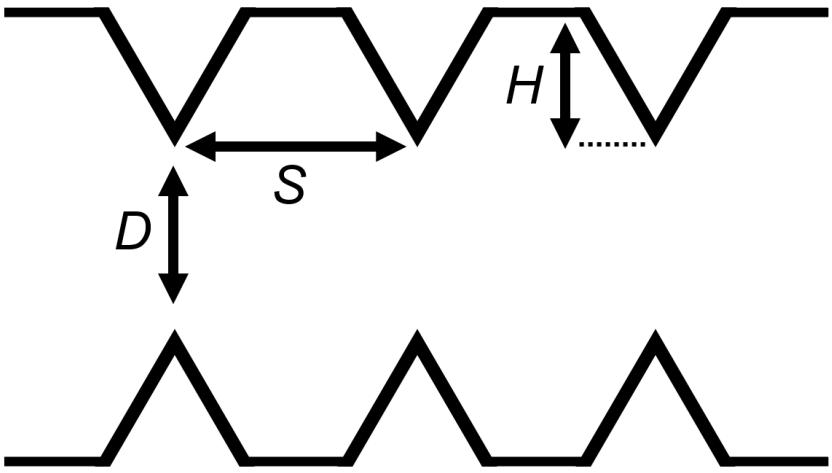


**Figure 97: Diagram showing crucial dimensions of the 'teeth' designs for crack patterning optimisation.**

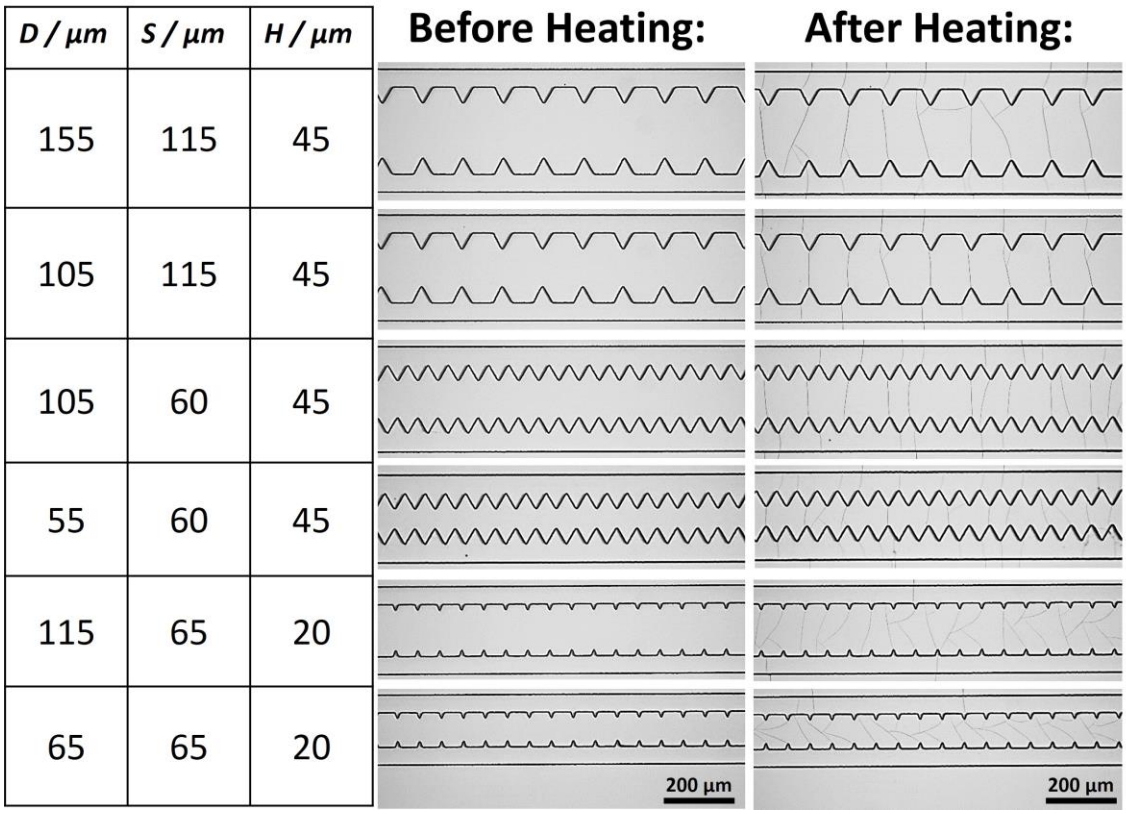


**Figure 98: 'Teeth' patterns with varying dimensions, fabricated by curing PDMS on lithographically-prepared SU-8 templates. Images both before and after heat-induced cracking are shown**

A few of the designs were found to be unsuitable as the desired cracks did not form consistently, even after optimisation of feature size and spacing (Figure 99). Both the small and large square array designs consistently produced arrays of patterned cracks upon heating (Figure 100), and so were investigated further.

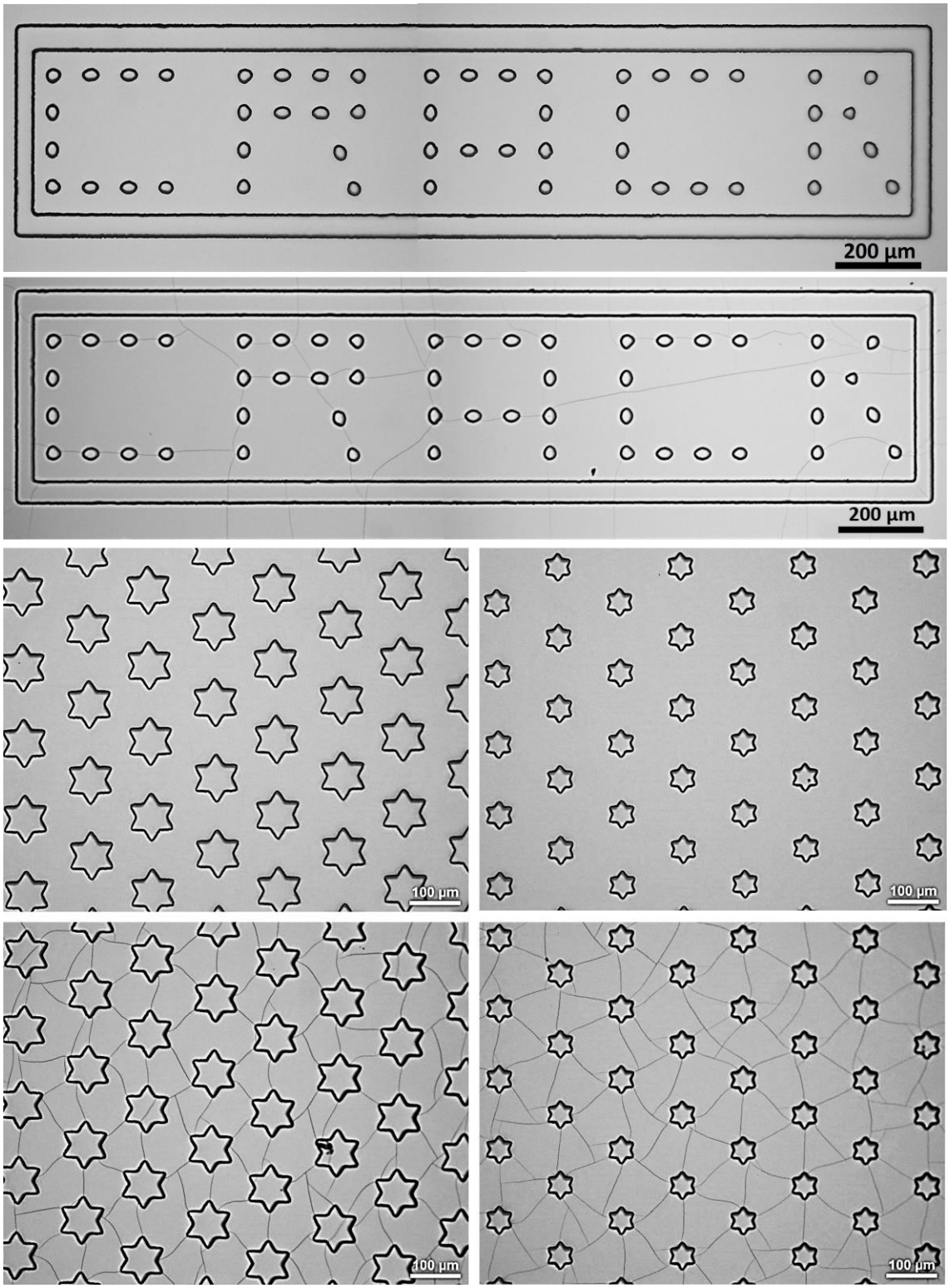


**Figure 99: Poor crack patterning results were achieved using text-based and hexagonal array designs.**

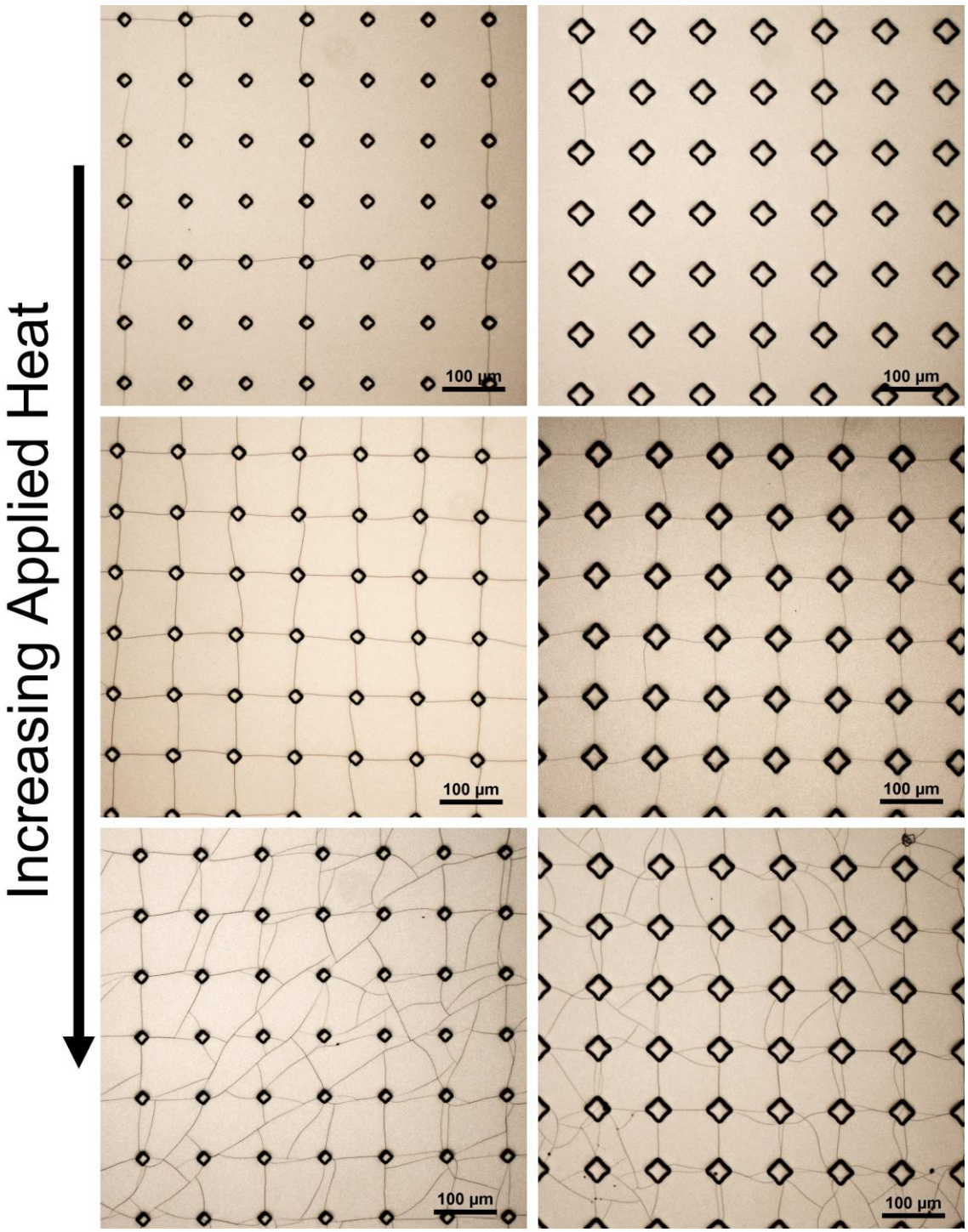


**Figure 100: Small and large square arrays after too little (~5-10 s), too much (~30-60 s), and the perfect amount of heat (~10-30 s) applied by a heat gun.**

Crystallisation of calcium carbonate on samples with patterned cracks resulted in the formation of very few crystals anywhere on the surface (Figure 101). This was due to a combination of two overlooked aspects of the experimental setup. Firstly, stress resulting from rapid de-swelling as a result of the water washing step

resulted in the formation of additional cracks in interstitial regions of the original array of cracks. These could be avoided if water was gradually added to ethanol-submerged substrates over the course of 5 minutes, until the mixture became entirely water.

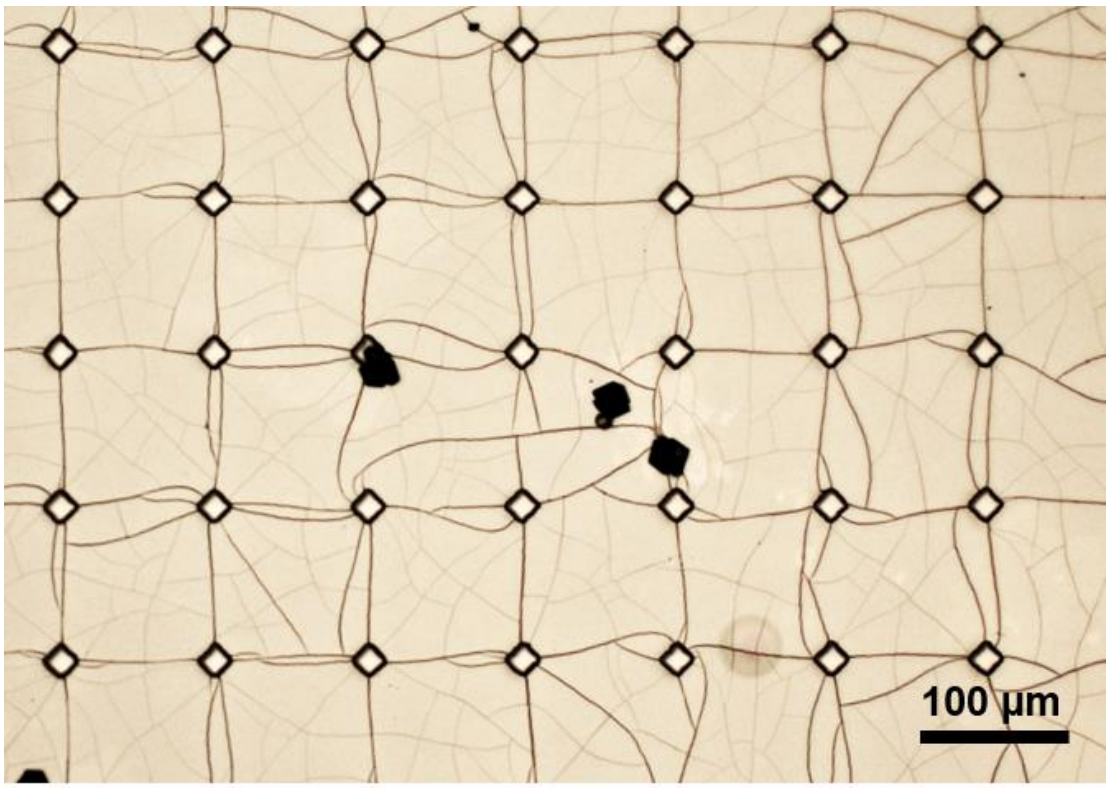


**Figure 101: Initial results from attempting to crystallise $CaCO_3$ on 16MHDA-functionalised patterned iridium cracks.**

Once unintentional crack formation was eliminated, crystals preferentially formed in the patterned cracks (Figure 102A). However, the number density of crystals was low as many $CaCO_3$ crystals formed on the glass supports, which reduced nucleation on the FC-Ir-PDMS cracks. To overcome this, a PDMS sheet was used as a support instead of glass, due to its much weaker activity as a nucleant for $CaCO_3$. With a robust protocol established, many $CaCO_3$ crystals could now be produced on patterned cracks (Figure 102B).

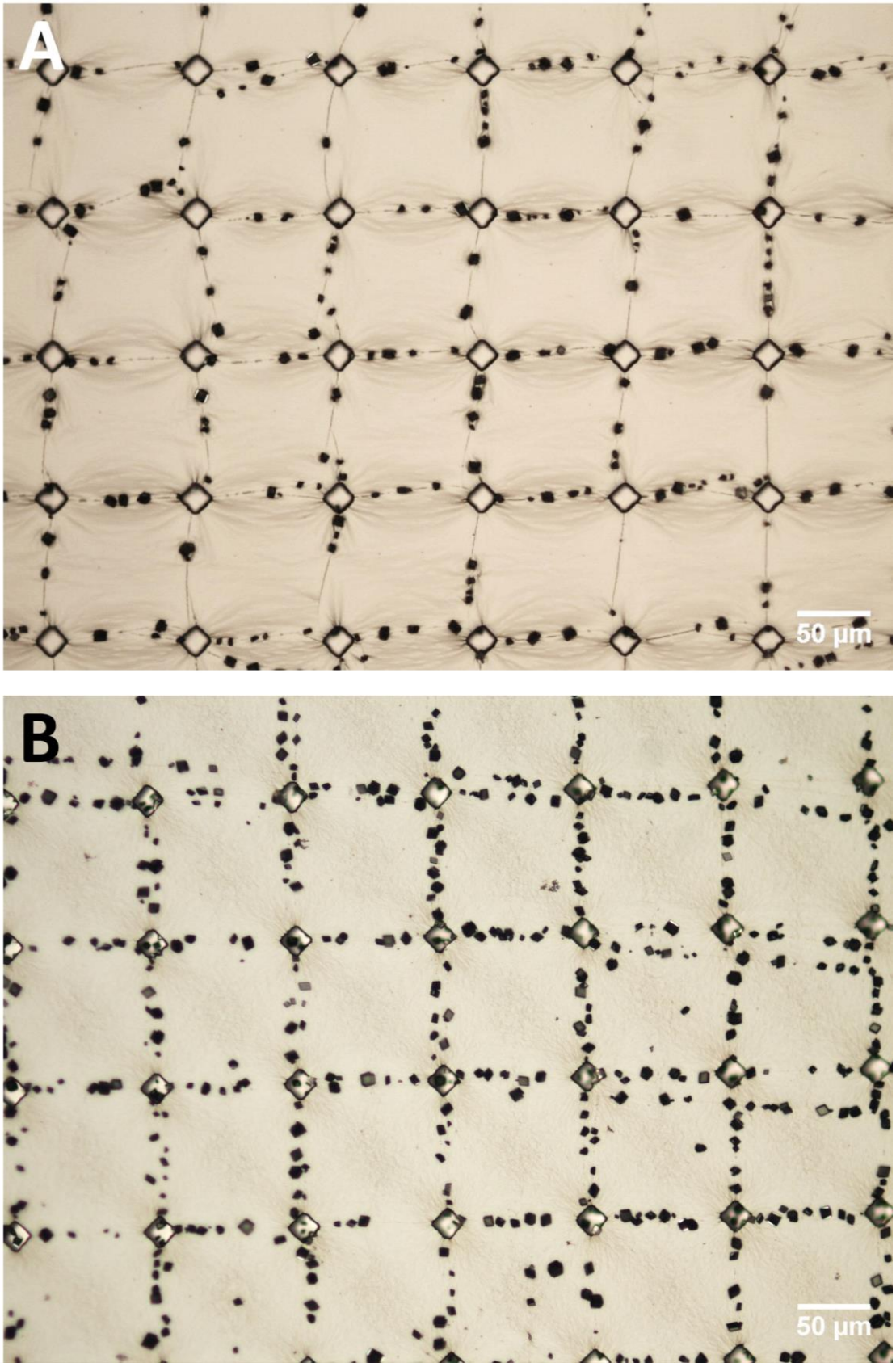


**Figure 102: Crystallisation on functionalised patterned cracks (A) with glass supports and (B) with PDMS supports.**

## 4.4 Discussion

Solvent-induced swelling, heating and mechanical squeezing all produced cracks that could selectively crystallise calcium carbonate. However, cracks made using air plasma were inactive. This was thought to be due to formation of an iridium oxide film which does not support the formation of high quality SAMs.[244] In general, cracks made by mechanical stress (needle tip pressing and shadow-masked lines) were effective as nucleants for $CaCO_3$, but it was very difficult to control the degree or locations of cracking. This was because the degree of stress in the iridium film (and therefore cracking) was highest near the point of contact (i.e. the needle tip or tweezers), and diminished away from this point. Greater control was achieved by photolithographically patterning the PDMS, coating it with iridium, and inducing cracks by heating.

Interestingly, the selectivity for calcium carbonate crystallisation on the functionalised iridium cracks was far higher than on functionalised chromium/gold films. This could be a result of two different features of the surfaces. Firstly, gold is much more ductile than iridium, which may cause it to rip rather than crack under applied stress. The topography of the rips may have been less sharp than cracks. Secondly, gold films may have been more effective nucleants than iridium films, which would explain why many crystals were located away from cracks. In the future, AFM could be used to assess whether there are substantial differences between the topographies that arise when iridium fractures under tensile stress, compared to chromium/gold films.

## 4.5 Conclusions

Three methods were explored for patterning crystallisation by patterning cracks on FC-Ir-PDMS – needle tip pressing, stretchable shadow-masked lines, and photolithographic patterning. The latter offered the greatest degree of control over crack formation and hence the localisation of crystallisation, because it relied on thermal expansion, which was more controllable and isotropic than mechanical means of forming cracks. These results show that the apparent randomness of crack formation can be harnessed to create localised surface topographies, which decides where crystallisation is promoted on a surface.

# Chapter 5

# Investigation of the Universality of Hair as a Nucleant

## 5.1 Introduction

### 5.1.1 Overview

The work described here investigates why hair is such an excellent crystal nucleant, and explores the physicochemical properties which are responsible for this phenomenon. A variety of hairs from different animals were tested as nucleants, however dog and human hair were principally studied. The efficacy of hair for nucleating protein and ice has already been demonstrated[245–247], however until this point there has been no evidence to suggest that hair is effective at crystallising minerals. A range of minerals were therefore crystallised on the hair samples, with quantitative assessment of the nucleation of potassium nitrate and calcium carbonate. $KNO_3$ and calcium carbonate were selected for their natural abundance, contrasting solubilities and contrasting growth rates. Hairs were treated with either water, ethanol, petroleum ether or $H_2O_2$, which allowed for variations in charge, chemistry, and topography to be measured and correlated with nucleating properties.

Crystallisation of $KNO_3$ on dog and human hairs was studied first using a novel microdroplet-based methodology, which allowed for kinetics of nucleation on both hair and glass to be semi-quantitatively compared, as glass has been previously identified as a 'universal nucleant'[232]. Results from the $KNO_3$ microdroplet experiments also revealed insights into the importance of scattered nucleation sites on the hair surface for promoting nucleation.

Next, calcium carbonate was crystallised on dog and human hairs following the same set of chemical treatments. Here, both hair type and chemical treatment were found to strongly impact the promotion of crystallisation. Notably, dog hair washed with ethanol was identified as an incredibly active nucleant for calcium carbonate. The large numbers of calcite crystals formed on the hairs allowed for their locations to be assessed, which was aided by exfoliating crystals from the hairs using resin. After analysing the exfoliated crystals, the cuticle edges of hair were found to strongly promote nucleation.

XPS was then used to characterise the chemistry of the hair surfaces following chemical treatments, which revealed that the as-acquired human hair was already damaged prior to chemical treatments. There was no detectable oxidation of the surface of dog hair, implying that the protein state was an important factor to consider for rationalising the activity of the hairs. SICM was used to produce a surface charge/topography map, showing how the surface charge and chemistry varied across the outer surface of the hair.

After identifying that ethanol-treated dog hair was the most active towards calcium carbonate, a variety of sparingly soluble minerals were crystallised on these hairs to determine whether there were specific chemistries of crystals which were abundantly nucleated by hair. Lastly, a variety of other animal hairs were tested for their efficacy as nucleants towards calcium carbonate, including mole, bat, elk, squirrel, camel and mink. Surprisingly, each hair type promoted calcium carbonate nucleation to a different extent, and mink hair was even able to crystallise a metastable polymorph.

## 5.1.2 Background

### 5.1.2.1 Universal Nucleants

Heterogeneous nucleation can occur many orders of magnitude faster than homogeneous nucleation under the same solution conditions[85], and concomitantly the critical nucleus can be reduced in size from several hundred molecules down to several molecules[248]. This allows for high-quality single crystals to be grown from slightly-supersaturated conditions in the presence of nucleants, where otherwise higher supersaturations would be needed to induce nucleation, reducing the quality of the crystals. Nucleants can also give control over polymorphism[172,173] by reducing the energy barrier for one polymorph over another. Identifying effective crystal nucleants is not easily achieved, however. Whilst epitaxial nucleants are often effective and their activities are well-understood[153,154,227,249], there are some surfaces that have epitaxial relationships to a crystal and yet are poor nucleants, such as is the case with $BaF_2$ and ice [57]. Likewise, there are many nucleants that do not have a structural relationship with a crystal they are effective at nucleating, such as is the case with steroids and

ice[58,59]. Identifying effective crystal nucleants therefore often requires trial and error and thus lengthy and costly screening experiments.

Universal nucleants can allow scientists to skip this step entirely. The rationale behind their functionality relies on two fundamental properties – surface activity, and non-uniformity. Considering the former firstly, there should be strong interactions between a nucleant surface and the crystals it nucleates, and these are dictated by the nucleant surface chemistry and charge. As for the latter, non-uniformity is simply the range of surface chemistries, charges and topographies expressed by a surface. This increases the variety of nucleation sites expressed by the surface, increasing the chance that a highly active nucleation site is present. Surfaces with small numbers of highly active nucleation sites are more effective as nucleants than well-defined surfaces with an abundance of moderately-active nucleation sites. Importantly, the surface sites of a non-uniform nucleant that are highly active towards one crystal system are not expected to be the same set of sites which are active towards another crystal system  Hence, a less-uniform surface is typically capable of nucleating a wide range of crystals.

Chayen and co-workers demonstrated how the topographical non-uniformity of porous glass enables them to nucleate a range of proteins [89,231,232,250,251]. Porous media are effective at immobilising proteins, allowing high concentrations to accumulate within them, leading to crystallisation. The wide range of pore sizes available also increases their activity, allowing them to nucleate proteins with varying sizes and structures.

#### 5.1.2.2 Crystal Nucleants of Biological Origin

Nucleants of biological origin often perform better than nucleants of mineral or synthetic origins. One particularly effective example is Snomax™, a bacteria-derived additive used commercially to generate artificial snow[252]. This can nucleate ice at -2 °C[253], which is even higher than the widely-used cloud-seeding agent silver iodide, which nucleates ice at -4 °C [56]. Fungal spores, lichen and pollen are also highly active ice nucleants[254].

Historically, various types of animal hair have been used to induce protein crystallization in streak-seeding experiments, where the retention of existing microseeds on the complex hair surface is used to initiate crystal growth[247]. It

was later demonstrated that hair can also be an excellent nucleant[255,256] and could be incorporated into high-throughput screening trials of protein crystallization[257,258] (see Figure 103). Hair was used by Ukichiro Nakaya to nucleate the first artificial snowflakes ever made[245]. Reportedly, one day after three years of failed nucleation experiments using cotton and wool thread, he noticed a snowflake at the tip of a rabbit fur coat, which he later replicated in controlled conditions. As the influence of modification on hair has high commercial and societal value, a large amount of knowledge has been generated for how different treatments affect the surface chemistry, hydrophobicity, surface charge, and topographical structure of hair, all properties relevant for nucleation[259–261]. Hair is therefore an exciting biomaterial to study as a nucleant, but its properties have only been explored for a limited number of compounds. Georgieva and co-workers have performed the most in-depth study of the nucleating properties of hair to date, and showed that the nucleating properties are sensitive to harsh chemical treatment with NaOH and are uneven across the surface[262].

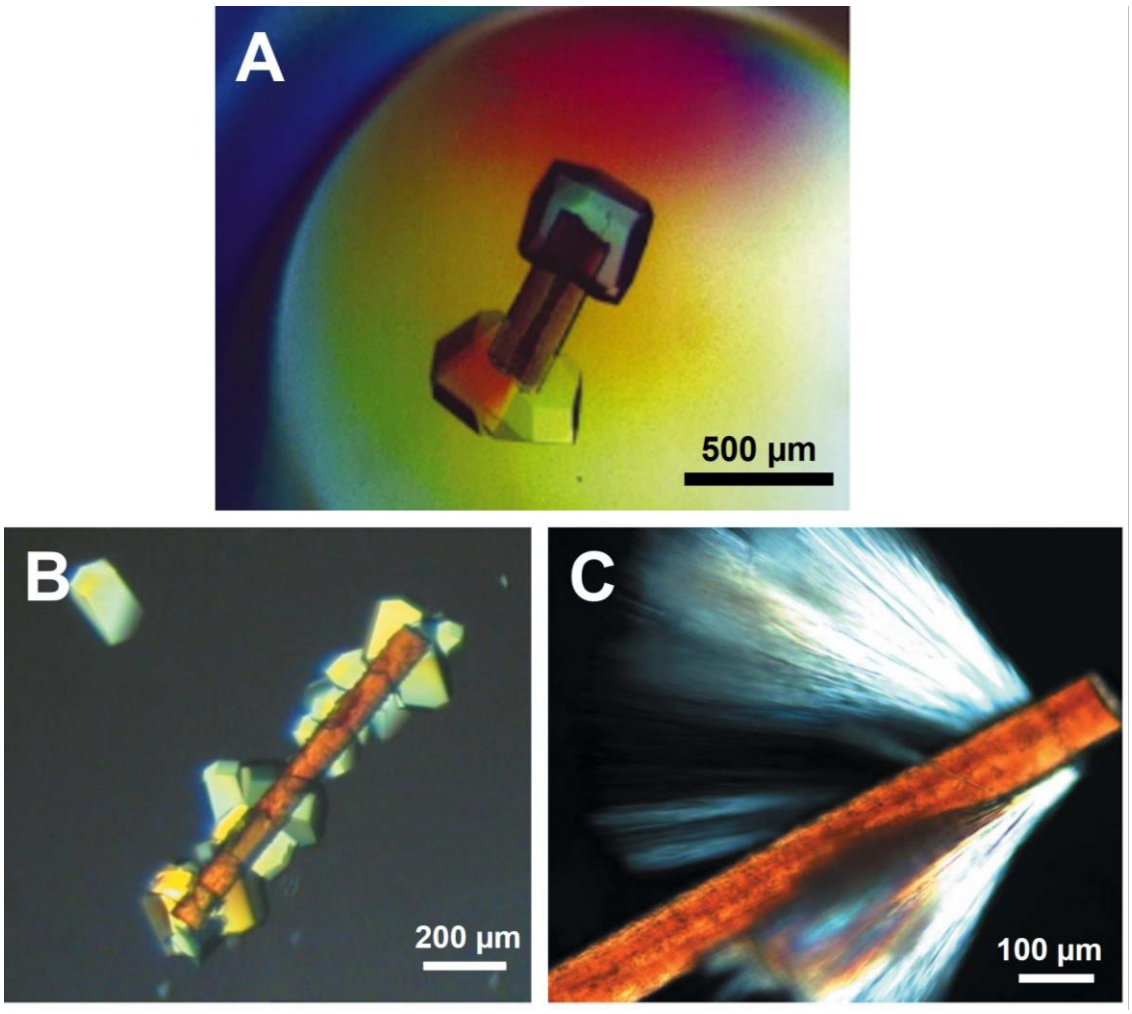


**Figure 103: Various protein crystals grown on hair, including (A) Fab-D[263], and (B/C) two forms of lysozyme[246]. Reproduced with permission from the International Union of Crystallography.**

### 5.1.2.3 The Structure of Hair

Hair is a protein-based structure that varies in composition and morphology between species. There are 2 major domains found in every hair – the cortex and cuticles - and in many cases a medulla is also present[264]. The cortex contains densely packed elongated keratinised cells which give the hair the majority of its mechanical strength. Melanin granules are embedded amongst these cells to give hair its colour. The cuticle is the outermost section of the hair, and primarily protects the hair from mechanical damage whilst allowing for flexibility. The medulla is a porous cylindrical region at the core of hair fibres, the exact role of which is not known. Each of these domains in a hair fibre contains ‘hard’ keratin, which is distinguished from the ‘soft’ keratin found in the epidermis by the amount

of cysteine present. This is associated with the formation of more rigid disulfide linkages[261]. Cysteine is by far the most abundant amino acid residue present in mammalian hair, and comprises approximately 15-20% of the total protein content [265,266]. The keratin in the cuticle layer is assembled into a dense macrofibrillar network that is aligned with the long axis of the hair[266–268]. The cuticle layer also has a hydrophobic surface due to the presence of free lipids, of which 18-methyl eicosanoic acid makes up the vast majority[266], and bound lipids, which are bonded to the hair surface through thioester linkages[260]. Also present are some cholesterol esters, and cholesterol. Cuticles are arranged as a series of scales on the hair surface, and at the edge of each scale is a rough step-like geometry which slightly exposes the inner cuticle structure (Figure 104). The structure of both the cuticle surface and edges vary between species and with damage, by UV or excessive washing/bleaching[266].

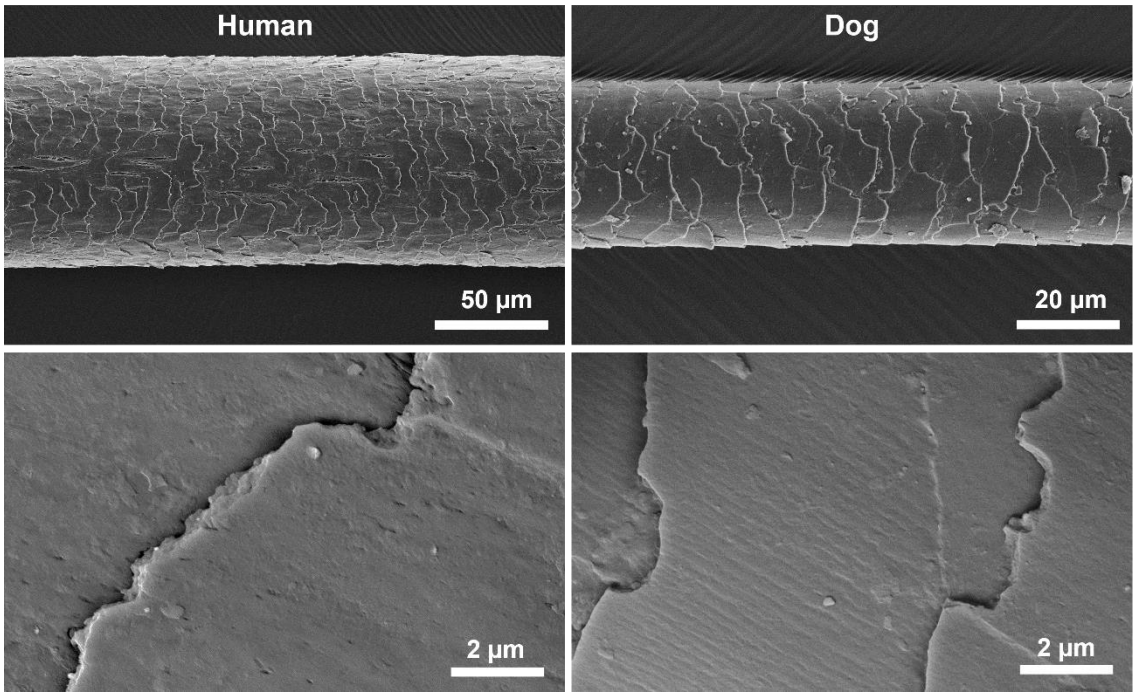


**Figure 104: SEM images showing the morphologies of the hair fibre and cuticle edges for dog and human hair.**

### 5.1.3 Crystallisation in Microdroplets

In droplet-based microfluidic technologies, droplets are physically isolated from one another, allowing for a vast number of individual experiments to be run in

parallel. This is highly beneficial for measurement of crystallisation kinetics, such as induction time, nucleation rate and growth rate, where large numbers of repeats are required to account for the inherent stochasticity of nucleation. Additionally, the division of a volume of liquid into many droplets greatly reduces the chance of any one droplet being contaminated by foreign particles[269].

Microfluidic droplets can be analysed using synchrotron x-ray techniques (diffraction, small/wide angle scattering), to measure nucleation kinetics and monitor polymorphic transitions[270,271]. The displacement of the droplets from their injection/mixing point to the point where they crystallise is an indirect measure of the induction time. Thus, positioning the device such that the beam passes through certain areas of flowing droplets allows large amounts of data to be collected at varying timepoints.

Studies involving static microdroplets can be much simpler to run, and can be equally effective for studying crystallisation kinetics. Arrays of droplets can be deposited on a substrate and their crystallisation studies with an optical microscope[272]. Grossier and co-workers investigated the nucleation kinetics of NaCl using static microdroplets[273,274], which were deposited on a surface by 'jetting' a solution with a nanopipette. They were able to produce distribution curves of induction times by analysing optical microscope images. This technique has also been used to produce arrays of highly supersaturated KCl droplets, in which nucleation could be induced by touching the droplets with a sharp tungsten wire[275]. In many cases, droplets had to be tapped repeatedly with the wire, due to the wire being a poor nucleant.

## 5.2 Overview of Analytical Techniques

### 5.2.1 X-Ray Photoelectron Spectroscopy (XPS)

X-ray photoelectron spectroscopy (XPS) is used to gather the energies of electrons in a material, and display these as spectra with distinct bands, corresponding to different elements in different bonding states. X-rays are emitted from the source (usually a metal anode bombarded with electrons), and are absorbed by atoms in the sample, causing them to eject electrons. This is known as the photoelectric effect. These electrons are then detected, typically by

a hemispherical electron energy analyser, and this signal is used to produce a spectrum with signal counts plotted against binding energy (in eV). Due to the small penetration depth of the x-rays, only the top few nanometres of the surface are sampled, which makes XPS highly effective for characterising the chemistry of the outermost surface.

One of the major limitations of conventional XPS is that it operates at extremely low pressures ($10^{-6}$ – $10^{-7}$ mbar) to eliminate noise, which may damage some samples which are sensitive to drying. Near-ambient pressure (NAP) XPS is a more recent development of the technique, and allows for much higher pressures (up to 10 mbar) to be used whilst retaining an acceptable signal to noise ratio.

### 5.2.2 Scanning Ion-Conductance Microscopy (SICM)

Scanning ion-conductance microscopy measures the charge and topography of a surface by measuring the resistance between two Ag/AgCl electrodes in an electrolyte solution with varying proximity to a surface (Figure 105). One electrode is placed in the electrolyte solution, and one is mounted within a nanopipette with an aperture of tens to several hundreds of nanometres. A voltage is applied between the electrodes by a potentiostat, establishing a steady flow of ions from anode to cathode. The nanopipette is navigated slowly towards the surface using piezoelectric manipulators. As it approaches, a large resistance spike is measured as the flow of ions becomes restricted. Precise calibration along with comparison to simulated models of the system allows the exact geometry of the surface to be mapped, along with its charge.

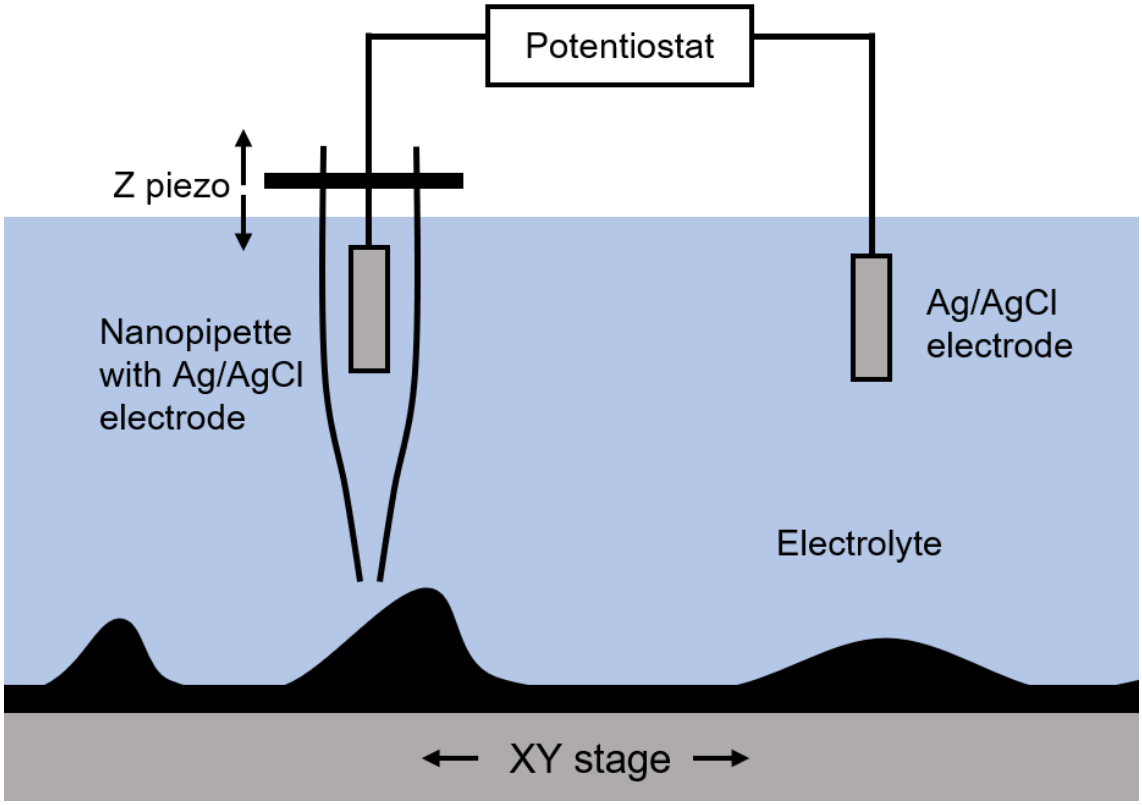


**Figure 105: Diagram showing the operating principle of SICM.**

## 5.3 Methods

### 5.3.1 Procurement and Treatment of Hairs

Human hair was generously supplied by Ms Zhao Jiang. Dog hair was (reluctantly) supplied by Charlie the miniature Irish-doodle. Mole, mink, squirrel, camel and elk hairs were taken from a selection box of fly-tying materials. Bat hairs were kindly supplied by South Yorkshire Bat Group and Northumberland Bat Group. Hairs were cut into approximately 1.5 cm lengths (or as close to 1.5 cm as possible) using microscopy scissors.

#### 5.3.1.1 Water Washing

Hair samples were placed in a vial, and water was added. The vial was mixed using a vortex mixer (IKA MS 3 basic), and the water was decanted away. This was repeated until three washing steps had been performed. Samples were immersed in water until used further.

#### 5.3.1.2 Ethanol Treatment

Hair samples were placed in a vial, and ethanol (10 mL) was added. This was left for 15 minutes, before the ethanol was decanted and fresh ethanol was added. This was repeated until three washing steps had been performed. Lastly, the hairs were washed with water as detailed in Section 5.3.1.1.

#### 5.3.1.3 Petroleum Ether Treatment

Hair samples were placed in a vial, and petroleum ether (10 mL) was added. This was left for 15 minutes, before the petroleum ether was decanted and fresh petroleum ether was added. This was repeated until three washing steps had been performed. Lastly, the hairs were washed with water as detailed in Section 5.3.1.1.

#### 5.3.1.4 $H_2O_2$ Treatment

Hair samples were placed in a vial, and were first immersed in water (10 mL) for 15 minutes to improve wettability. The water was decanted, and $H_2O_2$ (10 mL) was added, taking care to ensure that hairs were fully immersed, after which they were left for 30 minutes. Lastly, the hairs were washed with water as detailed in Section 5.3.1.1.

### 5.3.2 Nucleation of $KNO_3$ Microdroplets

Borosilicate glass slides were washed with isopropyl alcohol and air dried, then cleaned with piranha solution. They were then treated with Aquapel for 1 minute. The slide was removed, washed with isopropyl alcohol, gently polished with a lint-free wipe followed by a final washing step with isopropyl alcohol and air drying. This slide was mounted on an inverted light microscope (Zeiss Axio Observer 7 Material) and a small pool of silicone oil was added on top.

Glass nanopipettes were fabricated by loading borosilicate glass capillaries into a micropipette puller (Sutter Model P-2000). The programme was set using the following parameters to produce nanopipettes with tip diameters of 420nm: HEAT=350, FIL=3, VEL=40, DEL=220, then HEAT=350, FIL=3, VEL=40,

DEL=180, PUL=80. Nanopipettes were dipped in Aquapel to increase their hydrophobicity. This nanopipette was loaded with $KNO_3$ solution (2.5 M), and connected to an Eppendorf InjectMan System. The nanopipette tip was lowered through the silicone oil layer to the glass surface, and a few test droplets were deposited to calibrate the injection pressure and time, which varied depending on minor differences between fabricated nanopipettes. Once droplets could be reliably deposited with an outer diameter of ~130 µm, the injection pressure and time were fixed, and several arrays of 9 droplets were injected, arranged into a 3x3 square. Images of droplets were taken as soon as they were deposited, and saved with specific filenames to allow for automated analysis (further details in Section 5.4.1.3).

Glass rod nucleants were prepared by mounting borosilicate glass rods in a micropipette puller (Sutter Model P-2000). The programme was set using the following parameters: HEAT=550, FIL=4, VEL=38, DEL=175, PUL=30, then HEAT=500, FIL=4, VEL=36, DEL=125, PUL=70. The pulled glass rods were then pushed gently through a paper wipe to produce tips with end diameters of 20-50 µm. Rods were washed with isopropyl alcohol, air dried and then plasma treated using a cleaner (Diener Atto) set to 200W for 2 minutes. Glass tips were used within 1 hour of plasma treatment.

Hair samples were mounted on a syringe needle using epoxy resin, and this was screwed into a custom steel rod with a Luer lock attachment which was connected to a micromanipulator (Sutter MPC-385). After waiting for approximately 1-2 hours, droplets became supersaturated with respect to $KNO_3$, and a nucleant was slowly lowered through the silicone oil layer and touched to a droplet for 10 seconds. The result (i.e. whether or not a crystal was produced) was recorded, the hair washed thoroughly with water and then the next droplet was touched with a hair (Figure 106). Each nucleant was used for 9 droplets before being replaced. The droplet supersaturations were calculated from a full video recording of the experiment using custom macros written for ImageJ and Excel (further details in Section 5.4.1.3).

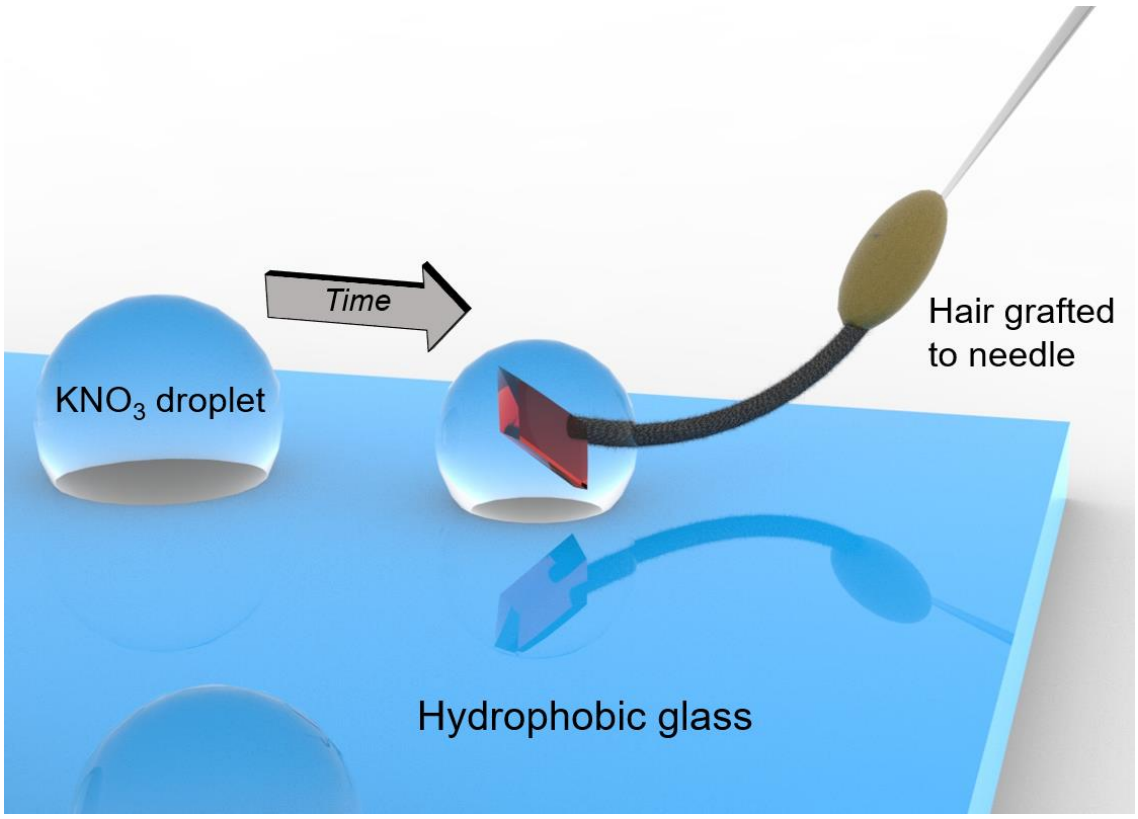


**Figure 106: Diagram showing how hairs were used to nucleate $KNO_3$ droplets over a range of concentrations.**

### 5.3.3 Temperature Measurement

A three-wire PT-100 temperature probe was submerged in a thin layer of silicone oil adjacent to the experimental setup, to mimic the droplet environment. This was connected to a PicoTech PT-104 temperature logger, which outputted the temperature to PicoLog 6 every second. This temperature was copied into a table, alongside the droplet code (e.g. A1, B2, C3) and the result of the nucleation trial. A USB temperature logger (Lascar EL-USB-1) was placed adjacent to the experimental setup, and was used for preliminary temperature measurements.

### 5.3.4 Crystallisation by Direct Mixing

$CaCO_3$, $CaSO_4$, $BaSO_4$, $SrSO_4$, $CaF_2$, $BaCO_3$ and $CuCO_3$ were crystallised using a direct mixing method. As a general rule, substrates were immersed in a solution of alkali metal ions in a 5 mL square multiwell plate, then a second solution of anions with the same concentration was added without mixing. The identities and

concentrations of the primary and secondary solutions are shown in Table 5. Substrates were left for a defined period of time to crystallise. After crystals were formed, substrates were washed gently with water, then ethanol, and then were air dried. All aqueous solutions were passed through a Millex® cellulose ester syringe filter (pore size 0.22 µm).

| Mineral | Solution 1 | Solution 2 | Incubation time |
|---|---|---|---|
| **$CaCO_3$** | $CaCl_2$ (2.5 mL, 5 mM) | $Na_2CO_3$ (2.5 mL, 5 mM) | 20 minutes |
| **$CaSO_4$** | $CaCl_2$ (2.5 mL, 600 mM) | $Na_2SO_4$ (2.5 mL, 600 mM) | 5 minutes |
| **$BaSO_4$** | $BaCl_2$ (2.5 mL, 0.5 mM) | $Na_2SO_4$ (2.5 mL, 0.5 mM) | 2 hours |
| **$SrSO_4$** | $SrCl_2$ (2.5 mL, 50 mM) | $Na_2SO_4$ (2.5 mL, 50 mM) | 5 minutes |
| **$CaF_2$** | $CaCl_2$ (2.5 mL, 12 mM) | NaF (2.5 mL, 12 mM) | 30 minutes |
| **$BaCO_3$** | $BaCl_2$ (2.5 mL, 2 mM) | $Na_2CO_3$ (2.5 mL, 2 mM) | 1 hour |
| **$CuCO_3$** | $CuCl_2$ (2.5 mL, 10 mM) | $Na_2CO_3$ (2.5 mL, 10 mM) | 1 hour |

**Table 5: Solution compositions and incubation times used for direct mixing experiments to produce the crystals listed.**

### 5.3.5 Resin Exfoliation of Crystals on Hairs

Conductive carbon resin (Demotec® 70) was prepared by thoroughly mixing a 1:1 weight ratio of the solid and liquid components. Once the viscosity began to increase, the mixture was poured into a 20 mm diameter cylindrical silicone mould to a depth of 5 mm. A hair sample with $CaCO_3$ crystals grown on top was gently placed onto the liquid resin mixture, then the system was covered with a petri dish and left for 24 hours to completely cure. Once cured, hair was gently peeled away, and the sample was trimmed into a small square using a razor blade. Finally, an air jet was used to clean the surface ready for analysis by SEM.

### 5.3.6 X-Ray Photoelectron Spectroscopy

XPS spectra were collected by Dr Mark Walker at the University of Warwick and analysed by Dr Sebastian Amland Skaanvik. Samples were mounted by twisting a bundle of hair and pressing it onto carbon tape. XPS spectra were collected on a Kratos Axis Ultra DLD spectrometer (base pressure less than 1 x $10^{-10}$ mbar) equipped with a monochromated Al Kα X-ray source (1486.69 eV, 120W, and analysis area of 300 mm x 700 mm). Survey spectra were collected using an analyser pass energy of 160 eV (1 eV increments and 500 ms dwell time). High-resolution spectra were collected using an analyser pass energy of 20 eV (0.1 eV increments). All samples were charge-compensated by a low-energy electron gun.

The spectrometer work function and binding energy scale were calibrated using the Fermi edge and $3d_{5/2}$ peak recorded from a polycrystalline Ag sample. XPS spectra were referenced to the peak maximum of the aliphatic C 1s component at a binding energy of 285 eV [276]. S 2p peaks were fitted to the Gaussian-Lorentzian line shapes and Shirley background. Quantification from survey spectra were carried out using O 1s, N 1s, C 1s, S 2s, Si 2p (contaminant) core-level peaks and were calibrated for intensity using an instrument transmission function. Data analysis was carried out using the CasaXPS package[277].

### 5.3.7 Near-Ambient Pressure X-Ray Photoelectron Spectroscopy (NAP-XPS)

NAP-XPS was run by Dr Andrew Britton at the Leeds University Versatile XPS facility. The hair samples were mounted by twisting each of them into a single strand and affixing the ends to a large SEM stub with an adhesive putty. Environmental XPS spectra were collected with a SPECS EnviroESCA NAP-XPS equipped with a monochromatic Al Kα X-ray source (1486.71 eV) operating at 42 W. The samples were illuminated with a ~300 μm-diameter beam footprint. Spectra were collected at ambient temperature in 7 mbar of nitrogen with a hemispherical Phoibos NAP 150 analyzer operating in a small-area mode with a source−analyzer angle of 55° and a 1D delay-line detector. The gas purity was cross-checked using a mass spectrometer. Under NAP conditions in the EnviroESCA instrument, electrically insulating sample surfaces are charge-

neutralized through ionization of gas phase atoms by energetic electrons emitted from the sample and, to a lesser extent, the X-ray beam itself. Survey spectra were collected in one scan with a step size of 1 eV, a pass energy of 100 eV, and a dwell time of 0.1 s. High-resolution C 1s, N 1s, O 1s and S 2p core-level spectra were collected with a step size of 0.1 eV, a dwell time of 100 ms per data point, and a pass energy of 50 eV. Spectra were calibrated for intensity using an instrument transmission function. Data analysis was carried out using the CasaXPS package [277].

### 5.3.8 Scanning Ion-Conductance Microscopy

SICM measurements were carried out by Dr Ian McPherson and Dr Sebastian Amland Skaanvik using a home-built instrument mounted on a Zeiss Axiovert 40 CFL microscope running the Warwick Electrochemical Scanned Probe Microscopy (WECSPM) software. The instrument was equipped with a Nano-Bio300 300 µm xy-piezo (MadCityLabs, USA) and a P-753.2 LISA 38 µm z-piezo (PI, Germany). Current was measured using a home-build current follower and brick wall filter. It was sampled every 2.56 ms, and the steady-state current was found from the last data point in an *i-t* trace. The approach rate was 2 µm $s^{-1}$ and the approach and pulse potentials were 50 mV and -400mV, respectively. The electrolyte was $KNO_3$ (45 mM) and KCl (5 mM). Nanopipettes were fabricated from borosilicate glass capillaries (BF120-69-10, Sutter instruments) using a Sutter P-2000 laser puller with the following protocol: HEAT 350/350, FIL 3/3, VEL 30/40, DEL 220/180, -/120. The pipette dimensions and surface charge were evaluated according to described methods using STEM and finite-element modelling.[278]

### 5.3.9 Atomic Force Microscopy

Dr Sebastian Amland Skaanvik performed AFM measurements. These were carried out in tapping mode under ambient conditions using a Bruker Innova instrument. Bruker RFESP-75 probes were used (k = 3 N/m, $f_0$ = 75 kHz).

### 5.3.10 Raman Spectroscopy

Raman spectra were collected from crystals embedded in hairs using a Horiba LabRAM HR Evolution Raman microscope with a 50 W 532 nm (green) laser passing through an edge filter. A hole size of 50 and laser powers of 1-10% were used.

## 5.4 Results

### 5.4.1 Investigation of $KNO_3$ Nucleation on Hair Using Microdroplets

Initial work by Dr Xuefeng He and Dr Cedrick O'Shaughnessy established an initial method for producing and monitoring the concentration of arrays of oil-submerged aqueous $KNO_3$ microdroplets. My own work involved developing and automating this method, along with all data collection and analysis, which is detailed herein.

#### 5.4.1.1 Calculation of Microdroplet Concentrations

Microdroplets were deposited by nanopipette on hydrophobic glass, and since their contact angles were >90°, they adopted the geometry shown in Figure 107. When viewed by inverted optical microscopy, two concentric circles were observed. The outer circle gave the overall diameter of the droplet, whereas the inner circle gave the diameter of the contact line between the droplet, the oil and the hydrophobic glass.

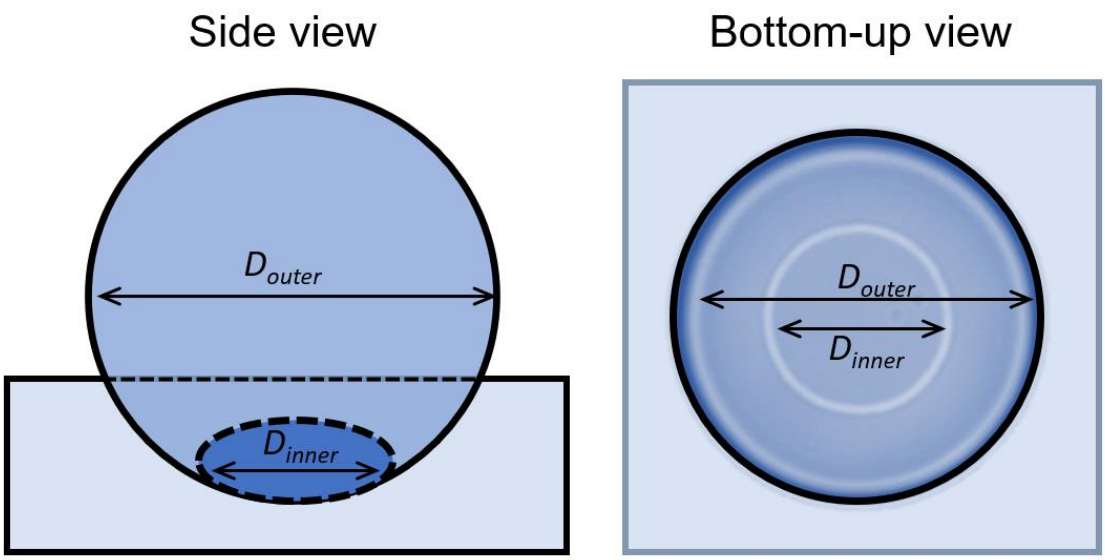


**Figure 107: Diagram showing the droplet geometries when sitting on hydrophobic glass, and how this appeared when viewed from the bottom-up by inverted optical microscopy.**

The assumption that the droplet is spherical only holds true in the absence of gravitational and buoyancy forces. Exact calculation of the droplet geometry would require iterative solution of a nonlinear differential equation following the procedure reported by Lubarda and Talke[279], using accurate interfacial energies between each of the phases. Fortunately, the densities of 2.5 - 7 M $KNO_3$ and silicone oil are extremely close (1.1 – 1.25 g $cm^{-3}$ and 1.04 g $cm^{-3}$ respectively), and the interfacial tension between the two liquids is high (>35 mN $m^{-1}$ [280]). This means that for the sizes of droplets used in this series of experiments (~100 µm diameter ~1 nL), any deviation from a spherical shape would be immeasurably small. It is therefore assumed that all droplets have the geometry shown in Figure 107. Droplet volumes were therefore calculated using Figure 108 and Equation 28.

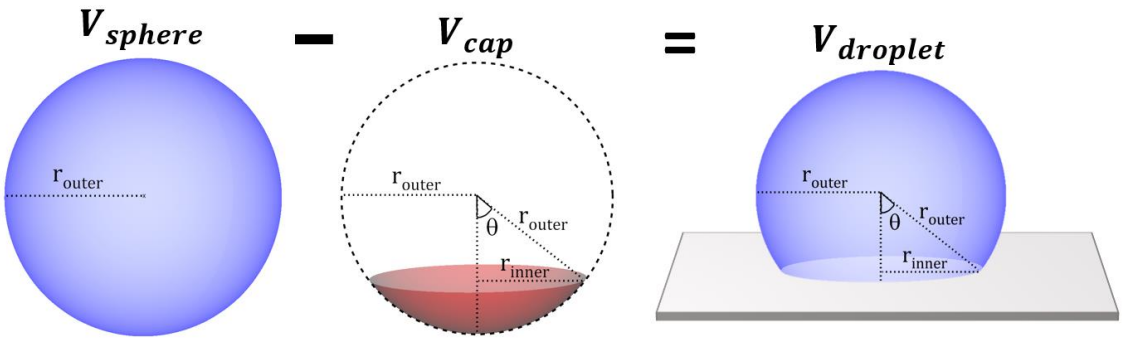


**Figure 108: Diagram showing how Equation 28 could be used to calculate the droplet volume from its inner and outer radii.**

$$V_{droplet} = \frac{4\pi r_{outer}^3}{3} - \frac{\pi r_{outer}^3}{3}\left(2 + \cos\left(\sin^{-1}\left(\frac{r_{inner}}{r_{outer}}\right)\right)\right)\left(1 - \cos\left(\sin^{-1}\left(\frac{r_{inner}}{r_{outer}}\right)\right)\right)^2$$

**Equation 28**

Once the microdroplets were deposited, water diffused into the silicone oil, causing a gradual decrease in volume and increase in concentration. Knowing the initial $KNO_3$ concentration to be 2.5 M and measuring the initial droplet volume $V_0$ and its volume after a time $V_t$, the concentration at this time $C_t$ could be calculated using Equation 29.

$$C_t = C_0\left(\frac{V_0}{V_t}\right) = 2.5\left(\frac{V_0}{V_t}\right)$$ **Equation 29**

#### 5.4.1.2 Temperature Monitoring to Calculate Supersaturation

The steep rise in $KNO_3$ solubility with increasing temperature[48] meant that fluctuations in ambient temperature would affect the saturation concentration. A robust temperature controlled setup could have been established, however this would have been challenging to fit on the microscope stage without obscuring the imaging. Instead, the temperature was recorded at each nucleation event and was used to calculate the supersaturation using Equation 30, where C is concentration and T temperature

$$S_r = \frac{C}{C_{sat}} = \frac{101.1C}{132.17+2.52T(\ln T)}$$ [281] **Equation 30**

Initially, the temperature of the laboratory was monitored for 22 hours using two different temperature logging devices with different degrees of precision (Figure 109). The USB logger had 0.5 $^oC$ precision, and the PicoTech three-wire PT-100 logger had 0.001 $^oC$ precision. Fluctuations in temperature were caused by the air conditioning system of the room, body heat, and the position of the sun.

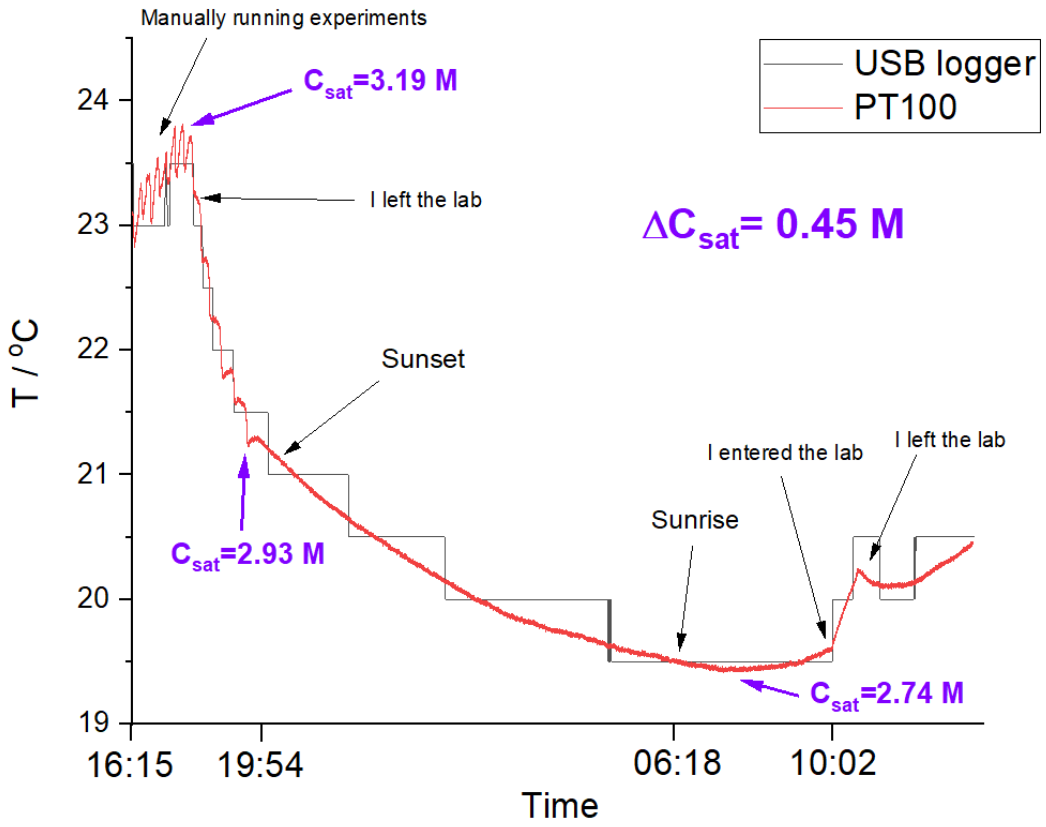


**Figure 109: Log of laboratory temperature over a 22 hour period using a USB data logger and a PicoTech PT-100 logger. The difference in saturation concentration of $KNO_3$ was calculated to be 0.45 M between the highest and lowest temperatures.**

To reduce this variability in temperature, experiments were moved to a separate laboratory with a newer air conditioning system. There was still some variation due to the system cycling, but overall temperature control was much better here (Figure 110).

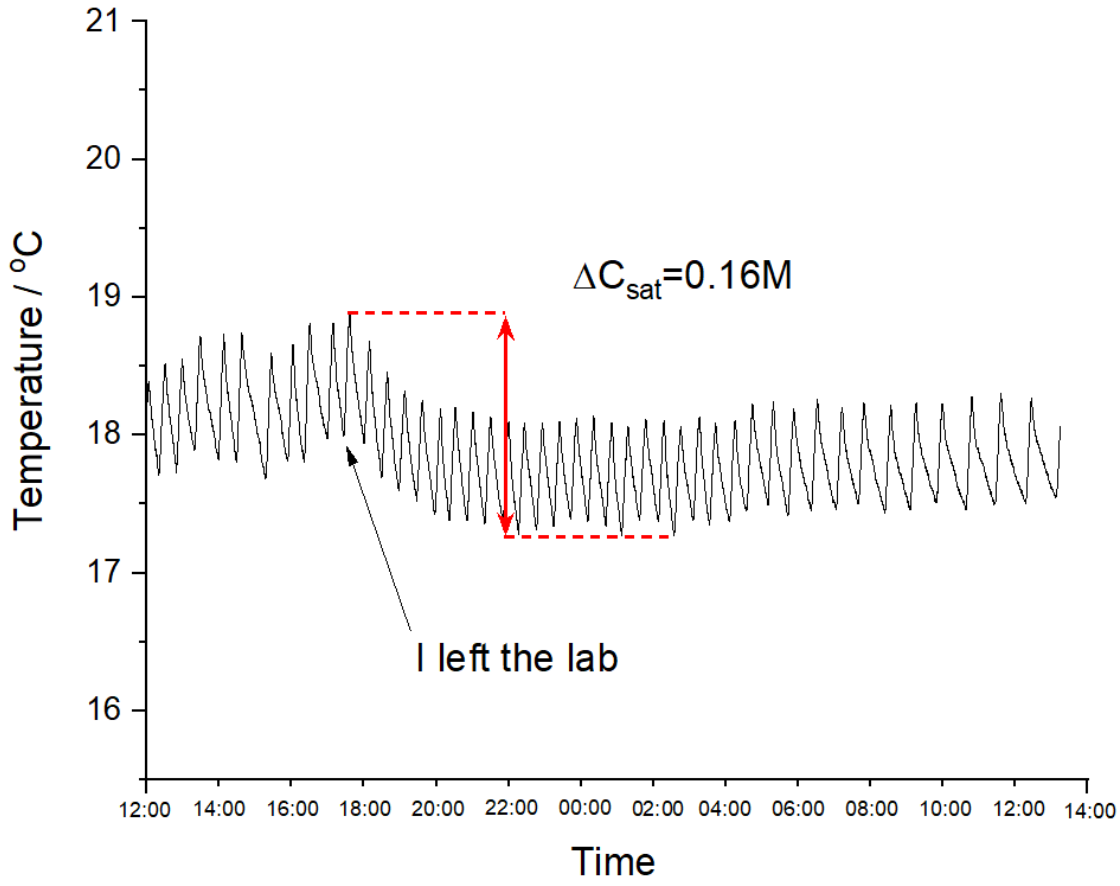


**Figure 110: Log of second laboratory temperature over a 24 hour period using a PicoTech PT-100 logger. The difference in saturation concentration of $KNO_3$ was calculated to be 0.16 M between the highest and lowest temperatures.**

#### 5.4.1.3 Optimisation and Automation of Microdroplet Supersaturation Measurement

The aim of the work was to compare the kinetics of $KNO_3$ nucleation on hairs, so a large amount of data was required to have confidence in the conclusions. Therefore, it was necessary to find an efficient way to collect large amounts of high quality data, and to analyse it quickly.

The rate of data acquisition using different sizes and numbers of droplet arrays was firstly explored. Depositing and analysing 8 arrays of droplets in a 3x3 pattern was found to be optimal because they could be arranged into a square of evenly spaced droplets that fitted in the microscope camera field of view. More tightly-packed arrays of 16 droplets were more challenging to deposit with precise

spacings, and their close proximities to one another meant that the silicone oil became locally saturated with water, significantly slowing the rate of concentration of the droplets. This effect was particularly pronounced at the centre of the arrays.

Data analysis was then automated. This task was well suited to ImageJ, a macro-enabled modular image analysis software package. Since the droplets were highly circular, a Hough Circle Transform algorithm was used to find and measure radii. However, images needed to be processed before this algorithm could reliably find the correct circles in the images. This process is outlined for both outer radii (Figure 111) and inner radii (Figure 112).

The final images of droplets only contained a single droplet. However, the initial images contained multiple arrays of droplets. Droplets were therefore automatically assigned names based on their x and y positions in the array. All of the filtering, thresholding and measurements were performed using a macro written for ImageJ (Figure 113 to Figure 116). The ImageJ plugin 'Read and Write to Excel' was used to dump the circle radius measurements to an Excel file for calculations.

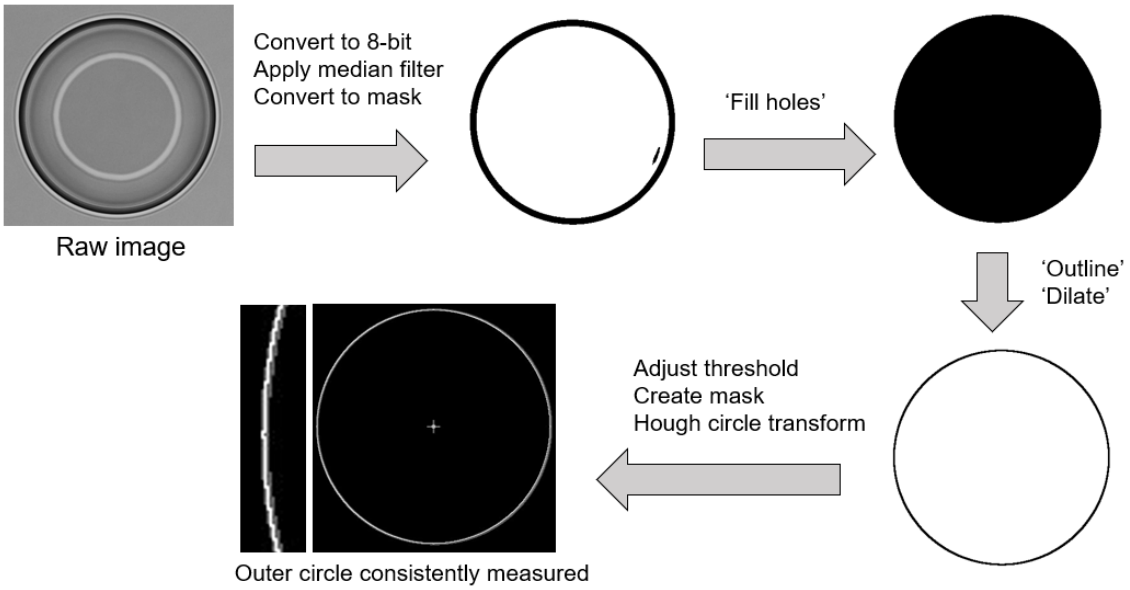


**Figure 111: Outline of the image processing steps required to measure droplet outer radii.**

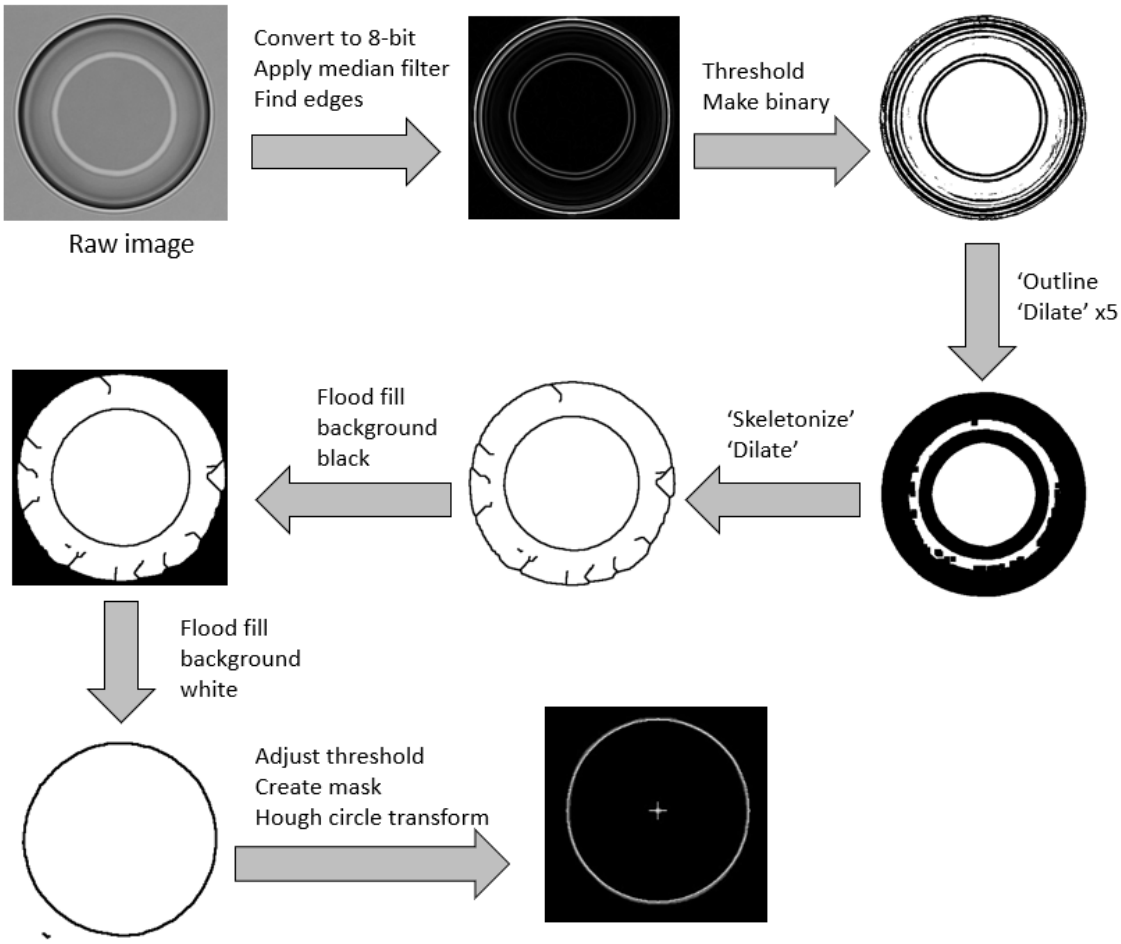


**Figure 112: Outline of the image processing steps required to measure droplet inner radii.**

Setting the file path

```
input = getDirectory("FILE_PATH_GOES_HERE");
filelist = getFileList(input + "Final volume_1_to_9");
```

Opening the initial droplet array image

```
open(input + File.separator + "Initial_noSB.tif");
```

Scaling and running a series of filters and transformations

```
run("8-bit");
run("Set Scale...", "distance=296 known=100 unit=micron");
run("Median...", "radius=7");
run("Find Edges");
setOption("BlackBackground", false);
run("Convert to Mask");
run("Fill Holes");
run("Outline");
run("Dilate");
run("Create Mask");
```

Running the Hough Circle Transform algorithm

```
run("Hough Circle Transform","minRadius=150, maxRadius=250, inc=1,
minCircles=9, maxCircles=9, threshold=0.5, resolution=30, ratio=1.0,
bandwidth=10, local_radius=10,  reduce show_mask results_table");
close("*");
while(nImages==0)wait(1000);
```

Saving images of detected circles to check errors

```
saveAs("jpeg", input + "Circles_overlaid" + File.separator +
"Initial_image_outer");
```

Saving the data to Excel

```
run("Read and Write Excel");
run("Clear Results");
```

**Figure 113: Section of the ImageJ macro used to establish the file path, then gather the droplet initial outer radii and dump this to an Excel file.**

Opening each final droplet image in series

```
for (i = 0; i < lengthOf(filelist); i++) {
    if (endsWith(filelist[i], ".tif")) {
        open(input + "Final volume_1_to_9" + File.separator
        + (i+1) + ".tif");
```

Scaling and running a series of filters and transformations

```
        run("8-bit");
        run("Set Scale...", "distance=296 known=100 unit=micron");
        run("Median...", "radius=7");
        run("Find Edges");
        setOption("BlackBackground", false);
        run("Convert to Mask");
        run("Fill Holes");
        run("Outline");
        run("Dilate");
        run("Create Mask");
```

Running the Hough Circle Transform algorithm

```
        run("Hough Circle Transform","minRadius=100, maxRadius=300,
        inc=1, minCircles=1, maxCircles=1, threshold=0.5, resolution=100,
        ratio=1.0, bandwidth=10, local_radius=10,  reduce show_mask
        results_table");
        close("*");
        while(nImages==0)wait(1000);
```

Saving images of detected circles to check errors

```
        saveAs("jpeg", input + "Circles_overlaid" + File.separator +
        "Outer" + (i+1));
        wait(300);
        close("*");
        wait(1000);
    }
}
```

Saving the data to Excel

```
run("Read and Write Excel");
run("Clear Results");
wait(2000);
```

**Figure 114: Section of the ImageJ macro used to gather the droplet final outer radii and dump this to an Excel file.**

Opening each final droplet image in series

Scaling and running a series of filters and transformations

Running the Hough Circle Transform algorithm

Saving images of detected circles to check errors

Saving the data to Excel

```
for (i = 0; i < lengthOf(filelist); i++) {
    if (endsWith(filelist[i], ".tif")) {
        open(input + "Final volume_1_to_9" + File.separator
        + (i+1) + ".tif");

        run("8-bit");
        run("Set Scale...", "distance=296 known=100 unit=micron");
        run("Median...", "radius=7");
        run("Find Edges");
        setAutoThreshold("Default dark");
        run("Threshold...");
        setThreshold(12, 255);
        setOption("BlackBackground", false);
        run("Make Binary");
        run("Dilate");
        run("Dilate");
        run("Dilate");
        run("Dilate");
        run("Dilate");
        run("Skeletonize");
        run("Dilate");
        setForegroundColor(0, 0, 0);
        floodFill(1, 1);
        setForegroundColor(255, 255, 255);
        floodFill(1, 1);
        setAutoThreshold("Default");
        run("Create Mask");

        run("Hough Circle Transform","minRadius=50, maxRadius=150,
        inc=1,      minCircles=1, maxCircles=1, threshold=0.4,
        resolution=100, ratio=1.0, bandwidth=10, local_radius=10,
        reduce show_mask results_table");
        close("*");
        while(nImages==0)wait(1000);

        saveAs("jpeg", input + "Circles_overlaid" + File.separator
        + "Inner" + (i+1));
        close("*");
    }
}

run("Read and Write Excel");
run("Clear Results");
```

**Figure 115: Section of the ImageJ macro used to gather the droplet final inner radii and dump this to an Excel file.**

Opening the initial droplet array image

```
open(input + File.separator + "Initial_noSB.tif");
```

Scaling and running a series of filters and transformations

```
run("8-bit");
run("Set Scale...", "distance=296 known=100 unit=micron");
run("Median...", "radius=7");
run("Find Edges");
setAutoThreshold("Default dark");
run("Threshold...");
setThreshold(12, 255);
setOption("BlackBackground", false);
run("Make Binary");
run("Dilate");
run("Dilate");
run("Dilate");
run("Dilate");
run("Dilate");
run("Skeletonize");
run("Dilate");
setForegroundColor(0, 0, 0);
floodFill(1, 1);
setForegroundColor(255, 255, 255);
floodFill(1, 1);
setAutoThreshold("Default");
run("Create Mask");
```

Running the Hough Circle Transform algorithm

```
run("Hough Circle Transform","minRadius=50, maxRadius=150,
inc=1, minCircles=9, maxCircles=9, threshold=0.2,
resolution=30, ratio=1.0, bandwidth=10, local_radius=10,
reduce show_mask results_table");
close("*");
while(nImages==0)wait(1000);
```

Saving images of detected circles to check errors

```
saveAs("jpeg", input + "Circles_overlaid" + File.separator
+ "Initial_image_inner");
```

Saving the data to Excel

```
run("Read and Write Excel");
run("Clear Results");
close("*");
```

**Figure 116: Section of the ImageJ macro used to gather the droplet initial inner radii and dump this to an Excel file.**

With the results in an Excel file, a Visual Basic macro was written to transform this data to a table where a supersaturation ratio value would be automatically calculated for each droplet. Whether or not nucleation occurred, and which polymorph was produced, were then entered manually (Figure 117).

| Droplet code | Init. outer r / µm | Fin. outer r / µm | Fin. inner r / µm | Init. inner r / µm | Final conc / M | Temp / C | Supersat Ratio | Result |
|---|---|---|---|---|---|---|---|---|
| A1 | 73.986 | 58.446 | 30.743 | 31.081 | 5.12 | 18.11 | 1.959 | B |
| A2 | 73.986 | 61.149 | 31.419 | 31.419 | 4.46 | 18.03 | 1.712 | B |
| A3 | 73.986 | 56.757 | 31.419 | 30.743 | 5.62 | 17.97 | 2.159 | B |
| B1 | 72.973 | 60.811 | 31.081 | 30.743 | 4.35 | 18.09 | 1.666 | B |
| B2 | 72.635 | 58.446 | 31.081 | 31.081 | 4.85 | 17.97 | 1.863 | None |
| B3 | 72.973 | 60.473 | 30.405 | 30.068 | 4.43 | 18.02 | 1.698 | None |
| C1 | 73.311 | 56.757 | 31.419 | 30.743 | 5.46 | 18.09 | 2.091 | B |
| C2 | 72.973 | 60.135 | 31.757 | 30.743 | 4.51 | 18.03 | 1.731 | B |
| C3 | 72.973 | 57.095 | 31.419 | 30.068 | 5.29 | 18.07 | 2.027 | None |

**Figure 117: Example results table automatically produced from one array of droplets. 'B' denotes β-$KNO_3$, 'A' (not shown) denotes *α*-$KNO_3$, and 'None' was recorded when no nucleation was observed.**

As a final note, all of the microscope optics had to be kept meticulously clean to reduce the chances of the circle detection algorithm failing. Examples of adequate and inadequate images are shown in (Figure 118).

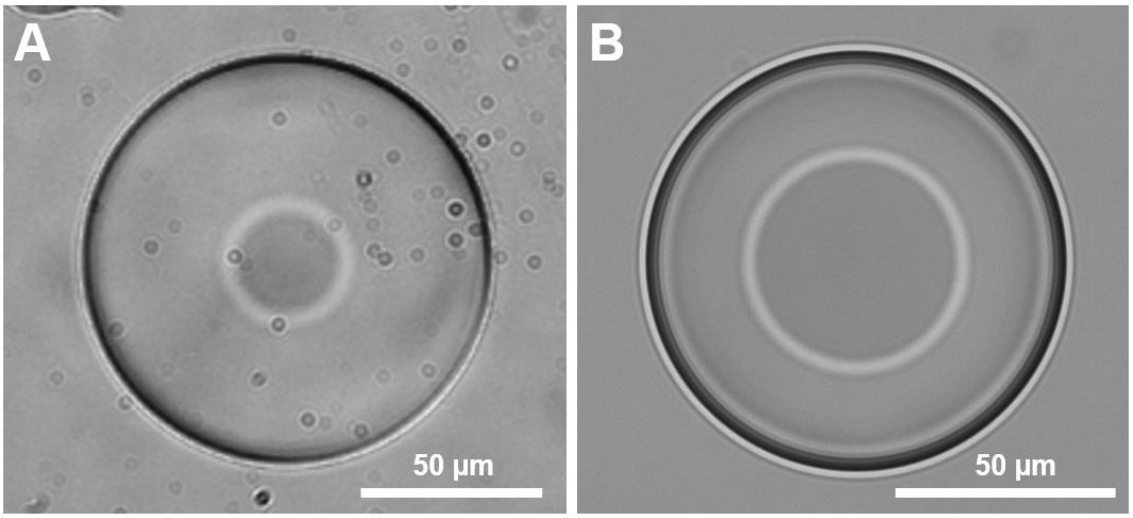


**Figure 118: Droplets imaged by inverted light optical microscopy (A) before cleaning the optics and (B) after cleaning the optics.**

With a robust data collection methodology established, a control experiment was conducted in the absence of an exogenous nucleant to measure how quickly droplets could be expected to nucleate, and also to put into perspective how effective nucleants were as compared with when they were absent. Droplets were

allowed to increase in concentration until they crystallised spontaneously, and the supersaturations were plotted (Figure 119). Droplets at the corners were observed to reduce in volume fastest, followed by those at the edges, and the droplets in the middle were slowest. This was due to the degree of saturation of the silicone oil with water, which was greatest at the centre of the array and least at the corners. All droplets crystallised between supersaturation ratios of 2.33 and 2.77, and within 4.5 hours.

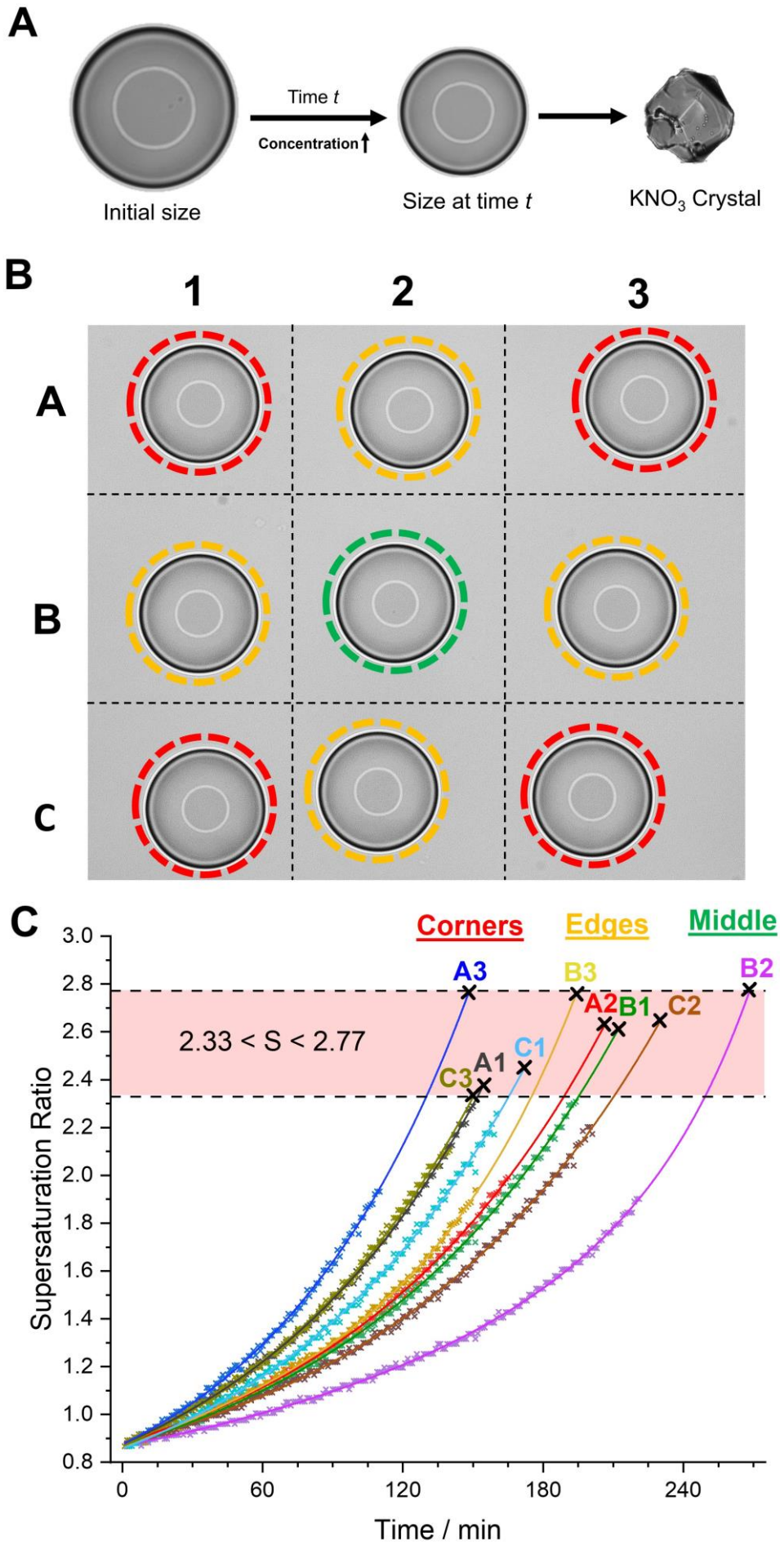
A
Time t
Concentration
Initial size
Size at time t
KNO3 Crystal
B
1
2
3
A
B
C
C
Corners
Edges
Middle
A3
B3
B2
A2
B1
C2
C1
A1
C3
2.33 < S < 2.77
Supersaturation Ratio
Time / min
3.0
2.8
2.6
2.4
2.2
2.0
1.8
1.6
1.4
1.2
1.0
0.8
0
60
120
180
240

**Figure 119: (A) Schematic showing how $KNO_3$ droplets reduced in volume and increased in supersaturation over time as water diffused out of the droplets into the surrounding silicone oil. (B) Assignment of droplet codes based on their positions in the 3 x 3 array. Colours correspond to whether they exist at the corners, edges or middle of the array. (C) Graph showing tracked droplet supersaturations over time. The point at which droplets crystallised is denoted with a cross.**

#### 5.4.1.4 Assessment of $KNO_3$ Polymorphism

A reliable way off assessing the polymorph of the $KNO_3$ crystals produced in the droplets was required to determine whether the polymorph was governed by the system, nucleant or concentration. After running a set of experiments using each nucleant type, optical microscopy images showed that there were a few distinct crystal morphologies (Figure 120A). Raman spectroscopy was used to determine the polymorph of each, since *β*-$KNO_3$ would show a peak at 125 $cm^{-1}$ and *α*-$KNO_3$ would exhibit two peaks at 52 $cm^{-1}$ and 85 $cm^{-1}$ (Figure 120B). Crystals formed at concentrations of 4 - 4.5 M usually had rhombohedral shapes, while those formed between 4.5 and 6 M had hopper morphologies. Crystals were dendritic above 6 M. This sequence in morphologies with increasing concentration has been observed for many crystals, and simply reflects the shift from an attachment-limited to a diffusion-limited growth regime. Occasionally, *α*-$KNO_3$ crystals were observed, and these grew exclusively as needles, so were easy to distinguish from any of the morphologies of β-$KNO_3$.

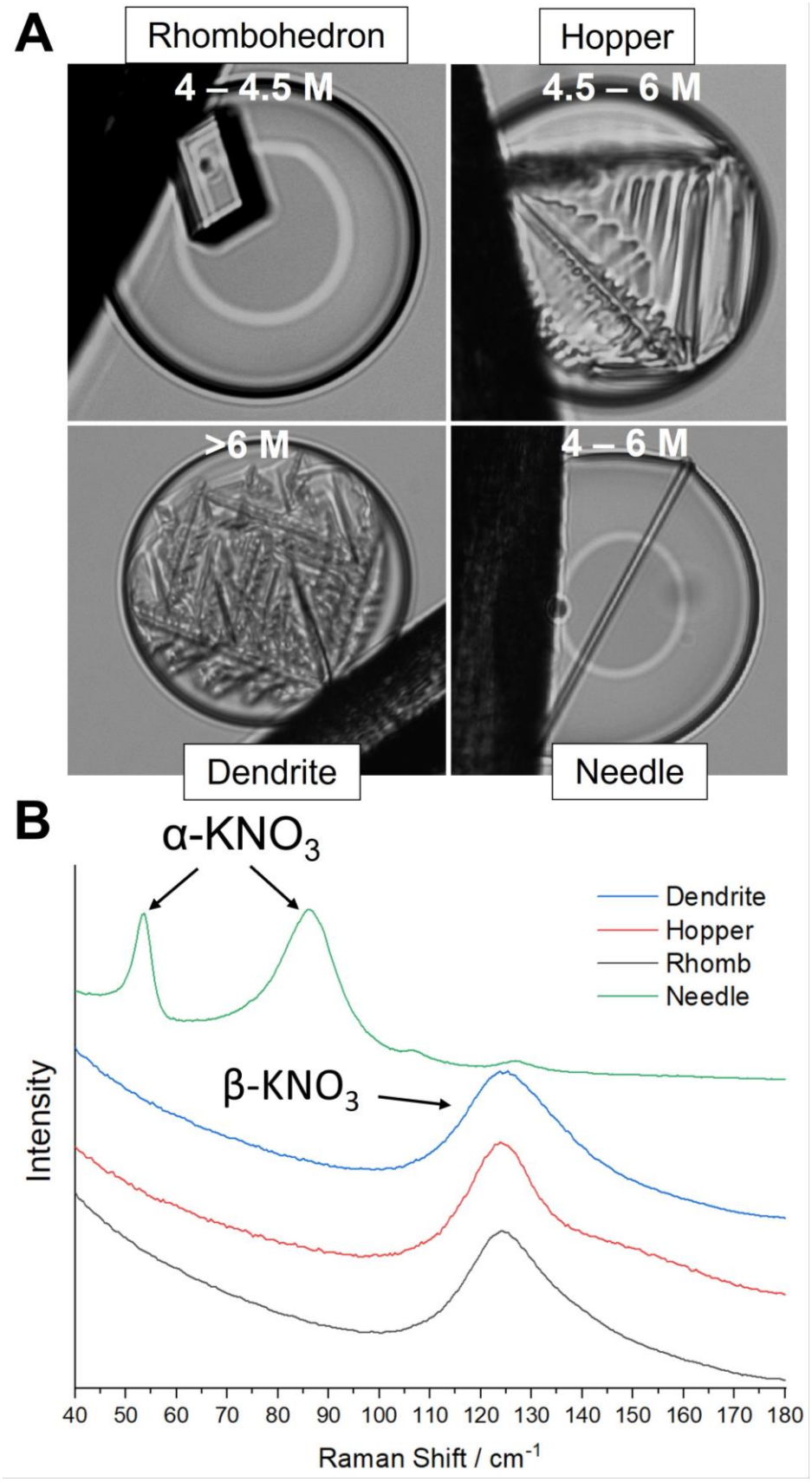


**Figure 120: (A) Optical microscopy images of distinct $KNO_3$ crystal morphologies. (B) Raman spectra showing the polymorph of each crystal type.**

### 5.4.1.5 $KNO_3$ Crystallisation on Hair from Microdroplets – Data Processing

Microdroplet nucleation data was collected for a range of nucleants (Figure 121), which included a pristine glass rod, and human and dog hairs following water, ethanol or petroleum ether washing, or $H_2O_2$ immersion. Data collection was stopped once 100 droplets had been touched by each nucleant type. It was found that ≈99% of crystals produced were *β*-$KNO_3$. *α*-$KNO_3$ only formed occasionally, and apparently at random, so the potential polymorph control of $KNO_3$ using hair was not pursued further.

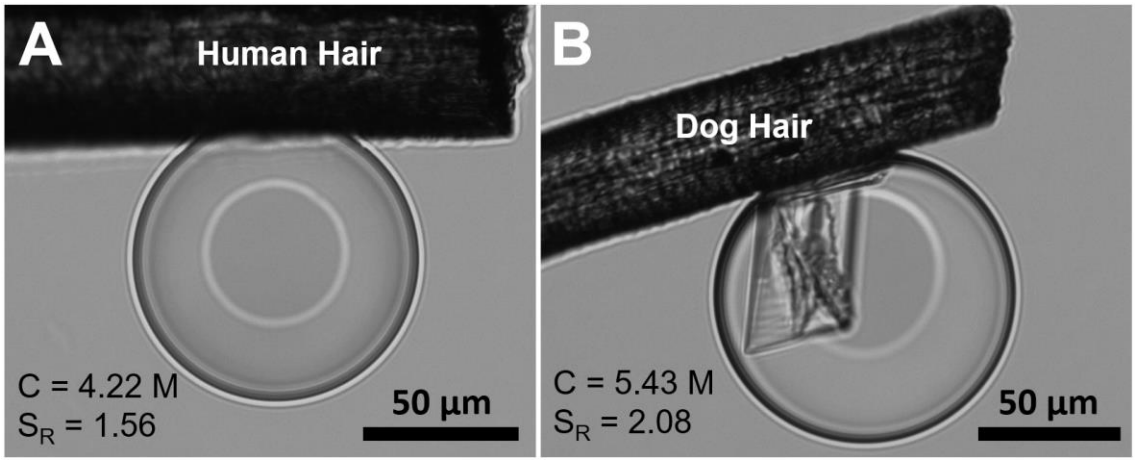


**Figure 121: Typical results of touching (A) human hair and (B) dog hair to a $KNO_3$ droplet at different supersaturations.**

From the full set of Excel spreadsheets containing droplet array data, the 'Supersaturation Ratio' and 'Result' columns were combined into a single table for each nucleant type, and the results were arranged by ascending order of supersaturation ratio. This data was split into groups of 10 rows, and the average supersaturation ratio (with standard deviation) and proportion of droplets which nucleated were calculated within each group (Figure 122).

| Supersaturation ratio | Result | Avg Supersat | Supersat Std Dev | Proportion |
|---|---|---|---|---|
| 1.740 | None | | | |
| 1.752 | None | | | |
| 1.758 | None | | | |
| 1.762 | None | | | |
| 1.765 | Beta | 1.773 | 0.019 | 0.1 |
| 1.780 | None | | | |
| 1.788 | None | | | |
| 1.789 | None | | | |
| 1.795 | None | | | |
| 1.798 | None | | | |
| 1.798 | None | | | |
| 1.806 | Beta | | | |
| 1.811 | None | | | |
| 1.814 | None | | | |
| 1.820 | Beta | 1.830 | 0.022 | 0.3 |
| 1.829 | Beta | | | |
| 1.843 | None | | | |
| 1.855 | None | | | |
| 1.858 | None | | | |
| 1.864 | None | | | |

**Figure 122: A snippet of processed data, showing how data was grouped into subsets of 10 datapoints, which were used to calculate the proportion of droplets which nucleated at an averaged supersaturation ratio value.**

Plotting the cumulative fraction of droplets nucleated against the supersaturation ratio of each datapoint is a more conventional approach, and can be used to gain information about the crystallisation process when the droplet supersaturation is a stochastic independent variable[274]. However, in my work, the droplet supersaturation was an input variable but was not stochastic because droplets were intentionally nucleated. This unfortunately meant that variation in the sampling width of the data would skew its gradient, which is demonstrated with a set of dummy data in Figure 123. The two curves in Figure 123A describe a nucleant with identical nucleation behaviour, but the chosen width between datapoints skews the gradient considerably. Figure 123B shows how this effect was minimised by grouping the data and plotting the fraction of droplets nucleated within that group against the average supersaturation ratio of the group.

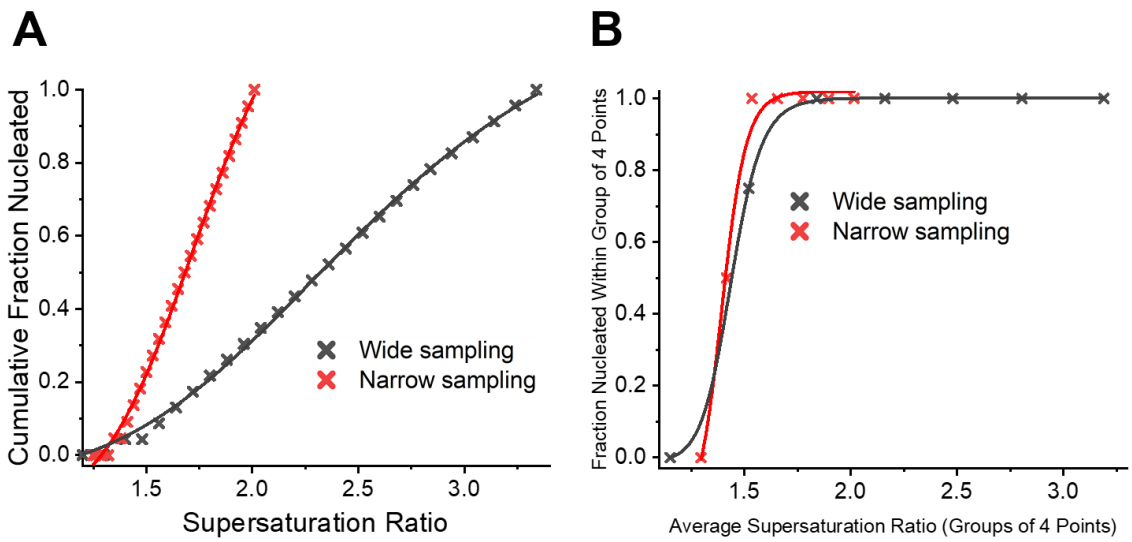


**Figure 123: Dummy data showing the effect of uneven sampling width on data for (A) plotting cumulative fraction of droplets nucleated against supersaturation ratio, and (B) fraction of droplets nucleated within a group against average supersaturation ratio of the group.**

The processed nucleation data were plotted for each nucleant type (Figure 124). The fitted curves shown in Figure 124 are based on a simplified version of Equation 31, which calculates the rate of nucleation on a surface. This is expressed as a sum of all of the rates of nucleation on every site at the surface. Each rate is expressed by a prefactor *A* and a thermodynamic rate parameter *B*. *S* is the supersaturation.

$$Rate = \sum_{i=1}^{n} A_i S e^{\frac{B_i}{ln^2 S}}$$ **Equation 31**

Given that the number of nucleation sites on the hair surface is technically infinite, an approximation is needed to avoid overfitting curves to the data. The equation is therefore approximated to Equation 32, where the two terms represent two classes of nucleation site.

$$Rate = A_1 S e^{\frac{B_1}{ln^2 S}} + A_2 S e^{\frac{B_2}{ln^2 S}}$$ **Equation 32**

The first class comprises sites that are poor nucleators, but which are abundant on the surface. This is seen in the high exponential prefactor $A$, and low exponent $B$. The second class comprises sites that are much higher in activity, but which are scarce on the surface. These have a low prefactor (because this encompasses the probability of the site being expressed) and a high exponent. Curve fitting was performed by iterating $A_1$, $B_1$, $A_2$ and $B_2$ to minimise $\chi^2$.

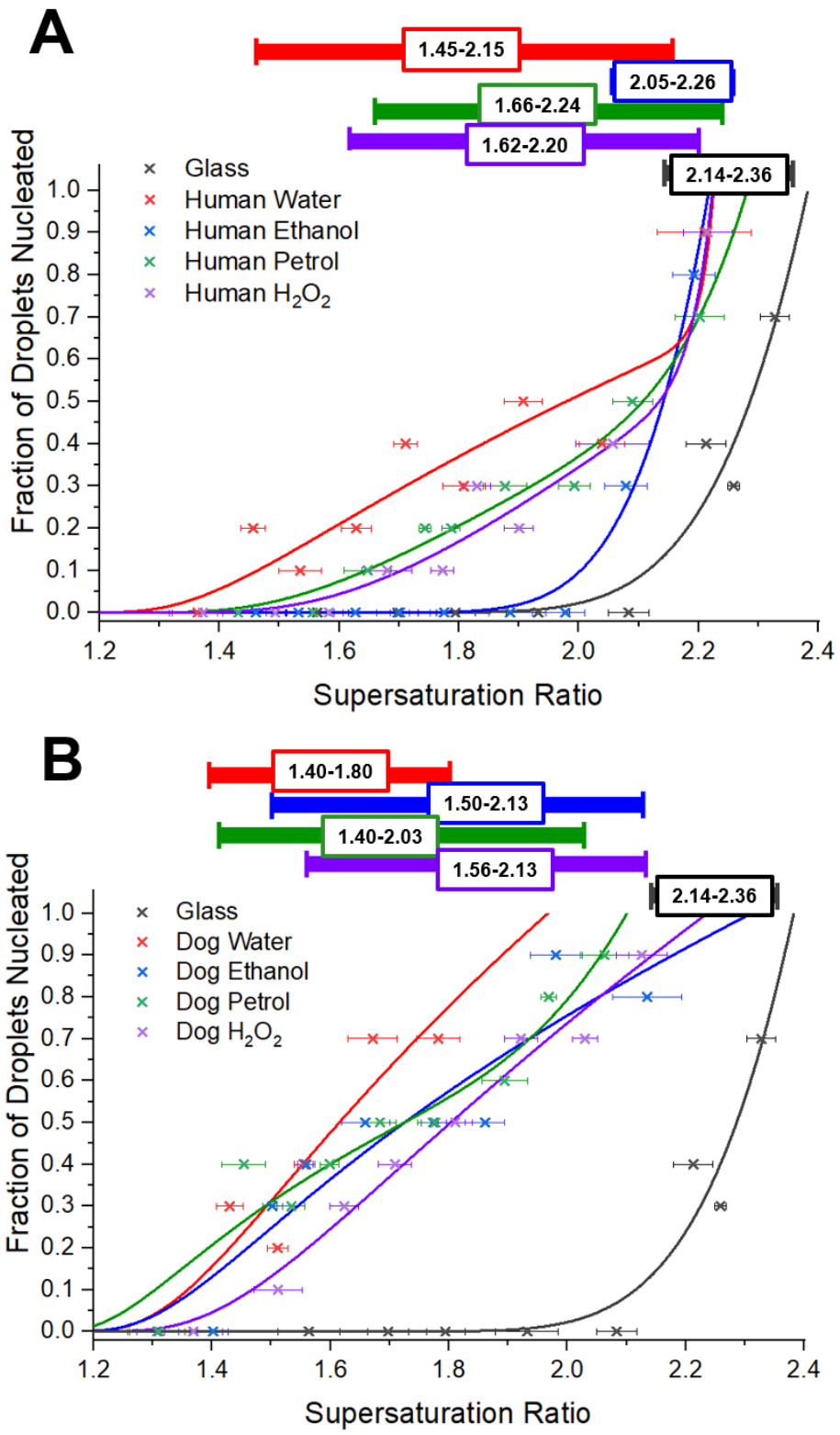


**Figure 124: Graphs showing the fraction of $KNO_3$ droplets nucleated vs. the supersaturation ratio. (A) Human hair after various treatments compared to pristine glass. (B) Dog hair after various treatments compared to pristine glass. The bars at the top show the supersaturation of $KNO_3$ at which the first nucleation event was recorded (onset) and the highest supersaturation at which a droplet did not nucleate (endpoint).**

The results show that all hair samples were able to nucleate $KNO_3$ at lower supersaturations than glass, and dog hair was the more effective nucleant for $KNO_3$ of the two types tested. Most of the chemical treatments made little difference to the efficacy of the hair, aside from ethanol treatment for human hair, where a dramatic loss of activity was recorded.

### 5.4.2 $CaCO_3$ Crystallisation on Hair

In contrast to the $KNO_3$ studies, $CaCO_3$ grows much more slowly relative to its nucleation rate, which means that many crystals could grow on a hair surface in a single experiment. The number densities of crystals produced on each hair type can therefore be compared, and their spatial distributions evaluated to help to establish where the key nucleation sites were located.

#### 5.4.2.1 Bulk-Phase $CaCO_3$ Crystallisation on Hair

The same treatment methods used in the $KNO_3$ experiments were employed, where human and dog hairs were washed with water, ethanol or petroleum ether, or were treated with $H_2O_2$. Each hair was immersed in a 5 mL solution of $CaCl_2$ (2.5 mM) and $Na_2CO_3$ (2.5 mM) and were left to crystallise for 20 minutes. After being washed with water, the hairs were imaged by SEM (Figure 125 and Figure 126).

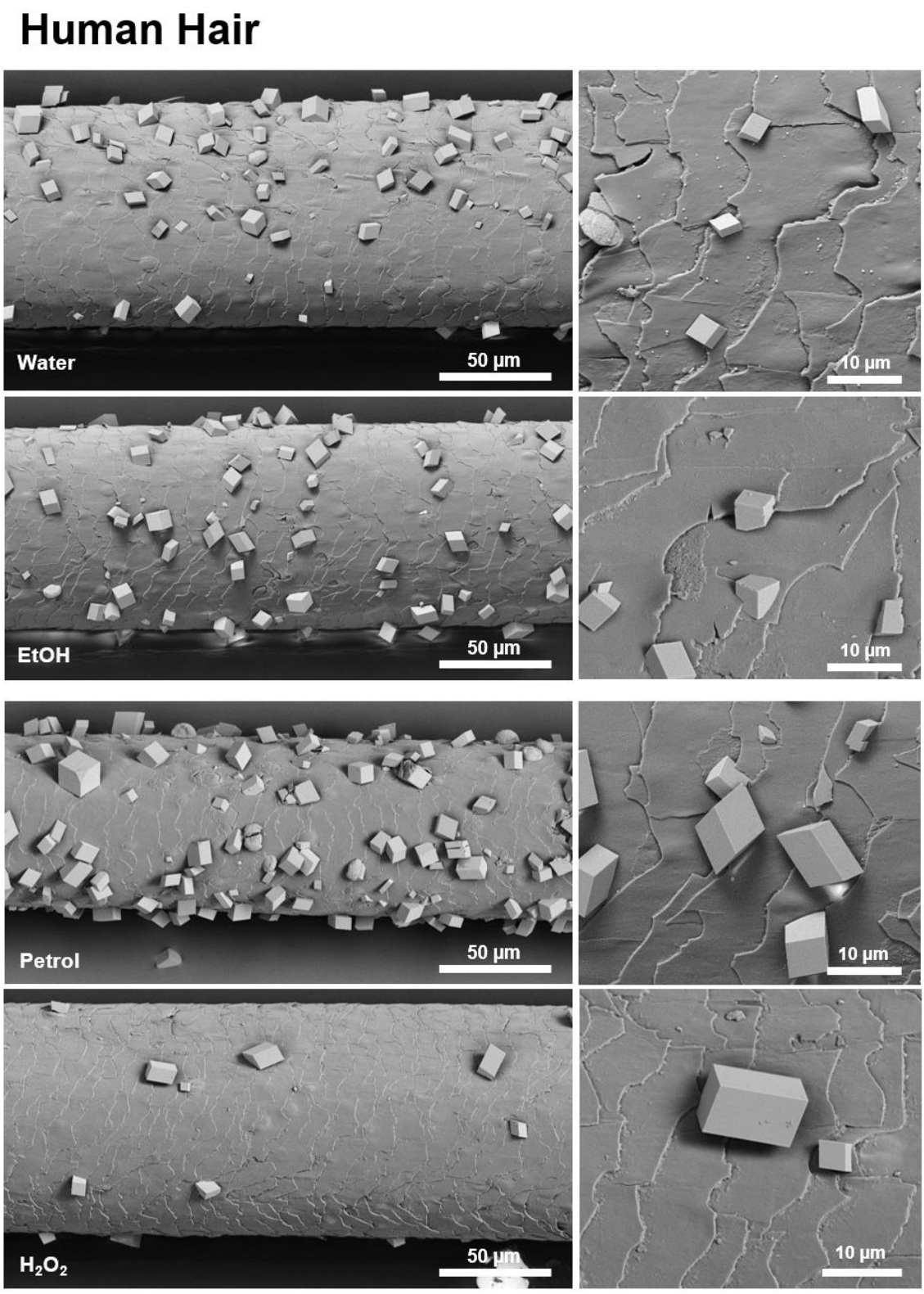


**Figure 125: SEM images showing results of crystallising $CaCO_3$ on human hair after various chemical treatments.**

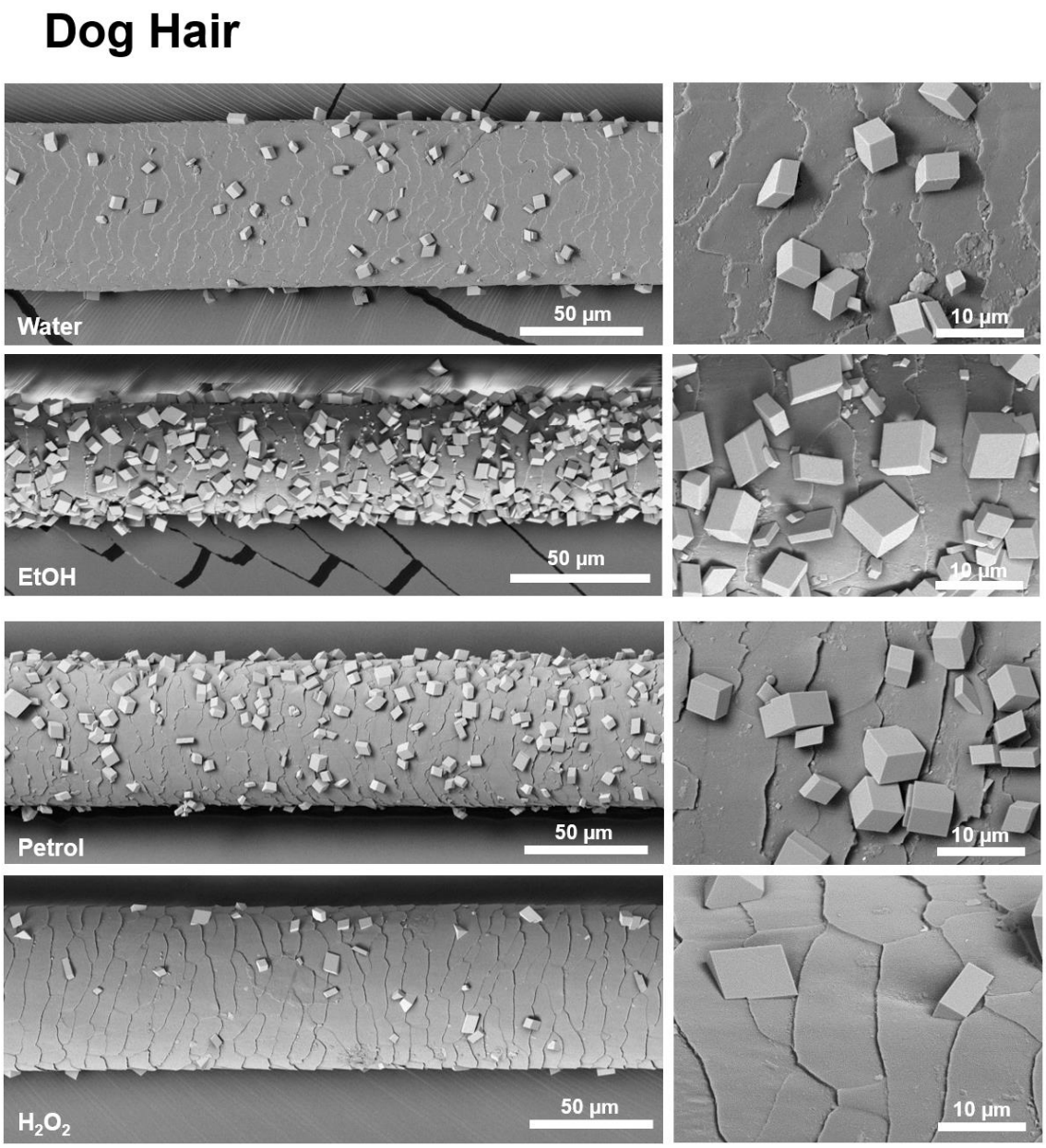


**Figure 126: SEM images showing results of crystallising $CaCO_3$ on dog hair after various chemical treatments.**

Three SEM images were taken for each hair type, and the numbers of crystals on each hair were counted (an example is shown in Figure 127).

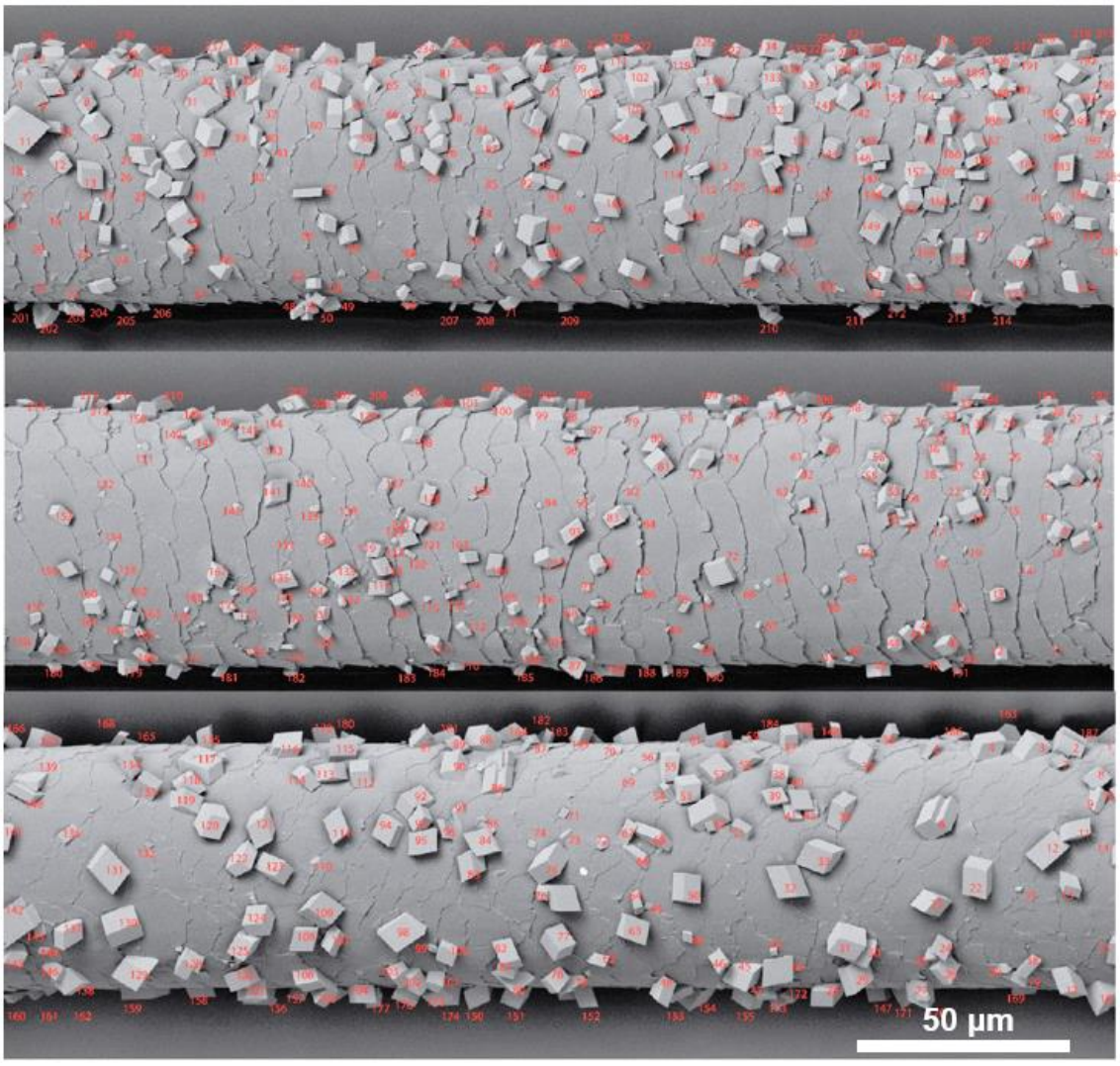


**Figure 127: Three SEM images of $CaCO_3$ crystals embedded in hairs were taken for each hair type, and the number of crystals counted. Here, the dataset for dog hair treated with petroleum ether is shown.**

By first calculating the projected surface area of the hair in each image, Equation 33 allowed the number density of crystals to be calculated, where *r* was measured as half of the average width of each hair and *l* was the length.

$$Number\ density = \frac{N_{crystals}}{\pi r l} \qquad \textbf{Equation 33}$$

A bar chart comparing the number densities of crystals is shown in Figure 128, where, as with the $KNO_3$ data, pristine glass was used as a reference point (again averaging nucleation density measurements from three images).

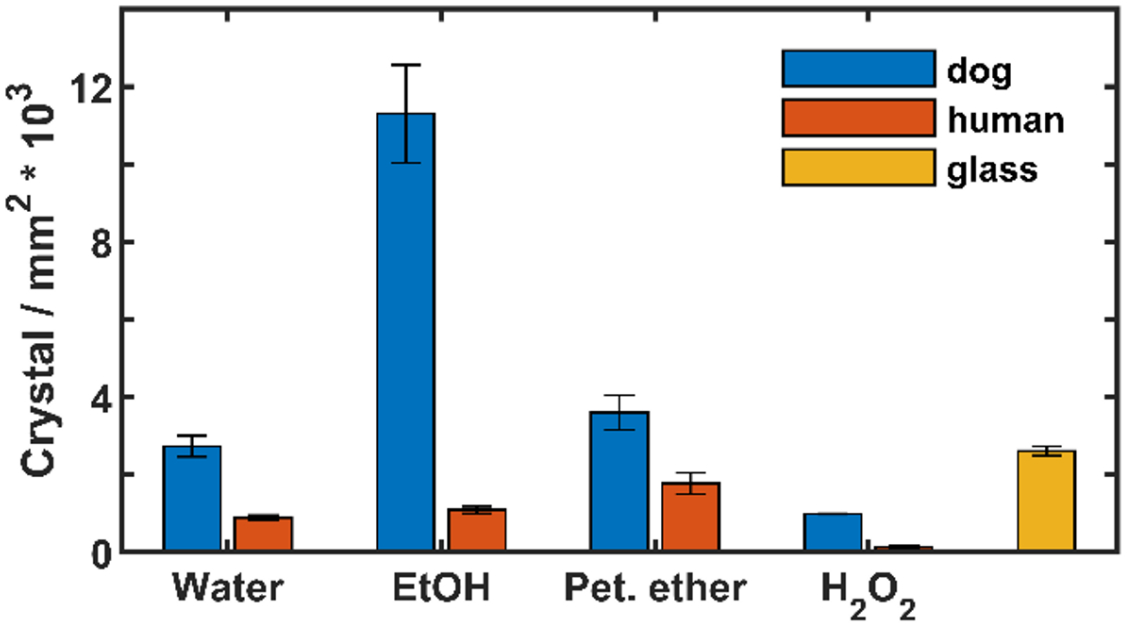


**Figure 128: Bar chart comparing the number densities of $CaCO_3$ crystals produced on each hair type and treatment.**

As is shown, all dog hair samples nucleated more crystals than the human hair after equivalent chemical treatments. Pristine glass was more effective than any of the human hair samples, but was less effective than dog hair treated with either ethanol or petroleum ether. As for the chemical treatments, treating hairs with ethanol or petroleum ether increased the numbers of crystals produced, with ethanol drastically increasing the number of crystals formed on dog hair. $H_2O_2$ treatment significantly reduced the crystallisation of $CaCO_3$ on both human and dog hair, and was almost completely suppressed on human hair.

### 5.4.2.2 Locating Nucleation Sites by Resin Exfoliation of Crystals

As shown in Figure 125 and Figure 126, crystals often appeared to be located close to the hair cuticle edges. However it was difficult to assess this. A resin exfoliation method was therefore developed where the crystal-encrusted hair was placed onto liquid resin and was allowed to cure. The hair was then pulled away, leaving an imprint of the hair with the crystals embedded and their bases exposed (Figure 129).

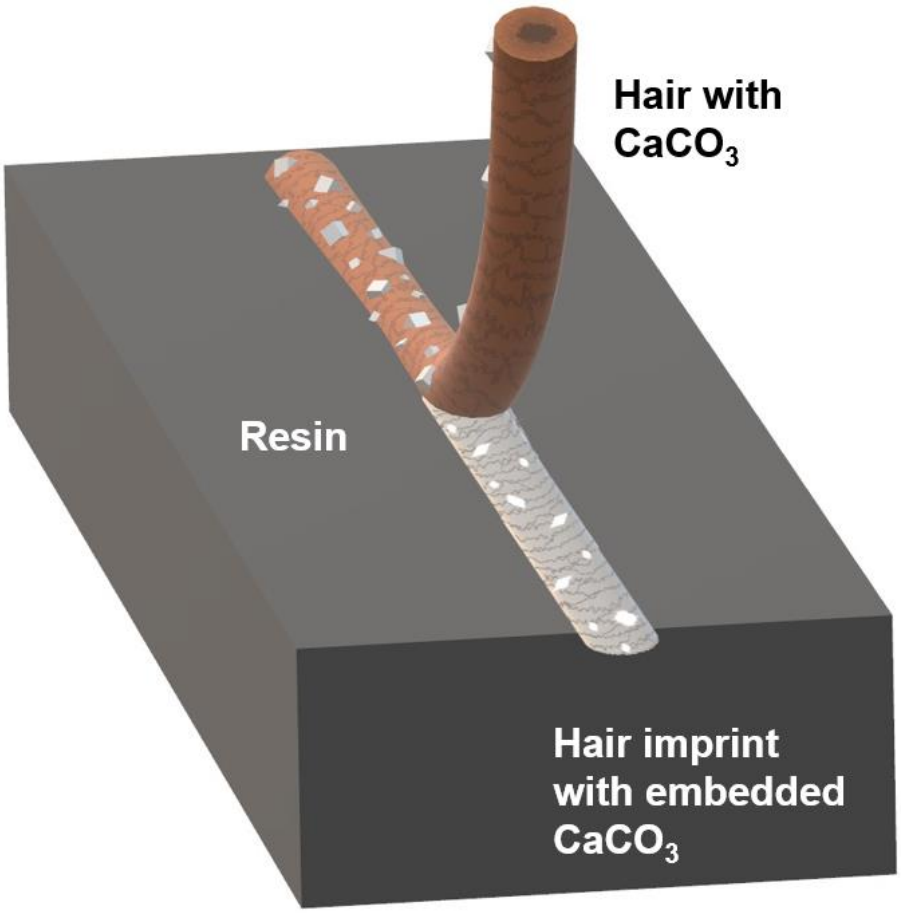


**Figure 129: Diagram showing how resin was used to exfoliate crystals from hairs, creating an imprint to be analysed by SEM.**

Each of these imprints was analysed by SEM, as shown in Figure 130 and Figure 131. The high electron density of the calcite crystals makes them appear bright, such that they stand out against the darker and lower electron density resin. Where crystals had nucleated directly on cuticle edges, their morphology was templated by the hair surface. In all samples, a greater proportion of crystals were located at the cuticle edges than on the flat face of the cuticles. This was especially true for hairs treated with EtOH and $H_2O_2$, where cuticle edges appeared to be the primary nucleation sites.

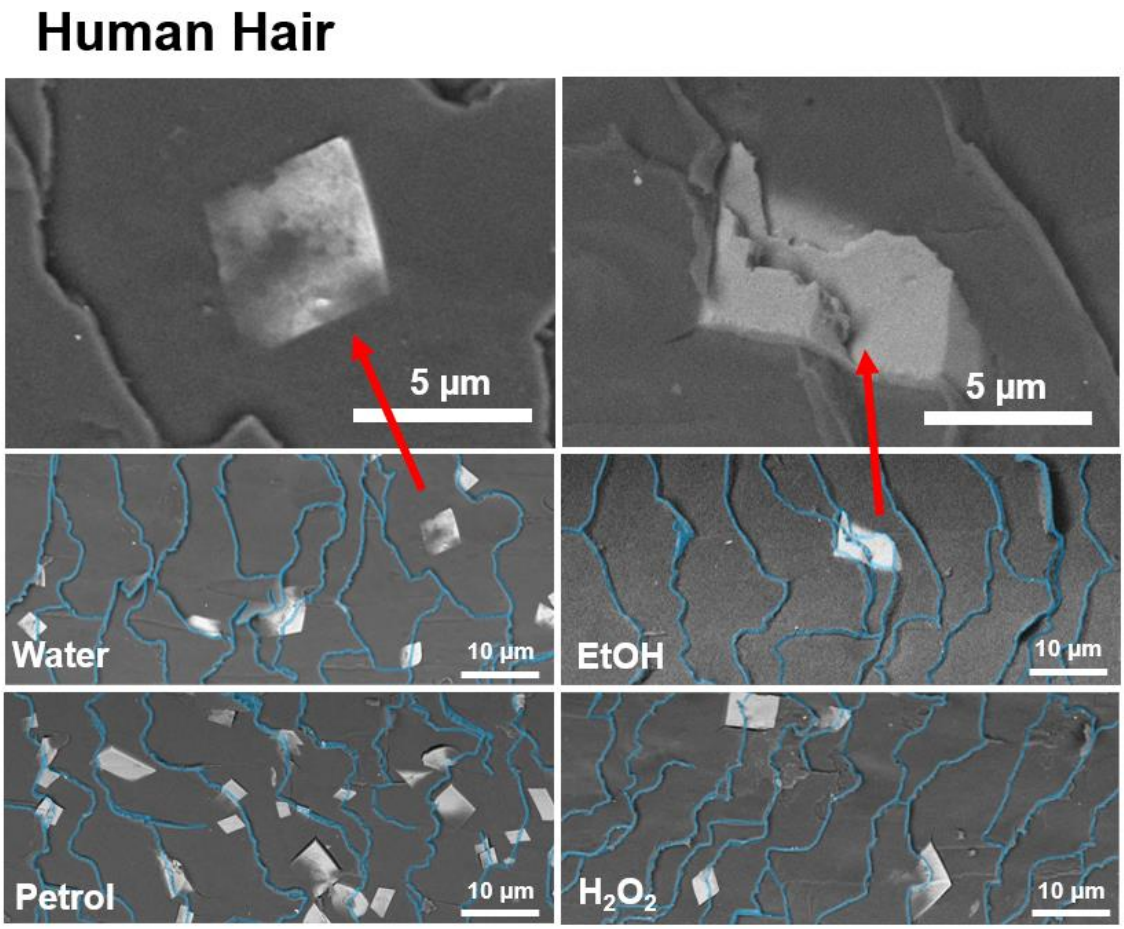


**Figure 130: SEM images showing imprints of human hairs (after various chemical treatments) in conductive carbon resin, embedded with $CaCO_3$ crystals with their undersides exposed. Blue outlines mark the cuticle edges, and red arrows direct the eye to enlarged images of crystals.**

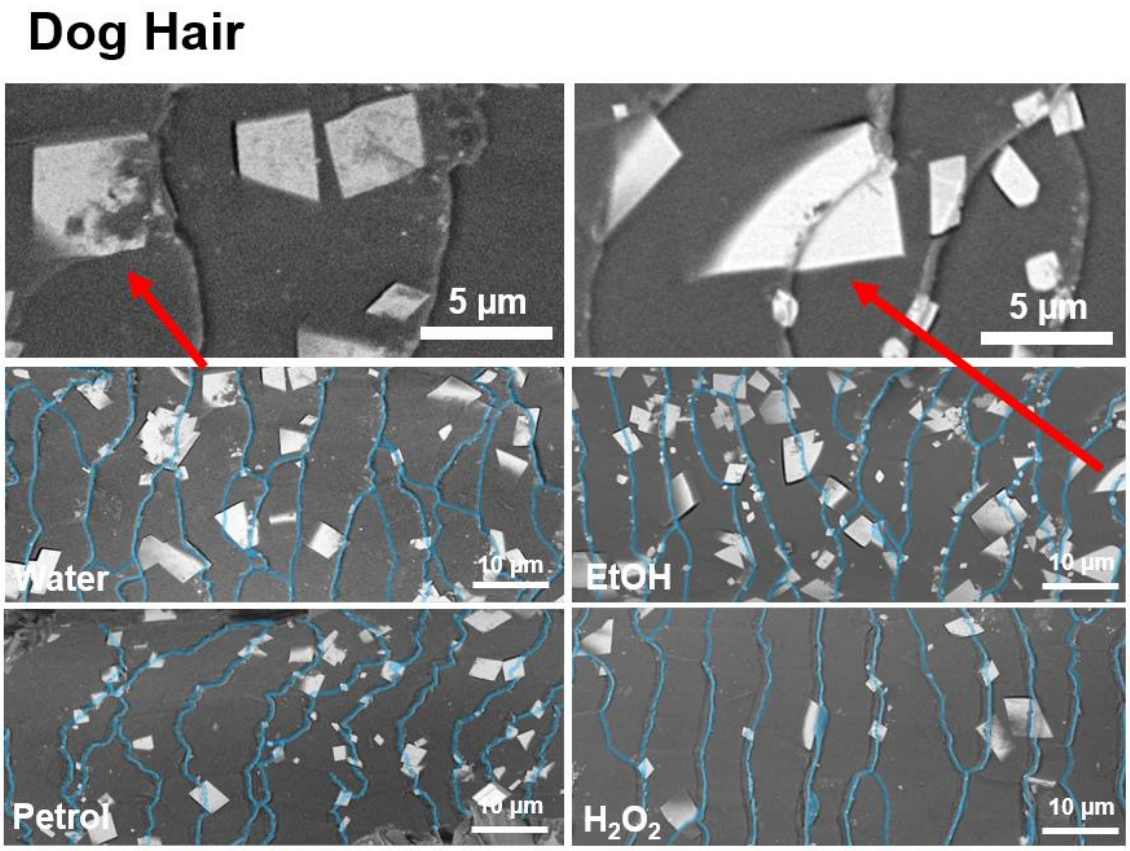


**Figure 131: SEM images showing imprints of dog hairs (after various chemical treatments) in conductive carbon resin, embedded with $CaCO_3$ crystals with their undersides exposed. Blue outlines mark the cuticle edges, and red arrows direct the eye to enlarged images of crystals.**

### 5.4.3 Surface Analysis of Hair

The surface chemistry, charge and topography of the hairs was characterised using x-ray photoelectron spectroscopy (XPS), scanning ion-conductance microscopy (SICM) and atomic force microscopy (AFM) in order to rationalise results from the $KNO_3$ and $CaCO_3$ crystallisation experiments.

#### 5.4.3.1 Surface Chemistry Analysis – X-Ray Photoelectron Spectroscopy (XPS)

XPS spectra of human and dog hair were recorded following all chemical treatments using an ultra-low vacuum spectrometer (an image taken during measurements is shown in Figure 132).

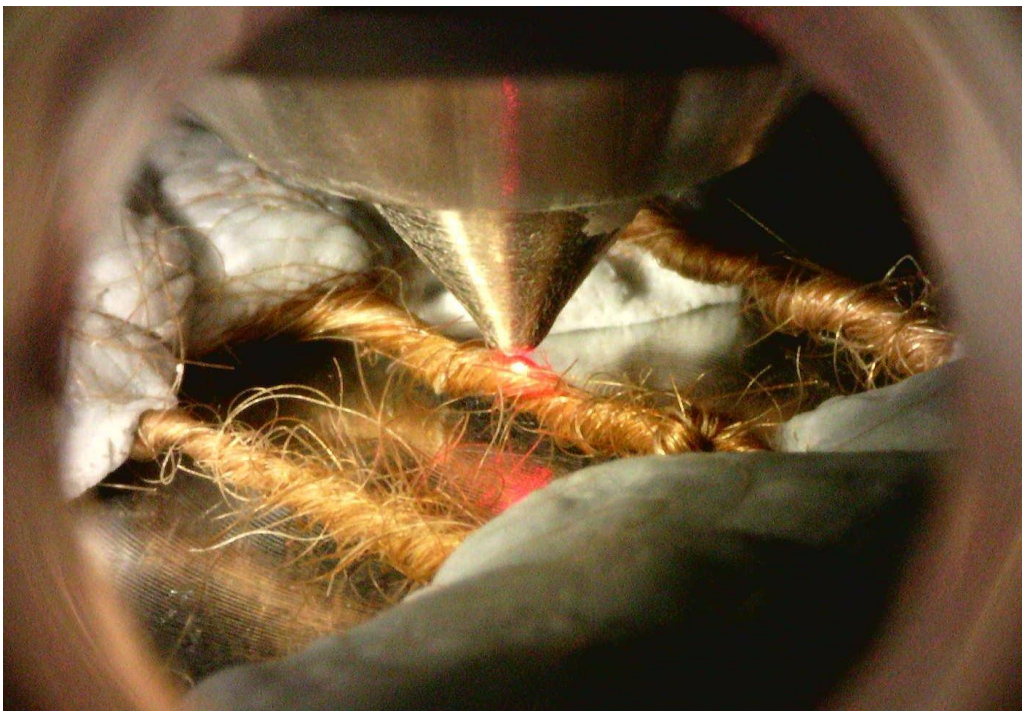

**Figure 132: Dog hair samples were twisted into tight bundles for XPS measurements.**

A typical XPS survey scan of a dog hair is shown in Figure 133. The O 1s signal appears at 533 eV, N 1s at 400 eV, C 1s at 285 eV, and S 2p at 164 eV.

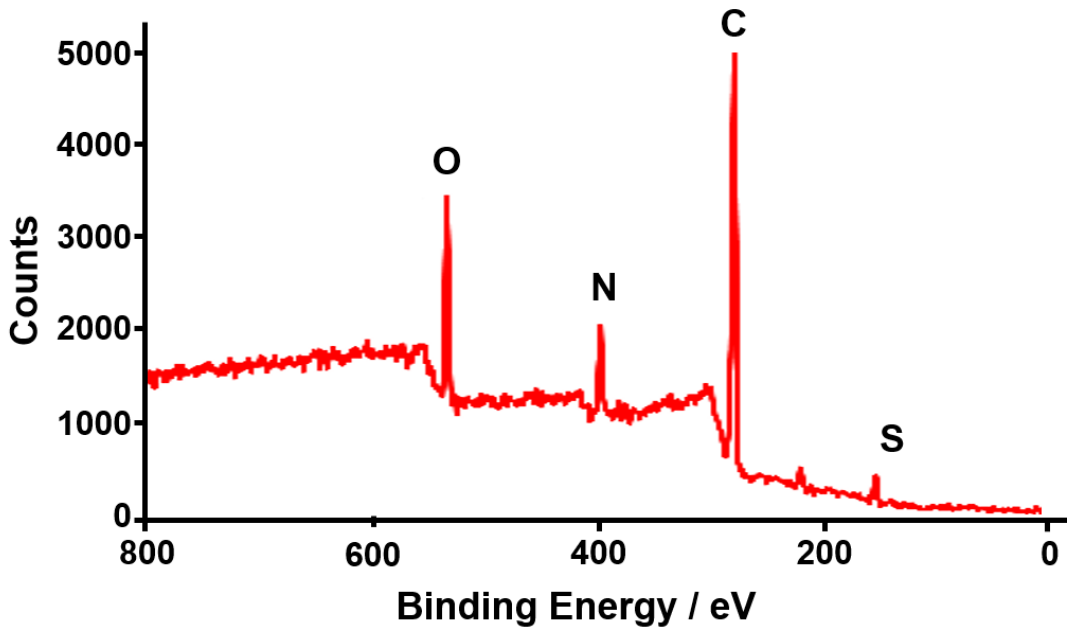


**Figure 133: XPS survey spectrum of petroleum ether treated dog hair, showing the O, N, C and S regions of the signal.**

The characteristic spectral bands from the XPS data (i.e. C 1s, S 2p) were analysed using CasaXPS. Peak intensities were then integrated and used to calculate the elemental composition and oxidation states of atoms at the surface (hydrogen is not detected by XPS). The carbon content of human hair was relatively insensitive to any of the treatments (Figure 134A), and contributed around 70% of the composition of the surface in all human hair samples. The carbon content of dog hair was highly sensitive to treatment with ethanol and petroleum ether, dropping 15% and 10% respectively. The drop in carbon content was assumed to be indicative of the removal of unbound lipids from the hair surface.

The nitrogen signal for human hair was also indifferent to any of the treatments. For dog hair treated with ethanol and petroleum ether, an inverse relationship was identified between its nitrogen and carbon content. This is consistent with the suggestion that removal of unbound lipids exposes more (nitrogen-containing) protein. Interestingly, a drop in the nitrogen signal was detected after $H_2O_2$ treatment of dog hair but not human hair. This suggests that nitrogen was lost with no concomitant change in the carbon content.

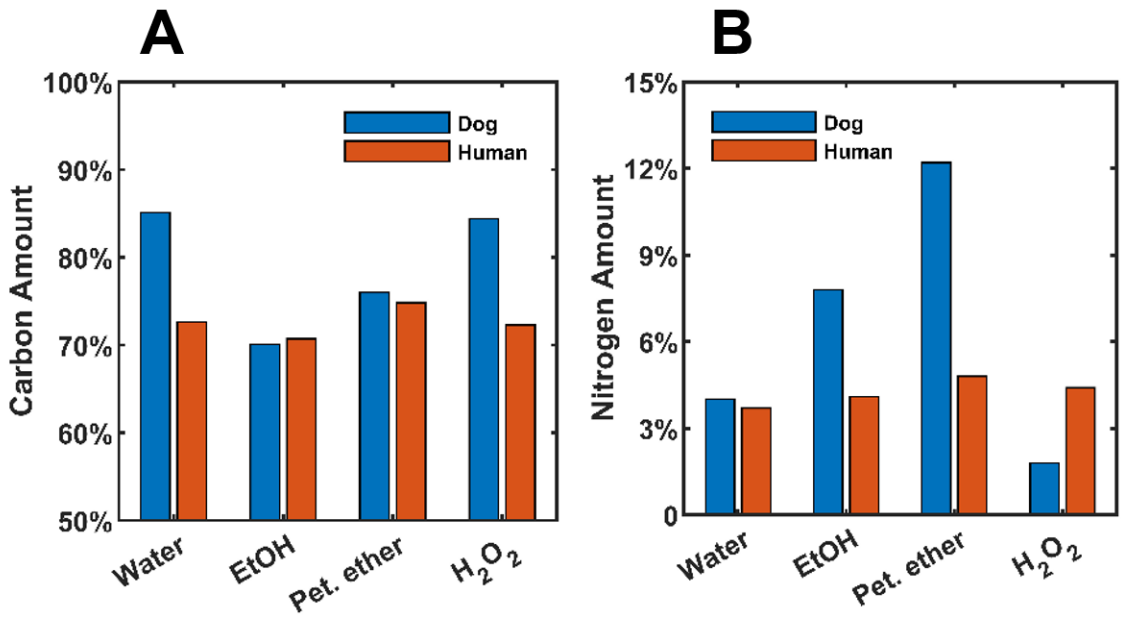


**Figure 134: Elemental compositions calculated from XPS integrated peak intensities for (A) carbon and (B) nitrogen.**

The sulfur 2p region was found to be the most valuable part of the spectrum for assessing the oxidation state of the hair surface. Sulfur is found in the cysteine residues of keratin, both as disulfide groups (-1 oxidation state) and thiol groups which bond lipids to the surface (-2 oxidation state). Sulfur is the only species which is expected to appreciably oxidise following $H_2O_2$ treatment in these experiments, forming sulfonates (oxidation state +4).

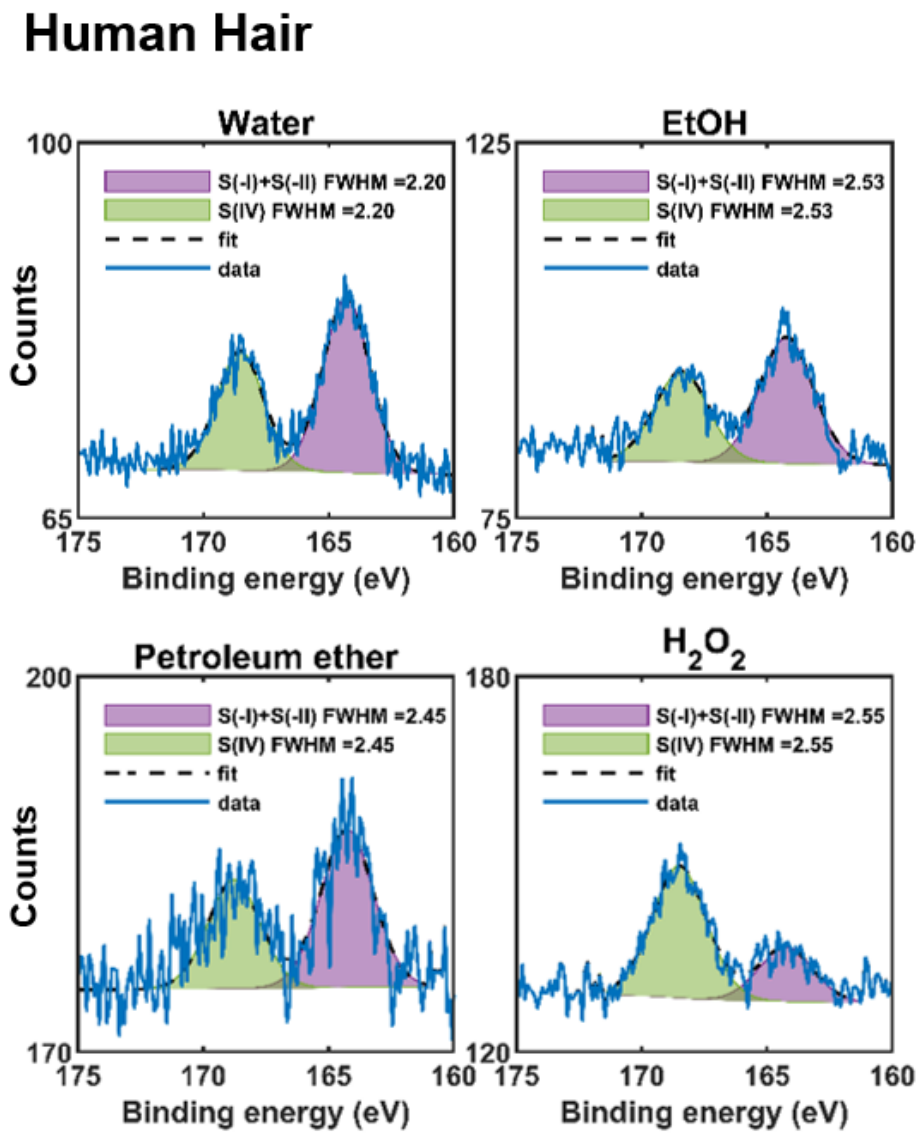


**Figure 135: Fitted S 2p XPS spectra for human hair after various chemical treatments.**

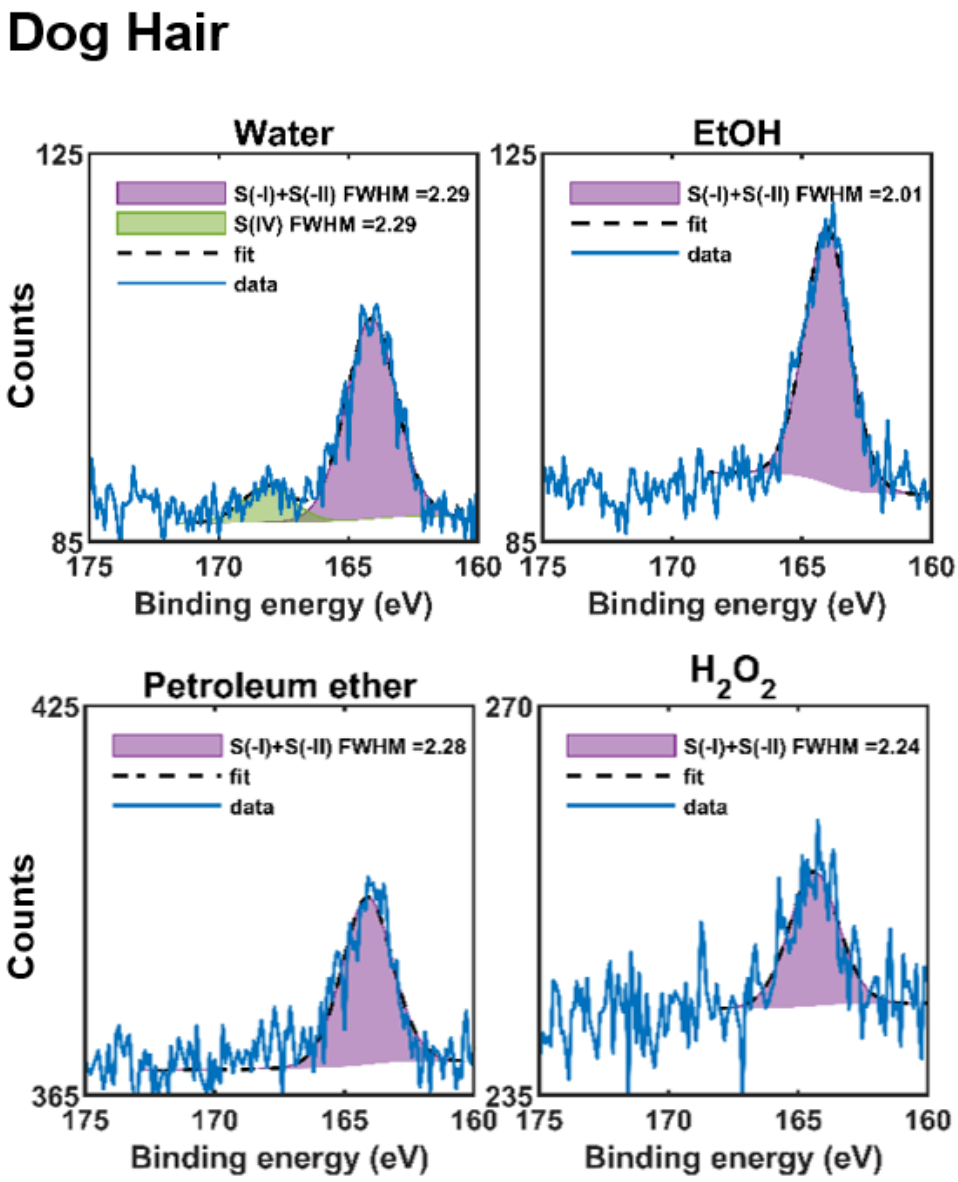


**Figure 136: Fitted S 2p XPS spectra for dog hair after various chemical treatments.**

Once fitted, the ratio of peak intensities was used to determine the ratio of reduced to oxidised sulfur at each hair surface (Figure 137). It was found that water-washed human hair contained a substantial amount of pre-existing oxidised sulfur at its surface, whereas dog hair contained only a small amount. The remaining reduced sulfur groups in human hair were oxidised to sulphonate groups with hydrogen peroxide treatment, but dog hair was remarkably resistant to the same treatment.

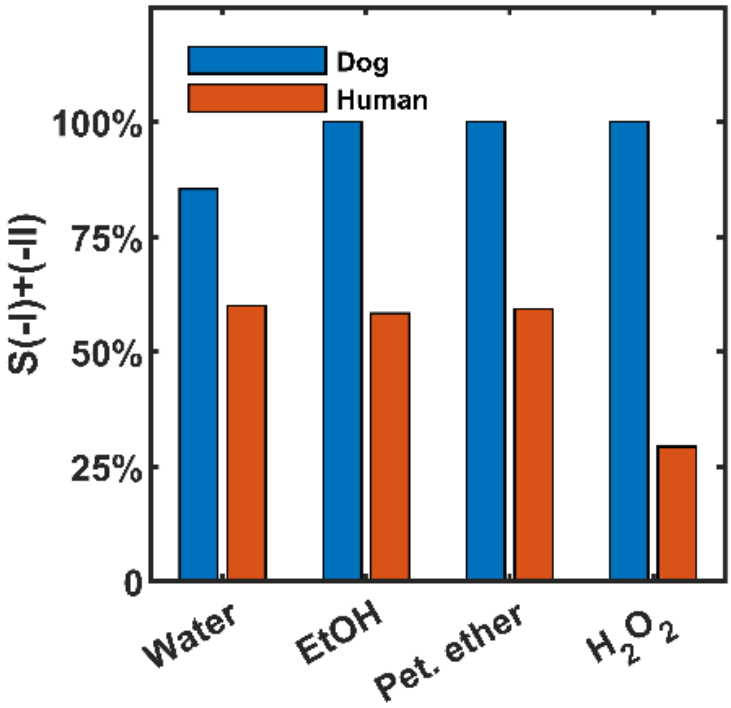


**Figure 137: Proportion of total sulfur which exists in the native, reduced state (thiol/disulfide). The rest of the sulfur contribution is oxidised (sulfonate).**

To improve confidence in this result and provide additional data, more samples were analysed by near-ambient pressure (NAP) XPS. Three samples were measured: dog hair treated with petroleum ether, $H_2O_2$, or petroleum ether followed by $H_2O_2$ (Figure 138). Again, there was little to no oxidised sulfur present after $H_2O_2$ or petroleum ether treatment. Also, no oxidised sulfur was present on the dog hair following both treatments, which showed that unbound lipids were not responsible for protecting the surface from oxidation. If they had, then their removal by petroleum ether would have facilitated their oxidation by $H_2O_2$.

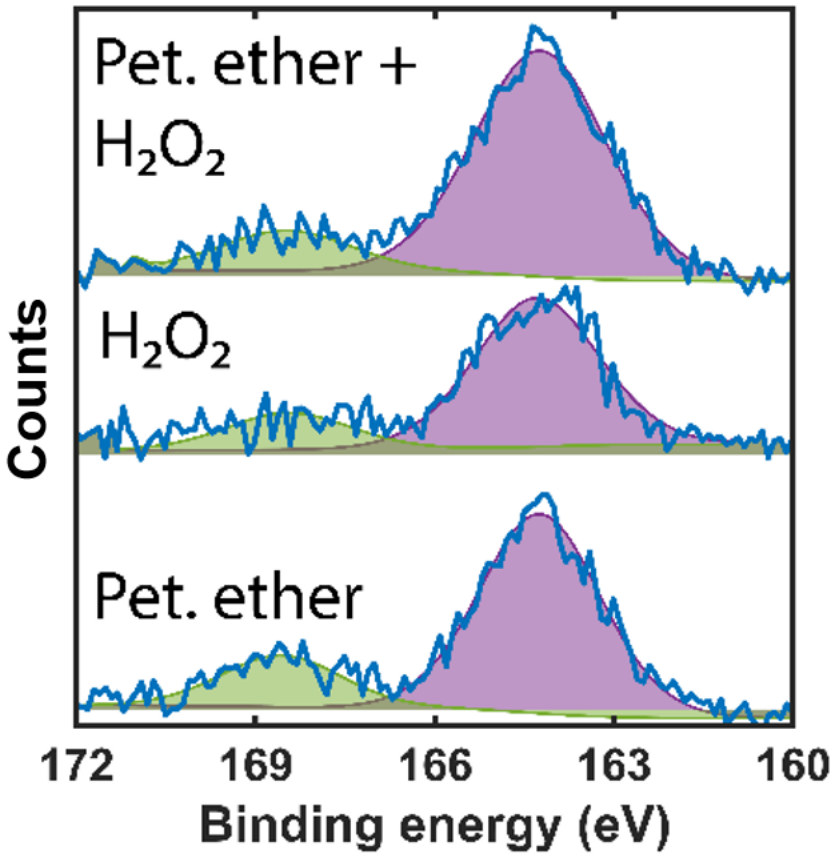


**Figure 138: Environmental XPS S 2p scans showing signals from reduced (purple) and oxidised (green) sulfur species after petroleum ether treatment, $H_2O_2$ treatment, and petroleum ether treatment followed by $H_2O_2$ treatment.**

#### 5.4.3.2 Surface Charge Analysis – Scanning Ion-Conductance Microscopy (SICM)

Scanning ion-conductance microscopy was performed to try to understand how surface charge might have impacted the nucleation efficacy of the surfaces. When the nanopipette was scanned across the hair surface, the ionic current measured by the Ag/AgCl electrodes not only measured the topography of the surface through its proximity to the nanopipette tip, but also the charge of the surface. Figure 139 shows the distribution of surface charges from these measurements for ethanol-treated human and dog hairs, and $H_2O_2$ treated dog hairs. Ethanol-treated dog hairs were more negatively charged than ethanol-treated human hairs. The dog hair also became more negatively charged when treated with $H_2O_2$, indicating that a chemical change had occurred. However,

there were small regions of ethanol washed dog hair that were more negatively charged than either of the other samples.

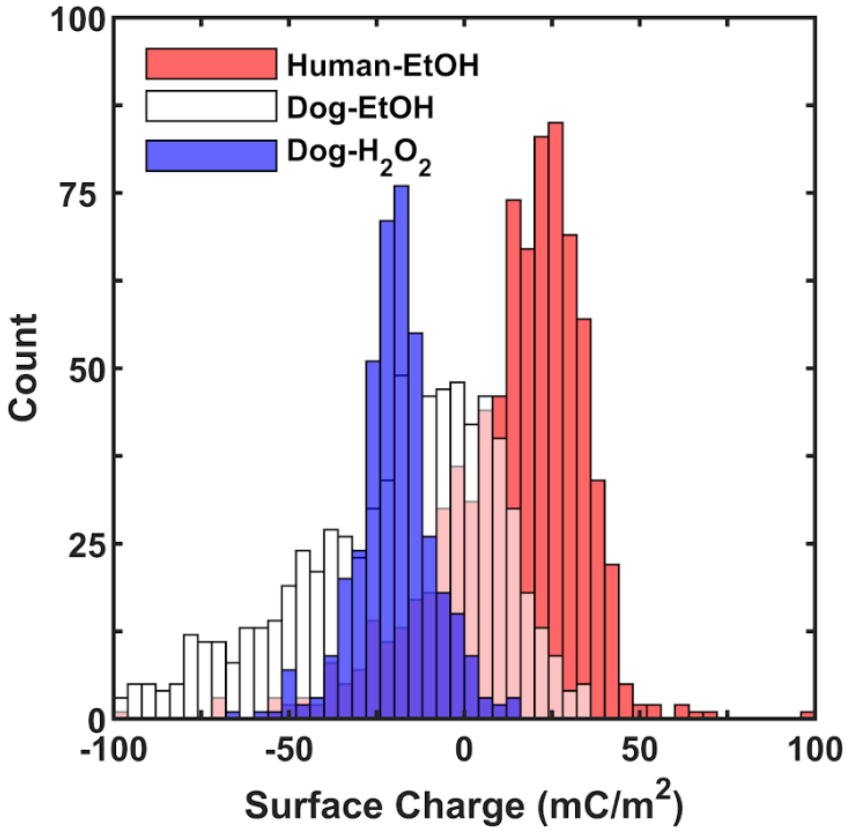


**Figure 139: Distribution of surface charges measured by SICM surface charge mapping of ethanol-treated human and dog hairs, and $H_2O_2$ treated dog hairs.**

The spatial distribution of charges was further investigated by constructing a correlated topography and surface charge map over two sets of cuticle edges of an ethanol-treated dog hair using SICM. One of the cuticle edges appeared to be much more negatively charged than the other. This site of unusual surface charge likely also carried a unique surface chemistry, which may identify it as a nucleation site.

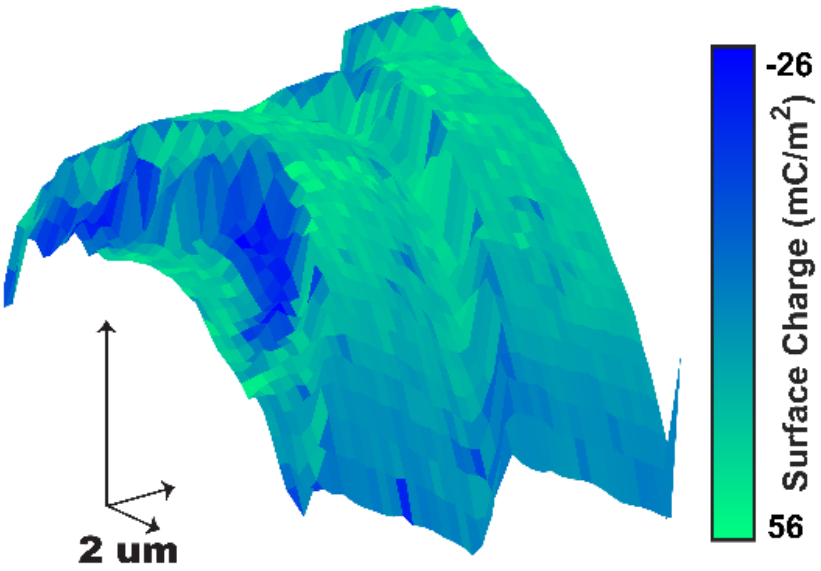


**Figure 140: SICM correlated topography and surface charge map of two sets of cuticle edges of an ethanol-treated dog hair.**

### 5.4.3.3 Surface Topography Analysis – Atomic Force Microscopy (AFM)

Atomic force microscopy was performed to identify any major topographical differences between dog and human hair (Figure 141). The fibrillar structure of the surface of human hair was faint and poorly aligned. Dog hair on the other hand, had a prominent fibrillar structure, consisting of undulating ridges with a periodicity of 100-200 nm.

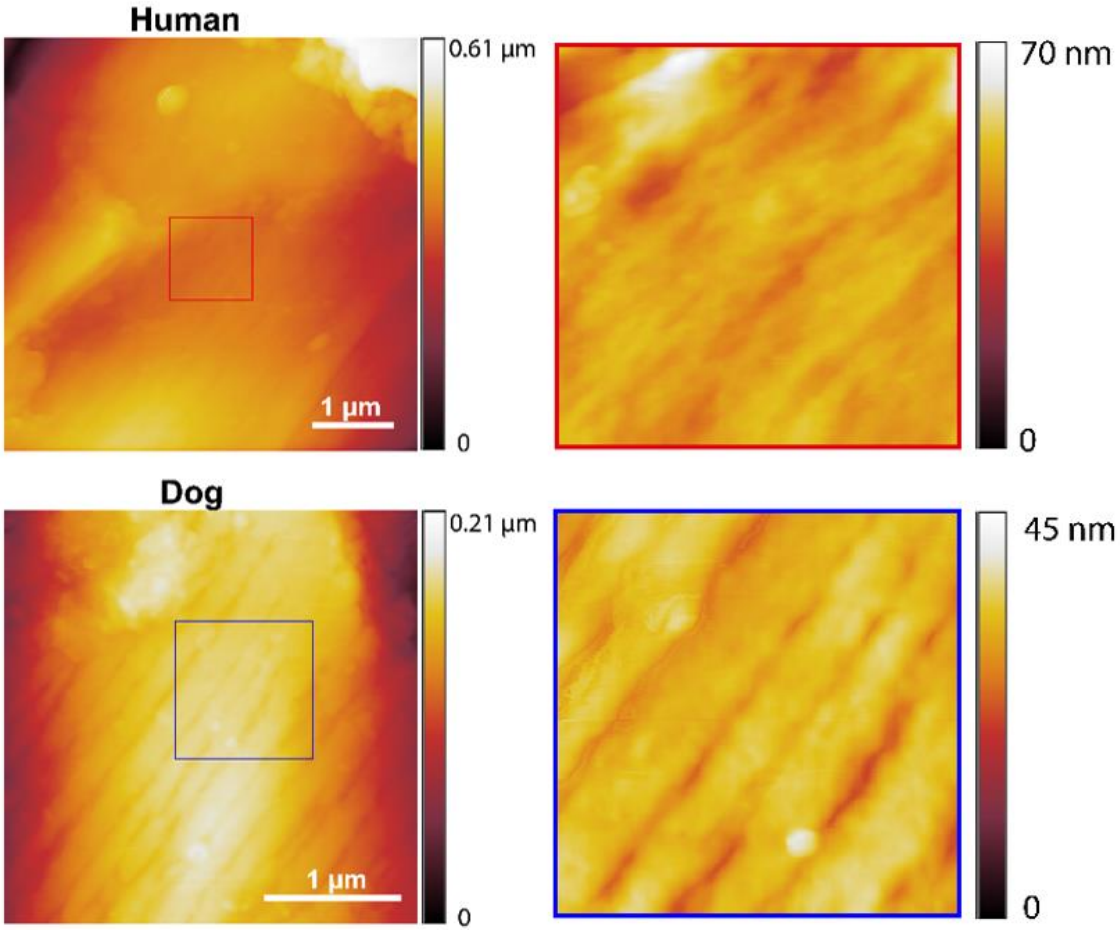


**Figure 141: Atomic force microscopy (AFM) images showing the topography of ethanol-treated human and dog hairs.**

### 5.4.4 Crystallisation of Other Sparingly Soluble Minerals on Hair

The results of the $KNO_3$ and $CaCO_3$ crystallisation experiment showed that dog hair treated with ethanol was the most promising universal nucleant. The breadth of this universality was investigated by crystallising a range of minerals ($CaSO_4$, $BaSO_4$, $SrSO_4$, $BaCO_3$, $CuCO_3$ and $CaF_2$) on these hair samples (Figure 142). A high density of crystals of all minerals tested formed on the ethanol-treated dog hair. $CaF_2$ in particular appeared to nucleate predominantly at the cuticle edges, providing further evidence for these being the most active nucleation sites.

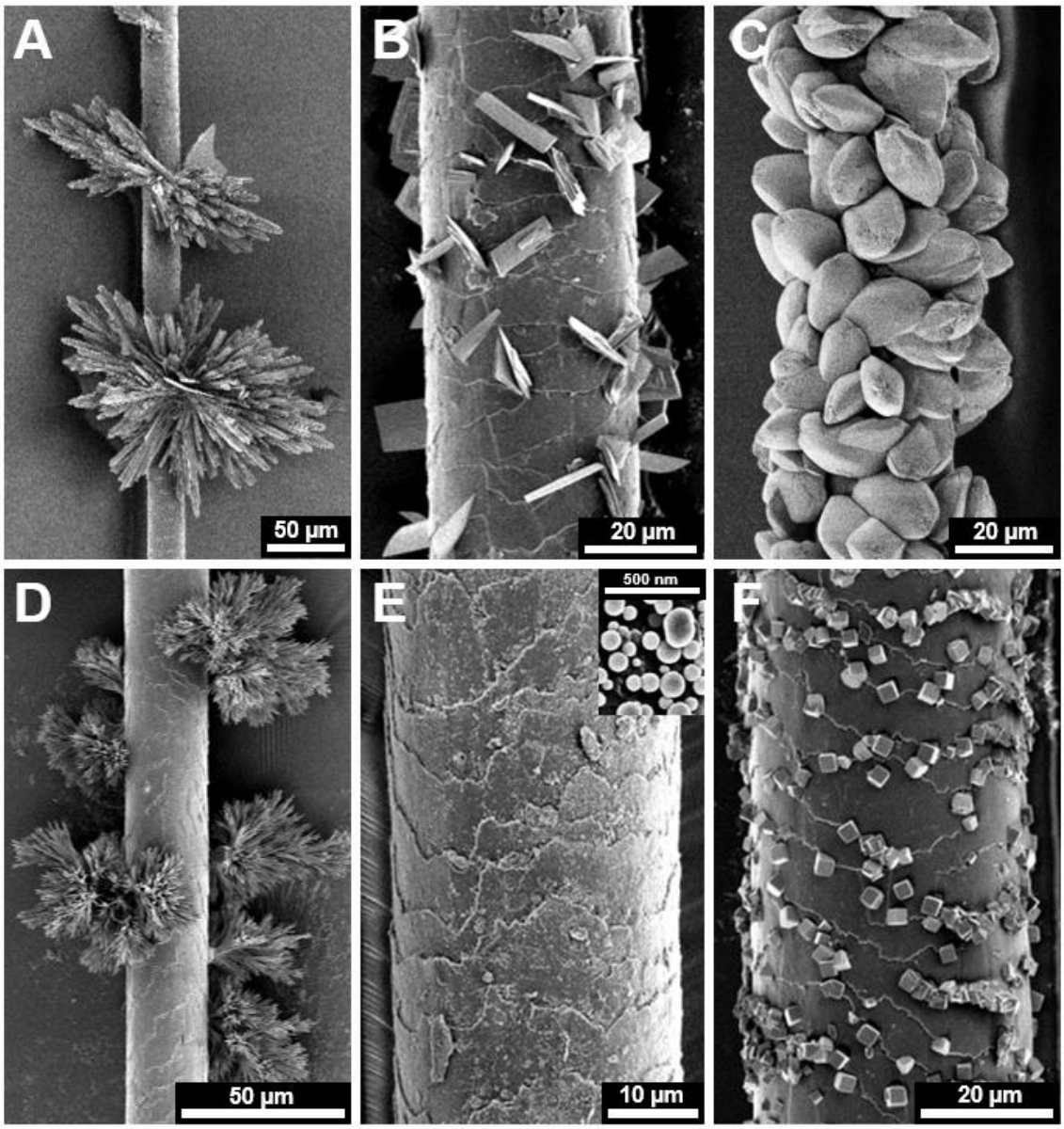


**Figure 142: SEM images showing (A) $CaSO_4$ (B) $BaSO_4$ (C) $SrSO_4$ (D) $BaCO_3$ (E) $CuCO_3$ (F) $CaF_2$ grown on ethanol-treated dog hair.**

### 5.4.5 $CaCO_3$ Crystallisation on Other Animal Hairs

The diverse range of morphologies expressed by different animals offered a unique opportunity to discover some highly effective crystal nucleants. Several hair samples from different animals were acquired, and $CaCO_3$ was crystallised to assess how these surfaces behaved as nucleants, both in terms of the density of crystals produced as well as the locations of these crystals (Figure 143 and Figure 144).

Of the hairs tested, only three were comparatively poor at nucleating $CaCO_3$ crystals – mole, bat and elk. Interestingly, although each of these hair types exhibited different sizes and cuticular structures, crystals were observed exclusively at the cuticles. Squirrel and camel hair more closely resemble human and dog hair in terms of size and morphology, and performed similarly to these hair types at producing $CaCO_3$ crystals. The most striking result, however, came from crystallization of $CaCO_3$ upon mink hair, where the most abundant polymorph switched from calcite to vaterite, as confirmed by Raman spectroscopy (Figure 145).

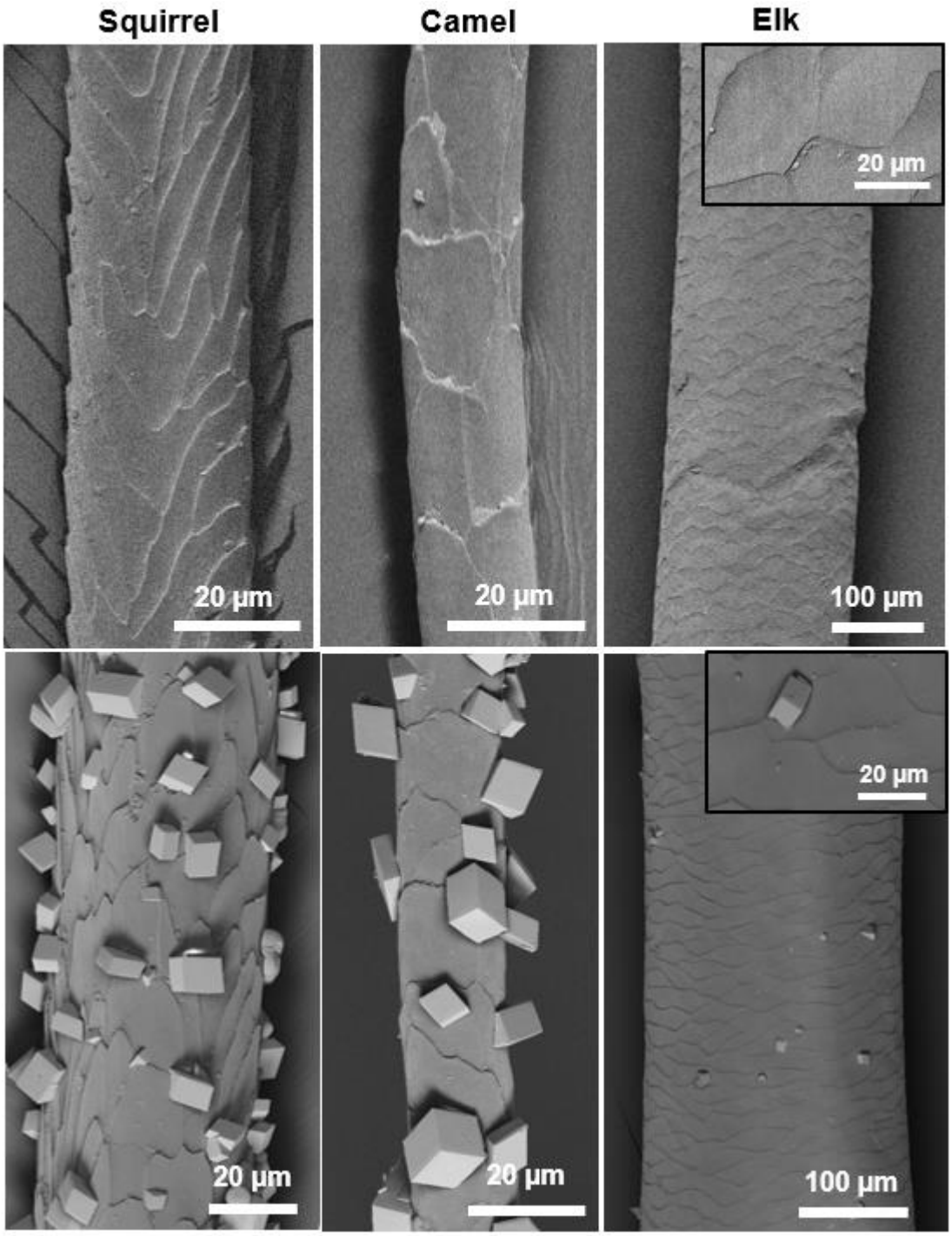


**Figure 143: SEM images showing $CaCO_3$ crystals grown on squirrel, camel and elk hairs.**

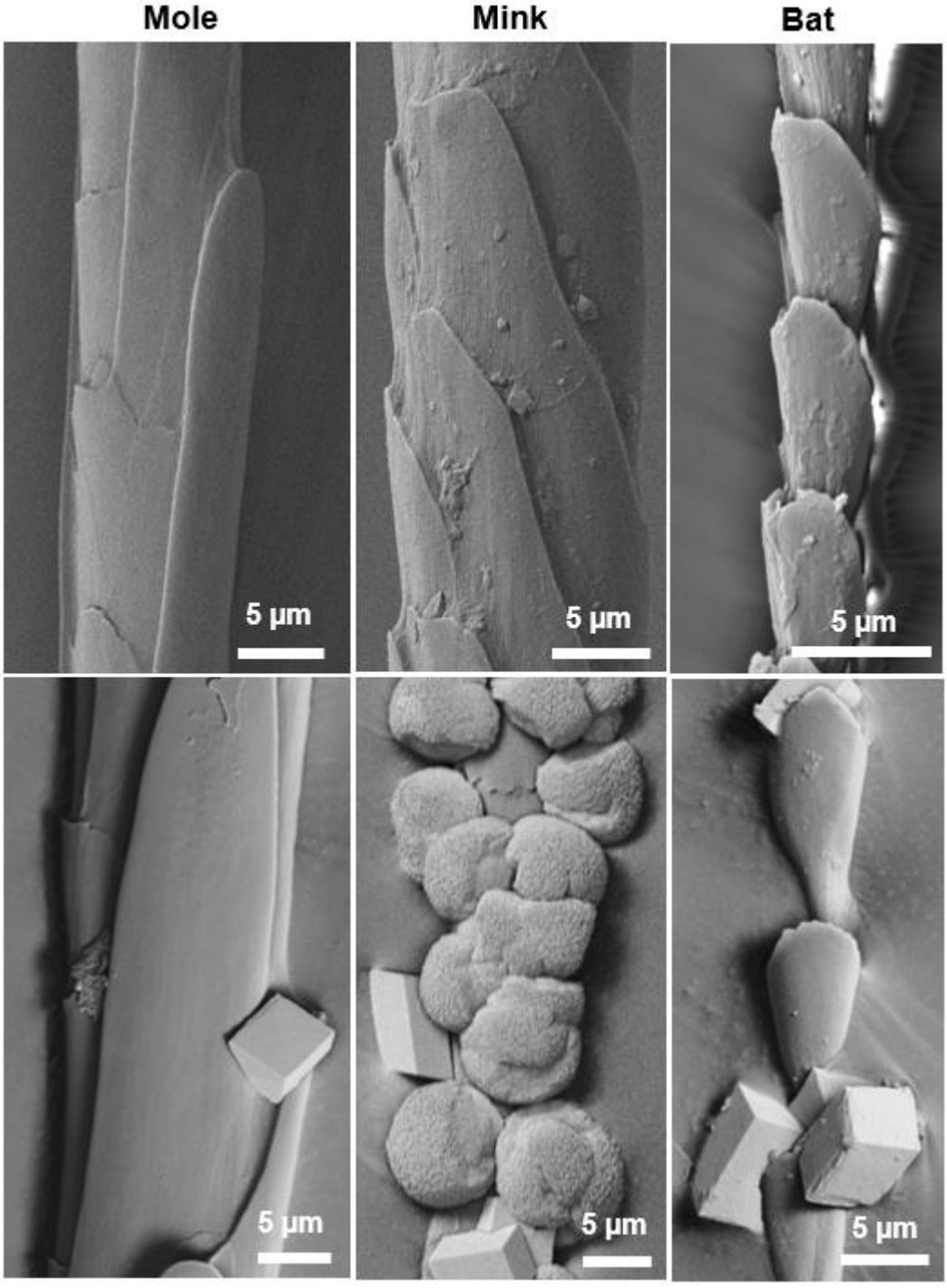


**Figure 144: SEM images showing $CaCO_3$ crystals grown on mole, mink and bat hairs.**

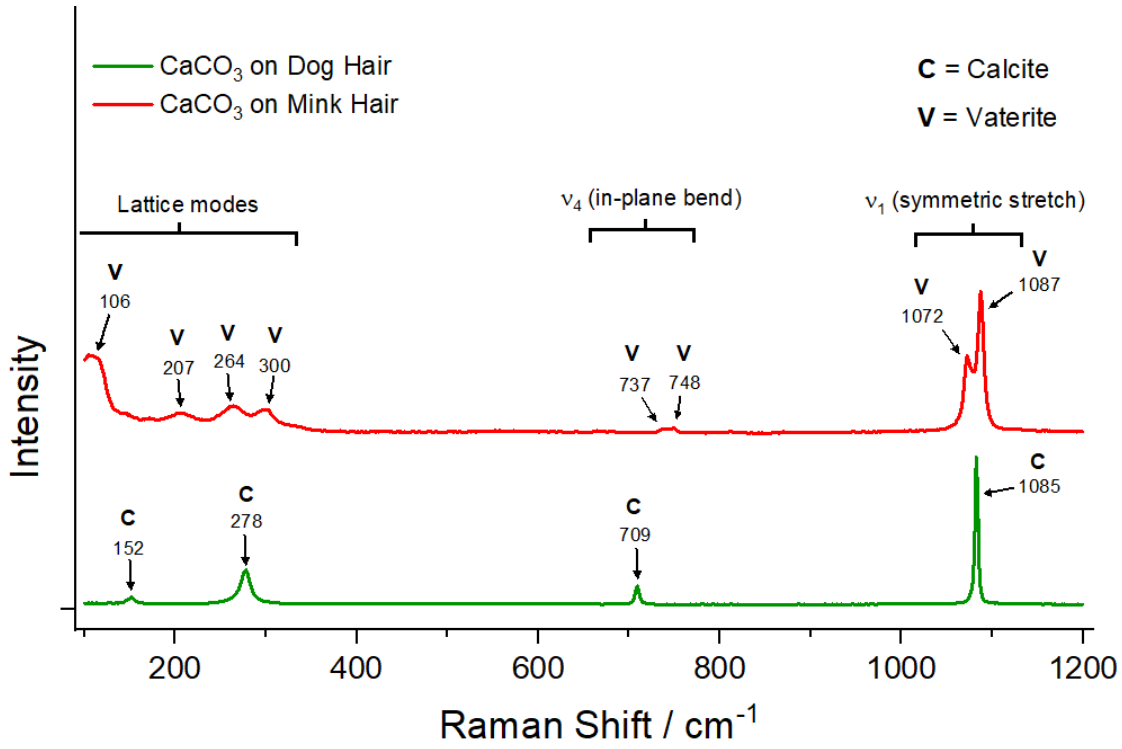


**Figure 145: Raman spectrum showing the polymorphism of $CaCO_3$ crystals formed on dog and mink hairs was calcite and vaterite respectively.**

## 5.5 Discussion

Discovering or designing an effective nucleant for a specific crystal is highly challenging, and with a limited number of studies investigating in depth the properties of highly effective but structurally complex nucleants, there is little rationale for narrowing down a list of promising candidates. Effective nucleants can be extremely beneficial however, creating higher quality crystals for structural elucidation by x-ray crystallography, better drug formulations and offering better control over where crystals form in anti-scaling applications. The search for universal nucleants that can effectively nucleate a wide range of crystals has been an ongoing effort for a long time, and as is shown here, mammalian hair is a promising candidate.

The data presented in this chapter shows that hair can effectively nucleate slightly supersaturated microdroplets of $KNO_3$ and produce many crystals of calcium carbonate in millilitre-scale experiments, in both cases outperforming glass which is generally considered an effective 'universal nucleant'[282]. Nucleation efficacy was found to be highly dependent on the hair type, where dog hair was generally much more effective than human hair.

Treatment with petroleum ether or $H_2O_2$ generally had little effect on the nucleation efficacy of hairs towards $KNO_3$ nucleation. By assessing the shapes of curves fitted to the droplet nucleation data, it was found that nucleation of $KNO_3$ with hair was driven by rare but highly active sites on the hair surface, which was reflected by their shallow gradient and high variability. Dog hair was a more effective nucleant than human hair, implying that there was an increased likelihood of the microdroplets encountering an active nucleation site. Dog hair has a higher surface density of cuticle edges than human hair, which may partly account for this result. In contrast, all chemical treatments strongly influenced nucleation properties of hair for $CaCO_3$. Thus, hair type and treatment are critical parameters to consider when using hair as a nucleant; ethanol-treatment was found to completely switch off the nucleating properties of human hair towards $KNO_3$ nucleation, while dramatically improving nucleating properties of dog hair towards $CaCO_3$ nucleation. This result shows that hair's efficacy can be tuned using different treatment types, and also highlights the importance of considering the outcomes of treatments such as ethanol when incorporating hair into crystallization trials[283].

Comparing findings from surface chemical analysis with the results of crystallization experiments, the increased number density of calcium carbonate crystals with delipification can be correlated with the quantity of protein expressed on the hair surfaces. XPS is effective at analysing the surface composition of a wide range of materials, including those containing protein. Carbon, nitrogen and oxygen produce signal bands centred at ≈285, ≈400 and ≈532 eV, the exact positions of which vary depending on the bonding states of the atoms. XPS showed a stronger nitrogen signal for dog hair than human hair, which corresponds to a greater expression of surface protein. The carbon signal of dog hair dropped after treatment with ethanol and petroleum ether, showing that as-obtained dog hair contained a greater amount of unbound lipids. These lipids were removed easily, which significantly improved the activity of dog hairs towards promoting $CaCO_3$ crystallisation.

Sulfur produces a signal band centred at ≈167 eV. Sulfur exists in organic materials not only in various bonding states, but also in a variety of oxidation states. It is present at disulfide groups in the -1 oxidation state, and thiol groups in the -2 oxidation state, both of which can be oxidised to form sulfonates with oxidation state +4. In the sulfur 2p region of x-ray photoelectron spectra, two distinct bands at 163-167 eV and 167-171 eV exist, corresponding to reduced sulfur species (thiol, disulfide) and oxidised sulfur species (sulfonate) respectively. This means that sulfur XPS can effectively be used to degree of oxidation of protein.

The ability of the hairs to promote $CaCO_3$ crystallisation reduced as a result of $H_2O_2$ treatment, which can be linked to the degree of surface oxidation. Human hair has been previously reported to contain a greater amount of cysteine than dog hair, although both generally contain larger quantities than other animal hairs[284,285]. Human hair had a greater amount of oxidised sulfur than dog hair however, which may have been responsible for its lower nucleation activity. This can be attributed to a greater degree of oxidative damage from washing, mechanical damage, and UV-light exposure[286]. Dog hair was inherently more resistant to sulfur oxidation, perhaps as a result of the more intact layer of bound lipids on its surface. The nitrogen signal of dog hair dropped following $H_2O_2$ treatment however, suggesting that this led to a loss of surface protein.

Nucleation properties of a surface are also influenced by physical properties such as topography and surface charge[116,287,288]. The structure at the surface of dog hair exhibited more prominent undulating ridges than human hair. This may have enhanced nucleation to some degree as crystallisation is often observed at small features and crevices[126,151,288–290]. The cuticle edges of dog hair were also more negatively charged than the rest of the hair surface, which indicates that this region is chemically unique. The inner cuticle encompasses the endocuticle region, which has been shown to express the highly active calcium binding protein S100A3[291–293]. This protein contains an extremely high proportion of cysteine residues, making this region especially active towards calcium binding[294], a crucial first stage in calcium carbonate nucleation. We confirmed by resin exfoliation and SEM imaging that the cuticle edges were the primary nucleation sites; a combination of unique surface chemistry and topography in this environment rationalises the observed nucleation properties. These regions may have also been able to mechanically regenerate their nucleating properties after chemical damage. Slight exfoliation of the cuticles may have revealed small quantities of fresh keratin from the inner cuticle to the crystal growth solution[266]. Enhanced nucleation at cuticle edges was observed for both calcium carbonate and $CaF_2$.

Keratinous hairs are highly evolved and are formed by a huge number of mammals. Although human hairs are morphologically similar to the hairs of some other animals, there are many more with quite different microscale morphologies. For example, hair structures may have evolved to offer protection from solar UV[295], to protect skin from cuts and grazes, to facilitate perspiration and regulation of body temperature, or to offer a low friction surface that allows an animal to move through water or soil when burrowing[296]. This provides an extensive natural resource of nucleants with a variety of surface topography and chemistry. As shown here, the morphological differences between different hair types can also lead to surprising results, such as the promotion of vaterite crystallization on mink hair. The substantial topographical variation in the fibrillar structure of the hair surfaces provides a rich playground to explore topographical effects in crystal nucleation, which is underexplored but has been shown to be capable of completely changing how substances crystallise at surfaces[287].

## 5.6 Conclusions

The results in this chapter demonstrate that hair is a highly promising but underexplored universal nucleant for both highly and sparingly soluble minerals. The quality and quantity of exposed surface protein was found to dictate the nucleation behaviour of hairs, which can be altered by chemical treatments. Since more, less-oxidised protein was found to be characteristic of surfaces that were more active towards nucleation, hair treatments that remove free lipids whilst maintaining protein integrity such as petroleum ether and ethanol are desirable for maximising nucleating efficacy of hair. Crystallisation of $CaCO_3$ and $CaF_2$ was particularly promoted at the cuticle edges, where there was a step-like topography and localised negative surface charge. This shows that nucleant surfaces can be highly effective when they are chemically and topographically non-uniform, due to their expression of rare but highly active nucleation sites. With the plethora of varieties of hair available, the scope for further exploration of crystallisation processes on specific hair types is vast.

# Final Conclusions

The work presented here reveals new insights into the ways in which topography can be used to control crystal nucleation.

In chapter 2, substrates were fabricated to test prevalent ideas for how surface topography can promote crystal nucleation. Firstly, the promotion of calcium carbonate crystallisation on glass substrates following abrasion with diamond powder showed that fracturing glassy materials can be an effective way to manufacture nucleation sites using topography alone. Next, crystallisation of calcium carbonate was explored on crazed ceramics, where it was thought that the highly acute crazes may have hosted nucleation sites. There was only a slight enhancement of crystallisation within the crazes, and this may have been hindered by restrictions on ion transport in the highly confined features. These experiments demonstrate how effective crystal nucleants often express a wide variety of topographical features. When surfaces contain a smaller variety of features, the likelihood of any of these being effective at promoting nucleation is reduced.

Two types of substrates were then fabricated to test whether angle-directed nucleation is likely to be a viable mechanism for promotion of crystal nucleation in real systems. Square-edged gold templates were fabricated using a novel NaCl crystal shadow masking approach. These were slightly effective at enhancing crystallisation of face-centred cubic $CaF_2$, but ineffective at achieving polymorph control over $KNO_3$ crystallisation. $CaCO_3$-shaped pits were then fabricated using resin to make novel substrates. Vaterite-shaped pits were generally effective at crystallising vaterite, and calcite generally crystallised within calcite-shaped pits. Angle-directed nucleation may be plausibly related to this phenomenon, however more evidence is needed to confidently make this assertion.

Chapter 3 investigated the enhanced nucleation of calcite at -COOH functionalised iridium cracks supported on PDMS squares. This result presented an exciting opportunity to study how the topography at the cracks was responsible for crystals being entirely localised to the cracks. Not only were there jagged edges of the cracks which may have directly enhanced crystal nucleation, but they also supported a highly disordered SAM, which is thought to be extremely effective at promoting nucleation[202,203].

The ability of these substrates to crystallise a range of compounds was also explored. Various minerals, organic compounds and a zeolitic imidazolate framework preferentially crystallised at the cracks. Sulfates were not able to be selectively crystallised at the cracks however, which was thought to be due to their chemistry.

Chapter 4 extended the scope of chapter 3, exploring how the formation of iridium cracks could be controlled, which allowed crystal nucleation to be patterned. Three different methods of patterning cracks were explored, and photolithographic patterning of the underlying PDMS was the most controlled and reproducible method. Together, chapters 3 and 4 provide a fascinating example of how preferential crystallisation of a range of compounds can be promoted at patternable cracks, demonstrating a rare degree of control over the stochastic nature of crystal nucleation.

In chapter 5, hair was explored as a potential universal nucleant for a range of minerals. Dog hair was found to be more effective than human hair at nucleating $CaCO_3$ and $KNO_3$, however both were more effective than glass. XPS and SICM measurements revealed that the quality and quantity of exposed surface protein were found to dictate the nucleation behaviour of hairs. This could be altered by chemical treatments, where delipifying treatments were generally beneficial towards promoting nucleation and oxidising treatments were detrimental. Crystallisation was particularly promoted at the cuticle edges, where a unique surface topography and chemistry were presented.

The scope for further exploration of the effect of surface topography on nucleation is vast, and it appears promising that precise engineering of surface topography will help to solve real world problems regarding crystallisation processes.

# References


[1] J. Wilkins, B. J. Schoville, R. Pickering, L. Gliganic, B. Collins, K. S. Brown, J. von der Meden, W. Khumalo, M. C. Meyer, S. Maape, A. F. Blackwood, A. Hatton, *Nature* **2021**, *592*.

[2] S. Domínguez-Bella, *Archaeometry and Cultural Heritage: the Contribution of Mineralogy.* **2012**, *99*, 5.

[3] Plinius Secundus Gaius, *Naturalis Historiæ*, **1669**.

[4] Compagnie des Alpes, “Futuroscope theme park in Poitiers in France,” can be found under https://www.futuroscope.com/, **2005**.

[5] J. Betts, “John Betts Fine Minerals,” can be found under http://www.johnbetts-fineminerals.com/, **2008**.

[6] H. Schoen, C. S. Grove, J. Palermo, *Journal of Chemical Education* **1956**, *33*, 373.

[7] R. Boyle, *The Origine of Formes and Qualities*, **1666**.

[8] Wöhler, Liebig, *Annalen der Pharmacie* **1832**, *3*, 249.

[9] M. Volmer, A. Weber, *Zeitschrift für Physikalische Chemie* **1926**, *119U*, 277.

[10] M. I. Aroyo, Ed., *International Tables for Crystallography*, International Union Of Crystallography, Chester, England, **2016**.

[11] K. R. Seddon, M. Zaworotko, *Crystal Engineering the Design and Application of Functional Solids*, Springer, Dordrecht, Netherlands, **2010**.

[12] W. Ostwald, *Zeitschrift für Physikalische Chemie* **1897**, *22*, 289.

[13] D. Erdemir, A. Y. Lee, A. S. Myerson, *Crystal Nucleation*, **2019**.

[14] D. Erdemir, A. Y. Lee, A. S. Myerson, in *Handbook of Industrial Crystallization* (Eds.: A. Y. Lee, A. S. Myerson, D. Erdemir), Cambridge University Press, Cambridge, **2019**, pp. 76–114.

[15] B. K. Chakraverty, G. M. Pound, *Acta Metallurgica* **1964**, *12*, 851.

[16] C. A. Sholl, N. H. Fletcher, *Acta Metallurgica* **1970**, *18*, 1083.

[17] R. O. David, C. Marcolli, J. Fahrni, Y. Qiu, Y. A. Perez Sirkin, V. Molinero, F. Mahrt, D. Brühwiler, U. Lohmann, Z. A. Kanji, *Proceedings of the National Academy of Sciences of the United States of America* **2019**, *116*, 8184.

[18] R. P. Sear, *International Materials Reviews* **2012**, *57*, 328.

[19] J. Dziadkowiec, B. Zareeipolgardani, D. K. Dysthe, A. Røyne, *Scientific Reports* **2019**, *9*, 1.

[20] C. J. Stephens, S. F. Ladden, F. C. Meldrum, H. K. Christenson, *Advanced Functional Materials* **2010**, *20*, 2108.

[21] K. Henzler, E. O. Fetisov, M. Galib, M. D. Baer, B. A. Legg, C. Borca, J. M. Xto, S. Pin, J. L. Fulton, G. K. Schenter, N. Govind, J. I. Siepmann, C. J. Mundy, T. Huthwelker, J. J. De Yoreo, *Science Advances* **2018**, *4*.

[22] R. Demichelis, P. Raiteri, J. D. Gale, D. Quigley, D. Gebauer, *Nature Communications* **2011**, *2*.

[23] Q. Hu, M. H. Nielsen, C. L. Freeman, L. M. Hamm, J. Tao, J. R. I. Lee, T. Y. J. Han, U. Becker, J. H. Harding, P. M. Dove, J. J. De Yoreo, *Faraday Discussions* **2012**, *159*, 509.

[24] M. J. Wheeler, A. K. Bertram, *Atmospheric Chemistry and Physics* **2012**, *12*, 1189.

[25] M. A. Sharaf, R. A. Dobbins, *Journal of Chemical Physics* **1982**, *77*, 1517.

[26] P. G. Vekilov, *Crystal Growth and Design* **2010**, *10*, 5007.

[27] Y. Georgalis, J. Schüler, J. Frank, M. D. Soumpasis, W. Saenger, *Advances in Colloid and Interface Science* **1995**, *58*, 57.

[28] A. Laaksonen, R. McGraw, H. Vehkamäki, *Journal of Chemical Physics* **1999**, *111*, 2019.

[29] M. A. Durán-Olivencia, P. Yatsyshin, S. Kalliadasis, J. F. Lutsko, *New Journal of Physics* **2018**, *20*.

[30] D. Erdemir, A. Y. Lee, A. S. Myerson, *Accounts of Chemical Research* **2009**, *42*, 621.

[31] W. Pan, A. B. Kolomeisky, P. G. Vekilov, *Journal of Chemical Physics* **2005**, *122*.

[32] D. Gebauer, M. Kellermeier, J. D. Gale, L. Bergström, H. Cölfen, *Chemical Society Reviews* **2014**, *43*, 2348.

[33] A. L. Boskey, *Connective Tissue Research* **2003**, *44*, 5.

[34] F. C. Meldrum, *International Materials Reviews* **2003**, *48*, 187.

[35] J. Ihli, Y. W. Wang, B. Cantaert, Y. Y. Kim, D. C. Green, P. H. H. Bomans, N. A. J. M. Sommerdijk, F. C. Meldrum, *Chemistry of Materials* **2015**, *27*, 3999.

[36] F. C. Meldrum, H. Cölfen, *Chemical Reviews* **2008**, *108*, 4332.

[37] J. Aizenberg, *Advanced Materials* **1996**, *8*, 222.

[38] E. Loste, R. M. Wilson, R. Seshadri, F. C. Meldrum, *Journal of Crystal Growth* **2003**, *254*, 206.

[39] S. Zhang, O. Nahi, X. He, L. Chen, Z. Aslam, N. Kapur, Y. Y. Kim, F. C. Meldrum, *Advanced Functional Materials* **2022**, *32*.

[40] R. A. Berner, *Geochimica et Cosmochimica Acta* **1975**, *39*, 489.

[41] W. Sun, S. Jayaraman, W. Chen, K. A. Persson, G. Ceder, *Proceedings of the National Academy of Sciences of the United States of America* **2015**, *112*, 3199.

[42] M. M. Reddy, G. H. Nancollas, *Journal of Crystal Growth* **1976**, *35*, 33.

[43] M. M. Reddy, K. K. Wang, *Journal of Crystal Growth* **1980**, *50*, 470.

[44] S. C. Parker, E. T. Kelsey, P. M. Oliver, J. O. Titiloye, *Faraday Discussions* **1993**, *95*, 75.

[45] M. Farhadi-Khouzani, D. M. Chevrier, P. Zhang, N. Hedin, D. Gebauer, *Angewandte Chemie - International Edition* **2016**, *55*, 8117.

[46] F. Jurado-Lasso, N. Jurado-Lasso, J. Ortiz, J. F. Jurado, *Dyna* **2016**, *83*, 244.

[47] J. K. Nimmo, B. W. Lucas, *Acta Crystallographica B* **1976**, *32*, 1968.

[48] P. Laval, C. Giroux, J. Leng, J. B. Salmon, *Journal of Crystal Growth* **2008**, *310*, 3121.

[49] I. Markov, S. Stoyanov, *Contemporary Physics* **1987**, *28*, 267.

[50] C. A. Mitchell, L. Yu, M. D. Ward, *Journal of the American Chemical Society* **2001**, *123*, 10830.

[51] A. McPherson, P. Shlichta, *Journal of Crystal Growth* **1988**, *90*, 47.

[52] A. McPherson, P. Shlichta, *Science* **1988**, *239*, 385.

[53] C. Balik, A. Hopfinger, *Macromolecules* **1980**, *13*, 999.

[54] K. M. Geib, J. E. Mahan, R. G. Long, M. Nathan, G. Bai, *Journal of Applied Physics* **1991**, *70*, 1730.

[55] R. T. Bruintjes, *Bulletin of the American Meteorological Society* **1999**, *80*, 805.

[56] B. Vonnegut, *Journal of Applied Physics* **1947**, *18*, 593.

[57] P. Conrad, G. E. Ewing, R. L. Karlinsey, V. Sadtchenko, *Journal of Chemical Physics* **2005**, *122*, 11.

[58] R. B. Head, *Nature* **1961**, *191*, 1058.

[59] G. C. Sosso, T. F. Whale, M. A. Holden, P. Pedevilla, B. J. Murray, A. Michaelides, *Chemical Science* **2018**, *9*, 8077.

[60] A. O. F. Jones, B. Chattopadhyay, Y. H. Geerts, R. Resel, *Advanced Functional Materials* **2016**, *26*, 2233.

[61] T. Fukuma, R. Garcia, *ACS Nano* **2018**, *12*, 11785.

[62] J. N. Israelachvili, R. M. Pashley, *Nature* **1983**, *306*, 249.

[63] G. Gonella, E. H. G. Backus, Y. Nagata, D. J. Bonthuis, P. Loche, A. Schlaich, R. R. Netz, A. Kühnle, I. T. McCrum, M. T. M. Koper, M. Wolf, B. Winter, G. Meijer, R. K. Campen, M. Bonn, *Nature Reviews Chemistry* **2021**, *5*, 466.

[64] D. Martin-Jimenez, E. Chacon, P. Tarazona, R. Garcia, *Nature Communications* **2016**, *7*, 1.

[65] R. Freitas, E. J. Reed, *Nature Communications* **2020**, *11*, 3260.

[66] E. Breynaert, M. Houlleberghs, S. Radhakrishnan, G. Grübel, F. Taulelle, J. A. Martens, *Chemical Society Reviews* **2020**, *49*, 2557.

[67] S. J. Cox, S. M. Kathmann, B. Slater, A. Michaelides, *Journal of Chemical Physics* **2015**, *142*.

[68] W. D. Kaplan, Y. Kauffmann, *Annual Review of Materials Research* **2006**, *36*, 1.

[69] R. G. Alberstein, J. L. Prelesnik, E. Nakouzi, S. Zhang, J. J. De Yoreo, J. Pfaendtner, F. A. Tezcan, C. J. Mundy, *Journal of Physical Chemistry Letters* **2023**, *14*, 80.

[70] H. Pyles, S. Zhang, J. J. De Yoreo, D. Baker, *Nature* **2019**, *571*, 251.

[71] F. C. Meldrum, C. O'Shaughnessy, *Advanced Materials* **2020**, *32*, 2001.

[72] H. K. Christenson, *CrystEngComm* **2013**, *15*, 2030.

[73] C. Alba-Simionesco, B. Coasne, G. Dosseh, G. Dudziak, K. E. Gubbins, R. Radhakrishnan, M. J. P. C. M. Sliwinska-Bartkowiak, *Journal of Physics: Condensed Matter* **2006**, *18*, 14.

[74] H. K. Christenson, *Journal of Physics: Condensed Matter* **2001**, *13*, 95.

[75] L. Fumagalli, A. Esfandiar, R. Fabregas, S. Hu, P. Ares, A. Janardanan, Q. Yang, B. Radha, T. Taniguchi, K. Watanabe, G. Gomila, K. S. Novoselov, A. K. Geim, *Science* **2018**, *360*, 1339.

[76] M. Jazdzewska, M. M. Śliwinska-Bartkowiak, A. I. Beskrovnyy, S. G. Vasilovskiy, S. W. Ting, K. Y. Chan, L. Huang, K. E. Gubbins, *Physical Chemistry Chemical Physics* **2011**, *13*, 9008.

[77] S. Chiashi, Y. Saito, T. Kato, S. Konabe, S. Okada, T. Yamamoto, Y. Homma, *ACS Nano* **2019**, *13*, 1177.

[78] K. Morishige, H. Yasunaga, Y. Matsutani, *Journal of Physical Chemistry C* **2010**, *114*, 4028.

[79] R. Kröger, A. Verch, *Minerals* **2018**, *8*.

[80] S. Faucher, N. Aluru, M. Z. Bazant, D. Blankschtein, A. H. Brozena, J. Cumings, J. Pedro De Souza, M. Elimelech, R. Epsztein, J. T. Fourkas, A. G. Rajan, H. J. Kulik, A. Levy, A. Majumdar, C. Martin, M. McEldrew, R. P. Misra, A. Noy, T. A. Pham, M. Reed, E. Schwegler, Z. Siwy, Y. Wang, M. Strano, *Journal of Physical Chemistry C* **2019**, *123*, 21309.

[81] S. Stolyarova, E. Baskin, Y. Nemirovsky, *Journal of Crystal Growth* **2012**, *360*, 131.

[82] J. M. Ha, J. H. Wolf, M. A. Hillmyer, M. D. Ward, *Journal of the American Chemical Society* **2004**, *126*, 3382.

[83] G. T. Rengarajan, D. Enke, M. Steinhart, M. Beiner, *Journal of Materials Chemistry* **2008**, *18*, 2537.

[84] T. Koop, *Proceedings of the National Academy of Sciences of the United States of America* **2017**, *114*, 797.

[85] D. Turnbull, *Journal of Chemical Physics* **1950**, *18*, 198.

[86] A. J. Page, R. P. Sear, *Physical Review Letters* **2006**, *97*, 1.

[87] J. M. Campbell, F. C. Meldrum, H. K. Christenson, *Proceedings of the National Academy of Sciences of the United States of America* **2017**, *114*, 810.

[88] J. M. Campbell, H. K. Christenson, *Physical Review Letters* **2018**, *120*, 165701.

[89] C. Nanev, L. Govada, N. E. Chayen, *IUCrJ* **2021**, *8*, 270.

[90] P. Grosfils, J. F. Lutsko, *Crystals* **2021**, *11*, 1.

[91] X. X. Zhang, M. Chen, M. Fu, *Journal of Chemical Physics* **2014**, *141*.

[92] P. Asanithi, *Journal of Biomedical Materials Research A* **2014**, *102*, 2590.

[93] Y. X. Liu, X. J. Wang, J. Lu, C. B. Ching, *Journal of Physical Chemistry B* **2007**, *111*, 13971.

[94] A. B. Unni, R. Winkler, D. M. Duarte, K. Chat, K. Adrjanowicz, *Journal of Physical Chemistry B* **2022**, *126*, 8072.

[95] M. Yamamoto, N. Nishikawa, H. Mayama, Y. Nonomura, S. Yokojima, S. Nakamura, K. Uchida, *Langmuir* **2015**, *31*, 7355.

[96] G. Di Profio, E. Fontananova, E. Curcio, E. Drioli, *Crystal Growth and Design* **2012**, *12*, 3749.

[97] L. Cao, A. K. Jones, V. K. Sikka, J. Wu, D. Gao, *Langmuir* **2009**, *25*, 12444.

[98] C. Antonini, M. Innocenti, T. Horn, M. Marengo, A. Amirfazli, *Cold Regions Science and Technology* **2011**, *67*, 58.

[99] J. L. Holbrough, J. M. Campbell, F. C. Meldrum, H. K. Christenson, *Crystal Growth and Design* **2012**, *12*, 750.

[100] J. M. Campbell, F. C. Meldrum, H. K. Christenson, *Crystal Growth and Design* **2013**, *13*, 1915.

[101] J. M. Campbell, F. C. Meldrum, H. K. Christenson, *Journal of Physical Chemistry C* **2015**, *119*, 1164.

[102] A. Kirakosian, R. Bennewitz, J. N. Crain, T. Fauster, J. L. Lin, D. Y. Petrovykh, F. J. Himpsel, *Applied Physics Letters* **2001**, *79*, 1608.

[103] S. Yoshida, T. Sekiguchi, K. M. Itoh, *Applied Physics Letters* **2005**, *87*, 1.

[104] N. Kornblum, A. Katsman, B. Pokroy, *Journal of Physical Chemistry C* **2019**, *123*, 8770.

[105] K. Cao, J. Cai, R. Chen, *Chemistry of Materials* **2020**, *32*, 2195.

[106] D. Y. Petrovykh, “Templates for Self-Assembly of Nanostructures,” can be found under https://biointerface.org/nano/templates/, **2021**.

[107] T. Takarada, H. Takezawa, N. Nakagawa, K. Kato, *Diamond and Related Materials* **1993**, *2*, 323.

[108] A. R. Kirkpatrick, *Journal of Vacuum Science & Technology B: Microelectronics and Nanometer Structures* **1989**, *7*, 1947.

[109] F. Arezzo, N. Zacchetti, W. Zhu, *Journal of Applied Physics* **1994**, *75*, 5375.

[110] P. A. Dennig, D. A. Stevenson, *Materials Science Monographs* **1991**, *73*, 383.

[111] R. Polini, *Journal of Applied Physics* **1992**, *72*, 2517.

[112] J. C. Arnault, L. Demuynck, C. Speisser, F. Le Normand, *European Physical Journal B* **1999**, *11*, 327.

[113] L. Vescan, K. Grimm, M. Goryll, B. Holländer, *Materials Science and Engineering B* **2000**, *69*, 324.

[114] E. Curcio, G. Di Profio, E. Drioli, *Journal of Crystal Growth* **2008**, *310*, 5364.

[115] E. Curcio, E. Fontananova, G. Di Profio, E. Drioli, *Journal of Physical Chemistry B* **2006**, *110*, 12438.

[116] N. E. Chayen, E. Saridakis, R. El-Bahar, Y. Nemirovsky, *Journal of Molecular Biology* **2001**, *312*, 591.

[117] N. E. Chayen, E. Saridakis, R. P. Sear, *Proceedings of the National Academy of Sciences of the United States of America* **2006**, *103*, 597.

[118] B. D. Hamilton, M. A. Hillmyer, M. D. Ward, *Crystal Growth and Design* **2008**, *8*, 3368.

[119] Y. Diao, A. S. Myerson, T. A. Hatton, B. L. Trout, *Langmuir* **2011**, *27*, 5324.

[120] O. R. Grawe, *The Journal of Geology* **1936**, *44*, 173.

[121] L. Germinario, C. T. Oguchi, *Environmental Earth Sciences* **2022**, *81*.

[122] N. R. Chevalier, *Journal of Physical Chemistry C* **2014**, *118*, 17600.

[123] X. Xing, Z. Zhao, X. Shi, J. Liu, *Crystallography Reports* **2019**, *64*, 1150.

[124] M. Gavish, J. L. Wang, M. Eisenstein, M. Lahav, L. Leiserowitz, *Science* **1992**, *256*, 815.

[125] P. Conrad, G. E. Ewing, R. L. Karlinsey, V. Sadtchenko, *Journal of Chemical Physics* **2005**, *122*.

[126] J. J. Schlotheuber née Brunner, B. Maier, F. Kirner, S. Sturm, H. Cölfen, E. V. Sturm, *Crystal Growth and Design* **2021**.

[127] M. Niederberger, H. Cölfen, *Physical Chemistry Chemical Physics* **2006**, *8*, 3271.

[128] X. Zhang, Y. Wu, Y. Lv, Y. Yu, Z. Dong, *Surface and Coatings Technology* **2020**, *386*, 125483.

[129] A. Montenero, G. Gnappi, F. Ferrari, M. Cesari, E. Salvioli, *Journal of Materials Science* **2000**, *5*, 2791.

[130] L. Tang, Y. B. Huang, D. Q. Liu, J. L. Li, K. Mao, L. Liu, Z. J. Cheng, W. M. Gong, J. Hu, J. H. He, *Acta Crystallographica Section D* **2005**, *61*, 53.

[131] W. De Poel, J. A. W. Münninghoff, J. A. A. W. Elemans, W. J. P. Van Enckevort, A. E. Rowan, E. Vlieg, *Crystal Growth and Design* **2018**, *18*, 763.

[132] A. Sengupta Ghatak, A. Ghatak, *Langmuir* **2013**, *29*, 4373.

[133] K. S. Kim, D. Lee, C. S. Chang, S. Seo, Y. Hu, S. Cha, H. Kim, J. Shin, J. H. Lee, S. Lee, J. S. Kim, K. H. Kim, J. M. Suh, Y. Meng, B. I. Park, J. H. Lee, H. S. Park, H. S. Kum, M. H. Jo, G. Y. Yeom, K. Cho, J. H. Park, S. H. Bae, J. Kim, *Nature* **2023**, *614*.

[134] J. Kim, J. Chung, J. Hyon, T. Kwon, C. Seo, J. Nam, Y. Kang, *Chemical Communications* **2014**, *50*, 10258.

[135] M. J. Kreder, J. Alvarenga, P. Kim, J. Aizenberg, *Nature Reviews Materials* **2016**, *1*.

[136] J. Chen, J. Liu, M. He, K. Li, D. Cui, Q. Zhang, X. Zeng, Y. Zhang, J. Wang, Y. Song, *Applied Physics Letters* **2012**, *101*, 95.

[137] A. K. Metya, J. K. Singh, F. Müller-Plathe, *Physical Chemistry Chemical Physics* **2016**, *18*, 26796.

[138] Y. Hou, M. Yu, Y. Shang, P. Zhou, R. Song, X. Xu, X. Chen, Z. Wang, S. Yao, *Physical Review Letters* **2018**, *120*, 75902.

[139] T. S. Wong, S. H. Kang, S. K. Y. Tang, E. J. Smythe, B. D. Hatton, A. Grinthal, J. Aizenberg, *Nature* **2011**, *477*, 443.

[140] W. Vogel, N. J. Kreidl, M. Lopes Barreto, *Glass Chemistry*, Springer, Berlin, Germany, **2011**.

[141] G. V. Samsonov, *The Oxide Handbook*, Springer US, **1973**.

[142] J. R. Taylor, A. C. Bull, *Ceramic Glaze Technology*, Butterworth-Heinemann, Oxford, England, **1986**.

[143] E. J. Kramer, in *Crazing in Polymers* (Ed.: H. H. Kausch), Springer, Berlin, Heidelberg, **1983**, pp. 1–56.

[144] R. P. Kambour, *Journal of Polymer Science: Macromolecular Reviews* **1973**, *7*, 1.

[145] T. Nonaka, B. Bril, R. Rein, *Journal of Human Evolution* **2010**, *59*, 155.

[146] S. P. McJunkins, J. I. Thornton, *Forensic Sciences* **1973**, *2*, 1.

[147] B. D. Lauterwasser, E. J. Kramer, *Philosophical Magazine A: Physics of Condensed Matter, Structure, Defects and Mechanical Properties* **1979**, *39*, 469.

[148] C. R. Kurkjian, W. R. Prindle, *Journal of the American Ceramic Society* **2005**, *81*, 795.

[149] N. Bouras, M. A. Madjoubi, M. Kolli, S. Benterki, M. Hamidouche, *Physics Procedia* **2009**, *2*, 1135.

[150] E. A. Leed, C. G. Pantano, *Journal of Non-Crystalline Solids* **2003**, *325*, 48.

[151] J. M. Campbell, F. C. Meldrum, H. K. Christenson, *Crystal Growth and Design* **2013**, *13*, 1915.

[152] Y. Bi, B. Cao, T. Li, *Nature Communications* **2017**, *8*, 1.

[153] A. J. Page, R. P. Sear, *Journal of the American Chemical Society* **2009**, *131*, 17550.

[154] S. J. Bonafede, M. D. Ward, *Journal of the American Chemical Society* **1995**, *117*, 7853.

[155] T. L. Malkin, B. J. Murray, C. G. Salzmann, V. Molinero, S. J. Pickering, T. F. Whale, *Physical Chemistry Chemical Physics* **2015**, *17*, 60.

[156] C. Li, R. Tao, S. Luo, X. Gao, K. Zhang, Z. Li, *Journal of Physical Chemistry C* **2018**, *122*, 25992.

[157] S. R. Yeandel, C. L. Freeman, J. H. Harding, *Journal of Chemical Physics* **2022**, *157*.

[158] R. Innocenti Malini, A. R. Finney, S. A. Hall, C. L. Freeman, J. H. Harding, *Crystal Growth and Design* **2017**, *17*, 5811.

[159] A. R. Finney, M. Salvalaglio, *Faraday Discussions* **2021**, *235*, 56.

[160] X. Li, S. Tanyan, S. Xie, R. Chen, Q. Liao, X. Zhu, X. He, *Separation and Purification Technology* **2022**, *292*.

[161] L. Liu, Y. Wang, S. Guo, Z. Wang, W. Wang, *Journal of Biomedical Materials Research Part B: Applied Biomaterials* **2012**, *100B*, 956.

[162] Z. Zhou, X. Liu, Q. Liu, *Journal of Macromolecular Science, Part B: Physics* **2008**, *47*, 667.

[163] W. Luo, M. Charara, M. C. Saha, Y. Liu, *Applied Nanoscience* **2019**, *9*, 1309.

[164] B. Wucher, W. Yue, A. N. Kulak, F. C. Meldrum, *Chemistry of Materials* **2007**, *19*, 1111.

[165] J. M. Galloway, Z. P. Aslam, S. R. Yeandel, A. Kulak, M. A. Ilett, Y. Y. Kim, A. Bejarano-Villafuerte, B. Pokroy, R. M. Drummond-Brydson, C. L.

Freeman, J. H. Harding, N. Kapur, F. C. Meldrum, *Chemical Science* **2023**.

[166] Y. Diao, T. Harada, A. S. Myerson, T. A. Hatton, B. L. Trout, *Nature Materials* **2011**, *10*, 867.

[167] S. M. D'Souza, C. Alexander, S. W. Carr, A. M. Waller, M. J. Whitcombe, E. N. Vulfson, *Nature* **1999**, *398*, 312.

[168] L. Esposito, A. Salem, A. Tucci, A. Gualtieri, S. H. Jazayeri, *Ceramics International* **2005**, *31*, 233.

[169] P. Grosfils, J. F. Lutsko, *Crystals* **2021**, *11*.

[170] J. M. Campbell, F. C. Meldrum, H. K. Christenson, *Journal of Physical Chemistry C* **2015**, *119*, 1164.

[171] E. Bormashenko, V. Valtsifer, *Advances in Colloid and Interface Science* **2021**, *296*, 102510.

[172] M. Beiner, G. T. Rengarajan, S. Pankaj, D. Enke, M. Steinhart, *Nano Letters* **2007**, *7*, 1381.

[173] G. Graubner, G. T. Rengarajan, N. Anders, N. Sonnenberger, D. Enke, M. Beiner, M. Steinhart, *Crystal Growth and Design* **2014**, *14*, 78.

[174] Z. Zhang, W. A. Ducker, *Langmuir* **2022**.

[175] S. N. Kerisit, J. J. De Yoreo, *Journal of Physical Chemistry C* **2020**, *124*, 5480.

[176] M. Nazari, A. Davoodabadi, D. Huang, T. Luo, H. Ghasemi, *ACS Nano* **2020**, *14*, 16348.

[177] H. K. Christenson, *Journal of Physics Condensed Matter* **2001**, *13*.

[178] K. Wu, Z. Chen, J. Li, J. Xu, K. Wang, R. Li, S. Wang, X. Dong, *Langmuir* **2019**, *35*, 8867.

[179] A. J. Page, R. P. Sear, *Journal of the American Chemical Society* **2009**, *131*, 17550.

[180] A. J. Page, R. P. Sear, *Physical Review Letters* **2006**, *97*.

[181] N. N. Greenwood, A. Earnshaw, *Chemistry of the Elements*, Butterworth-Heinemann, Oxford ;, **1997**.

[182] G. Sui, J. Wang, C. C. Lee, W. Lu, S. P. Lee, J. V. Leyton, A. M. Wu, H. R. Tseng, *Analytical Chemistry* **2006**, *78*, 5543.

[183] Z. Wang, Y. Luo, F. Zheng, N. Zhang, C. Yin, J. Li, C. He, X. Peng, Z. Huang, P. Fang, *Surface and Interface Analysis* **2018**, *50*, 819.

[184] D. Bodas, C. Khan-Malek, *Sensors & Actuators, B: Chemical* **2007**, *123*, 368.

[185] Y. Y. Kim, C. L. Freeman, X. Gong, M. A. Levenstein, Y. Wang, A. Kulak, C. Anduix-Canto, P. A. Lee, S. Li, L. Chen, H. K. Christenson, F. C. Meldrum, *Angewandte Chemie - International Edition* **2017**, *56*, 11885.

[186] M. A. Levenstein, L. A. Bawazer, C. S. Mc Nally, W. J. Marchant, X. Gong, F. C. Meldrum, N. Kapur, *Microfluidics and Nanofluidics* **2016**, *20*.

[187] M. A. Levenstein, C. Anduix-Canto, Y. Y. Kim, M. A. Holden, C. González Niño, D. C. Green, S. E. Foster, A. N. Kulak, L. Govada, N. E. Chayen, S. J. Day, C. C. Tang, B. Weinhausen, M. Burghammer, N. Kapur, F. C. Meldrum, *Advanced Functional Materials* **2019**, *29*.

[188] J. Chen, J. Zheng, Q. Gao, J. Zhang, J. Zhang, O. M. Omisore, L. Wang, H. Li, *Applied Sciences* **2018**, *8*.

[189] S. Coyle, C. Majidi, P. LeDuc, K. J. Hsia, *Extreme Mechanics Letters* **2018**, *22*, 51.

[190] G. R. Gossweiler, C. L. Brown, G. B. Hewage, E. Sapiro-Gheiler, W. J. Trautman, G. W. Welshofer, S. L. Craig, *ACS Applied Materials Interfaces* **2015**, *7*, 22431.

[191] C. Jin, Z. Wang, A. A. Volinsky, A. Sharfeddin, N. D. Gallant, *Polymer Testing* **2016**, *56*, 329.

[192] M. A. Eddings, M. A. Johnson, B. K. Gale, *Journal of Micromechanics and Microengineering* **2008**, *18*.

[193] G. Van Anders, D. Klotsa, N. K. Ahmed, M. Engel, S. C. Glotzer, *Proceedings of the National Academy of Sciences of the United States of America* **2014**, *111*, 4812.

[194] Y. Geng, G. van Anders, P. M. Dodd, J. Dshemuchadse, S. C. Glotzer, *Science Advances* **2019**, *5*.

[195] A. Ulman, *Chemical Reviews* **1996**, *96*, 1533.

[196] K. Gou, Y. Wang, X. Guo, Y. Wang, Y. Bian, H. Zhao, Y. Guo, Y. Pang, L. Xie, S. Li, H. Li, *Acta Biomaterialia* **2021**, *134*, 576.

[197] J. Aizenberg, A. J. Black, G. M. Whitesides, *Journal of the American Chemical Society* **1999**, *121*, 4500.

[198] Y. J. Han, J. Aizenberg, *Journal of the American Chemical Society* **2003**, *125*, 4032.

[199] C. L. Freeman, Q. Hu, M. H. Nielsen, J. Tao, J. J. De Yoreo, J. H. Harding, *Journal of Physical Chemistry C* **2013**, *117*, 5154.

[200] A. S. Côté, R. Darkins, D. M. Duffy, *Journal of Physical Chemistry C* **2014**, *118*, 19188.

[201] C. Anduix-Canto, M. A. Levenstein, Y. Y. Kim, J. R. A. Godinho, A. N. Kulak, C. G. Niño, P. J. Withers, J. P. Wright, N. Kapur, H. K. Christenson, F. C. Meldrum, *Advanced Functional Materials* **2021**, *31*.

[202] J. Aizenberg, A. J. Black, G. M. Whitesides, *Nature* **1998**, *394*, 868.

[203] J. Aizenberg, *Journal of the Chemical Society, Dalton Transactions* **2000**, 3963.

[204] V. Marinova, C. L. Freeman, J. H. Harding, *Faraday Discussions* **2022**, *235*, 289.

[205] A. W. Thompson, Z. D. Harris, J. T. Burns, *Micron* **2019**, *118*, 43.

[206] D. L. Graf, *American Mineralogist* **1961**, *46*, 1283.

[207] G. Fiquet, P. Richet, G. Montagnac, *Physics and Chemistry of Minerals* **1999**, *27*, 103.

[208] T. M. Willey, A. L. Vance, T. Van Buuren, C. Bostedt, A. J. Nelson, L. J. Terminello, C. S. Fadley, *Langmuir* **2004**, *20*, 2746.

[209] A. M. Travaille, J. J. J. M. Donners, J. W. Gerritsen, N. A. J. M. Sommerdijk, R. J. M. Nolte, H. Van Kempen, *Advanced Materials* **2002**, *14*, 492.

[210] J. N. Lee, C. Park, G. M. Whitesides, *Analytical Chemistry* **2003**, *75*, 6544.

[211] S. Farsang, R. N. Widmer, S. A. T. Redfern, *American Mineralogist* **2021**, *106*, 581.

[212] R. L. Frost, M. L. Weier, *Journal of Raman Spectroscopy* **2003**, *34*, 776.

[213] A. L. Lebedev, V. L. Kosorukov, *Geochemistry International* **2017**, *55*, 205.

[214] A. G. Collins, J. W. Davis, *Environmental Science & Technology* **1971**, *5*, 1039.

[215] J.-C. Hsueh, K. L. Yeh, H. L. Lee, T. Lee, *Reaction Chemistry & Engineering* **2021**, *6*, 2292.

[216] N. V. Surovtsev, S. V. Adichtchev, V. K. Malinovsky, A. G. Ogienko, V. A. Drebushchak, A. Y. Manakov, A. I. Ancharov, A. S. Yunoshev, E. V. Boldyreva, *Journal of Chemical Physics* **2012**, *137*.

[217] T. D. Bennett, Y. Yue, P. Li, A. Qiao, H. Tao, N. G. Greaves, T. Richards, G. I. Lampronti, S. A. T. Redfern, F. Blanc, O. K. Farha, J. T. Hupp, A. K. Cheetham, D. A. Keen, *Journal of the American Chemical Society* **2016**, *138*, 3484.

[218] A. Phan, C. J. Doonan, F. J. Uribe-Romo, C. B. Knobler, M. Okeeffe, O. M. Yaghi, *Accounts of Chemical Research* **2010**, *43*, 58.

[219] A. Deacon, L. Briquet, M. Malankowska, F. Massingberd-Mundy, S. Rudić, T. I. Hyde, H. Cavaye, J. Coronas, S. Poulston, T. Johnson, *Communications Chemistry* **2022**, *5*.

[220] K. Hirai, H. Ishikawa, T. Chervy, J. A. Hutchison, H. Uji-i, *Chemical Science* **2021**, *12*, 11986.

[221] M. Jian, B. Liu, R. Liu, J. Qu, H. Wang, X. Zhang, *RSC Advances* **2015**, *5*, 48433.

[222] K. Kida, M. Okita, K. Fujita, S. Tanaka, Y. Miyake, *CrystEngComm* **2013**, *15*, 1794.

[223] P. Ascarelli, S. Fontana, *Applied Surface Science* **1993**, *64*, 307.

[224] H. K. Christenson, *Physical Review Letters* **1995**, *74*, 4675.

[225] M. A. Holden, T. F. Whale, M. D. Tarn, D. O'Sullivan, R. D. Walshaw, B. J. Murray, F. C. Meldrum, H. K. Christenson, *Science Advances* **2019**, *5*.

[226] D. McKechnie, S. Anker, S. Zahid, P. A. Mulheran, J. Sefcik, K. Johnston, *Journal of Physical Chemistry Letters* **2020**, *11*, 2263.

[227] C. Marcolli, B. Nagare, A. Welti, U. Lohmann, *Atmospheric Chemistry and Physics* **2016**, *16*, 8915.

[228] N. Fukuta, B. J. Mason, *Journal of Physics and Chemistry of Solids* **1963**, *24*, 715.

[229] A. McPherson, P. J. Shlichta, *Journal of Crystal Growth* **1987**, *85*, 206.

[230] A. R. Finney, I. J. McPherson, P. R. Unwin, M. Salvalaglio, *Chemical Science* **2021**, *12*, 11166.

[231] C. N. Nanev, E. Saridakis, N. E. Chayen, *Scientific Reports* **2017**, *7*.

[232] E. Saridakis, N. E. Chayen, *Trends in Biotechnology* **2009**, *27*, 99.

[233] A. M. Travaille, L. Kaptijn, P. Verwer, B. Hulsken, J. A. A. W. Elemans, R. J. M. Nolte, H. Van Kempen, *Journal of the American Chemical Society* **2003**, *125*, 11571.

[234] J. Aizenberg, A. J. Black, G. M. Whitesides, *Nature* **1999**, *398*, 495.

[235] D. Kashchiev, G. M. Van Rosmalen, *Crystal Research and Technology* **2003**, *38*, 555.

[236] T. Pompe, S. Herminghaus, *Physics Review Letters*, **2000**, *85*, 1930.

[237] R. J. Davey, S. L. M. Schroeder, J. H. Ter Horst, *Angewandte Chemie - International Edition* **2013**, *52*, 2166.

[238] L. M. Hamm, A. J. Giuffre, N. Han, J. Tao, D. Wang, J. J. De Yoreo, P. M. Dove, *Proceedings of the National Academy of Sciences of the United States of America* **2014**, *111*, 1304.

[239] J. Liu, S. Pancera, V. Boyko, A. Shukla, T. Narayanan, K. Huber, *Langmuir* **2010**, *26*, 17405.

[240] J. Bolze, B. Peng, N. Dingenouts, P. Panine, T. Narayanan, M. Ballauff, *Langmuir* **2002**, *18*, 8364.

[241] S. Zhang, F. Ye, X. Wang, R. Chen, H. Zhang, L. Zhan, X. Jiang, Y. Li, X. Ji, S. Liu, M. Yu, F. Yu, Y. Zhang, R. Wu, Z. Liu, Z. Ning, D. Neher, L. Han, Y. Lin, H. Tian, W. Chen, M. Stolterfoht, L. Zhang, W.-H. Zhu, Y. Wu, *Science* **2023**, *380*, 404.

[242] T. Baëtens, E. Pallecchi, V. Thomy, S. Arscott, *Scientific Reports* **2018**, *8*, 1.

[243] M. Kim, D. Ha, T. Kim, *Nature Communications* **2015**, *6*, 1.

[244] Y. Sato, *Jpn Journal of Applied Physics* **1986**, *25*, 189.

[245] Ukichiro Nakaya, *Snow Crystals, Natural and Artificial*, Harvard University Press, **1954**.

[246] D. G. Georgieva, M. E. Kuil, T. H. Oosterkamp, H. W. Zandbergen, J. P. Abrahams, *Acta Crystallographicaaphica Section D-Biological Crystallography* **2007**, *63*, 564.

[247] C. J. Leung, B. T. Nall, G. D. Brayer, *Journal of Molecular Biology* **1989**, *206*, 783.

[248] J. W. P. Schmelzer, G. Röpke, V. B. Priezzhev, *Nucleation Theory and Applications*, Wiley, **2005**.

[249] H. Zhang, D. Chiappe, J. Meersschaut, T. Conard, A. Franquet, T. Nuytten, M. Mannarino, I. Radu, W. Vandervorst, A. Delabie, *Journal of Chemical Physics* **2017**, *146*.

[250] N. E. Chayen, E. Saridakis, R. P. Sear, *Proceedings of the National Academy of Sciences of the United States of America* **2006**, *103*, 597.

[251] S. Khurshid, E. Saridakis, L. Govada, N. E. Chayen, *Nature Protocols* **2014**, *9*, 1621.

[252] O. Möhler, D. G. Georgakopoulos, C. E. Morris, S. Benz, V. Ebert, S. Hunsmann, H. Saathoff, M. Schnaiter, R. Wagner, *Biogeosciences* **2008**, *5*, 1425.

[253] H. Beydoun, M. Polen, R. C. Sullivan, *Atmospheric Chemistry and Physics* **2017**, *17*, 13545.

[254] B. J. Murray, D. O'Sullivan, J. D. Atkinson, M. E. Webb, *Chemical Society Reviews* **2012**, *41*, 6519.

[255] A. D'Arcy, A. Mac Sweeney, A. Haber, *Acta Crystallographica Section D* **2003**, *59*, 1343.

[256] A. S. Thakur, G. Robin, G. Guncar, N. F. W. Saunders, J. Newman, J. L. Martin, B. Kobe, *PLoS One* **2007**, *2*, 1091.

[257] A. D'Arcy, A. Mac Sweeney, A. Haber, *Journal of Synchrotron Radiation* **2004**, *11*, 24.

[258] I. Nederlof, R. Hosseini, D. Georgieva, J. Luo, D. Li, J. P. Abrahams, *Crystal Growth and Design* **2011**, *11*, 1170.

[259] M. Okamoto, K. Ishikawa, N. Tanji, S. Aoyagi, *Surface and Interface Analysis* **2012**, *44*, 736.

[260] M. Okamoto, N. Tanji, T. Habe, S. Inoue, S. Tokunaga, H. Tanamachi, *Surface and Interface Analysis* **2011**, *43*, 298.

[261] J. Yu, D. wen Yu, D. M. Checkla, I. M. Freedberg, A. P. Bertolino, *Journal of Investigative Dermatology* **1993**, *101*, 56.

[262] D. G. Georgieva, M. E. Kuil, T. H. Oosterkamp, H. W. Zandbergen, J. P. Abrahams, *Acta Crystallographica Section D* **2007**, *63*, 564.

[263] A. D'Arcy, A. Mac Sweeney, A. Haber, *Acta Crystallographica Section D* **2003**, *59*, 1343.

[264] L. Hausman, *The Scientific Monthly* **1930**, *30*, 258.

[265] S. K. Areida, M. F. Ismail, E. K. Abdel Hady, A. O. Osman, *The Egyptian Journal of Hospital Medicine* **2006**, *23*, 287.

[266] C. R. Robbins, *Chemical and Physical Behavior of Human Hair*, Springer Berlin Heidelberg, Berlin, Heidelberg, **2012**.

[267] G. E. Rogers, *Annals of the New York Academy of Sciences* **1959**, 378.

[268] V. Stanić, J. Bettini, F. E. Montoro, A. Stein, K. Evans-Lutterodt, *Scientific Reports* **2015**, *5*, 1.

[269] F. V. Hodzhaoglu, C. N. Nanev, *Crystal Research and Technology* **2010**, *45*, 281.

[270] M. A. Levenstein, L. Wayment, C. D. Scott, R. Lunt, P.-B. Flandrin, S. J. Day, C. C. Tang, C. C. Wilson, F. C. Meldrum, N. Kapur, K. Robertson, *Analytical Chemistry* **2020**, *92*, 7754.

[271] M. A. Levenstein, C. Anduix-Canto, Y. Y. Kim, M. A. Holden, C. G. Nino, D. C. Green, S. E. Foster, A. N. Kulak, L. Govada, N. E. Chayen, S. Day, C. C. Tang, B. Weinhausen, M. Burghammer, N. Kapur, F. C. Meldrum, *Advanced Functional Materials* **2019**, *29*.

[272] Z. Hammadi, N. Candoni, R. Grossier, M. Ildefonso, R. Morin, S. Veesler, *Comptes Rendus Physique* **2013**, *14*, 192.

[273] R. Grossier, A. Magnaldo, S. Veesler, *Journal of Crystal Growth* **2010**, *312*, 487.

[274] R. Cedeno, R. Grossier, N. Candoni, N. Levernier, A. E. Flood, S. Veesler, *Journal of Chemical Physics* **2023**, *158*.

[275] R. Grossier, Z. Hammadi, R. Morin, S. Veesler, *Physical Review Letters* **2011**, *107*.

[276] M. C. Biesinger, *Applied Surface Science* **2022**, *597*, 153681.

[277] N. Fairley, V. Fernandez, M. Richard-Plouet, C. Guillot-Deudon, J. Walton, E. Smith, D. Flahaut, M. Greiner, M. Biesinger, S. Tougaard, D. Morgan, J. Baltrusaitis, *Applied Surface Science Advances* **2021**, *5*, 100112.

[278] D. Perry, D. Momotenko, R. A. Lazenby, M. Kang, P. R. Unwin, *Analytical Chemistry* **2016**, *88*, 5523.

[279] V. A. Lubarda, K. A. Talke, *Langmuir* **2011**, *27*, 10705.

[280] F. Peters, D. Arabali, *Colloids and Surfaces A: Physicochemical and Engineering Aspects* **2013**, *426*, 1.

[281] O. D. Linnikov, I. G. Grigorov, I. V. Rodina, E. V. Polyakov, *Doklady Physical Chemistry* **2011**, *439*, 135.

[282] E. Saridakis, N. E. Chayen, *Trends in Biotechnology* **2009**, *27*, 99.

[283] I. Nederlof, R. Hosseini, D. Georgieva, J. Luo, D. Li, J. P. Abrahams, *Crystal Growth and Design* **2011**, *11*, 1170.

[284] S. Y. Choi, M. G. Kim, H. Inoue, *Journal of Analytical and Applied Pyrolysis* **1995**, *32*, 127.

[285] H. Lindley, *Biochemical Journal* **1948**, *42*, 481.

[286] C. R. Robbins, M. K. Bahl, *Journal of the Society of Cosmetic Chemists* **1984**, *35*, 379.

[287] Y. Diao, T. Harada, A. S. Myerson, T. Alan Hatton, B. L. Trout, *Nature Materials* **2011**, *10*, 867.

[288] J. L. Holbrough, J. M. Campbell, F. C. Meldrum, H. K. Christenson, *Crystal Growth and Design* **2012**, *12*, 750.

[289] T. F. Whale, M. A. Holden, A. N. Kulak, Y. Y. Kim, F. C. Meldrum, H. K. Christenson, B. J. Murray, *Physical Chemistry Chemical Physics* **2017**, *19*, 31186.

[290] J. F. Willart, E. Dudognon, A. Mahieu, M. Eddleston, W. Jones, M. Descamps, *European Physical Journal: Special Topics* **2017**, *226*, 837.

[291] G. E. Rogers, *Cosmetics* **2019**, *6*, 32.

[292] K. Kizawa, H. Uchiwa, U. Murakami, *Biochimica et Biophysica Acta: Molecular Cell Research* **1996**, *1312*, 94.

[293] K. Kizawa, H. Troxler, P. Kleinert, T. Inoue, M. Toyoda, M. Morohashi, C. W. Heizmann, *Biochemical and Biophysical Research Communications* **2002**, *299*, 857.

[294] K. E. Smart, M. Kilburn, M. Schroeder, B. G. H. Martin, C. Hawes, J. M. Marsh, C. R. M. Grovenor, *Journal of Cosmetics Science* **2009**, *60*, 337.

[295] M. V. De Gálvez, J. Aguilera, J. L. Bernabõ, C. Sánchez-Roldán, E. Herrera-Ceballos, *Photochemistry and Photobiology* **2015**, *91*, 966.

[296] O. F. Chernova, O. V. Zherebtsova, *Zoologischer Anzeiger* **2022**, *301*, 59.